

DEPARTMENT OF PHYSICS
INDIAN INSTITUTE OF TECHNOLOGY MADRAS
CHENNAI – 600036

Synergies in analysing binary black hole mergers

*Effect of orbital eccentricity, spin-precession, and
non-quadrupole modes*

A Thesis

Submitted by

DIVYAJYOTI

For the award of the degree

Of

DOCTOR OF PHILOSOPHY

July 2024

“As the smaller black hole plunged towards the larger one, it knew its death wouldn’t be in vain. A billion years in the future, scientists on a tiny blue planet would listen to the song it sang before it went down for the final sleep...”

To Mukesh, my partner in work and in life...

LIST OF PUBLICATIONS

I. PUBLICATIONS IN REFEREED JOURNALS APPEARING IN THESIS

- a) **Divyajyoti**, Sumit Kumar, Snehal Tibrewal, Isobel M. Romero-Shaw, Chandra Kant Mishra
Blind spots and biases: the dangers of ignoring eccentricity in gravitational-wave signals from binary black holes
Physical Review D 109, 043037 (2024). arXiv:2309.16638. ([Divyajyoti et al., 2024b](#))
- b) **Divyajyoti**, N. V. Krishnendu, Muhammed Saleem, Marta Colleoni, Aditya Vijaykumar, K. G. Arun, Chandra Kant Mishra
Effect of double spin-precession and higher harmonics on spin-induced quadrupole moment measurements
Physical Review D 109, 023016 (2024). arXiv:2311.05506. ([Divyajyoti et al., 2024a](#))
- c) **Divyajyoti**, Preet Baxi, Chandra Kant Mishra, K. G. Arun
Detectability of gravitational higher modes in the third-generation era
Physical Review D 104, 084080 (2021). arXiv:2103.03241. ([Divyajyoti et al., 2021](#))
- d) Abhishek Chattaraj, Tamal RoyChowdhury, **Divyajyoti**, Chandra Kant Mishra, Anshu Gupta
High accuracy PN and NR comparisons involving higher modes for eccentric BBHs and a dominant mode eccentric IMR model
Physical Review D 106, 124008 (2022). arXiv:2204.02377. ([Chattaraj et al., 2022](#))
- e) The LIGO Scientific Collaboration (incl. **Divyajyoti**), the Virgo Collaboration, the KAGRA Collaboration
Tests of General Relativity with GWTC-3
Accepted for publication in Physical Review D (2022). arXiv:2112.06861. ([Abbott et al., 2021g](#))

II. PUBLICATIONS IN REFEREED JOURNALS (OTHERS)

- a) Mukesh Kumar Singh, **Divyajyoti**, Shasvath J Kapadia, Md Arif Shaikh, Parameswaran Ajith
Improved early-warning estimates of luminosity distance and orbital inclination of compact binary mergers using higher order modes of gravitational radiation
Monthly Notices of the Royal Astronomical Society 513 (3), 3798–3809

(2022). arXiv:2202.05802. ([Singh et al., 2022](#))

- b) The LIGO Scientific Collaboration (incl. **Divyajyoti**), the Virgo Collaboration, the KAGRA Collaboration
GWTC-2.1: Deep Extended Catalog of Compact Binary Coalescences Observed by LIGO and Virgo During the First Half of the Third Observing Run
Physical Review D 109, 022001 (2024). arXiv:2108.01045. ([Abbott et al., 2024](#))

ACKNOWLEDGEMENTS

- I feel great pleasure in writing that **Chandra Kant Mishra** was my thesis advisor. He guided me each and every step of the way, starting with my final year of B.Tech. followed by Ph.D. Looking at his interactions with other academics, I learned how to articulate words clearly yet with humility. He introduced me to various collaborators and always encouraged me to ask questions, however elementary. Time and again, he reminded me that I should not hesitate to disagree with him. He would listen to me patiently without dismissing my ideas or disagreements, and discuss my projects at length from different perspectives. I would never be able to thank him enough for everything that he has taught me.
- In addition to being in my Doctoral Committee (DC), **K. G. Arun** was like a co-guide to me throughout my Ph.D. Whenever I got lost in the technicalities of the projects, he always reminded me to take a step back and look at the big picture. Writing papers with him helped improve my scientific writing, and I learned various aspects of gravitational waves while attending his course. I will always be grateful to him for his encouragement and support.
- It was a great experience to collaborate with **Prayush Kumar** on *ESIGMA* project. During my conversations with him, on telecons and visits to ICTS, he taught me a great deal about Gravitational Wave data analysis, and countless programming tips and tricks. He inspires me to be a better programmer and scientist, and I look forward to working with him in the future.
- I thank **B. S. Sathyaprakash** and **Anuradha Gupta** for including me in the weekly Penn State telecons. Participating in the discussions with their groups gave me an insight into various aspects of gravitational physics with the next-generation detectors. I want to thank Sathya for inviting me to visit the Penn State University and for being a wonderful host.
- I would like to thank **L. Sriramkumar** for organising various GR and Cosmology seminars. Attending these seminars provided me with broad exposure to the field. I also thoroughly enjoyed his course on Quantum Mechanics II.
- I would like to thank **Dawood Kothawala** for his intuitive questions and comments during my DC meetings and other presentations. He helped me look at topics with a different perspective and inspired me to look deeper into the results.
- I am grateful to **Suresh Govindarajan** for his encouraging words as my DC chair in various review meetings and progress reports. I also thank **Sunethra Ramanan** for her insightful suggestions at the DC meetings.
- It was a pleasure to collaborate with **N. V. Krishnendu** and **Sayantani Datta** on

SIQM projects. Krishnendu guided me at every step and was always happy to help when I felt overwhelmed. Talking to Sayantani helped me keep my sanity when we were trying to meet the deadlines.

- I thank **Sumit Kumar, Aditya Vijaykumar, and Muhammed Saleem**, who played a major role in teaching me the subtleties of Bayesian inference pipelines and post-processing methods. Having them as collaborators on various projects was an absolute delight, and I look forward to working with them in the future.
- I would like to thank **Bala R. Iyer, Archana Pai, and Sukanta Bose** for guiding me from time to time on the rules and regulations of being a member of the LVK collaboration, and the members of the LIGO India Scientific Collaboration (LISC) for weekly meetings and discussions.
- I thank **Parameswaran Ajith** for the useful discussions I had while attending the group meetings at ICTS, and whenever I had a chance to meet him. It was a pleasure to collaborate with him along with **Shasvath J. Kapadia, Md Arif Shaikh, and Mukesh Kumar Singh** on the *early warning* project.
- I am thankful to **Gregory Ashton** for guiding me through GW event analyses. It was a delight to meet him in Cardiff and discuss various aspects of GW data analysis.
- I thank **Michalis Agathos** for inviting me to visit the University of Cambridge and for the useful discussions on *Test of GR* project. I also want to thank him and **Nathan Johnson-McDaniel**, for guiding me from time to time as TGR working group chairs.
- I thank **Isobel M. Romero-Shaw** for making my visit at Cambridge a pleasant stay. It was a pleasure to work with her on the *eccentricity* project, and I look forward to our collaboration in the future.
- I would like to thank **Stephen Fairhurst, Mark Hannam, Geraint Pratten, and Thomas Dent** for discussions on various aspects of GW science during my visits to the UK and the US.
- I thank ICTS for organizing gravitational wave summer schools. It was a pleasure to meet and discuss various topics on GW science with **Harald Pfeiffer** and **Geoffrey Lovelace** during the summer school.
- I thank **Nils Andersson** for inviting me to attend the *Masterclasses in Fluid Dynamics* at the University of Southampton, and for providing me with a signed copy of his book "A Gentle Wizard".
- I would like to thank Rahul Kashyap, Gayathri Raman, Pradeepkumar Yadav, and Lorenzo Gavassino for the wonderful time I spent in Southampton.

- I am thankful to Marta Colleoni, Sebastian Khan, Ajit Mehta, Ssohrab Borhanian, Collin Capano, Guillaume Faye, Patricia Schmidt, Alexandar H. Nitz, Rahul Dhurkunde, Pankaj Saini, Sajad A. Bhat, Archisman Ghosh, and Ish Gupta for their help in various projects.
- It was a pleasure to collaborate with Preet Baxi, Abhishek Chattaraj, Tamal RoyChowdhury, Snehal Tibrewal, Gayathri V, Sijil Jose, Kaushik Paul, and Anshu Gupta on various projects.
- I thank GWECs and LAAC council members for organizing various events for early career researchers, which provided me with multiple opportunities to interact with the LVK members.
- I would like to thank NIT Agartala for signing an MOU with IIT Madras which gave me the opportunity to transfer to IIT Madras in my final year of B.Tech. and started my journey in gravitational waves.
- Some of the work included in this thesis has made use of data or software obtained from the Gravitational Wave Open Science Center (GWOSC), a service of the LIGO Scientific Collaboration, the Virgo Collaboration, and KAGRA. This material is based upon work supported by NSF's LIGO Laboratory which is a major facility fully funded by the National Science Foundation, USA. I also acknowledge the Science and Technology Facilities Council (STFC) of the United Kingdom, the Max-Planck-Society (MPS), and the State of Niedersachsen/Germany for support of the construction of Advanced LIGO and construction and operation of the GEO600 detector. Additional support for Advanced LIGO was provided by the Australian Research Council. Virgo is funded, through the European Gravitational Observatory (EGO), by the French Centre National de Recherche Scientifique (CNRS), the Italian Istituto Nazionale di Fisica Nucleare (INFN) and the Dutch Nikhef, with contributions by institutions from Belgium, Germany, Greece, Hungary, Ireland, Japan, Monaco, Poland, Portugal, Spain. KAGRA is supported by Ministry of Education, Culture, Sports, Science and Technology (MEXT), Japan Society for the Promotion of Science (JSPS) in Japan; National Research Foundation (NRF) and Ministry of Science and ICT (MSIT) in Korea; Academia Sinica (AS) and National Science and Technology Council (NSTC) in Taiwan.
- I would like to acknowledge the following computing resources: LIGO lab clusters CIT, LHO, LLO (NSF Grant Nos. PHY-0757058 and PHY-0823459), Sarathi cluster at IUCAA, AQUA cluster and Powehi workstation at IIT Madras, Alice and SONIC clusters at ICTS-TIFR, and ATLAS cluster at AEI Hannover.
- I would like to thank the Science Engineering Research Board (SERB), DST, Govt. of India (SERB Grant No. ITS/2022/001695) for funding my travel to Cardiff University to present my work in LVK conference. I would also like to acknowledge the support of SERB's Core Research Grant No. CRG/2022/007959

for supporting part of the work presented in this thesis.

- I thank the Centre for Strings, Gravitation, and Cosmology, Department of Physics, IIT Madras, and University of Cambridge for funding my academic visit to Kavli Institute of Cosmology, Cambridge.
- I would like to thank Newton-Bhabha/STFC funded collaboration between UK and LIGO-India, and IIT Madras Alumni fund for sponsoring my visit to University of Southampton.
- I would like to thank the developers of the following software and packages which made my life easy and saved a lot of my time: LALSuite, bilby, bilby_pipe, PyCBC, MATHEMATICA, gwbench, pesummary, corner, matplotlib, seaborn, pickle, h5py, deepdish, pandas, numpy, scipy, gwpy, dynesty, TeXMaker, Overleaf, Jupyter, Spyder, VS code.

Finally I would like to acknowledge the love and support of my friends and family:

- I would like to thank all the members of GW group at IIT Madras for the interesting discussions and fun outings that we had. In particular I would like to thank Soham, Nidhi, Sweta, Rimo, Pranav, Sijil, Chinmay, Aravind, Omkar, Pratul, Shashank, Dipthi, and Diksha.
- I would like to thank my friends at IITM: Santosh, Sourin, and Subhojit for their friendship.
- My years at IIT Madras were made pleasant in the company of Kaushik, Abhishek, and Laxman. I look back at our humorous discussions and outings, and I cannot imagine my life at IITM without them. It feels highly formal to say that I thank them for their love and care.
- I thank Uddepta, Souvik, and Anup for all the fun I had whenever I visited ICTS, and for making me feel part of their family with Mukesh. I especially thank Uddepta for planning all our excursions in and around Bengaluru. I also thank Srashti for guiding me from time to time as a loving senior whenever I was at ICTS.
- I thank Poulami, Pankaj, Parthapratim, and Sayantani for interesting discussions during our joint group meetings with the Chennai Mathematical Institute, and for always making me feel welcome when I visited their campus.
- I thank my B.Tech. friends from NIT Agartala Siddarth, Shashank, Pushplata, and Simran for their love and care.
- I would like to thank Adithyan, Bhavesh, Ashwin, and Rachana for making my final year of B.Tech. at IIT Madras pleasant.

- I am grateful to Sahaj Marg system (Heartfulness Meditation) for being an integral part of my life and shaping me into what I am today.
- I want to thank my family for the part they played in my Ph.D. – my father, Dr. Vikas Saxena, for sparking my interest in astronomy from childhood; my mother, Manisha Saxena, for reminding me to look at life in a simple manner whenever I over-complicated things; my sisters, Purnima and Lakshmi, who were always ready for a video call whenever I needed to de-stress; and my grandmother, Chandra Lekha Saxena, for celebrating the tiniest of my achievements with love and blessings. I also thank my in-laws for their love and care.
- Joining directly after B.Tech., Ph.D. coursework was the most stressful part of my life. I would not have reached this stage if it wasn't for Mukesh, to whom this thesis is dedicated. He spent countless hours helping me bridge the gaps in my understanding of physics, and I learned innumerable things from him during my Ph.D. It is an honor and joy to call myself his wife.

ABSTRACT

KEYWORDS Gravitational waves; Binary Black holes; test of GR; eccentricity; non-quadrupole/higher modes; spin-induced quadrupole moment, spin-precession.

While the first direct detection of gravitational wave (GW) signal was from a “vanilla” binary black hole (BBH) system, additional physical effects have been observed in the subsequent GW signals. Even though binary black hole mergers are one of the cleanest systems to model in general relativity, currently, there are no waveform models that include all physical effects. In order to correctly characterize the source properties of a GW signal, it is imperative to understand and quantify the biases which are introduced due to missing physics in the current waveforms. In this thesis, we have focussed on three different physical effects, namely, the orbital eccentricity, spin-precession, and non-quadrupole/higher order modes (HMs). We have studied the interplay of these effects on the analysis of GW signals, highlighting the short-comings and emphasizing the need for more advanced waveforms.

Most gravitational wave events observed so far by the LIGO and Virgo detectors are consistent with mergers of binary black holes on quasi-circular orbits. However, some events, such as GW190521, are also consistent with having non-zero orbital eccentricity at detection, which can indicate that the binary formed via dynamical interactions. Active GW search pipelines employing quasi-circular waveform templates are inefficient for detecting eccentric mergers. Additionally, analysis of GW signals from eccentric BBH, with waveform models neglecting eccentricity, can lead to biases in the recovered parameters. [Divyajyoti *et al.* \(2024b\)](#) explores the detectability and characterisation of eccentric signals when searches and analyses rely on quasi-circular waveform models. We find that for a reference eccentric population, the fraction of events having fitting factor (FF) < 0.95 can be up to $\approx 2.2\%$ compared to $\approx 0.4\%$ for the baseline population.

This results in the loss in signal recovery fraction for up to 6% for the region in parameter space with non-negligible eccentricity ($e_{10\text{Hz}} > 0.01$) and high mass ratio ($q > 3$). We also perform parameter estimation (PE) for non-spinning and aligned-spin eccentric injections of GWs from binaries of total mass $M = 35 M_{\odot}$, based on numerical relativity simulations and an EOB based inspiral-merger-ringdown model (TEOBResumS), and recover them using both quasi-circular and eccentric waveform models. For $e_{20\text{Hz}} \sim 0.1$, analyses using quasi-circular waveform models are unable to recover the injected chirp mass within the 90% credible interval. Further, for these low-mass injections, spin-induced precession *does not* mimic eccentricity, with PE correctly ruling out high values of effective precession parameter χ_p . For injections of $e_{20\text{Hz}} \sim 0.1$, PE conducted with an inspiral-only eccentric waveform model correctly characterises the injected signal to within 90% confidence, and recovers the injected eccentricities, suggesting that such models are sufficient for characterisation of low-mass eccentric BBH. Additionally, [Chattaraj et al. \(2022\)](#) shows that the state-of-the-art quasi-circular models including the effect of higher modes will not be adequate in extracting source properties for signals with initial eccentricities $e_{20\text{Hz}} \gtrsim 0.1$. Findings of [Divyajyoti et al. \(2024b\)](#) and [Chattaraj et al. \(2022\)](#) form the subject matter for Chapter 2.

Just like eccentricity, detection of a precessing spin system can be an indicator of a binary formed in a dynamical environment. Moreover, in the past few years, many of the waveform families have been upgraded to include spin-precession and higher-order modes, and are routinely used for parameter estimation and the subsequent downstream analyses, such as tests of general relativity. One of the tests which has used a precessing spin waveform model (IMRPhenomPv2) for the events in the third gravitational wave transient catalogue (GWTC-3) to gauge the binary black hole nature of the source ([Abbott et al., 2021g](#)), is the spin-induced quadrupole moment (SIQM) test. In this test, bounds are obtained on a deviation parameter ($\delta\kappa$) related to the parameter (κ) that quantifies the degree of deformation due to the spin of individual binary components on leading (quadrupolar) spin-induced moment. In [Abbott et al. \(2021g\)](#), it was found that the

spin-induced quadrupole moments of the binary black hole constituents of GWTC-3 events were consistent with those of Kerr black holes in GR. [Divyajyoti *et al.* \(2024a\)](#) extends the earlier SIQM-based null tests for BBH nature, by employing waveform models that account for double spin-precession and higher modes. We find that waveform with double spin-precession gives better constraints for $\delta\kappa$, compared to waveform with single spin-precession. We also revisit earlier constraints on the SIQM-deviation parameter for selected GW events observed through the first three observing runs (O1–O3) of LIGO-Virgo detectors. Additionally, the effects of HMs on the test are also explored for a variety of mass-ratio and spin combinations by injecting simulated signals in zero-noise. Our analyses indicate that binaries with mass-ratio greater than 3 and significant spin precession may require waveforms that account for spin-precession and HMs to perform the parameter estimation reliably. Results based on [Divyajyoti *et al.* \(2024a\)](#) and those presented in SIQM section of [Abbott *et al.* \(2021g\)](#) are included in Chapter 3.

The relative contribution from HMs becomes significant for binaries with asymmetric masses and/or whose orbital planes are not optimally inclined towards the line of sight. [Divyajyoti *et al.* \(2021\)](#) explores the detection of HMs in third-generation ground-based detectors such as Cosmic Explorer and Einstein Telescope. Using the astrophysical population of binary black holes based on events reported in the second gravitational wave transient catalog by LIGO and Virgo (GWTC-2), in conjunction with the Madau-Dickinson model for redshift evolution of the binary black hole mergers, we assess the detectability of these HMs using a network consisting of three third-generation detectors. We find that the two sub-leading modes [(3,3) and (4,4)] can be detected in approximately 30% of the population with a network signal-to-noise ratio of 3 or more, and for nearly 10% of the sources, the five leading modes will be detectable. Besides, a study concerning the effect of binary's mass ratio and its orbital inclination with the observer's line-of-sight in detecting various modes is presented. For a few selected events of the LIGO-Virgo catalog, we identify the modes that would have been detected if a third-generation detector was operational when these events were recorded. We

also compute the detectability of HMs by Voyager and find that only $\sim 6\%$ and 2% of the detectable population will have an associated detection of (3,3) and (4,4) modes, respectively. Observing these HMs in the 3G era would have a huge impact on the science possible with these detectors, ranging from astrophysics and cosmology to testing strong-field gravity. The findings of [Divyajyoti *et al.* \(2021\)](#) are included in Chapter 4 of the thesis.

CONTENTS

		Page
	ACKNOWLEDGEMENTS	i
	ABSTRACT	vii
	LIST OF TABLES	xiii
	LIST OF FIGURES	xv
	ABBREVIATIONS	xix
	LIST OF WAVEFORM MODELS USED	xxi
	NOTATION	xxiii
CHAPTER 1	INTRODUCTION	1
1.1	History of gravitational waves	1
1.2	Sources	7
	1.2.1 Chirps	9
	1.2.2 Continuous Gravitational Waves	9
	1.2.3 Gravitational Wave Bursts	10
	1.2.4 Stochastic Gravitational Wave Background	12
1.3	Detectors	13
	1.3.1 Response of a ground-based interferometric detector	15
	1.3.2 Current interferometric detectors	18
	1.3.3 Future detectors	20
1.4	Observed events and their implications	24
	1.4.1 Exceptional events	26
	1.4.2 Population of merging compact binaries	29
	1.4.3 Tests of general relativity	31
1.5	Searches and parameter estimation	33
	1.5.1 Search pipelines	35
	1.5.2 Binary Black Hole parameter space	36
	1.5.3 Bayesian inference	37
	1.5.4 Samplers	40
1.6	Physical effects in GW signals from binary black hole mergers	43
	1.6.1 Orbital eccentricity	44
	1.6.2 Spin-precession	49
	1.6.3 Non-quadrupole modes	51
	1.6.4 Impact of spin-precession and higher modes on SIQM test	55
	1.6.5 Interplay of orbital eccentricity, spin-precession, and higher modes	58

CHAPTER 2	DETECTION AND PARAMETER ESTIMATION OF ECCENTRIC BINARY BLACK HOLE MERGERS	63
2.1	Introduction	63
2.2	Reduced GW search sensitivity to eccentric binaries	64
2.2.1	Reduced detectability of eccentric systems	65
2.3	Mischaracterizing eccentric binaries with parameter estimation	71
2.3.1	Dominant mode, non-spinning, eccentric injections	75
2.3.2	Dominant mode, aligned-spin, eccentric injections	87
2.3.3	Simulated noise injections: dominant mode, non-spinning and eccentric	94
2.3.4	Higher mode, non-spinning, eccentric injections	95
2.4	Summary and Conclusions	102
CHAPTER 3	TESTING FOR BLACK HOLE MIMICKERS IN GW DATA	105
3.1	Introduction	105
3.2	Analysis Setup	107
3.3	Results from GWTC-3	108
3.4	Results from simulated signals	111
3.4.1	Comparison of $\delta\kappa_s$ estimates: IMRPhenomXP and IMRPhenomPv2	114
3.4.2	Effect of higher modes and possible systematic biases	124
3.5	Revisiting real events with models including the effect of spin-precession and higher modes	128
3.6	Summary	131
CHAPTER 4	DETECTABILITY OF NON-QUADRUPOLE MODES IN FUTURE DETECTORS	133
4.1	Introduction	133
4.2	Detection criteria and detector networks	134
4.2.1	Detection criteria	134
4.3	Detecting higher modes of GWTC-2 events using 3G detectors	137
4.4	Higher modes in different regions of the parameter space	138
4.5	Population Study	143
4.5.1	Population models	143
4.5.2	Detector networks	146
4.5.3	SNR distribution of higher modes	148
4.6	Summary	150
CHAPTER 5	CONCLUSIONS AND FUTURE DIRECTIONS	153
APPENDIX A	SPIN-INDUCED QUADRUPOLE MOMENT	157
BIBLIOGRAPHY		161

LIST OF TABLES

Table	Caption	Page
1	List of quasi-circular, frequency-domain, phenomenological waveforms	xxi
2	List of eccentric waveform models	xxi
2.1	<i>SRF</i> for various injection sets quantifying the reduced detectability of eccentric signals when circular template bank is used	69
2.2	Priors for parameters used in various quasi-circular and eccentric recoveries	73
2.3	List of non-spinning, eccentric NR hybrid simulations (Chattaraj et al., 2022) and injections based on aligned-spin eccentric EOB model TEOBResumS (Nagar et al., 2018)	74
2.4	List of non-spinning, eccentric NR hybrid simulations (Chattaraj et al., 2022) used for HM injections	95
3.1	List of waveform models used in SIQM chapter	106
3.2	List of events analysed for SIQM test	109
3.3	Priors for parameters used in precessing spin recoveries	112
3.4	Values of spin parameters for mass ratio variation study.	115
3.5	Values of spin parameters for χ_{eff} variation study.	120
3.6	Values of spin parameters for χ_p variation study.	124
4.1	Detectability of higher modes in GWTC-2 events using a 3G detector	137
4.2	Values of model parameters for mass models used in the population study.	144
4.3	The detector locations used in HM detectability study	147

LIST OF FIGURES

Figure	Caption	Page
1.1	A sketch of Weber’s cylinder detector	4
1.2	Gravitational wave chirp from GW150914	8
1.3	Sketch of a rotating neutron star emitting continuous GWs	10
1.4	Frequency evolution of a continuous wave GW signal	11
1.5	Diagram showing different epochs since the Big Bang and when gravitational waves and the CMB came into existence.	12
1.6	A monochromatic gravitational wave of pulsation $\omega = 2\pi/T$ propagates along the z- direction	14
1.7	The relative orientation of the sky and detector frames	16
1.8	Basic Michelson interferometer with Fabry Perot cavities and Power Recycling mirror	20
1.9	Detector sensitivity curves for various ground-based detectors	21
1.10	The gravitational-wave spectrum probed by strain-sensitive gravitational-wave detectors, ranging from 10^{-9} Hz to more than 1000 Hz	23
1.11	Masses of announced gravitational-wave detections, and black holes and neutron stars previously constrained through electromagnetic observations	25
1.12	A simplified schematic summarizing the main steps in LIGO–Virgo data processing	38
1.13	Mitigation of the glitch in LIGO-Livingston data for GW170817	41
1.14	A diagram illustrating the relationship between the various angular elements in a binary system with orbital eccentricity e , reduced mass μ , and total mass M	45
1.15	Artist’s depiction of two black holes falling into a dance as they spiral towards each other and eventually collide	46
1.16	Diagram of the vectors and angles that define the spinning BBH problem	50
1.17	Diagrams showing the effect of including higher modes, spins, and orbital eccentricity in a binary black hole gravitational waveform	59
2.1	Cumulative fraction of events above a given Fitting Factor (FF) for various populations	67
2.2	The Fitting Factor (FF) varying with mass ratio (q) and eccentricity measured at 10 Hz ($\log_{10}(e)$)	68
2.3	PN-NR hybrid waveform corresponding to NR simulation SXS:BBH:1364	72
2.4	Chirp mass posteriors for non-spinning injections with mass ratios ($q = 2, 3$)	76
2.5	Posteriors for $q = 1$ for non-spinning quasi-circular and eccentric injections	77
2.6	Corner plot for $q = 2$ showing posteriors on \mathcal{M} , χ_{eff} , and χ_p , for precessing-spin recovery of both quasi-circular and eccentric, non-spinning injections	79
2.7	Corner plot for $q = 3$ showing posteriors on \mathcal{M} , χ_{eff} , and χ_p , for the precessing-spin recovery of both quasi-circular and eccentric, non-spinning injections	80

2.8	Corner plot for $q = 1$ showing posteriors on \mathcal{M} , χ_{eff} , and χ_p , for the precessing-spin recovery of both quasi-circular and eccentric, non-spinning injections	81
2.9	Recovery with TaylorF2Ecc for eccentric and quasi-circular injections in the form of violin plots	83
2.10	Eccentricity posteriors for $q=(1, 2, 3)$ when the injections are non-spinning and eccentric, and the recovery is with TaylorF2Ecc in eccentric, non-spinning configuration	84
2.11	Corner plot showing \mathcal{M} , q , and e_{20} posteriors, for $q = 1$, non-spinning recovery from Fig. 2.9 performed using TaylorF2Ecc	85
2.12	Same as Fig. 2.11 but for $q = 2$ (top) and $q = 3$ (bottom).	86
2.13	Eccentric and quasi-circular aligned-spin injections, recovered in quasi-circular aligned-spin (AS), eccentric aligned-spin (e-AS), and eccentric non-spinning (e-NS), and quasi-circular precessing-spin (PS) configurations	88
2.14	Same as Fig. 2.6, but for aligned-spin injections with mass ratios $q = 1.25$ (top) and $q = 2$ (bottom).	89
2.15	Same as Fig. 2.14 but for $q = 3$	90
2.16	Eccentricity posteriors for $q = (1.25, 2, 3)$ when the injections are aligned-spin and eccentric, and the recovery is with TaylorF2Ecc in eccentric, aligned-spin configuration	91
2.17	Corner plot of \mathcal{M} , q , χ_{eff} , and e , for $q = 1.25$ aligned spin recovery from Fig. 2.13 performed using TaylorF2Ecc	92
2.18	Same as Fig. 2.17 but for $q = 2$ (top) and $q = 3$ (bottom).	93
2.19	The chirp mass posteriors, for injections with mass ratios $q = 1, 2, 3$, compared between eccentric and quasi-circular non-spinning injections, all recovered using IMRPhenomXAS with zero spins	94
2.20	PN-NR hybrid waveform corresponding to NR simulation SXS:BBH:1364, an asymmetric mass binary with mass ratio $q=2$	96
2.21	Chirp-mass recovery of circular and eccentric injections using quasi-circular higher mode waveforms	97
2.22	Corner plot for higher mode injections of $q = 1$	99
2.23	Same as Fig 2.22 but for $q = 2$	100
2.24	Same as Fig 2.22 but for $q = 3$	101
3.1	The posterior probability distribution on the SIQM deviation parameter, $\delta\kappa_s$, from the O3b events listed Table 3.2	110
3.2	Violin plots showing posterior distributions for the SIQM-deviation parameter for various injection studies using IMRPhenomXP	113
3.3	Corner plot for fixed spin magnitudes and angles given in Table 3.4 for $q = 1$	116
3.4	Same as Fig. 3.3 but for $q = 1.5$	117
3.5	Same as Fig. 3.3 but for $q = 3$	118
3.6	Same as Fig. 3.3 but for $q = 5$	119
3.7	Corner plot for $q = 1.5$, $\chi_p = 0.3$, and $\chi_{\text{eff}} = 0.3$	121
3.8	Same as Fig. 3.7 but for $\chi_{\text{eff}} = 0.5$	122
3.9	Same as Fig. 3.7 but for $\chi_{\text{eff}} = 0.7$	123

3.10	Posterior distributions of the SIQM deviation parameter for higher mode, precessing-spin injections	125
3.11	Corner plot for $q = 1$ showing posterior on $\delta\kappa_s$, \mathcal{M} , q , χ_{eff} , and χ_p . . .	127
3.12	Posterior distributions on $\delta\kappa_s$ for observed GW events	129
3.13	Corner plot for GW190412 showing posteriors on $\delta\kappa_s$, χ_{eff} , and q	130
4.1	Fixed SNR (=3) contours for various higher modes, corresponding to different total mass systems in the $(q - \iota)$ plane	140
4.2	Same as Fig. 4.1 but for low spin values $\chi_{1z} = 0.3$ and $\chi_{2z} = 0.2$	142
4.3	2D distribution of injected values of total mass (M) and redshift(z) . . .	145
4.4	Cumulative SNR histograms for six leading modes, with the two mass distribution models (PL+P and BPL) coupled with the MDBN model for redshift evolution	149
4.5	Cumulative histograms of SNR for various higher modes as a comparison between various generations of detectors	150

ABBREVIATIONS

Bilby	Bayesian inference library
LALSuite	LSC Algorithm Library Suite
PyCBC	Python-based toolkit for Compact Binary Coalescence signals
aLIGO	Advanced LIGO
BBH	Binary Black Hole
BH	Black Hole
BNS	Binary Neutron Star
CE	Cosmic Explorer
CMB	Cosmic Microwave Background
ECO	Exotic Compact Object
EM	Electro-Magnetic
EOB	Effective-One Body formalism
ET	Einstein Telescope
FAR	False Alarm Rate
FF	Fitting Factor
GR	General theory of Relativity
GRB	Gamma-Ray Burst
GW	Gravitational Wave
GWTC	Gravitational Wave Transient Catalog
HM	Higher Mode
IMR	Inspiral-Merger-Ringdown

ISCO	Innermost Stable Circular Orbit
KAGRA	KAmioka GRAvitational-wave detector
LIGO	Laser Interferometer Gravitational-wave Observatory
LISA	Laser Interferometer Space Antenna
LSC	LIGO Scientific Collaboration
LSO	Last Stable Orbit
LVK	LIGO-Virgo-KAGRA
MCMC	Markov Chain Monte Carlo
NR	Numerical Relativity
NSBH	Neutron-Star Black Hole
O1	First observing run. Similarly for O2, O3, and O4
PE	Parameter Estimation
PN	Post-Newtonian formalism
PSD	Power Spectral Density
PTA	Pulsar Timing Array
RIT	Rochester Institute of Technology catalog
SIQM	Spin-Induced Quadrupole Moment
SNR	Signal-to-Noise Ratio
SRF	Signal Recovery Fraction
SXS	Simulating eXtreme Spacetimes catalog
TB	Template Bank
TGR	Test of General Relativity

LIST OF WAVEFORM MODELS USED

Waveform name	Modes ($\ell, m $)	Features
IMRPhenomD	(2,2)	(Khan <i>et al.</i> , 2016) Aligned spin
IMRPhenomPv2	(2,2)	(Hannam <i>et al.</i> , 2014) Single-spin precession, based on IMRPhenomD
IMRPhenomHM	(2,2), (2,1), (3,3), (3,2), (4,4), (4,3)	(London <i>et al.</i> , 2018) Higher modes, aligned spin, based on IMRPhenomD
IMRPhenomXAS	(2,2)	(Pratten <i>et al.</i> , 2020) Aligned spin, multi-banding
IMRPhenomXHM	(2,2), (2,1), (3,3), (3,2), (4,4)	(García-Quirós <i>et al.</i> , 2020) Higher modes, aligned spin, multi-banding, based on IMRPhenomXAS
IMRPhenomXPHM	(2,2), (2,1), (3,3), (3,2), (4,4)	(Pratten <i>et al.</i> , 2021) Higher modes, double-spin precession, multi-banding, based on IMRPhenomXHM
IMRPhenomXP	(2,2)	(Pratten <i>et al.</i> , 2021) Double spin-precession, multi-banding, limiting case of IMRPhenomXPHM

Table 1: Quasi-circular, frequency-domain, phenomenological waveforms, modelling the entire inspiral-merger-ringdown regime. The columns denote the name of the waveform approximant coded up in LALSuite, the spherical harmonic modes (in the co-precessing frame for waveforms with spin-precession), and main features of the waveform along with the most relevant publication.

Waveform name	Features
TaylorF2Ecc	(Moore <i>et al.</i> , 2016) Inspiral-only, frequency-domain, eccentricity corrections in phase, quasi-circular aligned spins
EccentricFD	(Huerta <i>et al.</i> , 2014) Inspiral-only, frequency domain, eccentricity corrections in both amplitude and phase, non-spinning
TEOBResumS ¹	(Chiaromello and Nagar, 2020) Inspiral-merger-ringdown, time-domain, eccentricity corrections in both amplitude and phase, aligned-spin
ENIGMA	(Huerta <i>et al.</i> , 2018) Inspiral-merger-ringdown, time-domain, eccentricity corrections in both amplitude and phase, non-spinning

Table 2: Eccentric, dominant mode, waveform models.

¹For TEOBResumS, the higher mode version TEOBiResumS_SM (Nagar *et al.*, 2020) is also available, but we have used the dominant mode version in this thesis.

NOTATION

α	Right ascension	rad
χ_{eff}	Effective inspiral spin parameter $\chi_{\text{eff}} = (\chi_1 m_1 + \chi_2 m_2)/(m_1 + m_2)$	–
χ_i	Aligned spin of i^{th} object: projection of the i^{th} object spin onto the orbital angular momentum (defined at a reference frequency) $\chi_i = a_i \cos(\theta_i)$	–
χ_i^\perp	i^{th} object in-plane spin: magnitude of the projection of the i^{th} object spin onto the orbital plane (defined at a reference frequency) $\chi_i^\perp = a_i \sin(\theta_i) $	–
δ	Declination	rad
$\delta\kappa_a$	Anti-symmetric combination of SIQM deviation parameter $\delta\kappa_a = (\delta\kappa_1 - \delta\kappa_2)/2$	–
$\delta\kappa_i$	SIQM deviation parameter of the i^{th} object $\kappa_i = 1 + \delta\kappa_i$	–
$\delta\kappa_s$	Symmetric combination of SIQM deviation parameter $\delta\kappa_s = (\delta\kappa_1 + \delta\kappa_2)/2$	–
η	Symmetric mass ratio: A definition of mass ratio which is independent of the identity of the primary/secondary mass $\eta = q/(1+q)^2 \leq 0.25$	–
$\eta_{\alpha\beta}$	Minkowski metric tensor	–
\hat{L}	Unit vector along the orbital angular momentum axis of the binary	–
ι	Inclination angle: Zenith angle between the orbital angular momentum and the line of sight	rad
κ_a	Anti-symmetric combination of SIQM parameter $\kappa_a = (\kappa_1 - \kappa_2)/2$	–
κ_i	SIQM parameter of the i^{th} object	–
κ_s	Symmetric combination of SIQM parameter $\kappa_s = (\kappa_1 + \kappa_2)/2$	–

\mathcal{M}	Chirp mass of the binary $\mathcal{M} = (m_1 m_2)^{3/5} / (m_1 + m_2)^{1/5}$	M_\odot
M_\odot	Solar mass	kg
ν	PN symmetry coefficient $\nu = m_1 - m_2 / (m_1 + m_2)$	–
ϕ_{JL}	Difference between total and orbital angular momentum azimuthal angles (defined at a reference frequency)	rad
ϕ_c	Phase of coalescence of the binary	rad
ϕ_{12}	Difference between the azimuthal angles of the individual spin vector projections onto the orbital plane (defined at a reference frequency)	rad
ψ	Polarization angle of the source	rad
χ_p	Effective spin-precession parameter (defined at a reference frequency) $\chi_p = \max\{\chi_1^\perp, \chi_2^\perp q(3 + 4q)/(4 + 3q)\}$	–
θ_{JN}	Zenith angle between the total angular momentum and the line of sight	rad
θ_i	Zenith angle between the spin and orbital angular momenta for the i^{th} object (defined at a reference frequency)	rad
\vec{S}_i	Spin angular momentum vector of the i^{th} object	–
a_i	Dimensionless spin magnitude of the i^{th} object (defined at a reference frequency) $a_i = c \vec{S}_i /(Gm_i^2)$	–
c	Speed of light in vacuum	m s^{-1}
d_L	Luminosity distance to the source	Mpc
e_{ref}	Orbital eccentricity defined at a reference frequency f_{ref} E.g. e_{20} is eccentricity defined at 20 Hz	–
G	Universal gravitational constant	$\text{kg}^{-1}\text{m}^3\text{s}^{-2}$
$g_{\alpha\beta}$	Metric tensor	–

h_+	Plus polarization of gravitational wave strain	–
h_\times	Cross polarization of gravitational wave strain	–
M	Total mass of the binary $M = m_1 + m_2$	M_\odot
m_1	Mass of the primary (heavier) object in the binary	M_\odot
m_2	Mass of the secondary (lighter) object in the binary	M_\odot
m_i^{source}	Source-frame mass of the i^{th} object $m_i^{\text{source}} = m_i/(1+z)$	M_\odot
p_{astro}	Probability of astrophysical origin	–
q	Mass ratio $q = m_1/m_2 \geq 1$	–
R	Ricci scalar	m^{-2}
$R_{\alpha\beta}$	Ricci tensor	m^{-2}
t_{gps}	GPS reference time at the geocenter	s
t_c	Time of coalescence of the binary	s
$T_{\alpha\beta}$	Stress-energy tensor	$\text{kg m}^{-1}\text{s}^{-2}$
z	Redshift of the source depending on specified cosmology	–

CHAPTER 1

INTRODUCTION

Gravity! A force as old as time itself! Since the beginning of civilisation, mankind has tried to make sense of nature's fundamental forces, to peek under the matrix and get answers to questions immemorial. Over time, as empires rose and fell, our understanding of the universe, fundamental forces and particles, physics and mathematics evolved, but one constant remained: *curiosity*. It is this curiosity that drives scientists today to look beyond the realms of the known, to look for objects which are beyond our imagination, and to look back in time in an attempt to uncover the greatest mysteries of the universe: how it was formed, how it evolved, and what will be its end. Gravitational wave astronomy (GWA) is one such branch of physics that attempts to answer these questions by looking for signatures of perturbations in the very fabric of spacetime. Standing on the shoulders of giants, in this **thesis**, I attempt to answer some of the questions which plague the gravitational wave community today.

1.1 HISTORY OF GRAVITATIONAL WAVES

Modern mathematical description of gravitational force goes back as early as the 16th and 17th century when a number of scientists, including Grimaldi and Riccioli (Heilbron, 1979), Robert Hooke (Hooke, 1674), Bullialdus and Borelli (Borelli, 1666; Boulliau, 1645), and Isaac Newton, (Newton, 1687) claim to have contributed towards the formulation of the inverse square law nature of the gravitational force. Only after Einstein published his work on the General Theory of Relativity (Einstein, 1916) did physicists perceive gravity as the curvature of spacetime instead of a force. The nature of this distortion of spacetime can be understood by looking at Einstein's field equations, which are a set of 10 coupled, non-linear partial-differential equations written compactly

as

$$R_{\alpha\beta} - \frac{1}{2}Rg_{\alpha\beta} = \frac{8\pi G}{c^4}T_{\alpha\beta} \quad (1.1)$$

The left-hand side of Eq. (1.1) describes the geometry/curvature of the spacetime around the gravitating body, and the right-hand side denotes the energy and momentum of the source. In Eq. (1.1), $R_{\alpha\beta}$ is the Ricci tensor, which represents how a volume in curved space differs from a volume in Euclidean space; R is the Ricci scalar which characterizes the curvature of spacetime; $g_{\alpha\beta}$ is the metric tensor; G and c are universal gravitational constant and speed of light in vacuum respectively; and $T_{\alpha\beta}$ is the stress-energy tensor that describes the density and flux of energy and momentum in spacetime, and is the source of the gravitational field. In 1905, Henri Poincaré suggested that accelerated masses in the relativistic field theory of gravity should produce gravitational waves, similar to an accelerating electric charge producing electromagnetic waves (Poincaré, 1906). Einstein pursued the idea that wave-like solutions were possible for his equations.

Far from the source (in the weak field regime), the metric $g_{\alpha\beta}$ appearing in Eq. (1.1) can be written as a linear perturbation to the Minkowski (flat) metric $\eta_{\alpha\beta}$ (Denson Hill and Nurowski, 2016) as:

$$g_{\alpha\beta} = \eta_{\alpha\beta} + h_{\alpha\beta} \quad (1.2)$$

where $h_{\alpha\beta}$ is a small metric perturbation ($|h_{\alpha\beta}| \ll |\eta_{\alpha\beta}|$). This leads to the linearized form of Einstein equations [Eq. (1.1)] which can be written as (see Maggiore, 2007, for complete derivation):

$$\square \bar{h}_{\alpha\beta} + \eta_{\alpha\beta} \partial^\mu \partial^\nu \bar{h}_{\mu\nu} - \partial^\mu \partial_\beta \bar{h}_{\alpha\mu} - \partial^\mu \partial_\alpha \bar{h}_{\beta\mu} = \frac{16\pi G}{c^4} T_{\alpha\beta}, \quad (1.3)$$

where

$$\bar{h}_{\alpha\beta} = h_{\alpha\beta} - \frac{1}{2}\eta_{\alpha\beta}\eta^{\mu\nu}h_{\mu\nu}, \quad (1.4)$$

and $\square \equiv \eta_{\alpha\beta}\partial^\alpha\partial^\beta = \partial_\alpha\partial^\alpha$ is the flat space d'Alembertian in the context of linearized

theory. Choosing the harmonic gauge:

$$\partial^\alpha \bar{h}_{\alpha\beta} = 0, \quad (1.5)$$

Eq. (1.3) reduces to:

$$\square \bar{h}_{\alpha\beta} = -\frac{16\pi G}{c^4} T_{\alpha\beta} \quad (1.6)$$

and outside the source ($T_{\alpha\beta} = 0$) gives:

$$\square \bar{h}_{\alpha\beta} = 0. \quad (1.7)$$

which is a system of relativistic wave equations. Since $\square = -(1/c^2)\partial_t^2 + \vec{\nabla}^2$, Eq. (1.7) implies that gravitational waves travel at the speed of light. Further, choosing the *transverse-traceless gauge*, or TT gauge (see [Maggiore, 2007](#), for complete derivation):

$$h^{0\beta} = 0, \quad h^i_i = 0, \quad \partial^j h_{ij} = 0 \quad (1.8)$$

Eq. (1.7) has plane wave solutions:

$$h_{ab}^{\text{TT}}(t, z) = \begin{pmatrix} h_+ & h_\times \\ h_\times & -h_+ \end{pmatrix}_{ab} \cos[\omega(t - z/c)] \quad (1.9)$$

where z is the direction of propagation, ω is the frequency of the wave, and $a, b = 1, 2$ are indices in the transverse (x, y) plane. Thus, GWs have two polarizations with h_+ and h_\times denoting the amplitudes of the "plus" and "cross" polarizations respectively.

In the years (decades) to come, there was much debate on the existence and propagation of gravitational waves ([Cervantes-Cota *et al.*, 2016](#); [Eddington, 1922](#); [Einstein and Rosen, 1937](#); [Kennefick, 2005](#); [Pirani, 1956](#)). More importantly, ideas were discussed on whether these waves were tangible enough to be detected, and whether they even carried energy ([American Institute of Physics, 1995](#); [Pirani, 1956](#); [Rickles and DeWitt, 2011](#)). Feynman with his "sticky bead argument" had a significant role in convincing many of the scientific minds at the Chapel Hill Conference 1957 that gravitational waves carry energy ([Bondi, 1957](#); [Feynman, 1961](#); [Rickles and DeWitt, 2011](#)). Joseph Weber, also

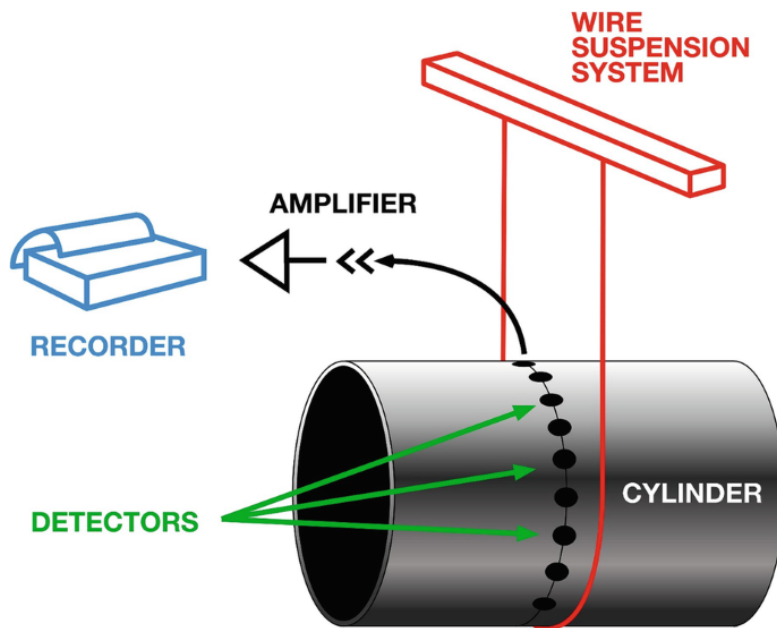


Figure 1.1: [Taken from *Beckman (2021)*] A sketch of Weber's cylinder detector.

present at the conference, was inspired by the discussions to build a detector to detect gravitational wave signals ([Weber, 1960](#)).

He built a detector that measured the vibrations induced in a large metal cylinder due to the passing of gravitational waves ([Weber, 1966](#)). A steel wire suspended the cylinder from a support built to isolate vibrations of its environment, and the whole setup was placed inside a vacuum chamber (Fig. 1.1). A belt of piezoelectric crystals placed around the cylinder measured the vibrations and converted them into electrical signals. Two such detectors were built, one at the University of Maryland and another at Argonne National Laboratory, 950 km apart, to eliminate spurious local signals ([Cervantes-Cota et al., 2016](#)). In 1969, Weber's team published the results claiming the detection of gravitational waves ([Weber, 1969](#)). The following year, Weber claimed to detect multiple signals originating from the center of the Milky Way ([Weber, 1970](#)). While Weber maintained his original position on the subject ([Weber, 1971](#)), the other scientific groups showed that the signals were unlikely to be gravitational wave signals ([Kafka, 1972](#); [Sciama et al., 1969](#)). Regardless of whether the scientific minds agreed on the credibility

of these detections, several groups started a hunt for gravitational wave signals, building their own detectors and improving upon the design of the cylindrical "antennas" (Thorne, 1987). In the years to come, with multiple detectors collecting data, there was a growing consensus among the community that no gravitational wave signals were being captured (Billing *et al.*, 1975; Billing and Winkler, 1976; Collins and Drever, 2005; Douglass *et al.*, 1975; Drever *et al.*, 1973; Endal and Sofia, 1977; Giffard, 1976; Hirakawa and Narihara, 1975; Hough *et al.*, 1975; Kafka and Schnupp, 1978; Levine and Garwin, 1974; Moss *et al.*, 1971). Just when gravitational wave searches were starting to lose hope, the detection of a binary pulsar system by Hulse and Taylor in 1974 (Taylor *et al.*, 1979) redoubled the efforts towards building broadband detectors to detect gravitational wave signals and added fuel to the idea of the interferometric method of gravitational wave detection (Allen and Christodoulides, 1975; Braginskii, 1966; Gertsenshtein and Pustovoit, 1962; Thorne, 1987; Weiss, 1976).

Interferometric gravitational wave detectors (which eventually led to the direct detection of gravitational waves in 2015) exploit the fact that a gravitational wave signal passing through matter stretches it in one direction while compressing it in the perpendicular direction. We have touched upon how this is done in the section dedicated to current and future detectors (Sec. 1.3). Robert L. Forward, in 1971, published the design for the first interferometric gravitational wave detector (Forward, 1978), acknowledging the contribution of Weber towards the idea (Moss *et al.*, 1971). Parallely, in the years that followed, Rainer Weiss, along with David Shoemaker, made several efforts towards solidifying an interferometric gravitational wave detector and received funding from the National Science Foundation (NSF) (Collins, 1976; De Sabbata and Weber, 1977; Shoemaker *et al.*, 1988; Weiss, 1976). Several other groups, either in collaboration or independently, worked on their own designs for interferometric detectors (Accadia *et al.*, 2012; Brilliet, 1985; Hough *et al.*, 1986; Hough *et al.*, 1989; Leuchs *et al.*, 1987; Shoemaker *et al.*, 1985; Weiss, 2000; Winkler *et al.*, 1985) but most were not materialised due to a lack of funding.

In the summer of 1975, Weiss and Kip Thorne discussed various ideas for ground-based and space-based laser interferometers (Levin, 2017; Weiss, 1976), and settled on a ground-based laser interferometer. To that effect, in 1978, Thorne offered the job of building the detector to Ronald Drever at Caltech, and in late 1979, the NSF granted funds to Caltech and MIT to build the detectors (albeit on a much smaller scale compared to the current detectors). In the meantime, Weiss was corresponding with the director of the NSF Gravitational Physics division, Richard Isaacson, to build detectors which had arms at the scale of kilometers. Since funding both the MIT and Caltech projects was not deemed feasible by NSF, a single project named "Laser Interferometer Gravitational-Wave Observatory" (LIGO) was started jointly by Caltech-MIT and was approved to be funded by the NSF (Levin, 2017; Linsay *et al.*, 1983; Ruthen, 1992) in 1988. Due to tensions between Weiss and Drever (Cervantes-Cota *et al.*, 2016; Collins, 2004, 2003; Niels Bohr Library & Archives, 2020), the project underwent a series of changes and delays, and finally, Barry C. Barish was appointed the director. Barish put an organisational structure to the project and a step-wise upgrade plan for the detectors *viz.* initial-LIGO (iLIGO) and advanced-LIGO (aLIGO). Two LIGO detectors, one in Hanford and another in Livingston, were proposed to be built, and the construction ended in 1997. The LIGO laboratory and LIGO Scientific Collaboration were also founded to take care of the administration of laboratories, and scientific & technological research, respectively.

In parallel, with the help of funding from German and British agencies, and donation of land by the University of Hanover and the State of Lower Saxony, construction of a 600 m detector (GEO 600) started in September 1995 (Max-Planck-Institut für Gravitationsphysik, 2005) in Germany. The detector started its operation in December 2002. While GEO 600 was being planned, the Virgo project, a collaboration between the French and Italian group of scientists, was approved by the French CNRS (Le Centre National de la Recherche Scientifique) in 1993 and Italian INFN (Istituto Nazionale di Fisica Nucleare) in 1994 (Bordé, 1985). The construction for Virgo started in 1996 but faced several hiccups between 1996-1999 (Shoemaker *et al.*, 1985). To continue the

project in a more organized manner, the European Gravitational Observatory (EGO) consortium was formed by CNRS and INFN. In June 2003, the construction of the initial Virgo detector was completed ([EGO Consortium, 2003](#); [Levin, 2017](#)).

Over the next decade or so, the alliance between LIGO, GEO 600, and Virgo detectors continued, improving the detector technologies. LIGO Scientific Collaboration (LSC) grew to become a worldwide collaboration with scientists from numerous countries working on various aspects of gravitational wave science and detection. The first observation run for initial LIGO was from 2002 to 2010, where it did not detect any GW signals. Between 2010 and 2015, various upgrades were made to the detectors, and aLIGO was formed.

It was 13th September 2015, and there were still four days until the start of the official observation run of Advanced LIGO, but nature was getting impatient. On the morning of 14th September 2015, a gravitational wave signal, originating from the merger of two inspiralling black holes 1300 million light years from Earth, passed through the LIGO detectors and created history. The signal was detected in both detectors, and calculations confirmed the time delay between the two triggers to be consistent with the general theory of relativity. The event was named GW150914¹ and, after rigorous checks and analyses, was published by the LIGO Scientific Collaboration and Virgo Collaboration in February 2016 ([Abbott *et al.*, 2016a](#)). The following year, on 3rd October 2017, Rainer Weiss, Barry C. Barish, and Kip S. Thorne were awarded the Nobel prize “for decisive contributions to the LIGO detector and the observation of gravitational waves” ([Nobel Prize, 2017](#)).

1.2 SOURCES

Gravitational waves can be represented as a time-dependent perturbation to the metric tensor for flat spacetime, produced by a time-varying quadrupole moment at the leading

¹GW followed by the detection date in YYMMDD format.

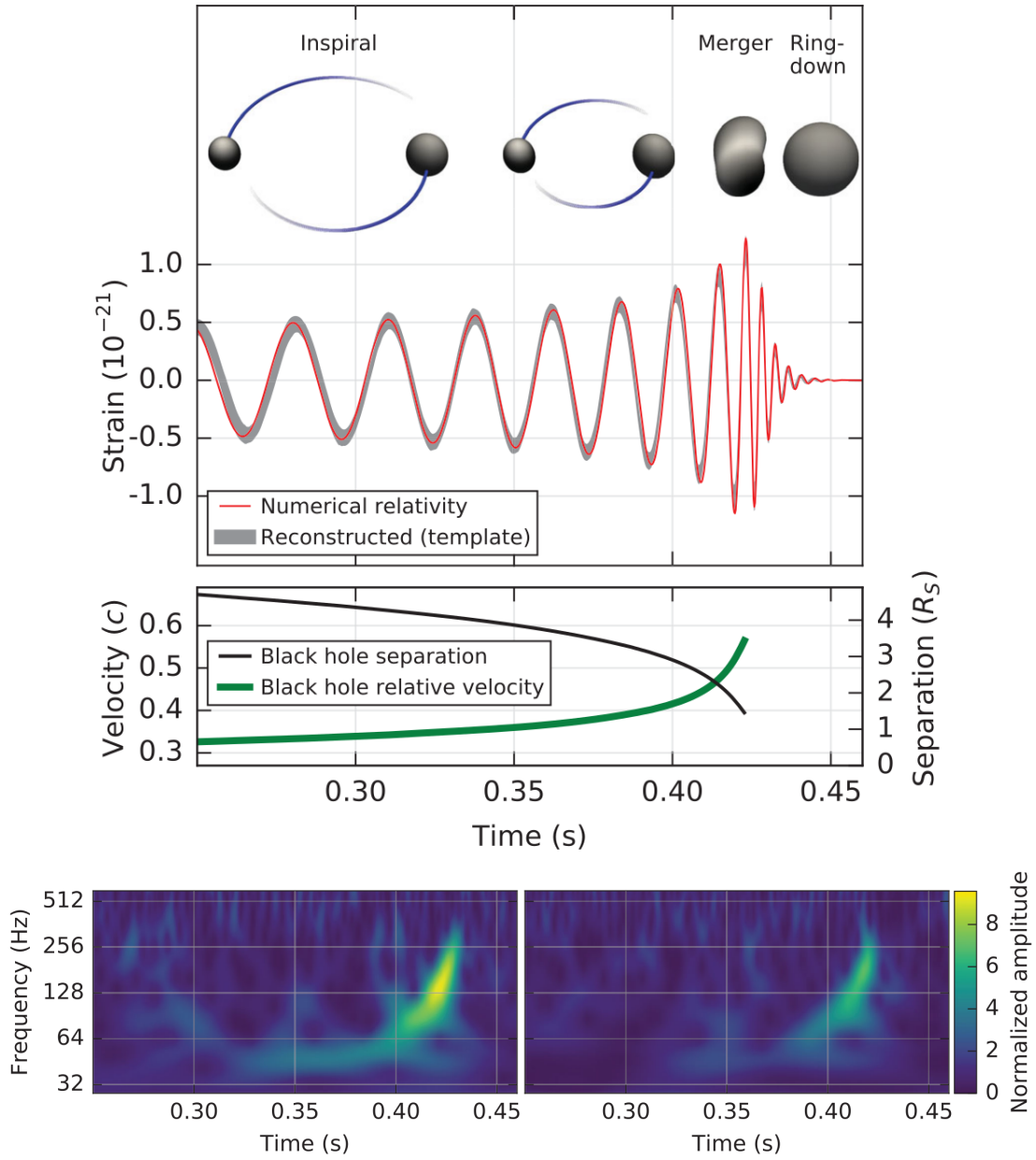


Figure 1.2: [Taken from [Abbott et al. \(2016a\)](#)] Top: Estimated gravitational-wave strain amplitude from GW150914 projected onto H1. The inset images show numerical relativity models of the black hole horizons as the black holes coalesce. Middle row: The Keplerian effective black hole separation in units of Schwarzschild radii ($R_S = 2GM/c^2$) and the effective relative velocity given by the post-Newtonian parameter $v/c = (GM\pi f/c^3)^{1/3}$, where f is the gravitational-wave frequency calculated with numerical relativity and M is the total mass ($65M_\odot$). Bottom row: A time-frequency representation ([Chatterji et al., 2004](#)) of the strain data in H1 (left) and L1 (right) detectors, showing the signal frequency increasing over time.

order. In other words, all time-dependent non-spherical movements will produce gravitational waves. The sources of GWs are generally classified into four categories: chirps, continuous, burst, and stochastic (LIGO Caltech, 2015a; LIGO Scientific Collaboration, 2015a).

1.2.1 Chirps

These are signals that are generally produced by inspiralling compact binary systems that are about to merge and are composed of neutron star and/or black holes. The two compact objects in a binary revolve around a common center of mass and lose energy and (angular) momentum due to the emission of gravitational radiation. As a consequence, the orbit of the binary system shrinks, and binary's orbital period decreases. The two objects come closer and closer, finally colliding at relativistic speeds to form a remnant. Depending on the mass of the compact objects, the final few cycles of this process up to the merger can be captured in the current ground-based gravitational wave detectors (Fig. 1.2). Since the signal's frequency and amplitude rapidly increase as it approaches the merger, it creates a chirping sound when converted to audio. Hence, these inspiralling gravitational waves are also known as chirps. Chirps are not only the strongest type of signals but are also the cleanest ones to model which (as we discuss below) is a prerequisite for their detection. Thus, it is no surprise that GW events detected by the LIGO-Virgo detectors till date are all chirp signals (Abbott *et al.*, 2019b, 2021b,c, 2024). One such signal is shown in Fig. 1.2 which was recorded by the LIGO Livingston and Hanford detectors for the event GW150914 (first direct detection of gravitational waves.)

1.2.2 Continuous Gravitational Waves

When a system emits a train of gravitational waves at nearly fixed frequencies (monochromatic), they are known as continuous gravitational waves (shown in the top panel of Fig. 1.4). Unlike chirps, these are not transient in nature. Some of the sources for these kinds of GWs can be long inspirals of compact binary systems where the merger is so far out in the future that the frequency remains nearly constant (although the

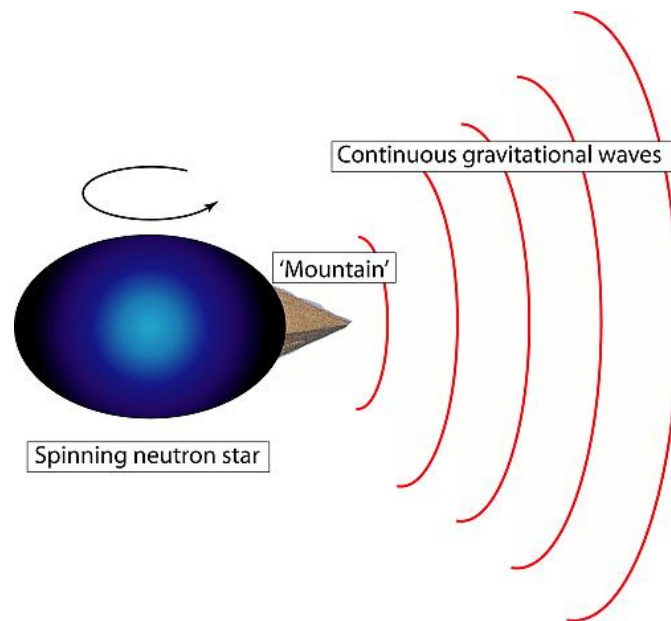
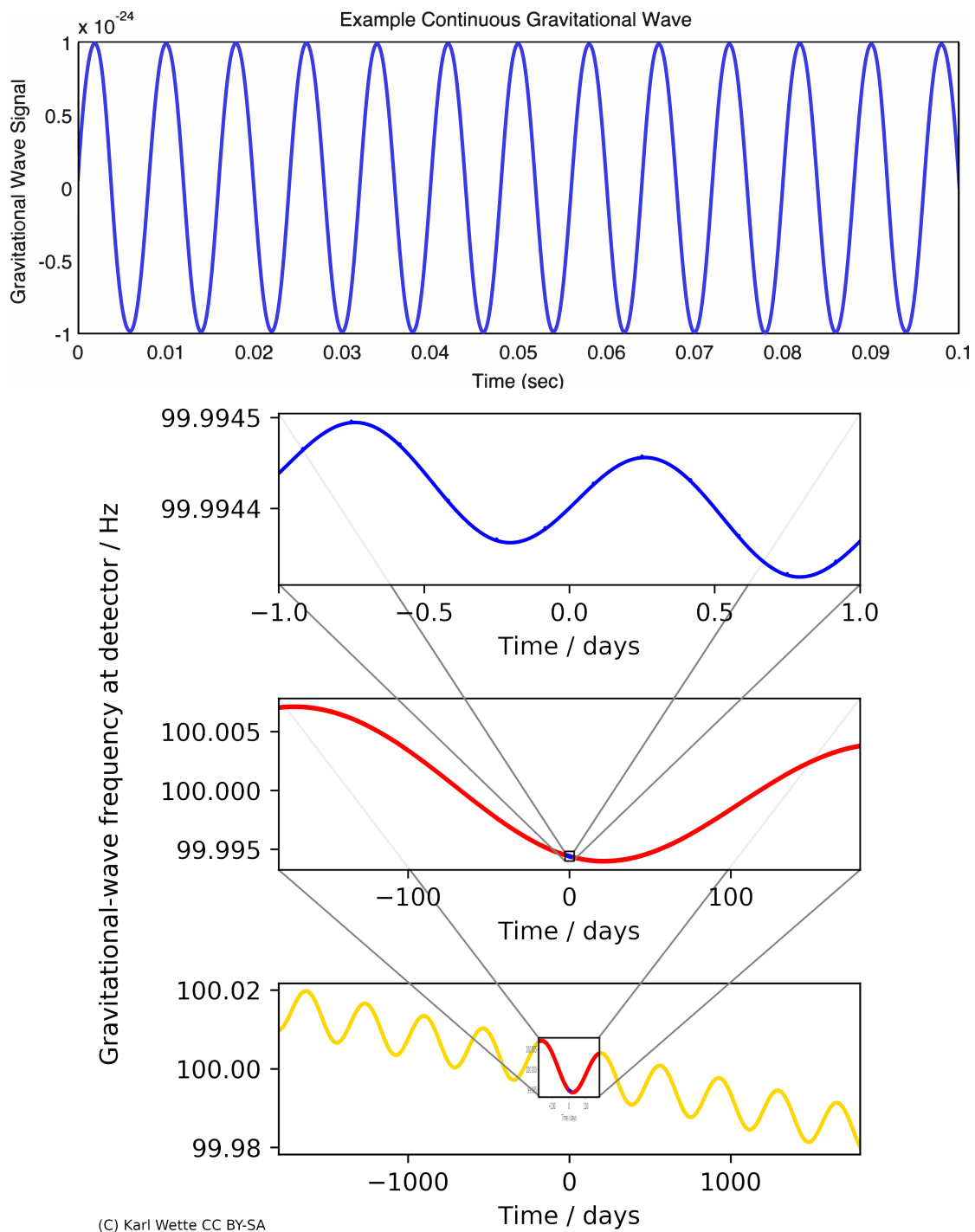


Figure 1.3: [Taken from [Drummond \(2018\)](#)] Sketch of a rotating neutron star with a mountain on the surface (not to scale) emitting continuous gravitational waves.

change in frequency can be detectable on longer time frames) in the detector band, or spinning compact stars with deformations such as a spinning neutron star with a “mountain” on the surface (see Fig. 1.3). The amplitude of continuous gravitational waves can be an order of magnitude (or more) weaker than chirp signals. The current ground-based GW detectors are searching for continuous waves from spinning neutron stars in the Milky Way and hope to monitor these signals (once detected) over long periods of time. While the frequency of these signals remains constant for a short duration, it changes over longer periods due to the spin-down of the neutron star as well as the rotation and revolution of Earth (Fig. 1.4). Spin-down, or slowing of the rotation of the neutron star, is expected as it loses energy through gravitational and electromagnetic waves. See [Riles \(2023\)](#) for a review on the search for continuous-wave gravitational radiation.

1.2.3 Gravitational Wave Bursts

Burst signals are short-lived gravitational wave signals which are expected to appear in the GW detectors similar to a ‘pop’ or ‘crackle’. The potential sources for these can



(C) Karl Wette CC BY-SA

Figure 1.4: [Taken from *LIGO Scientific Collaboration (2015b)*] From top to bottom row: 1. A short snippet from an example continuous gravitational wave signal, 2. Changing frequency of the signal due to the daily rotation of Earth about its axis, 3. Change in the signal frequency due to Earth's motion around the Sun, 4. Decrease in the frequency due to spin-down of the neutron star emitting the signal. Image credits: A. Stuver, K. Wette.

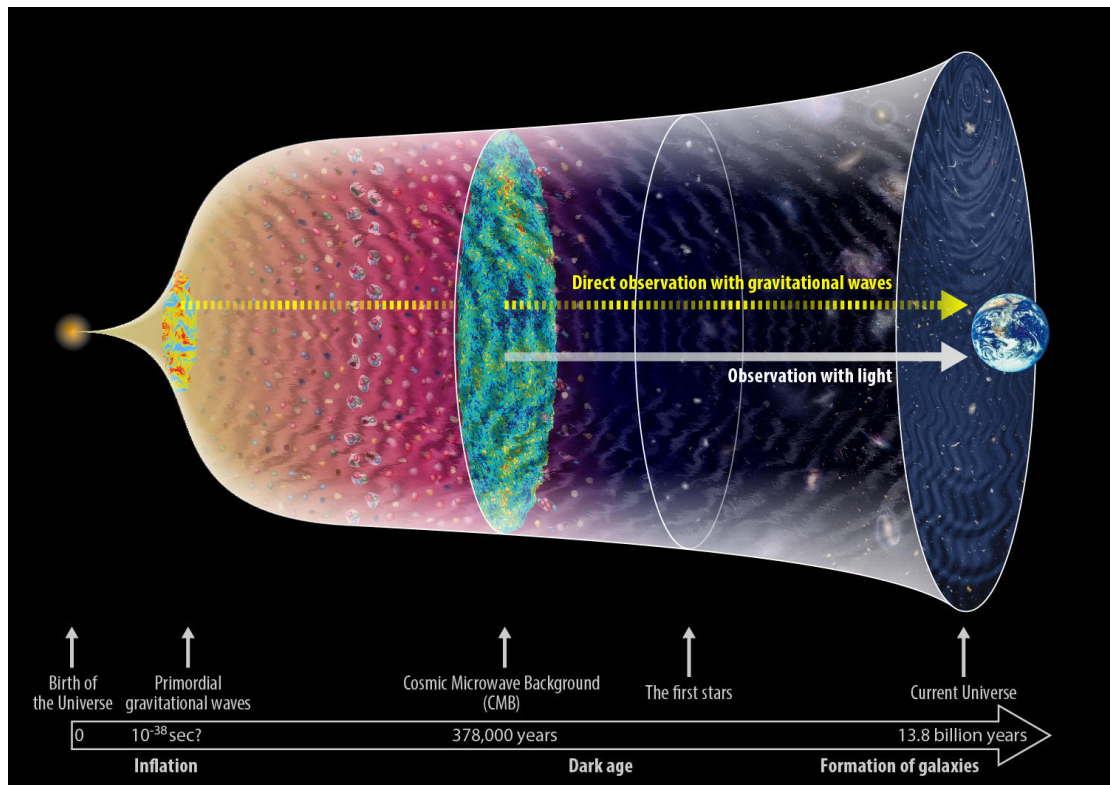


Figure 1.5: [Taken from [NAOJ \(2016\)](#)] Diagram showing different epochs in the universe’s evolution since the Big Bang and when gravitational waves and the CMB came into existence.

be asymmetric supernovae explosions, but little is known with certainty. Since these are unmodelled signals, the gravitational wave search algorithms used to look for these signals are often model-independent. See [Abbott *et al.* \(2021a\)](#) for an all-sky search for burst signals in the third gravitational wave observing run.

1.2.4 Stochastic Gravitational Wave Background

Stochastic gravitational wave signal is expected to be a mixture of random low amplitude gravitational wave signals originating from different kinds of sources. This kind of signal is also expected from the early evolution of the universe, much like the Cosmic Microwave Background (CMB) radiation. While the CMB comes from about 300,000 years after the Big Bang, stochastic gravitational waves can give us an idea about the universe as early as 10^{-36} to 10^{-32} seconds after the Big Bang (see Fig. 1.5). Another

candidate which can produce such a gravitational wave background is the overlap of numerous signals from inspirals of supermassive binary black holes in the nanohertz regime [see, for instance, a recent publication [Agazie et al. \(2023\)](#) by the International Pulsar Timing Array Collaboration ([IPTA, 2016](#))]. The pulsar timing array constitutes a set of galactic pulsars that are monitored to look for correlations between the pulses arriving on Earth and to infer gravitational wave background ([Lynch, 2015](#)).

1.3 DETECTORS

In Sec. 1.1, we briefly described the resonant mass antennas which were the first detectors constructed to capture GW signals. These have been pursued in parallel with the interferometric GW detectors and include room-temperature bar antennas (such as Weber bar and GEOGRAV), cryogenically cooled bar antennas (such as AURIGA, NAUTILAS, EXPLORER, ALLEGRO, NIOBE, ALTAIR), and cryogenically cooled spherical antennas (GRAIL, TIGA, SFERA, and Graviton). But, since the past few decades, due to lack of interest and funding, the projects have not gained as much momentum as the interferometric GW detectors. See [Aguilar \(2011\)](#) for a review on resonant-mass GW detectors. This section gives an overview of interferometric GW detectors. We begin by outlining the basic working principle for these detectors and subsequently discuss the current and future detectors.

A gravitational wave passing through a ring of freely falling masses distorts the assembly over one time period as shown in Fig. 1.6. The top row of figures denotes the ‘plus’ (+) polarization whereas the bottom row shows the ‘cross’ (×) polarization which is 45° apart ([Bergmann, 1968](#)). Hence, the changes produced in the distance of a perpendicularly placed pair of particles should indicate the passing of a gravitational wave. Alternatively, one can measure the time taken for the light to travel between these particles. Thus, an ‘L’ shaped detector with arms of equal length and freely falling test masses (mirrors) at the corners and end points of the ‘L’ is built. To quantify the strength of a gravitational

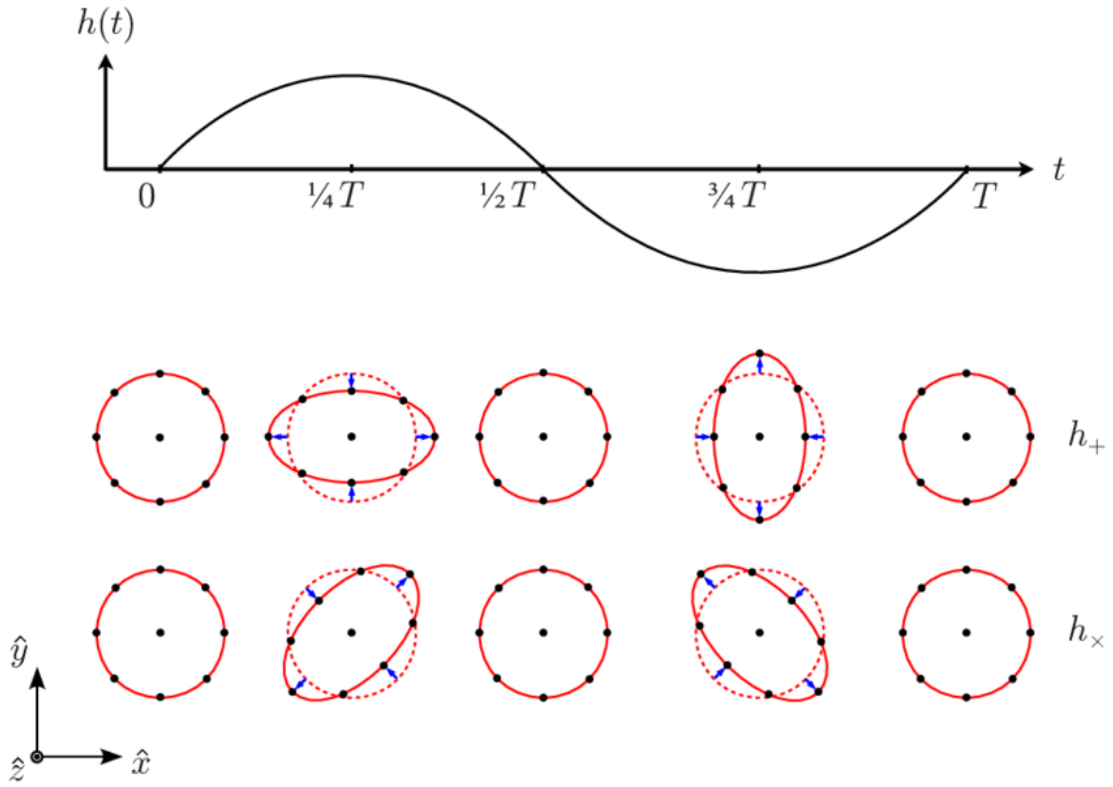


Figure 1.6: [Taken from [Le Tiec and Novak \(2017\)](#)] A monochromatic gravitational wave of pulsation $\omega = 2\pi/T$ propagates along the z - direction. The lower panel shows the effects of the plus and cross polarizations on a ring of freely falling particles, in a local inertial frame.

wave, a dimensionless strain ‘ h ’ can be defined, which denotes the maximum change in the detector’s arms per unit length. If l is the separation between the two mirrors along the arms of the detector and Δl is the change in the distance between the two mirrors due to the passage of the gravitational wave, then $\Delta l = h l/2$ in each arm of the detector. Thus, the total difference in the length between the two arms per unit length is ([Kokkotas, 2007](#))

$$h = \frac{\Delta l}{l}. \quad (1.10)$$

As it can be seen, for a fixed strain h , increasing the length l of the detector will lead to an increase in Δl leading to a better detection. This motivates the design of the current laser interferometers used to detect gravitational waves.

The current interferometric gravitational wave detectors are “L” shaped detectors with mirrors at the ends of the arms that reflect light to create an interference pattern. A photo-detector senses the interference pattern, converting the light into an electrical signal, which can then be analyzed. A single laser beam is split at the intersection of the two arms. Half of the laser light is transmitted into one arm while the other half is reflected into the second arm. Mirrors are suspended as pendula at the end of each arm and near the beam splitter. Laser light in each arm bounces back and forth between these mirrors, and finally returns to the intersection, where it interferes with light from the other arm. If the lengths of both arms have remained unchanged, then the two combined light waves should completely subtract each other (destructive interference), and there will be no light observed at the output of the detector. However, if a gravitational wave were to stretch one arm and compress the other slightly (about 1/1000 the diameter of a proton), the two light beams would no longer completely subtract each other, yielding light patterns at the detector output.

1.3.1 Response of a ground-based interferometric detector

The interferometer’s response to gravitational waves, known as the *antenna pattern response*, varies based on the detector’s geometry and the gravitational wave’s direction and polarization. Let \hat{N} be the direction of GW propagation, with radiation vectors \hat{e}_x^R and \hat{e}_y^R , such that \hat{e}_x^R lies in the plane formed by the wave propagation direction and one arm of the GW detector. Here, we assume that the arm of the detector lies along x -axis of the detector plane, and its unit vector is \hat{e}_x . Thus, the wave amplitude h^+ [see Eq. (1.9)] has \hat{e}_x^R and \hat{e}_y^R as the axes of its ellipse. The full metric perturbation due to a GW coming from the direction \hat{N} can be written as (Nishizawa *et al.*, 2009; Yunes and Siemens, 2013)²:

$$\tilde{\mathbf{h}}(t) = h^+(t)\tilde{\mathbf{e}}^+ + h^\times(t)\tilde{\mathbf{e}}^\times, \quad (1.11)$$

²We denote tensors with $\tilde{\circ}$ on top.

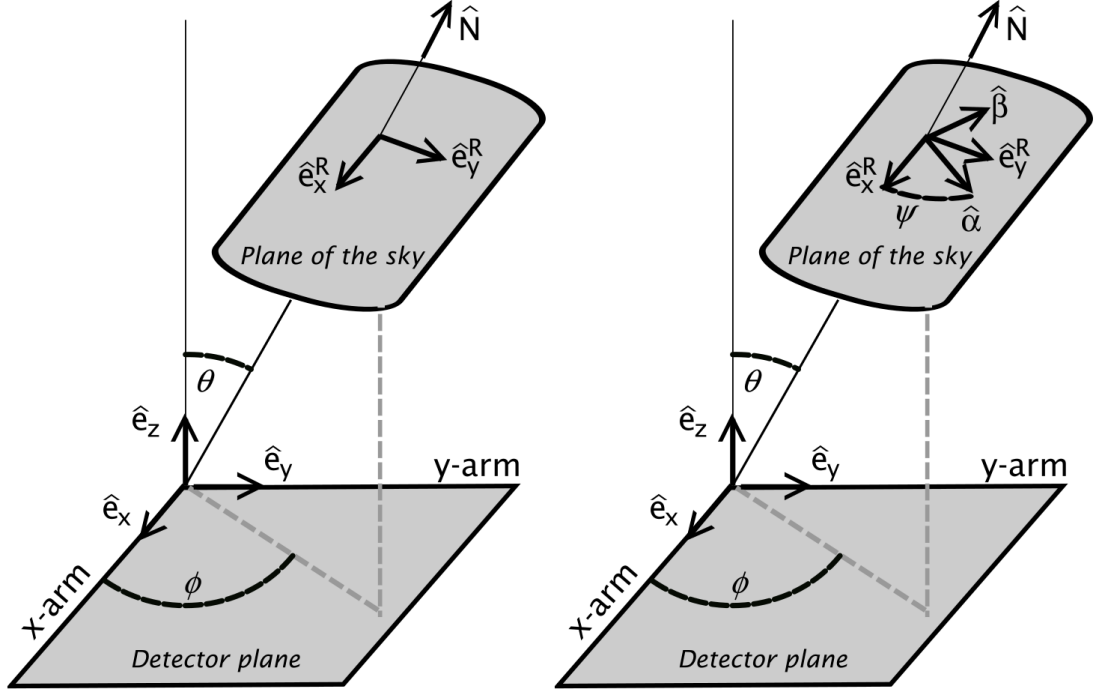


Figure 1.7: [Taken from *Sathyaprakash and Schutz (2009)*] The relative orientation of the sky and detector frames (left panel) and the effect of a rotation by the angle ψ in the sky frame (right panel).

where \tilde{e}^+ and \tilde{e}^\times are polarization tensors. If the direction of propagation for the gravitational wave is z -direction, these can be written as:

$$\tilde{e}^+ = \begin{pmatrix} 1 & 0 & 0 \\ 0 & -1 & 0 \\ 0 & 0 & 0 \end{pmatrix}, \tilde{e}^\times = \begin{pmatrix} 0 & 1 & 0 \\ 1 & 0 & 0 \\ 0 & 0 & 0 \end{pmatrix}. \quad (1.12)$$

Now, with the help of Fig. 1.7, we will explicitly write these above vectors and tensors in terms of the angles (θ, ϕ, ψ) for a GW propagating in an arbitrary direction \hat{N} . Let us take the detector plane unit vectors as:

$$\hat{e}_x = \begin{pmatrix} 1 \\ 0 \\ 0 \end{pmatrix}, \hat{e}_y = \begin{pmatrix} 0 \\ 1 \\ 0 \end{pmatrix}, \hat{e}_z = \begin{pmatrix} 0 \\ 0 \\ 1 \end{pmatrix}. \quad (1.13)$$

Then, looking at left panel of Fig. 1.7, the plane of the sky is rotated with respect to the detector plane by angles (θ, ϕ) . Hence, the radiation basis vectors can be written as:

$$\hat{\mathbf{e}}_x^R = \begin{pmatrix} \cos \theta \cos \phi \\ \cos \theta \sin \phi \\ -\sin \theta \end{pmatrix}, \hat{\mathbf{e}}_y^R = \begin{pmatrix} -\sin \phi \\ \cos \phi \\ 0 \end{pmatrix}, \hat{\mathbf{e}}_z^R = \begin{pmatrix} \sin \theta \cos \phi \\ \sin \theta \sin \phi \\ \cos \theta \end{pmatrix}. \quad (1.14)$$

Now, we can rotate the sky plane with respect to the GW propagation direction $\hat{\mathbf{N}}$ (right panel of Fig. 1.7) by a polarization angle ψ . Hence, in general, the new basis vectors $\hat{\boldsymbol{\alpha}}$ and $\hat{\boldsymbol{\beta}}$ can be written as:

$$\hat{\boldsymbol{\alpha}} = \hat{\mathbf{e}}_x^R \cos \psi + \hat{\mathbf{e}}_y^R \sin \psi \quad (1.15a)$$

$$\hat{\boldsymbol{\beta}} = -\hat{\mathbf{e}}_x^R \sin \psi + \hat{\mathbf{e}}_y^R \cos \psi. \quad (1.15b)$$

Now, we can re-write Eq. (1.12) using the generalized basis vectors as:

$$\tilde{\boldsymbol{\epsilon}}^+ = \hat{\boldsymbol{\alpha}} \otimes \hat{\boldsymbol{\alpha}} - \hat{\boldsymbol{\beta}} \otimes \hat{\boldsymbol{\beta}} \quad (1.16a)$$

$$\tilde{\boldsymbol{\epsilon}}^\times = \hat{\boldsymbol{\alpha}} \otimes \hat{\boldsymbol{\beta}} + \hat{\boldsymbol{\beta}} \otimes \hat{\boldsymbol{\alpha}}. \quad (1.16b)$$

For detectors with perpendicular arms, antenna pattern response functions can be written as the difference of projection of the polarization tensor onto each of the interferometer arms:

$$\begin{aligned} F^+ &= \frac{1}{2}(\hat{\mathbf{e}}_x \otimes \hat{\mathbf{e}}_x - \hat{\mathbf{e}}_y \otimes \hat{\mathbf{e}}_y)^{ij} \tilde{\boldsymbol{\epsilon}}_{ij}^+ \\ &= \frac{1}{2}(\hat{\mathbf{e}}_x^i \hat{\mathbf{e}}_x^j - \hat{\mathbf{e}}_y^i \hat{\mathbf{e}}_y^j)(\hat{\boldsymbol{\alpha}}_i \hat{\boldsymbol{\alpha}}_j - \hat{\boldsymbol{\beta}}_i \hat{\boldsymbol{\beta}}_j), \end{aligned} \quad (1.17a)$$

$$\begin{aligned} F^\times &= \frac{1}{2}(\hat{\mathbf{e}}_x \otimes \hat{\mathbf{e}}_x - \hat{\mathbf{e}}_y \otimes \hat{\mathbf{e}}_y)^{ij} \tilde{\boldsymbol{\epsilon}}_{ij}^\times \\ &= \frac{1}{2}(\hat{\mathbf{e}}_x^i \hat{\mathbf{e}}_x^j - \hat{\mathbf{e}}_y^i \hat{\mathbf{e}}_y^j)(\hat{\boldsymbol{\alpha}}_i \hat{\boldsymbol{\beta}}_j + \hat{\boldsymbol{\beta}}_i \hat{\boldsymbol{\alpha}}_j). \end{aligned} \quad (1.17b)$$

Substituting the values for the matrices defined above, we obtain:

$$F^+ = \frac{1}{2}(1 + \cos^2 \theta) \cos 2\phi \cos 2\psi - \cos \theta \sin 2\phi \sin 2\psi \quad (1.18a)$$

$$F^\times = \frac{1}{2}(1 + \cos^2 \theta) \cos 2\phi \sin 2\psi + \cos \theta \sin 2\phi \cos 2\psi, \quad (1.18b)$$

and Eq. (1.10) can be written as:

$$h(t) = F^+(\theta, \phi, \psi)h^+(t) + F^\times(\theta, \phi, \psi)h^\times(t). \quad (1.19)$$

These antenna pattern functions dictate the amplitude of the GW received in the detector, depending on the orientation of the detector with respect to the source. The maximum value of either F^+ or F^\times is 1. If the arms of the interferometer are not perpendicular to each other, the detector-plane coordinates x and y are defined so that the bisector of the angle between the arms aligns with the bisector of the angle between the coordinate axes. When averaged over all sky angles, these response functions take a value of $2/5$ (see also [Sathyaprakash and Schutz, 2009](#), for calculation of the rms values of antenna pattern functions).

1.3.2 Current interferometric detectors

Currently, 5 ground-based gravitational wave detectors are operational. These include the two LIGO ([Aasi *et al.*, 2015](#); [Buikema *et al.*, 2020](#)) detectors, both of which are located in the USA, one in Livingston, and the other in Hanford, Virgo ([Acernese *et al.*, 2015, 2019](#)) detector in Italy, GEO 600 ([Grote, 2010](#)) in Germany, and KAGRA (Kamioka Gravitational Wave Detector) in Japan ([Akutsu *et al.*, 2021](#); [Aso *et al.*, 2013](#)) which has recently joined the network. LIGO detectors have arms with 4 km length, but this is still not enough to detect the change in the length produced by a typical GW signal. Thus, in order to increase the length, Fabry Perot cavities are included in each of the arms, with an additional mirror in each arm near the beam splitter (Fig. 1.8). After entering the instrument via the beam splitter, the laser in each arm bounces between these two mirrors about 300 times before being merged with the beam from the other arm. In addition to increasing the arm length from 4 km to ~ 1200 km, this also builds up the laser light within the interferometer, which increases sensitivity (since more photons keep track of the lengths of the arms) ([LIGO Caltech, 2015b](#)). To increase the sensitivity, in addition

to the long length of the detectors' arms, the detector must operate at power (~ 750 kW) much higher than what enters the detector (~ 40 W). In order to achieve this, Power Recycling mirrors are introduced in the detectors (see Fig. 1.8). Inside the interferometer, light from the laser passes through the transparent side of a power recycling mirror to the beam splitter and is directed down the arms of the interferometer. The instrument's alignment and mirror coatings ensure that nearly all of the laser light entering the arms follows a path back to the reflective side of the power recycling mirror before it exits to the photo-detector. As laser power constantly enters the interferometer from the laser itself, the power recycling mirror continually reflects the laser light that has already travelled through the instrument back into the interferometer. This process greatly boosts the power of the laser light inside the Fabry Perot cavities without generating such a powerful laser beam at the outset. The boost in power generated by power recycling results in a sharpening of the interference fringes that appear when the two beams are superimposed.

These detectors also possess signal recycling mirrors, which further enhance the signal that is received by the photo-detector. Moreover, the interferometers have a seismic isolation system that dampens out unwanted vibrations (noise), making it easier for the instruments to sense the vibrations caused by gravitational waves. Virgo and KAGRA detectors are also similar in design but with arm lengths of 3 km. Further details about detector technologies can be seen at [LIGO Caltech \(2015d\)](#) for LIGO, [Virgo detector technology \(2021\)](#) for Virgo, and [Akutsu *et al.* \(2021\)](#) for KAGRA.

In addition to the interferometric detectors, a set of galactic pulsars forming a Pulsar Timing Array (PTA) is monitored and analysed to search for correlated signatures in the pulse arrival times on Earth. This array of millisecond pulsars is used to detect and analyse long wavelength gravitational-wave background such as that originating from the inspirals of supermassive black hole binaries ([Lynch, 2015](#)). There are several pulsar timing array projects ongoing around the world, and they have been collaborating under

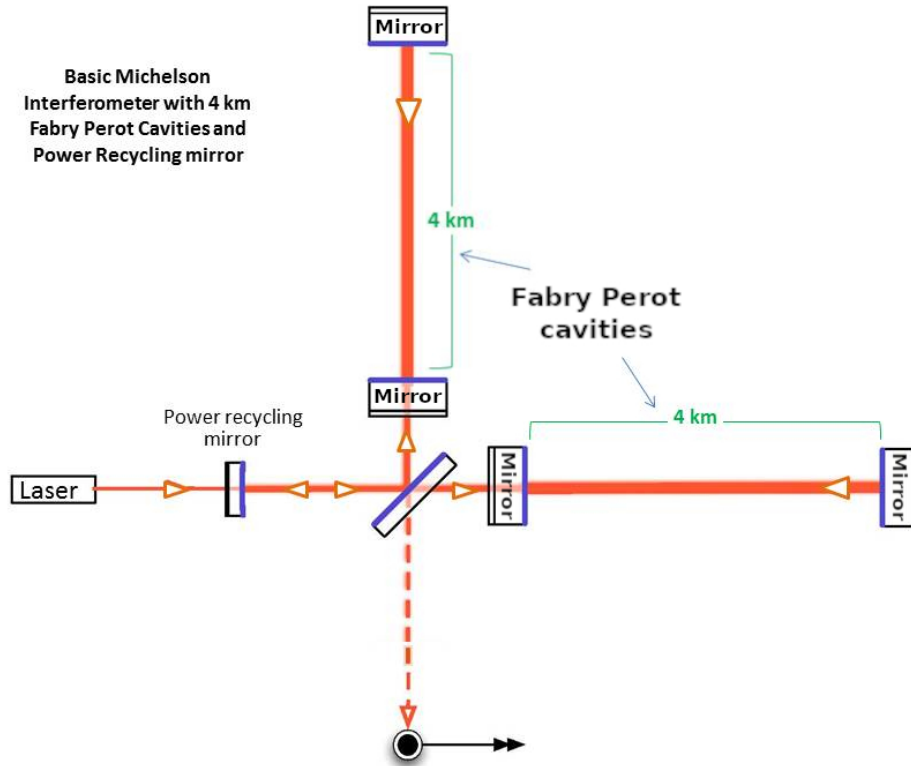


Figure 1.8: [Taken from *LIGO Caltech (2015c)*] Basic Michelson with Fabry Perot cavities and Power Recycling mirror. LIGO’s interferometers use multiple power recycling mirrors, but for simplicity, only one is shown. Image Credit: Caltech/MIT/LIGO Lab.

the title of International Pulsar Timing Array (IPTA, 2016).

1.3.3 Future detectors

There are multiple proposals for future ground-based as well as space-based GW detectors. LIGO-India (*LIGO-India., 2023; Saleem et al., 2022b; Unnikrishnan, 2024*) is one such detector which was approved recently, and the construction has begun. Further, there are planned upgrades for the current LIGO detectors to A+ (*Abbott et al., 2018b*), A# (*A-sharp, 2022*), and Voyager (*Adhikari et al., 2020; LIGO Voyager, 2023*) sensitivities. Going to the next generation, Cosmic Explorer (CE) (*Abbott et al., 2017b; Evans et al., 2021; Reitze et al., 2019*) and Einstein Telescope (ET) (*ET Science Team, 2011; Hild et al., 2011; Punturo et al., 2010a,b*) are among the leading proposals for the next generation of ground-based detectors. CE will be similar in layout to the current LIGO

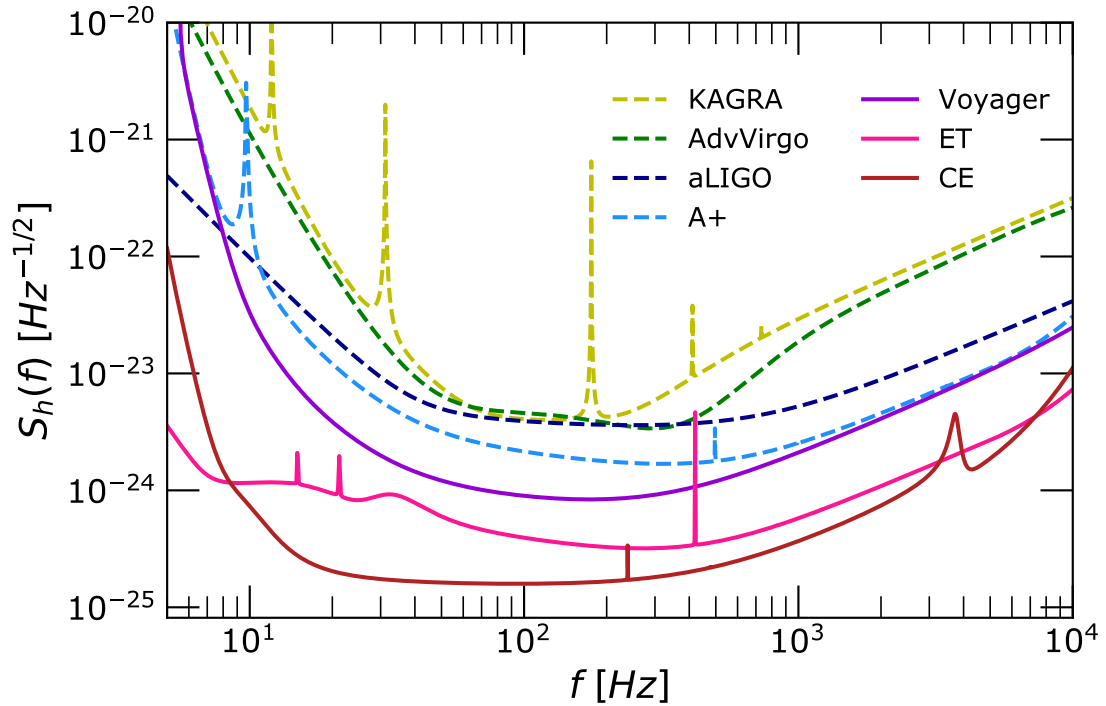


Figure 1.9: [Taken from [Divyajyoti et al. \(2021\)](#)] Detector sensitivity curves for various ground-based detectors. The dashed lines denote current detectors (or their upgrades), and the solid lines denote future detectors.

detectors, with two arms at a right angle to each other, forming an L shape. The length of these two arms is proposed to be 40 km each, which is 10 times longer than the advanced LIGO detector. ET, on the other hand, will have a different layout. It will consist of three arms forming an equilateral triangle³. Each arm will have a length of 10 km, and the whole setup is underground. Both detectors are expected to achieve a sensitivity that is roughly an order of magnitude better than the current 2G detectors (aLIGO), on average, and a low-frequency sensitivity in the range 1-5 Hz ([Chamberlain and Yunes, 2017](#)).

Going to the space-based detectors, the Laser Interferometer Space Antenna (LISA) [Babak et al. \(2021\)](#) is already under construction. The detector will be in the shape of an equilateral triangle with three spacecrafts on the three vertices of the triangle. Each spacecraft will contain two telescopes, two lasers, and two test masses, and the arrangement will be placed at the same distance from Sun as the Earth's orbit, but with

³The proposal for Einstein telescope is one of the most favoured proposals at the moment.

an angle of 20° lagging the Earth. The plane of the triangle formed by the spacecrafts will be tilted at 60° compared to the Ecliptic. With arm lengths of ~ 2.5 million kms, it will open the gravitational wave window to a range of low frequencies from 0.1 mHz to 100 mHz.

Other detector proposals include a number of space based GW detectors such as

- DECI-hertz Interferometer Gravitational-wave Observatory (DECIGO) ([Kawamura et al., 2021](#)): Japanese space-based GW observatory expected to be most sensitive in the 0.1 to 10 Hz frequency band, filling in the gap between the sensitive bands of LIGO and LISA.
- Big Bang Observer (BBO) ([Harry et al., 2006](#)): proposed successor to LISA by the European Space Agency with the primary scientific goal of observing the gravitational waves from the time shortly after the Big Bang.
- TianQin ([Luo et al., 2016](#)): proposed Chinese space-borne gravitational-wave observatory consisting of three spacecrafts in Earth orbit. The TianQin project is being led by Professor Luo Jun, President of Sun Yat-sen University.
- TianGO ([Kuns et al., 2020](#)): proposed space-based, decihertz gravitational-wave detector.
- Lunar Gravitational-Wave Antenna (LGWA) ([Harms et al., 2021](#)): detector to monitor the vibrations of Moon with the potential to reveal gravitational waves in the mHz band.

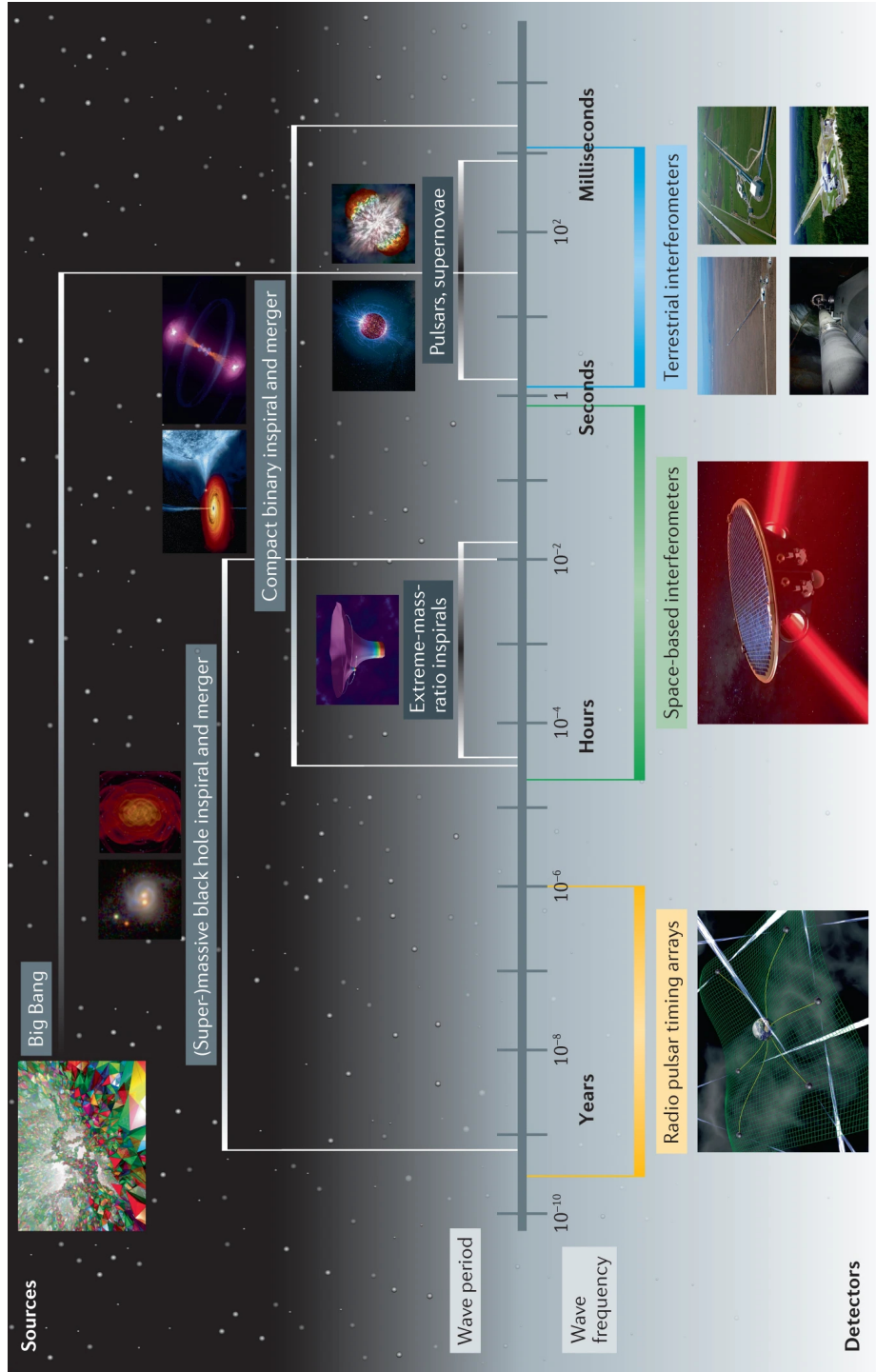


Figure 1.10: [Taken from Bailes et al. (2021)] The gravitational-wave spectrum probed by strain-sensitive gravitational-wave detectors, ranging from 10^{-9} Hz to more than 1000 Hz.

1.4 OBSERVED EVENTS AND THEIR IMPLICATIONS

Since the detection of the first gravitational wave event, GW150914, there have been three observation runs (O1-O3) of the current interferometric gravitational wave detectors, and the candidate events have been cataloged into four gravitational wave transient catalogs: GWTC-1 (Abbott *et al.*, 2019b), GWTC-2 (Abbott *et al.*, 2021b), GWTC-2.1 (Abbott *et al.*, 2024), and GWTC-3 (Abbott *et al.*, 2021c). The first observing run was from 12th September 2015 to 19th January 2016, and gravitational waves from three binary black hole (BBH) mergers were reported. The second observing run, which took place between 30th November 2016 and 25th August 2017, reported the first binary neutron star (BNS) merger and seven BBHs. These events, which all have a false alarm rate (FAR) of < 1 per year, are included in GWTC-1 along with 14 GW candidate events with FAR < 1 per 30 days. The first half of the third observing run (O3a) was from 1st April 2019 to 1st October 2019, and 39 additional GW candidates with FAR < 2 per year were added to the list (GWTC-2). Most of these events were BBHs, while some signals were consistent with BNS or Neutron Star-Black Hole (NSBH) systems, but the classification could not be made unambiguously. GWTC-2 was accompanied by GWTC-2.1, which is a deep extended catalog of CBCs from O3a with 1201 candidates that pass FAR < 2 per day. Finally, GWTC-3 adds 35 CBC candidates with the probability of astrophysical origin $p_{\text{astro}} > 0.5$ (see Sec. IV C and appendix D 7 of Abbott *et al.*, 2021c, for details on p_{astro} calculation) identified during the second half of the third observing run (O3b) which was from 1st November 2019 to 27th March 2020. These include signals from BBH and NSBH systems, along with 1048 subthreshold candidates which meet the threshold of FAR < 2 per day but do not meet the p_{astro} criteria. Overall, 90 GW candidates meet the p_{astro} criteria from the three observing runs to date. These are shown in Fig. 1.11. We now discuss a few events which have a special place in our hearts. The event nomenclature is GWYYMMDD (for events from O1-O2) or GWYYMMDD_hhmmss (for events from O3)⁴, which is GW followed by the time stamp (UTC) of the signal. For

⁴The last six digits indicating the time in addition to the date were added because the detector sensitivities increased in O3 such that multiple triggers were recorded per day.

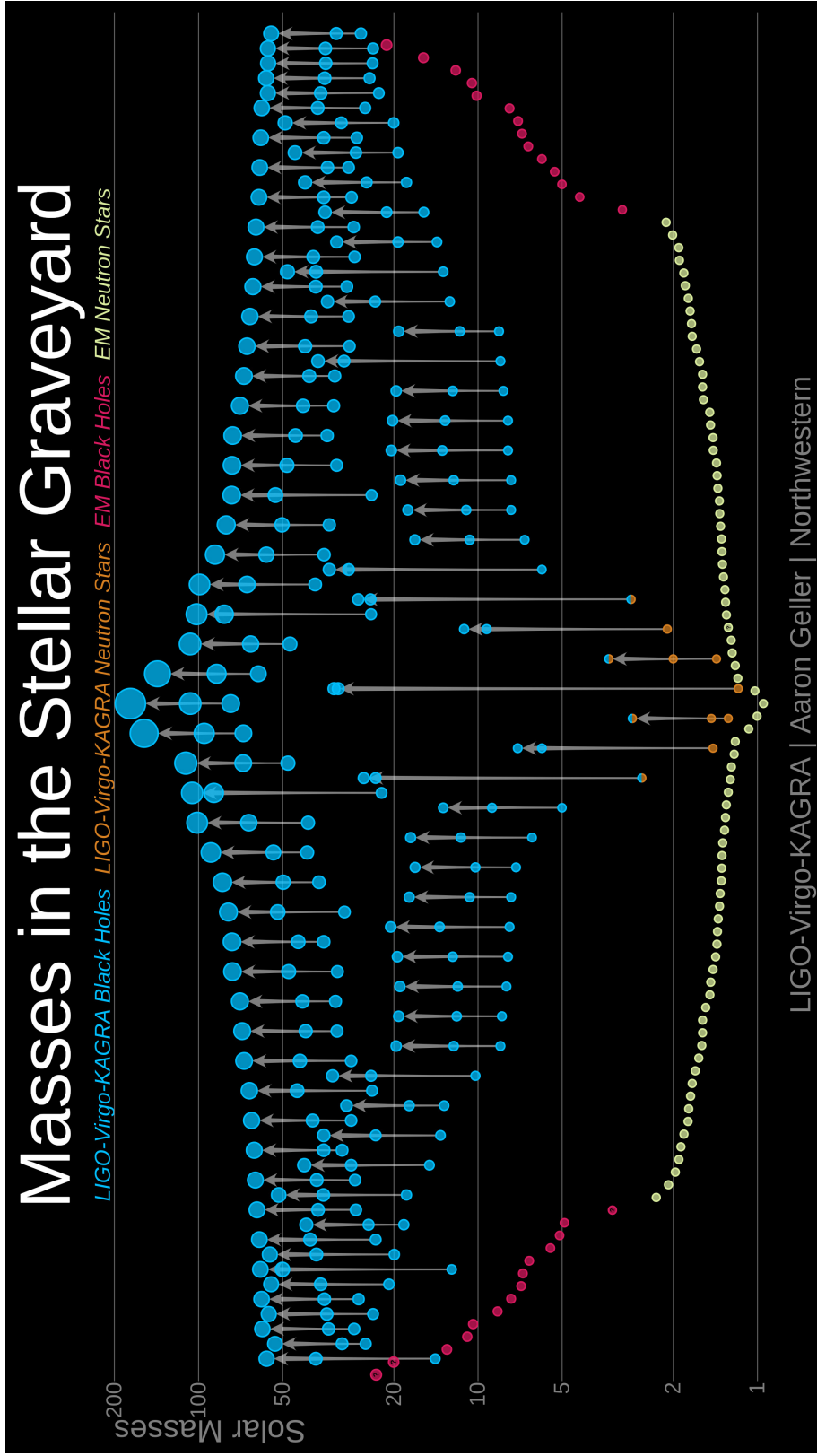


Figure 1.11: [Taken from *LIGO Caltech (2021)*] Graphic of masses of announced gravitational-wave detections, and black holes and neutron stars previously constrained through electromagnetic observations. This contains all GW events through the end of O3 with $p_{\text{astro}} > 0.5$. Image Credit: LIGO-Virgo / Aaron Geller / Northwestern University.

example, GW200220_124850 occurred on 2020-02-20 at 12:48:50.

1.4.1 Exceptional events

GW150914

This was the first direct detection of gravitational waves, which was observed with a false alarm rate of 1 per 203000 years or 5.1σ significance and a signal-to-noise ratio (SNR) of 24 (Abbott *et al.*, 2016d,f). The signal was strong enough to be detected in the filtered strain data without using any waveform models. It was consistent with the merger of two black holes with masses $36_{-4}^{+5}M_{\odot}$ and $29_{-4}^{+4}M_{\odot}$ at a redshift of $z = 0.09_{-0.04}^{+0.03}$. The final black hole had a mass of $62_{-4}^{+4}M_{\odot}$ with approximately $3_{-0.5}^{+0.5}M_{\odot}$ of mass emitted in the form of gravitational wave energy. We list here some of the astrophysical implications of this event (Abbott *et al.*, 2016b):

- Confirmed the prediction of Einstein’s general theory of relativity in very strong-field regime.
- Provided the **first direct evidence for the formation and merger of binary black holes** within the age of the universe.
- Both black holes were more massive than the previously inferred black holes from X-ray binary observations.
- Increased the lower limits on the merger rate of such events, ruling out certain theoretical models which predicted lower rates.
- Confirmed that the speed of gravitational waves was consistent with the speed of light with better constraints than earlier and improved the constraints on the graviton mass.

GW151226

This was a binary black hole merger of $14.2_{-3.7}^{+8.3}M_{\odot}$ and $7.5_{-2.3}^{+2.3}M_{\odot}$ component masses (Abbott *et al.*, 2016e) consistent with inferred masses of black holes found in x-ray binaries. The dimensionless spin magnitude of at least one companion black hole was greater than 0.2. This was the **first GW event with spinning black hole(s)**. Because of the signal’s smaller strain amplitude and time-frequency morphology, in other words,

the signal was buried deep inside the noise, the generic transient searches that initially identified GW150914 did not detect GW151226. Hence, the initial identification of this signal was confirmed by performing two independent offline matched-filter searches (Abbott *et al.*, 2016d; Messick *et al.*, 2017; Usman *et al.*, 2016) that used the waveform models in Pürrer (2016); Taracchini *et al.* (2014).

GW170817

This was the first detection of a binary neutron star merger (Abbott *et al.*, 2017f, 2019c) and the only gravitational wave event to date with a confirmed electromagnetic counterpart (Abbott *et al.*, 2017g). It was nearly a 100-second signal observed in the GW detectors of inspiralling pair of neutron stars, which ended in the merger (Abbott *et al.*, 2017c). Nearly 1.7 s after the GW signal ended, there was a gamma-ray burst (GRB) detected by FERMI and INTEGRAL spacecraft. It was confirmed that this burst came from the same source and **confirmed the hypothesis that binary neutron star mergers can produce short GRBs**. The aftermath of the signal was followed up by 70 observations by various telescopes on the ground and in space, and the emission was reported for days (months) after the GW event, in the whole range of electromagnetic spectrum from Gamma rays to radio waves. We list here some of the major astrophysical implications of this event:

- Event with the best sky localization measurement of just 16 sq. deg.
- A BNS event like this is expected to result in kilonova, followed by radioactive decay of heavy r-process nuclei, responsible for synthesizing heavy elements like gold and platinum found in our universe.
- The detection of electromagnetic counterpart, in addition to gravitational waves, started a new era in multi-messenger astronomy; nearly 100 preprints were submitted within a day of the announcement of this event.
- The difference between the speed of light and the speed of gravitational waves was improved by 14 orders of magnitude from its previous bound.
- An event like this can be used as a standard siren to make independent measurements of the Hubble constant. With more events like GW170817 in the future, the bounds on the Hubble constant can be tight enough to resolve the Hubble tension.

- This led to several new tests of GR in the strong field regime and ruled out several alternate theories of gravity.
- It provided novel opportunity to probe the properties of matter at extreme conditions such as those found in the interior of neutron stars, and constraints were placed on the neutron star radii and equations of state ([Abbott et al., 2018a](#)).

GW190412

This was the first event with considerable asymmetry in the component masses with the primary ($\sim 30M_{\odot}$) being nearly 3.75 times more massive than the secondary ($\sim 8M_{\odot}$) ([Abbott et al., 2020b](#)). Because of asymmetry, in addition to the dominant mode of gravitational radiation, a **subdominant mode was also detected for the first time**. This provided great advantage in the analysis with waveform models that include subdominant modes and resulted in the breaking of degeneracy between various parameters such as distance and inclination angle (orientation with respect to the line-of-sight) of the binary system.

GW190814

This is another event ([Abbott et al., 2020d](#)), like GW190412, where a subdominant mode was detected. In fact, the power in the subdominant mode was even higher than it was in GW190412. This was also the event where the spin magnitude of the primary is restricted to 0 with extremely high precision (upper bound of 0.07). The mass of the secondary lies entirely inside (including the 90% error bars) the lower mass gap between the mass of neutron stars and black holes, making it either the **heaviest neutron star or the lightest black hole** detected. There is still some debate about the nature of the secondary object.

GW190521

This is a merger of two black holes with $85^{+21}_{-14}M_{\odot}$ and $66^{+17}_{-18}M_{\odot}$ masses ([Abbott et al., 2020c,e](#)) where the primary black hole mass lies in the **mass gap produced by pulsational pair-instability supernova** processes, indicating alternative formation channels for this

kind of binary black hole system. The mass of the remnant was also high enough (142_{-16}^{+28}) to be considered in the intermediate-mass black hole range. This event has been shown to be consistent with a merger of a system with spin-induced orbital precession, and high orbital eccentricity, among other scenarios.

Honorable mentions

- GW170104: BBH with the effective spin parameter showing significance in the negative region indicating that black hole spins show a preference for system aligned away from the orbital angular momentum (Abbott *et al.*, 2017d).
- GW170814: First 3-detector observation of GW signal, thus constraining the sky localization to just 60 sq. deg. This enabled the test of GW polarizations and, subsequently, a new class of phenomenological tests of GR (Abbott *et al.*, 2017e).
- GW191219_163120: This event shows support for the highest mass ratio (~ 26.5) till date, also making it a potential NSBH candidate, but the uncertainty in p_{astro} which is dependent on the pipelines, and the mass ratio inference itself which is outside the calibration limit of the waveform models makes it hard to infer its properties with confidence (Abbott *et al.*, 2021c).
- GW200105_162426 and GW200115_042309: These were the first two neutron star - black hole merger events reported, and neither had a confirmed electromagnetic counterpart. Including these events in the catalog improved the estimates for the merger rate of NSBH events significantly (Abbott *et al.*, 2021d).

As we have discussed in the sections above, gravitational waves have opened a new window to the universe, allowing probes into new sectors of astrophysics and fundamental physics. Now, we focus on two important implications of gravitational wave astrophysics considering only the current detected events by the LIGO-Virgo detectors: population inference of compact binary systems and tests of general relativity possible with the GW detections.

1.4.2 Population of merging compact binaries

With a total of about 90 compact binary coalescences detected in the first three observing runs, it is possible to put constraints on the populations and merger rates of BBH, NSBH, and BNS systems. Although the detected events included in the catalogs meet some p_{astro}

threshold, a more stringent constraint⁵ (Abbott *et al.*, 2023) is put on the events when inferring the merger rates and population distributions in order to avoid contamination from signals of non-astrophysical origin. This reduces the total number of events to 76. Here, we list some of the key features of population distributions inferred from the detected GW events (Abbott *et al.*, 2023).

- NSBH binaries form a distinct population separate from BNS and BBH populations, and the merger rates of NSBH binaries are substantially larger than the BBH merger rates.
- There seems to be a relative dearth of observations of binaries which have component masses in the range $3-5 M_{\odot}$.
- While the Galactic BNS favour a peak at $1.35 M_{\odot}$ (Mapelli *et al.*, 2021; Olejak *et al.*, 2022; Shao and Li, 2021), the inferred mass distribution for BNS mergers from GWTC-3 does not exhibit a peak at this value.
- The observed BBH mass distribution seems to be clumped with multiple major and minor peaks showing in the chirp mass distribution. The primary mass distribution peaks near $\sim 10 M_{\odot}$ which suggests that globular clusters contribute subdominantly to the detected population (Fishbach *et al.*, 2020; Mapelli and Giacobbo, 2018; Regimbau, 2011). Dynamical formations in young clusters are also disfavoured (Callister *et al.*, 2020; Christensen, 2019; Romano and Cornish, 2017).
- The spin distribution of BBH population exhibits low overall spins, and the effective inspiral spin parameter (χ_{eff}) distribution is concentrated near 0.
- Considering the other peaks in the mass distribution and combining them with the spin distribution leads to the conclusion that BBH binaries originate from the initial BH mass function or are produced by different populations formed by separate physical processes or formation channels.
- The analysis of BBH rate evolution with redshift strongly disfavours the possibility that the merger rate does not evolve with redshift.

In this **thesis**, we utilize the population distributions inferred by the gravitational wave events to construct populations of black hole binary systems for our injection studies. For instance, we have used two different mass distributions taken from Abbott *et al.* (2021e) to construct the population of sources studied in Chapter 4. Moreover, in Chapter 2,

⁵A criteria of FAR < 1 per year is imposed on BBH events whereas an even stricter constraint of FAR < 0.25 per year is imposed for all analyses considering NS systems, due to the lower number of observations.

we use astrophysically motivated population models for redshift (Ng *et al.*, 2021) and eccentricity (Kremer *et al.*, 2020; Zevin *et al.*, 2021) to create the population of eccentric binary black hole mergers.

1.4.3 Tests of general relativity

Gravitational waves in modified theories of gravity may differ from general relativity in generation, propagation, and polarization. Thus, the tests of general relativity using GWs can be broadly classified into two categories: consistency tests and parametrized tests. Consistency tests check the consistency of the observed GW signal with the predicted GR waveform. These may be consistency tests of the signal morphology or the overall consistency of the GR signal with the data. Parametrized tests, on the other hand, introduce specific deviation parameters in the models to check for particular effects that may arise due to the violation of GR. We briefly describe the tests which were performed under these two categories for the events in GWTC-3 catalog (Abbott *et al.*, 2021g).

Consistency tests

- *Residuals test*: The random noise in different detectors can be taken to be incoherent. Detecting consistent noise in the network, even after eliminating the gravitational wave signal from the data, suggests a discrepancy between the signal present in the data and the GR template employed. The residual analysis is designed to detect such discrepancies in the data with GR (Abbott *et al.*, 2016g, 2019e, 2020e).
- *Inspiral–merger–ringdown consistency test*: checks the consistency of the mass and spin of the remnant BH inferred from the low- and high-frequency parts of the signal (Ghosh *et al.*, 2016, 2018).

Parametrized tests

- *Parametrized tests of GW generation*: This test introduces deviations at different post-Newtonian orders since post-Newtonian coefficients are sensitive to different physical effects. Measuring a non-zero value in these deviation parameters can point to limitations of the waveform models, which are based on GR (Arun *et al.*, 2006a,b; Blanchet and Sathyaprakash, 1994, 1995; Li *et al.*, 2012a,b; Mishra *et al.*, 2010; Yunes and Pretorius, 2009).
- *Modified GW dispersion relation*: In general relativity, it is predicted that

gravitational waves propagate non-dispersively. This characteristic is described by the dispersion relation $E^2 = p^2c^2$, where E and p represent the energy and momentum of the wave, respectively. Observing the dispersion of gravitational waves can be regarded as an indicative signature of alterations to GR. In this test, a parameterized model (Mirshekari *et al.*, 2012; Will, 1998) for dispersion of GWs is used that aids in investigating the potential existence of dispersion in the data without explicitly relying on the specifics of the modified theory.

- *Polarization test*: The assessment of the polarization content of gravitational waves serves as a means to limit potential deviations from GR. This limitation arises because the theory permits only two out of the six polarization states predicted by generic metric theories of gravity (Eardley *et al.*, 1973a,b).
- *Echoes searches*: The observed mergers of massive compact objects may involve not only black holes as predicted by classical GR but also different types of compact objects governed by exotic physics, collectively known as exotic compact objects (ECOs). This category encompasses entities such as firewalls (Almheiri *et al.*, 2013), fuzzballs (Lunin and Mathur, 2002), gravastars (Mazur and Mottola, 2004), boson stars (Liebling and Palenzuela, 2023), AdS black bubbles (Danielsson *et al.*, 2021), and dark matter stars (Giudice *et al.*, 2016). A shared characteristic among these objects is the absence of a horizon, leading to the reflection of ingoing gravitational waves (such as those generated during a merger) multiple times off effective radial potential barriers. This process results in wave packets leaking out to infinity, potentially exhibiting regular intervals, and these phenomena are termed "echoes" (Cardoso *et al.*, 2016a,b; Cardoso and Pani, 2017). Searches for echoes serve as constraints on the existence of recurring ringdown signals (Abedi *et al.*, 2017; Ashton *et al.*, 2016; Cardoso *et al.*, 2016a; Cardoso and Pani, 2017; Uchikata *et al.*, 2019; Westerweck *et al.*, 2018), which are anticipated in specific categories of Exotic compact objects (ECOs).
- *Ringdown test*: The gravitational radiation emitted from the highly distorted black hole remnant resulting from a merger is commonly known as ringdown. The waveform after the onset of the ringdown phase is a combination of quasi-normal modes (QNM) characterized by a complex frequency (Cunningham *et al.*, 1978; Vishveshwara, 1970). According to GR, the frequency and damping times for astrophysical black holes (BHs) are entirely dictated by the mass and spin of the resulting BH remnant (Carter, 1971; G urlebeck, 2015; Hansen, 1974; Penrose, 1969). The connection between frequency and remnant parameters establishes that the detection of multi-mode ringdown signals provides a distinctive assessment of the BH nature of the merger remnant (Berti and Cardoso, 2006; Dreyer *et al.*, 2004). This approach holds the potential to differentiate among various classes of ECOs (Berti *et al.*, 2015).
- *Spin-induced multipole moment test*: Spinning objects exhibit contributions to the multipole decomposition of their gravitational field, including quadrupole and higher-order terms arising from their rotational deformations. In accordance

with the no-hair conjecture, the spin-induced multipole moments assume unique values for black holes based on their mass and spin characteristics (Carter, 1971; Gürlebeck, 2015; Hansen, 1974). Gravitational waveforms that describe spinning compact binary systems encapsulate information regarding the effects of spin-induced multipole moments. Measuring the deviation from this spin-induced multipole parameter can point to the non-black hole nature of the components in a binary system. We discuss further details of this test in Sec. 1.6.4 and subsequent extensions using double spin-precessing and higher mode waveform models in Chapter 3.

1.5 SEARCHES AND PARAMETER ESTIMATION

The data collected at a gravitational wave detector has (if at all) signals which are buried deep within the noise of the detector. In order to search for such signals, most searches employed today are based on a technique known as **Matched Filtering**, which critically depends on our prior understanding of signal morphology. Matched filtering (also known as Weiner filtering) (Helström, 1968; Schutz, 1991; Thorne, 1987) is a technique where data is cross-correlated against a linear filter to find the signal buried within the noise. If we can construct a "template" which describes the form of the signal buried in the data, we can use that as a "filter" to extract the signal. The template is essentially a model based on theory (say general relativity), which is expected to accurately describe the signal in the data, or in other words, is our best guess of the signal waveform from theory. A bank of templates (template bank) is used with varying parameters, such as different values of masses and spins, in order to search for the filter which best describes the signal (since the form of the signal depends on these parameters and we don't know the binary parameter values *a priori*) (Allen *et al.*, 2012).

Let us consider the GW data stream represented by a time series $s(t)$. We assume that the data contains stationary Gaussian noise $n(t)$ with zero expectation value, and a signal $g(t)$. Then, the data can be written in the form

$$s(t) = n(t) + g(t) \tag{1.20a}$$

$$\langle n(t) \rangle = 0. \tag{1.20b}$$

Now, we hope to use a template $h(t, \theta_i)$ that can extract the signal from the data. The template is dependent on parameters θ_i , that characterize the source. Modelled searches perform matched filtering between signal templates $\tilde{h}(f)$ and the detector data $\tilde{s}(f)$ in the Fourier domain to apply the matched filters for different times of arrival efficiently.

For Gaussian and stationary noise, the one-sided power spectral density (PSD), $S_n(f)$, of noise $n(t)$ can be defined as

$$\langle \tilde{n}(f) \tilde{n}^*(f') \rangle \equiv \frac{1}{2} \delta(f - f') S_n(f), \quad (1.21)$$

where $\tilde{n}(f)$ is the Fourier transform of $n(t)$ given by

$$\tilde{n}(f) = \int_{-\infty}^{\infty} n(t) e^{-2\pi i f t} dt. \quad (1.22)$$

Using the definition for PSD, a noise weighted inner product between two functions a and b can be defined as (see [Maggiore, 2007](#), for detailed derivation),

$$\langle a|b \rangle = 4 \int_0^{\infty} \frac{\tilde{a}^*(f) \tilde{b}(f)}{S_n(f)} df, \quad (1.23)$$

which is nothing but the noise-weighted cross-correlation between a and b . Hence the filtered signal-to-noise ratio (SNR) (or simply matched filter SNR) can be defined as ([Owen and Sathyaprakash, 1999](#))

$$\frac{S}{N} = \frac{\langle g|h \rangle}{\text{rms} \langle n|h \rangle} = \frac{\langle g|h \rangle}{\sqrt{\langle h|h \rangle}}. \quad (1.24)$$

Now, an "optimal filter" which best describes the signal will be the signal itself, and so, if one assumes that the template has exactly the same form as the signal in the detector data, one can define the "optimal" SNR (ρ) ([Cutler and Flanagan, 1994](#); [Cutler et al., 1993](#); [Thorne, 1987](#)) as

$$\rho^2 = \langle h|h \rangle. \quad (1.25)$$

The SNRs from individual detectors can be combined into the SNR for the network

(Abbott *et al.*, 2021c; Pai *et al.*, 2001) as

$$\rho_{\text{network}} = \sqrt{\rho_1^2 + \rho_2^2 + \rho_3^2 + \dots} \quad (1.26)$$

where ρ_i denotes the SNR in the i^{th} detector. Hence for a network consisting of k detectors with similar sensitivities, we will have $\rho_{\text{network}} \propto \sqrt{k}$.

1.5.1 Search pipelines

Currently, gravitational wave searches are performed in two stages: online searches and offline searches. Online searches are performed in (near) real-time as the data is being collected and allow for the rapid release of public alerts associated with candidates to enable the search for multi-messenger counterparts. On the other hand, offline searches are done using the cleaned dataset, and get the advantage of improved background statistics, extensive data calibration, vetting and conditioning (Abbott *et al.*, 2021c). In the latest (third) gravitational wave transient catalog (GWTC-3) (Abbott *et al.*, 2021c), five search pipelines were used for online searches: Gstreamer LIGO Algorithm Library (GstLAL) (Cannon *et al.*, 2021; Hanna *et al.*, 2020; Messick *et al.*, 2017; Sachdev *et al.*, 2019), Multi-Band Template Analysis (MBTA) (Adams *et al.*, 2016; Aubin *et al.*, 2021), Python-based toolkit for Compact Binary Coalescence signals (PyCBC) (Allen, 2005; Allen *et al.*, 2012; Dal Canton *et al.*, 2014; Davies *et al.*, 2020; Nitz *et al.*, 2017; Usman *et al.*, 2016), Summed Parallel Infinite Impulse Response (SPIIR) (Chu *et al.*, 2022), and coherent WaveBurst (cWB) (Klimenko and Mitselmakher, 2004; Klimenko *et al.*, 2011, 2016). While the first four pipelines search based on CBC templates, cWB searches for burst signals with minimal assumptions about the sources. Except SPIIR, the other four pipelines were also used to conduct offline searches. The template banks for modelled searches were constructed in the parameter space which included component masses (m_1, m_2) of the binary system and corresponding dimensionless spins (χ_1, χ_2) aligned with the orbital angular momentum. We discuss the binary parameters in detail in Sec. 1.5.2.

1.5.2 Binary Black Hole parameter space

A typical gravitational wave signal from a binary black hole merger observed in ground-based detectors such as LIGO and Virgo can be characterized by a set of at least 15 parameters. These include the component masses (m_1 and m_2), spin vector components ($S_{1x}, S_{1y}, S_{1z}, S_{2x}, S_{2y}, S_{2z}$) corresponding to the two spin vectors (\vec{S}_1 and \vec{S}_2), source's luminosity distance (d_L), inclination angle (ι) of the binary, time of coalescence (t_c), phase of coalescence (ϕ_c), right ascension (α), declination (δ), and polarization angle (ψ). In addition to these, if the binary is on an elliptical orbit, the parameter space is extended by including additional orbital parameters such as orbital eccentricity (e) at a reference epoch (or equivalently at a reference frequency), and a parameter describing the orientation of the ellipse at the same epoch, e.g., the mean anomaly (l) (Ramos-Buades *et al.*, 2023). Moreover, if the source of the GW signal is not a binary black hole system, other parameters may be required to infer the source properties. For instance, for a binary neutron star system, tidal deformability parameters may be used to describe the deformation of the components and infer information about the equation of state of the neutron stars (see, for instance, Abbott *et al.*, 2019c, where bounds on $\tilde{\Lambda}$ were obtained for the GW event GW170817).

While performing parameter estimation of a GW signal, the parameters listed above can suitably be replaced by an equivalent set obtained by combining two or more parameters from the above set. This is usually done for several reasons: the combination of parameters may be better measured compared to the individual parameters, there exist degeneracies between the parameters such that all of them may not be accurately measured simultaneously, there is a reduction in computation time for a certain choice of parameters depending on the sampling algorithms, and so on. For instance, chirp mass (Blanchet *et al.*, 1995b; Finn and Chernoff, 1993; Poisson and Will, 1995) which is defined as

$$\mathcal{M} = \frac{(m_1 m_2)^{3/5}}{(m_1 + m_2)^{1/5}}, \quad (1.27)$$

is one of the best-measured parameters for a binary coalescence, and often used in combination with mass ratio, $q = m_1/m_2$, or symmetric mass ratio $\eta = m_1 m_2 / (m_1 + m_2)^2$ in the parameter space instead of sampling directly in m_1 and m_2 . Similarly, the individual spins of the binary components may not be measured with high precision due to various degeneracies between parameters. Hence, while the spin vector components (in cartesian or spherical polar coordinate system) may be used to sample the parameter space, often combinations of spins and mass ratio are used to infer the in-plane and out-of-plane contributions of the spin vectors. We describe these combinations in detail in Sec. 1.6.2 where we discuss the spin-induced orbital precession of a binary. Moreover, one or more deviation parameters are often introduced in the waveform models which, depending on the test of GR, help to constrain the deviation from a GR signal. One such deviation parameter ($\delta\kappa$) has been explored in detail in Chapter 3. We provide an exhaustive list of all the parameters used in this **thesis** at the beginning of this document (Notation).

1.5.3 Bayesian inference

After detecting a gravitational wave signal, various techniques (such as whitening⁶) are used to remove noise from the data (see Fig. 1.12 showing a simplified schematic of data processing). While this process is far from perfect, it usually yields a signal which can then be analysed to infer the parameters which describe the properties of the source. In this **Thesis**, we use Bayesian methods to infer the properties of both simulated and real gravitational wave signals.

The posterior probability for a parameter $\vec{\theta}$, given the data d and model \mathcal{H} , is given by the Bayes theorem as (Bayes and Price, 1763)

$$p(\vec{\theta}|d, \mathcal{H}) = \frac{\mathcal{L}(d|\vec{\theta}, \mathcal{H})\pi(\vec{\theta}|\mathcal{H})}{\mathcal{Z}(d|\mathcal{H})}, \quad (1.28)$$

where $\mathcal{L}(d|\vec{\theta}, \mathcal{H})$ denotes the likelihood, $\pi(\vec{\theta}|\mathcal{H})$ is the prior, and $\mathcal{Z}(d|\mathcal{H})$ represents

⁶The goal of a whitening procedure is to make the sequence of data delta-correlated (characterized by a normal or Gaussian distribution and a correlation between adjacent samples that approaches a delta function), removing all the correlation of the noise (Cuoco *et al.*, 2001). In other words, it normalizes the power at all frequencies so that excess power at any frequency is visible.

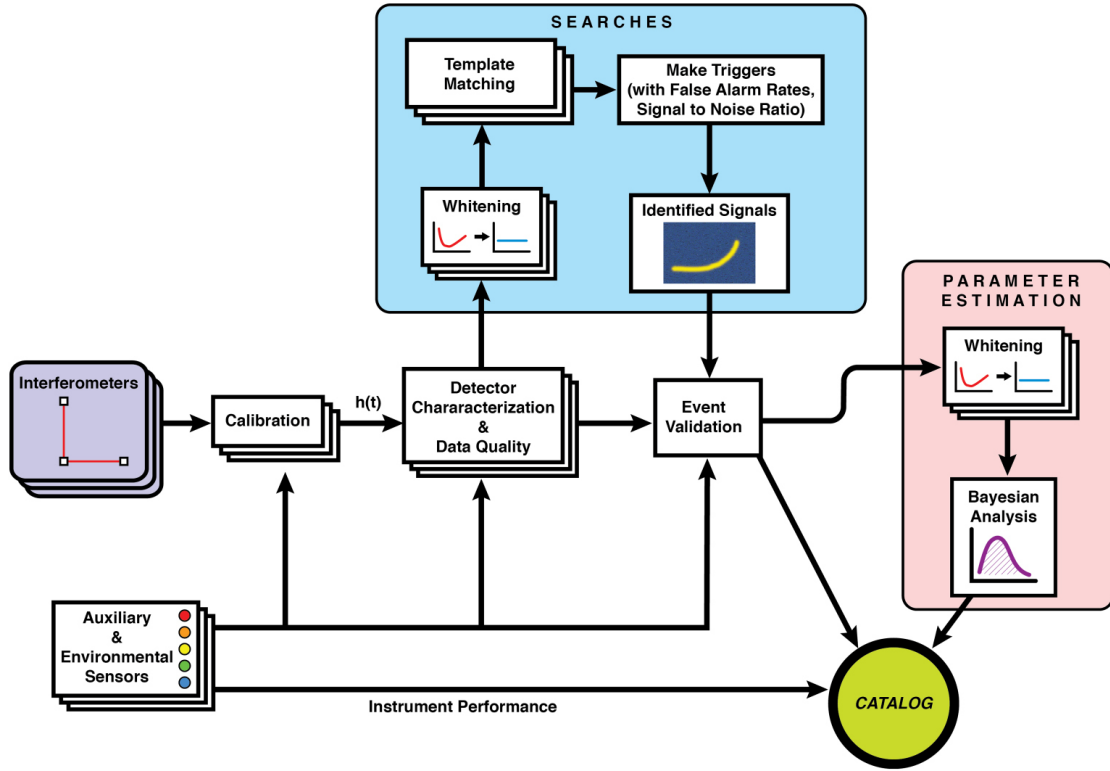


Figure 1.12: [Taken from [Abbott et al. \(2020a\)](#)] A simplified schematic summarizing the main steps in LIGO–Virgo data processing, from the output of the data to the results reported in a catalog of transient events.

the evidence. Prior is chosen such that it includes any *a priori* information we have about the parameters. An example of this is taking an appropriate range of values of the masses of the binaries that we expect to be detected by the current detectors. Likelihood function ($\mathcal{L}(d|\vec{\theta}, \mathcal{H})$) shows the probability of detectors measuring the data d , for a signal described by the model hypothesis \mathcal{H} (say a signal model based on GR) and source properties $\vec{\theta}$. Now, since the total probability of posterior when integrated over the entire range of the parameters $\vec{\theta}$ gives one, this leads us to the definition of evidence as:

$$\int p(\vec{\theta}|d, \mathcal{H})d\vec{\theta} = \int \frac{\mathcal{L}(d|\vec{\theta}, \mathcal{H})\pi(\vec{\theta}|\mathcal{H})}{\mathcal{Z}(d|\mathcal{H})}d\vec{\theta} = 1 \quad (1.29a)$$

$$\Rightarrow \mathcal{Z}(d|\mathcal{H}) = \int \mathcal{L}(d|\vec{\theta}, \mathcal{H})\pi(\vec{\theta}|\mathcal{H})d\vec{\theta} \quad (1.29b)$$

which is the marginalized likelihood that serves as a measure of how well the data is modelled by the hypothesis \mathcal{H} . Although, it is just a normalization constant in parameter

estimation, it serves a crucial role in Model selection. Consider two hypotheses \mathcal{H}_A and \mathcal{H}_B for some data d . The ratio between the evidence for both of these hypotheses yields the Bayes factor given by (Isi *et al.*, 2022)

$$\mathcal{B}_{A/B} = \frac{\mathcal{Z}(d|\mathcal{H}_A)}{\mathcal{Z}(d|\mathcal{H}_B)} = \frac{\int \mathcal{L}(d|\vec{\theta}_A, \mathcal{H}_A)\pi(\vec{\theta}_A|\mathcal{H}_A)d\vec{\theta}_A}{\int \mathcal{L}(d|\vec{\theta}_B, \mathcal{H}_B)\pi(\vec{\theta}_B|\mathcal{H}_B)d\vec{\theta}_B}, \quad (1.30)$$

where the marginalization is done for different sets of parameters $\vec{\theta}_A$ and $\vec{\theta}_B$ for \mathcal{H}_A and \mathcal{H}_B respectively. The definitions of hypotheses include the choice of priors and any other assumptions that go into the likelihoods. In this **thesis**, we use Bayes factor in multiple studies to compare the models used for analyses. For instance, in Chapter 2, we use it to investigate whether an eccentric waveform model is preferred over a quasi-circular model for the analysis of the injected GW signals. In Chapter 3, Bayes factor is used to quantify the probability that the GW events considered there are from binary black hole mergers and not from other exotic objects. If the Bayes Factor $\mathcal{B}_{A/B}$ is considerably larger than 1 [or equivalently $\log(\mathcal{B}_{A/B}) > 0$], then it indicates that data prefers hypothesis \mathcal{H}_A over \mathcal{H}_B . This can also be written in terms of the odds ratio, which is

$$O_{A/B} = \frac{\pi(\mathcal{H}_A)}{\pi(\mathcal{H}_B)}\mathcal{B}_{A/B}, \quad (1.31)$$

which indicates the betting odds in favour of one model over another. It is a common practice though to choose the priors for both hypotheses as the same i.e. $\pi(\mathcal{H}_A) = \pi(\mathcal{H}_B)$ so that there is no *a priori* preference for either hypothesis, in which case $O_{A/B} = \mathcal{B}_{A/B}$.

In the standard likelihood function, which is commonly used for the data analysis of GW transients (Finn, 1992; Romano and Cornish, 2017), both model and data are expressed in the frequency domain. It has stationary Gaussian noise, which is a decent approximation in most cases (Abbott *et al.*, 2017a, 2020a; Berry *et al.*, 2015) except for when the instruments are affected by a glitch (Pankow *et al.*, 2018; Powell, 2018) which, if they are, the Detector Characterization and data quality team informs the analysts that the signal may have data quality issues. Upon identifying a significant trigger through search

pipelines, analysts typically examine multi-resolution time-frequency scalograms of the data surrounding the trigger, commonly referred to as Q-scans. Q-scans serve as qualitative checks that necessitate visual inspection. These scans are instrumental in revealing the presence of any pronounced glitches in the data, as exemplified by the case of the binary neutron star event GW170817 (Abbott *et al.*, 2017f). Once the parameter estimation analyses have been run, a close examination of Q-scans of the residuals is conducted to identify any potential impact of unmodelled noise features on the analyses. For further details on noise mitigation techniques, kindly refer to Abbott *et al.* (2020a). Fig. 1.13 shows the glitch that was observed in LIGO Livingston during the detection of GW170817, and the steps that were taken to remove it.

1.5.4 Samplers

There are several approaches to parameter inference; for instance, BAYESTAR (Singer and Price, 2016; Singer *et al.*, 2016) performs rapid localization of GW sources by calculating probabilities on a multi-resolution grid of the sky, whereas RapidPE (Pankow *et al.*, 2015) and RIFT (Lange *et al.*, 2018) use highly-parallelized grid-based methods. There also exist various schemes which use machine learning algorithms for calculating posterior probabilities (Gabbard *et al.*, 2022; George and Huerta, 2018). However, in this **thesis**, we use packages like LALInference (Veitch *et al.*, 2015), PyCBCInference (Biver *et al.*, 2019), and bilby_pipe (Romero-Shaw *et al.*, 2020c) which employ *stochastic sampling* methods. These methods such as Markov-Chain Monte Carlo (MCMC) (Christensen and Meyer, 1998, 2001; Rover *et al.*, 2006, 2007; van der Sluys *et al.*, 2008a,b) and *Nested sampling* (Veitch and Vecchio, 2008, 2010) algorithms are implemented specifically for gravitational wave data analysis of ground-based detectors. Alternatively, there are algorithms which have been developed for other gravitational wave detectors, such as pulsar timing arrays (Lentati *et al.*, 2014; Vigeland and Vallisneri, 2014) and LISA (Babak *et al.*, 2008b, 2010). Additionally, methods like those shown in Zackay *et al.* (2018) use relative-binning (Cornish, 2010; Cornish and Shuman, 2020) to reduce the cost of computing the likelihood, whereas BayesWave (Cornish and Littenberg, 2015;

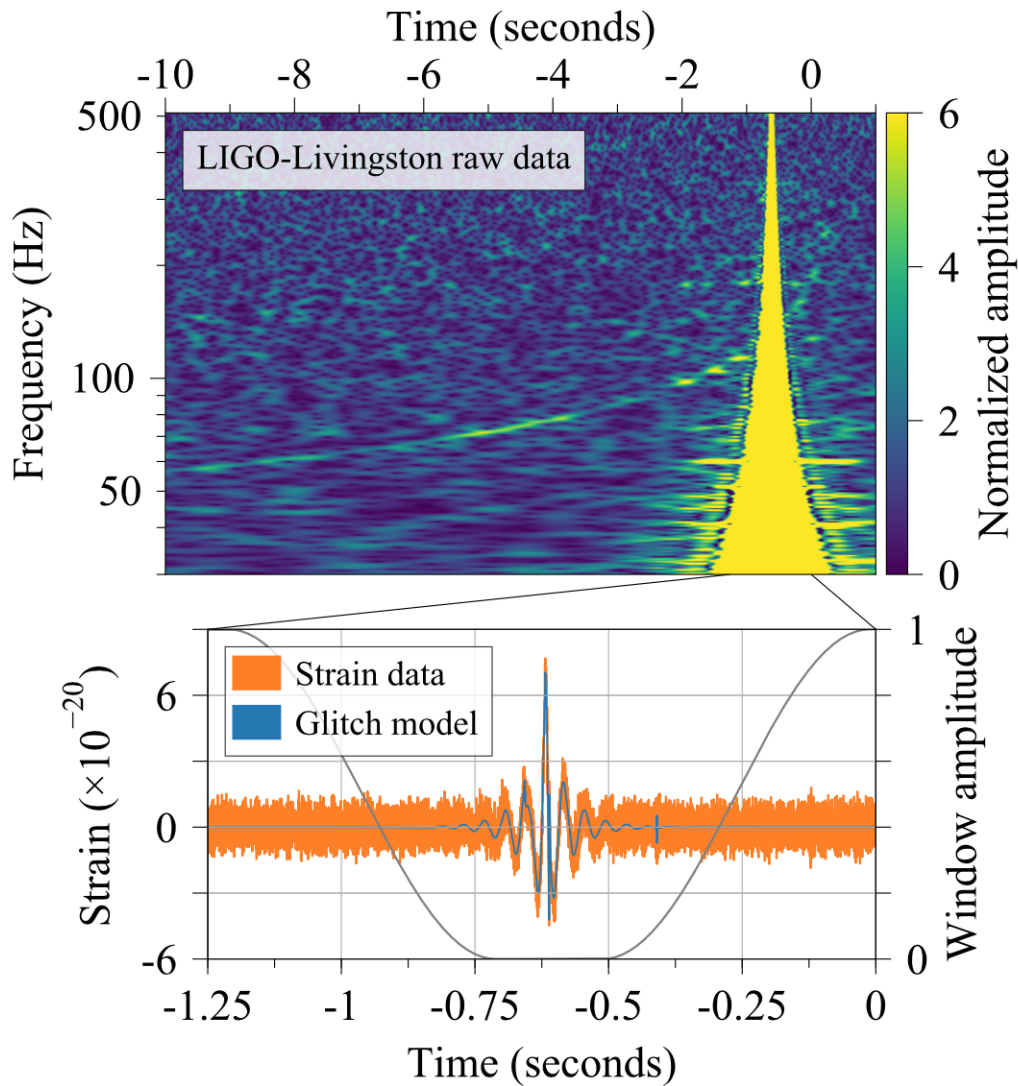


Figure 1.13: [Taken from [Abbott et al. \(2017f\)](#)] Mitigation of the glitch in LIGO-Livingston data for GW170817. Top panel: A time-frequency representation ([Chatterji et al., 2004](#)) of the raw LIGO-Livingston data used in the initial identification of GW170817. The coalescence time reported by the search is at time 0.4s in this figure, and the glitch occurs 1.1s before this time. The time-frequency track of GW170817 is clearly visible despite the presence of the glitch. Bottom panel: The raw LIGO-Livingston strain data (orange curve) showing the glitch in the time domain. To mitigate the glitch in the rapid reanalysis that produced the sky map, the raw detector data were multiplied by an inverse Tukey window (grey curve, right axis) that zeroed out the data around the glitch ([Usman et al., 2016](#)). To mitigate the glitch in the measurement of the source’s properties, a model of the glitch based on a wavelet reconstruction ([Cornish and Littenberg, 2015](#)) (blue curve) was subtracted from the data. The gravitational-wave strain amplitude of GW170817 is of the order of 10^{-22} and so is not visible in the bottom panel.

Littenberg and Cornish, 2015) uses trans-dimensional MCMC to fit an *a priori* unknown number of sine-Gaussian wavelets to the data.

Numerous Monte Carlo sampling schemes, in general, calculate the posterior probability for every point in the parameter space. While this works for a low-dimensional parameter space [for instance, if binary components are assumed to be non-spinning (Ajith and Bose, 2009)], it becomes highly inefficient and computationally expensive for parameter space in higher dimensions. Since gravitational wave inference deals with a parameter space of 15 dimensions or more, stochastic samplers offer a reasonable solution to this problem. The stochastic samplers can be divided broadly into two (not mutually exclusive) categories: MCMC (Hastings, 1970; Hogg and Foreman-Mackey, 2018; Metropolis *et al.*, 1953) and nested sampling (Skilling, 2004; Speagle, 2020). In both of these, independent samples are drawn stochastically (every point in the signal has a non-zero probability of being sampled, and the samples are non-uniformly spaced) from the posterior such that the number of samples in the range $(\vec{\theta}, \vec{\theta} + \Delta\vec{\theta}) \propto p(\vec{\theta}|d, \mathcal{H})\Delta\vec{\theta}$.

In MCMC, posterior samples are generated by noting the positions of particles (or *walkers*) undergoing a biased random walk⁷ through the parameter space where the transition probability of the Markov chain dictates the probability of moving to a new point in the space. Initial samples that are collected during the *burn-in* period⁸ are discarded, and the sampling process stops once a user-defined condition is met, such as a threshold number of posterior samples have been collected which can provide an accurate representation of the posterior. Thus, in short the MCMC sampler has a goal of collecting a specified number of samples, and the posterior is constructed in the *post-processing* stage. The goal for nested samplers, on the other hand, is slightly different.

In nested sampling methods, posterior samples are generated as a by-product of calculating

⁷A random walk where the evolving variable jumps from its current state to one of the various potential new states, but, unlike a pure random walk, the probabilities of the potential new states are not equal.

⁸The preliminary steps, during which the chain moves from its unrepresentative initial value to the modal region of the posterior. The goal of burn-in is to give the Markov chain time to reach its equilibrium distribution.

the evidence. The sampler starts with a fixed number of *live points* (a set of samples that are used to explore the posterior distribution), which are drawn from the prior distribution. At each iteration, the live point with the lowest likelihood gets discarded, and in turn, another point is chosen from a higher likelihood region of the parameter space. The product between the likelihood of the discarded point and the difference in the prior volume between successive iterations, when summed over all iterations, yields the evidence approximated with the trapezoidal rule [see Eq. (29) of [Veitch et al. \(2015\)](#)]. The nested samples, when weighted by the posterior probability at that point in the parameter space, get converted to the posterior samples. The sampler stops the process once a pre-defined condition has been met, such as when the fraction of evidence that remains in the prior volume is smaller than 0.1 (say). In other words, the condition dictates that the evidence estimate would not change by more than a factor of 0.1 if all the remaining prior support were at the maximum likelihood.

In this **thesis**, we have used nested samplers for the analyses. Specifically, we use `LALInferenceNest` ([Veitch et al., 2015](#)) for analysis done with `LALInference`, and `dynesty` ([Speagle, 2020](#)) for parameter estimation with `PyCBCInference` and `bilby_pipe`.

1.6 PHYSICAL EFFECTS IN GW SIGNALS FROM BINARY BLACK HOLE MERGERS

The current template based gravitational wave search pipelines rely on quasi-circular waveform models suitable⁹ for detecting GWs from compact binary mergers expected to be observed in ground-based GW detectors. While these models describe the complete evolution of binary through the inspiral, merger, and ringdown stages, they assume components with spins aligned with binary’s orbital angular momentum (i.e. non-precessing). Moreover, certain selection biases (we discuss some of these in the

⁹An eccentric compact binary system is expected to circularize by the time it reaches the late stages of inspiral due to emission of GWs ([Peters and Mathews, 1963](#)).

subsequent text) allow one to only model for the dominant quadrupole mode (i.e. these models neglect the presence of other modes in observed data). Further, while the effect of non-quadrupole modes and spin-precession are included when performing parameter estimation studies, the binary is again assumed to be on quasi-circular orbit. As we shall see later in this **thesis**, this latter assumption leads to biases in parameter estimation studies (Chapter 2). Here, we focus on all the three physical effects (orbital eccentricity, spin-precession, and non-quadrupole/higher order modes), and describe the importance of these effects in searches and parameter estimation of binary black hole systems.

1.6.1 Orbital eccentricity

While most of the detected signals are consistent with GW emission from inspiralling BBHs on quasi-circular orbits, a few events have been argued to be more consistent with coming from binaries with non-negligible orbital eccentricity at detection (e.g., [Iglesias *et al.*, 2022](#); [Romero-Shaw *et al.*, 2021, 2022](#)). In particular, GW190521 ([Abbott *et al.*, 2020c,e](#)) has been interpreted as coming from a moderate- to highly-eccentric BBH ([Gamba *et al.*, 2023](#); [Gayathri *et al.*, 2022](#); [Romero-Shaw *et al.*, 2020b](#)). Non-negligible orbital eccentricity measured at detection in the LIGO-Virgo-KAGRA (LVK) sensitive frequency range (above 10 Hz) implies that the radiating BBH was driven to merge by external influences: for example, as part of a field triple (e.g., [Antonini *et al.*, 2017](#)), in a densely-populated star cluster (e.g., [Rodriguez *et al.*, 2018](#)), or in the accretion disk of a supermassive black hole (e.g., [Tagawa *et al.*, 2021a](#)).

Search pipelines based on matched-filtering methods use quasi-circular waveform templates motivated by the expected efficient circularisation via GW emission of compact binary orbits during the late stages of their evolution ([Peters, 1964](#)). However, binaries formed through dynamical processes in dense stellar environments ([Banerjee, 2018](#); [Di Carlo *et al.*, 2019](#); [Downing *et al.*, 2010](#); [Mandel and Farmer, 2022](#); [Mapelli, 2020](#); [Portegies Zwart and McMillan, 2000](#); [Rodriguez *et al.*, 2016a](#)) or through Kozai-Lidov processes ([Kozai, 1962](#); [Lidov, 1962](#)) in field triples ([Martinez *et al.*, 2020](#); [Naoz, 2016](#)),

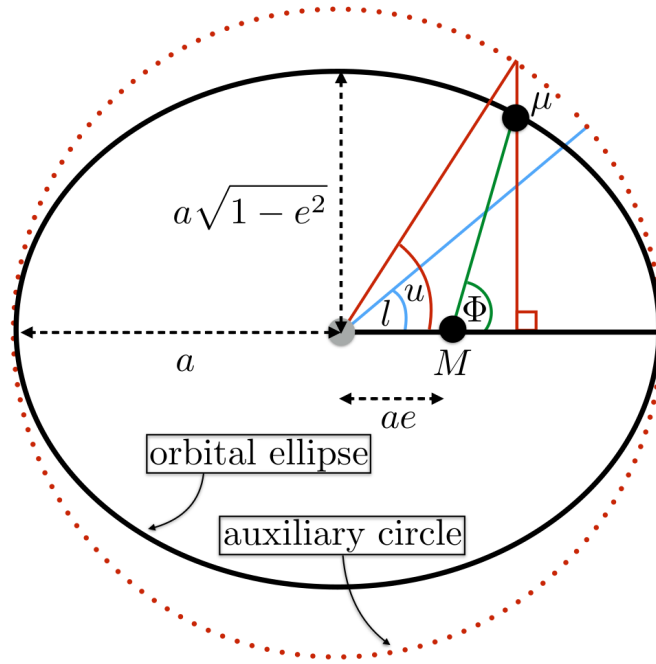


Figure 1.14: [Taken from [Taylor et al. \(2016\)](#)] A diagram illustrating the relationship between the various angular elements in a binary system with orbital eccentricity e , reduced mass μ , and total mass M . The semi-major and semi-minor axes are a and $a\sqrt{1-e^2}$, respectively. If we measure the angles from the moment of periapsis, then Φ is the true anomaly¹⁰, l is the mean anomaly, and u is the eccentric anomaly. The auxiliary circle has a radius equal to the orbital semi-major axis.

may be observed in ground-based detectors such as advanced LIGO and Virgo with residual eccentricities $\gtrsim 0.1$ (e.g., [Antonini et al., 2017](#); [Kowalska et al., 2011](#); [Lower et al., 2018](#); [Rodriguez et al., 2018](#); [Samsing and Ramirez-Ruiz, 2017](#); [Tagawa et al., 2021a](#); [Zevin et al., 2021](#)). While pipelines employing quasi-circular templates should be able to detect the majority of systems with eccentricities $e_{10} \lesssim 0.1$ at a GW frequency of 10 Hz ([Favata et al., 2022](#)) if observed with current LIGO-Virgo detectors, binaries with larger eccentricities would require constructing template banks for matched-filter searches including the effect of eccentricity (e.g., [Brown and Zimmerman, 2010](#); [Zevin et al., 2021](#)).

Moreover, the presence of even small eccentricities ($e_{10} \sim 0.01 - 0.05$) can induce bias in extracting source properties ([Abbott et al., 2017a](#); [Bhat et al., 2023](#); [Favata, 2014](#); [Favata et al., 2022](#); [Guo et al., 2022](#); [Narayan et al., 2023](#); [Ramos-Buades et al., 2020b](#); [Saini et al.,](#)

¹⁰The symbol Φ has been used for other angles throughout the **thesis**, and this is the *only* instance where it is used to indicate the true anomaly.

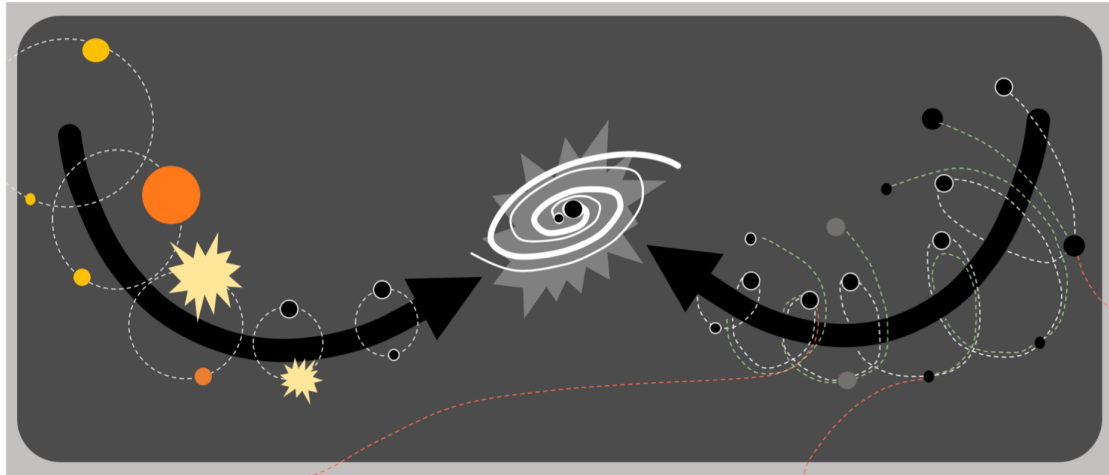


Figure 1.15: [Taken from *OzGrav* (2020)] Artist’s depiction of two black holes falling into a dance as they spiral towards each other and eventually collide. Image Credit: Isobel Romero-Shaw.

2022). As the detectors upgrade to the LIGO A+/Voyager configurations with improved low-frequency sensitivity, neglecting eccentricity in detection and parameter estimation pipelines may lead to failure in identifying the presence of eccentric signals in data, and/or incorrect inference of source properties. This problem is likely to be amplified in detections made with next-generation ground-based instruments such as Cosmic Explorer and Einstein Telescope since their sensitivity to frequencies $\sim 1 - 5$ Hz and above should enable them to frequently observe systems with detectable eccentricities (Chen *et al.*, 2021; Lower *et al.*, 2018).

In searches for compact binary coalescence signals, computation time and availability of accurate waveform models play crucial roles. In recent years, using the standard search pipelines such as cWB and PyCBC, there have been some targeted searches for eccentric systems (Abac *et al.*, 2023; Abbott *et al.*, 2019d; Cheeseboro and Baker, 2021; Cokelaer and Pathak, 2009; Lenon *et al.*, 2021; Martel and Poisson, 1999; Pal and Nayak, 2023; Ramos-Buades *et al.*, 2020a; Ravichandran *et al.*, 2023; Tai *et al.*, 2014; Taylor *et al.*, 2016; Wang and Nitz, 2021), and upper limits have been set in the absence of detection. For instance, with data from the first two observing runs of LIGO and Virgo detector

network, [Nitz *et al.* \(2019\)](#) provided 90% credible upper limits for binary neutron stars as ~ 1700 mergers $\text{Gpc}^{-3} \text{Yr}^{-1}$ for eccentricities ≤ 0.43 , for dominant mode frequency at 10 Hz. Using data from the third Gravitational wave transient catalog (GWTC-3), the LVK collaboration placed an upper limit for the merger rate density of high-mass binaries with eccentricities $0 < e \leq 0.3$ at $0.33 \text{ Gpc}^{-3} \text{ yr}^{-1}$ at 90% confidence level ([Abac *et al.*, 2023](#)). For sub-solar mass binaries, [Nitz and Wang \(2021\)](#) provided 90% credible upper limits for $0.5 - 0.5$ ($1.0 - 1.0$) M_{\odot} binaries to be 7100 (1200) $\text{Gpc}^{-3} \text{ Yr}^{-1}$.

As shown in [Peters \(1964\)](#), since most of the binary systems detected in the frequency band of current ground-based detectors are expected to be circularized, modelling eccentric waveforms has not always been required for accurate detection and parameter estimation. Further, including additional parameters has often led to difficulties in developing optimal template placement strategies to search for eccentric binaries. Moreover, modelling of eccentric binaries can often be challenging due to additional time scales involved along with frequency-dependent modulations of amplitude and phase due to eccentric nature of the binary orbits. Methods currently in use for eccentric searches ([Coughlin *et al.*, 2015](#); [Klimenko *et al.*, 2005](#); [Lower *et al.*, 2018](#); [Salemi *et al.*, 2019](#); [Tiwari *et al.*, 2016](#)) with little or no dependence on signal model are sensitive only to high masses (ideally $\gtrsim 70M_{\odot}$ [Abac *et al.*, 2023](#); [Abbott *et al.*, 2019d](#)). Nevertheless, one can infer the presence of orbital eccentricity in signals detected by standard searches tuned to quasi-circular BBH by employing available eccentric waveform models in parameter estimation studies (e.g., [Bonino *et al.*, 2023](#); [Gamba *et al.*, 2023](#); [Iglesias *et al.*, 2022](#); [Lenon *et al.*, 2020](#); [Lower *et al.*, 2018](#); [Romero-Shaw *et al.*, 2020a, 2023, 2019, 2021, 2022, 2020b](#)). Alternatively, one can also compare the GW strain data directly to numerical relativity waveform simulations of GW from eccentric BBH through marginal likelihood computation ([Gayathri *et al.*, 2022](#)) via direct Monte Carlo integration ([Lange *et al.*, 2018](#)) over a set of parameters.

While inspiral-only models for GW signals from eccentric compact binary systems

are sufficiently accurate and are rapid enough to generate for use in direct parameter estimation via Bayesian inference (Boetzel *et al.*, 2019; Ebersold *et al.*, 2019; Henry and Khalil, 2023; Khalil *et al.*, 2021; Klein, 2021; Klein *et al.*, 2018; Klein and Jetzer, 2010; Konigsdorffer and Gopakumar, 2006; Mishra *et al.*, 2015; Moore *et al.*, 2016; Moore and Yunes, 2019; Paul and Mishra, 2023; Tanay *et al.*, 2016; Yunes *et al.*, 2009), their use may be limited to low mass (typically $\lesssim 25M_{\odot}$) (Abadie *et al.*, 2012) eccentric binaries due to the absence of merger and ringdown in the signal model. Waveform models describing BBH evolution through inspiral, merger, and ringdown (IMR) stages are under development and/or available for use (e.g., Cao and Han, 2017; Chiaramello and Nagar, 2020; Hinder *et al.*, 2018; Huerta *et al.*, 2018; Liu *et al.*, 2023) but these are generally slower to generate than their quasi-circular counterparts, and Bayesian inference using these models has usually required reduction of accuracy conditions (e.g., O’Shea and Kumar, 2023), using likelihood reweighting techniques (e.g., Romero-Shaw *et al.*, 2019), or utilising highly computationally expensive parallel inference on supercomputer clusters (e.g., Romero-Shaw *et al.*, 2022; Smith *et al.*, 2020). Further, eccentric versions of effective-one-body (EOB) waveforms (Liu *et al.*, 2020) including higher modes (Chattaraj *et al.*, 2022; Iglesias *et al.*, 2022; Nagar *et al.*, 2021a; Ramos-Buades *et al.*, 2022) and an eccentric numerical relativity (NR) surrogate model (Islam *et al.*, 2021) are also available, and are expected to be even slower to generate as additional modes are to be computed together with the dominant mode. A caveat to all of the Bayesian inference studies mentioned above is the absence of spin-induced precession (Apostolatos *et al.*, 1994) in the waveform model employed. Since both eccentricity and misaligned spins introduce modulations to the gravitational waveform (O’Shea and Kumar, 2023; Romero-Shaw *et al.*, 2020b), it may be critical to account for both spin precession and eccentricity while aiming to measure either or both of the two effects, particularly for GWs from high-mass BBHs (Ramos-Buades *et al.*, 2020b; Romero-Shaw *et al.*, 2023). Even though the currently available eccentric waveform models may not include the

effect of spin-induced precession¹¹, these are still useful for studying systematic errors incurred due to the neglect of orbital eccentricity in waveform models used in detecting and analysing events included in LVK catalogues (e.g., [Abbott et al., 2021c](#)).

Chapter 2 of this **thesis** focuses on the effect of orbital eccentricity on the detection and parameter estimation of binary black hole systems.

1.6.2 Spin-precession

In a compact binary system, in general, one or both the objects may be spinning such that their spin vectors are not aligned with the orbital angular momentum vector (\vec{L}). In such a case where the total spin vector, $\vec{S} = \vec{S}_1 + \vec{S}_2$, is misaligned with \vec{L} (see Fig. 1.16), the orbital plane of the binary precesses about the total angular momentum \vec{J} ([Apostolatos et al., 1994](#)). This spin-induced precession gets imprinted on the gravitational wave signal in the form of modulations in amplitude and phase ([Apostolatos et al., 1994](#); [Cutler et al., 1993](#)). Ideally, in order to get complete information on the spins of the binary system, one would like to get good constraints on all the six component spins (three for each spin vector), but due to degeneracies, these may not always be well constrained. Thus, when performing parameter estimation, we often use a combination of spin magnitudes and angles to get information about the spins of a binary.

The two spin parameters, one for the out-of-plane spin effects - the effective spin parameter (χ_{eff}) ([Ajith et al., 2011](#); [Santamaria et al., 2010](#)), and another for the in-plane spin effects - the spin-precession parameter (χ_p) ([Hannam et al., 2014](#); [Schmidt et al., 2012, 2015](#)) are among the best-measured spin parameters in the parameter estimation of a GW signal. It has been demonstrated that χ_{eff} captures the spin effects along the direction of the angular momentum axis ([Ajith et al., 2011](#)) and χ_p measures the spin effects in the orbital plane of the binary ([Schmidt et al., 2015](#)). The effective spin parameter for a

¹¹While the model in [Klein \(2021\)](#) does include the effect of spin-precession and eccentricity, it is an inspiral-only prescription and thus might only be suitable for long inspiral signals such as those observed by LISA ([Babak et al., 2021](#)).

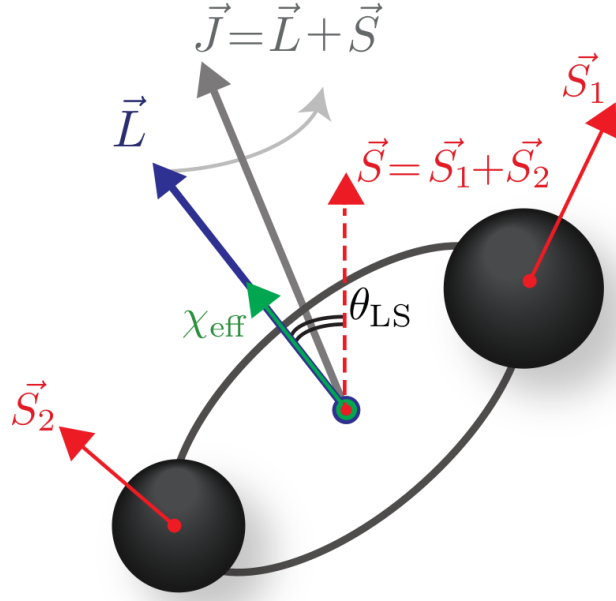


Figure 1.16: [Taken from [Rodriguez et al. \(2016b\)](#)] Diagram of the vectors and angles that define the spinning BBH problem. For any system where \vec{S} and \vec{L} are misaligned, orbital plane will precess about the total angular momentum, \vec{J} .

binary with dimensionless spin components, $\chi_i = (\vec{S}_i \cdot \hat{L})/m_i^2$, can be defined as

$$\chi_{\text{eff}} = \frac{\chi_1 m_1 + \chi_2 m_2}{m_1 + m_2}. \quad (1.32)$$

Here \vec{S}_i is the individual spin angular momentum vector of the compact object in the binary with mass m_i , and \hat{L} represents the unit vector along the angular momentum axis of the binary. The value of χ_{eff} varies from -1 (maximally spinning system where spin vectors are anti-aligned with the orbital angular momentum), 0 (non-spinning system, or a combination of aligned and anti-aligned spin vectors), to 1 (maximally spinning system where both spin vectors are aligned with the orbital angular momentum).

On the other hand, in terms of the perpendicular spin vectors, $S_{i\perp} = |\hat{L} \times (\vec{S}_i \times \hat{L})|$, the effective spin-precession parameter can be written as,

$$\chi_p = \frac{1}{A_1 m_1^2} \max(A_1 S_{1\perp}, A_2 S_{2\perp}), \quad (1.33)$$

where, $A_1 = 2 + (3/2q)$ and $A_2 = 2 + (3q/2)$ are mass parameters defined in terms of the

mass ratio $q = m_1/m_2 > 1$. χ_p varies from 0 to 1, indicating the degree of misalignment with \vec{L} .

Measuring the spins, in particular the orientation of the spin vector, of a binary black hole system can provide vital information about the formation channels (Abbott *et al.*, 2019a; Belczynski *et al.*, 2001; Farr *et al.*, 2018; Mandel and Farmer, 2022; Mapelli, 2020; Rodriguez *et al.*, 2016b, 2019; Safarzadeh, 2020). Binaries formed in isolation are expected to predominantly have aligned spins (Bavera *et al.*, 2020; Belczynski *et al.*, 2016, 2020; De Greve and De Loore, 1992; Dominik *et al.*, 2012, 2013; Gerosa *et al.*, 2018; Kalogera *et al.*, 2007; Olejak *et al.*, 2020; Tutukov and Yungelson, 1993; Voss and Tauris, 2003), whereas those formed through dynamical evolution (Antonini and Perets, 2012; Antonini and Rasio, 2016; Antonini *et al.*, 2018, 2017; Fragione and Kocsis, 2018, 2020; Park *et al.*, 2017; Portegies Zwart and McMillan, 2000; Portegies Zwart *et al.*, 2004; Rodriguez *et al.*, 2016a; Safarzadeh *et al.*, 2020; Samsing *et al.*, 2014; Ziosi *et al.*, 2014) or hierarchical mergers (Fragione *et al.*, 2020; Hamers, 2020; Hamers and Safarzadeh, 2020; Kimpson *et al.*, 2016; Lim and Rodriguez, 2020; Safarzadeh and Hotokezaka, 2020) are more likely to show signs of spin-precession. Additionally, it has been shown through numerical simulations of BBHs that the remnant's kick velocity may depend significantly on BH spin orientations (Amaro-Seoane *et al.*, 2017; Campanelli *et al.*, 2007; Gonzalez *et al.*, 2007a,b; Komossa and Merritt, 2008; Lousto and Zlochower, 2011; Merritt *et al.*, 2004; Sesana, 2007). In this **thesis**, we are interested in investigating the effect of spin-precession on tests of binary black hole mimickers such as spin-induced quadrupole moment test (Chapter 3) as well as the interplay of spin-precession and orbital eccentricity (Chapter 2).

1.6.3 Non-quadrupole modes

Another effect which plays an important role in the modelling of gravitational waveforms is the presence of non-quadrupole modes (also referred to as subdominant modes or higher modes) in signals from compact binary systems which are asymmetric (unequal

mass components) and/or whose orbital planes are not optimally inclined towards Earth (face-off binaries). Further, each mode can also have eccentricity-induced subdominant contaminant modes. The multipolar structure of the radiation field guarantees relatively weaker strengths of these modes compared to the dominant mode. In other words, we are more likely to detect the dominant mode from a near-equal mass/face-on binary than non-quadrupole modes from an unequal mass/face-off system. This detection bias makes it difficult to detect higher-order modes (HMs) in observed sources. Including higher modes in the waveforms proves to be very useful when extracting source properties and finds numerous implications in astrophysics (Abbott *et al.*, 2020*b,d*; Arun *et al.*, 2007*b*, 2014; Babak *et al.*, 2008*a*; Calderón Bustillo *et al.*, 2016, 2017; Chatziioannou *et al.*, 2019; Graff *et al.*, 2015; Kalaghatgi *et al.*, 2020; Kumar *et al.*, 2019; O’Shaughnessy *et al.*, 2014; Pürrer and Haster, 2020; Shaik *et al.*, 2020; Trias and Sintes, 2008; Van Den Broeck and Sengupta, 2007*a*; Varma and Ajith, 2017; Varma *et al.*, 2014), cosmology (Arun *et al.*, 2007*b*; Babak *et al.*, 2008*a*; Borhanian *et al.*, 2020) and fundamental physics (Pürrer and Haster, 2020; Shaik *et al.*, 2020).

The GW strain can be expressed as a linear combination of different modes defined using a basis of spin-weighted spherical harmonics of weight -2 as follows (Goldberg *et al.*, 1967)

$$h_+ - ih_\times = h(t, \vec{\lambda}, \Theta, \Phi) = \sum_{\ell \geq 2} \sum_{-\ell \leq m \leq \ell} h^{\ell m}(t, \vec{\lambda}) Y_{-2}^{\ell m}(\Theta, \Phi). \quad (1.34)$$

Here, t denotes the time coordinate, the intrinsic parameters like masses and spins are denoted by $\vec{\lambda}$, and (Θ, Φ) are the spherical angles in a source-centered coordinate system with total angular momentum along the z-axis. To relate the spin $[-2]$ weighted spherical harmonics ($Y_{-2}^{\ell m}$) with the usual spherical harmonic basis ($Y^{\ell m}$), we reproduce Eqs. (2.3)-(2.5) of Blanchet *et al.* (2008) here:

$$Y_{-2}^{\ell m} = \sqrt{\frac{2\ell + 1}{4\pi}} d_2^{\ell m}(\Theta) e^{im\Phi}, \quad (1.35a)$$

$$d_2^{\ell m} = \sum_{k=k_1}^{k_2} \frac{(-)^k}{k!} \frac{\sqrt{(\ell+m)! (\ell-m)! (\ell+2)! (\ell-2)!}}{(k-m+2)! (\ell+m-k)! (\ell-k-2)!} \left(\cos \frac{\Theta}{2} \right)^{2\ell+m-2k-2} \left(\sin \frac{\Theta}{2} \right)^{2k-m+2} \quad (1.35b)$$

where $k_1 = \max(0, m-2)$ and $k_2 = \min(\ell+m, \ell-2)$. The separate modes $h^{\ell m}$ can be obtained from the surface integral using the orthonormality properties of these harmonics

$$h^{\ell m} = \int d\Omega \left[h_+ - i h_\times \right] \bar{Y}_{-2}^{\ell m}(\Theta, \Phi), \quad (1.36)$$

where the bar or overline denotes the complex conjugate. Several waveforms, both numerical and phenomenological, have been developed which include higher modes (Blackman *et al.*, 2017; Cotesta *et al.*, 2018, 2020; Foucart *et al.*, 2021; García-Quirós *et al.*, 2020; Khan *et al.*, 2019, 2020; Liu *et al.*, 2022; London *et al.*, 2018; Mehta *et al.*, 2017, 2019; Nagar *et al.*, 2021a,b, 2020; Ossokine *et al.*, 2020; Pratten *et al.*, 2021; Rifat *et al.*, 2020; Varma *et al.*, 2019b,c). Many of these waveforms are incorporated in the LSC Algorithm Library Suite (LALSuite) (LIGO Scientific Collaboration, 2018). These waveforms make use of the analytical and semi-analytical treatment of the compact binary dynamics within the PN (Arun *et al.*, 2004; Arun and Will, 2009; Arun *et al.*, 2009; Blanchet, 1996; Blanchet *et al.*, 2006, 2004, 1995a,b, 2002a, 2008, 2002b, 1996; Bohe *et al.*, 2013; Buonanno *et al.*, 2013; Kidder, 1995, 2008; Marsat *et al.*, 2013, 2014; Mishra *et al.*, 2016; Porto *et al.*, 2011; Porto and Rothstein, 2008a,b) and effective-one-body (Buonanno and Damour, 1999, 2000; Cotesta *et al.*, 2018, 2020; Damour, 2001; Damour *et al.*, 2000, 2015; Goldberger and Rothstein, 2006; Sennett *et al.*, 2020) frameworks as well as of numerical relativity (NR) simulations [see Boyle *et al.* (2019) for a recent update on NR waveform catalog by the SXS collaboration, Jani *et al.* (2016) for Georgia Tech catalog, Ferguson *et al.* (2023) for second MAYA catalog following the Georgia Tech catalog, and Healy *et al.* (2017) for the RIT catalog]. A comparison between different numerical relativity schemes leading to simulations of BBH spacetimes can be found in Ajith *et al.* (2012); Bruegmann *et al.* (2008); Hinder *et al.* (2014).

Methods used for detecting the presence of these higher-order modes have been discussed in [Ghonge *et al.* \(2020\)](#); [Mills and Fairhurst \(2021\)](#); [O’Brien *et al.* \(2019\)](#); [Roy *et al.* \(2021\)](#). The effect of HMs on the detection and parameter estimation of binary black hole mergers has been studied extensively (see for instance, [Calderón Bustillo *et al.*, 2016](#); [Kalaghatgi *et al.*, 2020](#); [Krishnendu and Ohme, 2021](#); [Lange *et al.*, 2018](#); [Mills and Fairhurst, 2021](#); [Payne *et al.*, 2019](#); [Tagoshi *et al.*, 2014](#); [Varma and Ajith, 2017](#); [Varma *et al.*, 2014](#)).

Implications of higher-order modes

One of the most important consequences of including higher order modes into the gravitational waveforms can be linked to their sensitivity to frequencies that are inaccessible through the dominant (quadrupole) mode. Typically, including higher order modes into the waveforms will extend the GW spectrum to higher frequencies. For instance, inspiral for the dominant (quadrupole) mode ($\ell=2$, $|m|=2$ or simply the 22 mode) can be assumed to terminate at twice the orbital frequency at the last stable orbit (f_{LSO}), while the same for a higher mode waveform including the k th harmonic will be visible until the GW frequency becomes $k f_{\text{LSO}}$. A direct consequence of this is the increase in the mass reach of broadband detectors ([Arun *et al.*, 2007a](#); [Van Den Broeck and Sengupta, 2007b](#)).

The higher order modes, through amplitude corrections to gravitational waveforms, also bring in new dependencies in terms of mass ratio, component spins, and inclination angle into the gravitational waveforms; see for instance [Van Den Broeck and Sengupta \(2007a\)](#) (nonspinning case), and [Arun *et al.* \(2009\)](#) (for spinning case). By including them into the waveforms, one can break the degeneracies present in the waveform, such as those between inclination angle and luminosity distance ([Usman *et al.*, 2019](#)), and that between mass ratio and spins ([Hannam *et al.*, 2013](#); [Ohme *et al.*, 2013](#)). While better measurements of the luminosity distance allow putting tighter bounds on cosmological parameters such as the Hubble constant ([Borhanian *et al.*, 2020](#); [Sathyaprakash *et al.*,](#)

2010), improved inclination angle estimates can lead to better modeling of off-axis gamma ray bursts (Arun *et al.*, 2014).

Further, the use of higher modes has been shown to improve the efficiency of parametrized tests of GR (Mishra *et al.*, 2010; Yunes and Pretorius, 2009) and massive graviton tests (Arun and Will, 2009). A new test of GR based on the consistency of different modes of the gravitational waveform was proposed (Dhanpal *et al.*, 2019; Islam *et al.*, 2020; Shaik *et al.*, 2020) and performed on a few selected events from GWTC-2 (Capano and Nitz, 2020). A multipolar null test of GR was also proposed in Kastha *et al.* (2018, 2019) which would measure the contribution to the gravitational waveforms from various multipoles and test their consistency with the predictions of GR. Recently, it was shown that the detection of higher modes can improve the early warning time and localization of compact binary mergers, especially NS-BH systems (Kapadia *et al.*, 2020; Singh *et al.*, 2022, 2021).

In this **thesis**, we show results for higher mode eccentric injections in Chapter 2 and study the effect of higher-order modes on the measurement of spin-induced quadrupole moments, along with spin-precession in Chapter 3. In Chapter 4, we focus on the detectability of higher modes in the third generation detectors, commenting on the parameter space in which they are most relevant and showing that several of GWTC-2 events would've shown detection of higher modes if 3G detectors were operational at the time.

1.6.4 Impact of spin-precession and higher modes on SIQM test

Various methods exist for investigating a true nature of the compact object in a binary system (Abdelsalhin *et al.*, 2018; Chatziioannou *et al.*, 2016; Datta and Bose, 2019; Datta *et al.*, 2021; Gürlebeck, 2015; Hartle, 1973; Jiménez Forteza *et al.*, 2018; Johnson-Mcdaniel *et al.*, 2020; Laarakkers and Poisson, 1999; Le Tiec and Casals, 2021; Mendes and Yang, 2017; Pacilio *et al.*, 2020; Poisson, 1998; Ryan, 1997; Uchikata *et al.*, 2016).

An analysis based on the spin-induced multipole moments is one among them. Spin-induced multipole moments arise due to the spins of individual compact objects in the binary (Laarakkers and Poisson, 1999). Typically, the evolution of an inspiralling compact binary can roughly be divided into three stages: an early-inspiral, late-inspiral & merger, and the final ringdown. During the early inspiral stage, the separation between the compact objects in the binary is large, and hence, their evolution can be modelled as a perturbation series in the velocity parameter. The post-Newtonian (PN) theory provides an analytic expression for the inspiral phase incorporating various physical effects such as the spin-orbit effects, self-spin effects, cubic and higher order spin-effects, spin-precession effects, orbital eccentricity effects, etc (see for instance, Blanchet, 2002; Henry *et al.*, 2022; Mishra *et al.*, 2016). On the other hand, one needs to invoke numerical relativity techniques to model the highly non-linear relativistic merger phase (see Lehner, 2001, for a review on numerical relativity modelling techniques). Further, the ringdown part can again be modelled perturbatively using the BH perturbation theory techniques (Pretorius, 2009; Sasaki and Tagoshi, 2003), although all numerical relativity simulations evolve the BBH spacetimes through this final ringdown stage.

In the inspiral phase, the effect of spin-induced quadrupole moment (SIQM) starts to appear at 2PN, together with the other spin-spin terms. More precisely, the leading order PN coefficient is of the schematic form $Q = -\kappa\chi^2m^3$ (Poisson and Will, 1995), where the negative sign indicates the *oblate* deformation due to the spinning motion. The proportionality constant, κ , can take different values for different compact objects. For isolated black holes, κ_{BH} is 1.¹² Slowly spinning neutron stars can have κ values in the range $\kappa_{\text{NS}} \sim 2 - 14$ (Laarakkers and Poisson, 1999; Pappas and Apostolatos, 2012a,b). In contrast, for exotic stars like boson stars, this range can be $\kappa_{\text{BS}} \sim 10 - 100$ (Ryan, 1997) depending on internal composition. There also exist gravastar proposals where the value κ_{GS} can match the BH value but also allows for negative values and prolate

¹²For BBHs, κ_{BH} can deviate from 1, but the effect is negligible compared to the measurements being made here (Buonanno *et al.*, 2013).

deformations (Uchikata and Yoshida, 2016). Measuring the SIQM parameter (κ) from GW observations can thus provide unique information about the nature of the compact object.

In principle, the BH nature of the binary components can be probed by measuring their individual SIQM coefficients κ_1 and κ_2 , parametrized as deviations away from unity $\delta\kappa_1$ and $\delta\kappa_2$. However, for the stellar-mass compact binaries accessible to LIGO and Virgo, it is often difficult to simultaneously constrain $\delta\kappa_1$ and $\delta\kappa_2$ due to the strong degeneracies between the two parameters, and with other binary parameters like the spins and masses (Krishnendu *et al.*, 2017, 2019a). Hence, a symmetric combination of these deviation parameters may be used for probing the binary black hole nature of GW source, choosing the anti-symmetric combination to be zero.

The method for measurement of deviation on κ has been explored in detail (Krishnendu *et al.*, 2017, 2019a; Krishnendu and Yelikar, 2020; Krishnendu *et al.*, 2019b; Saleem *et al.*, 2022a) and applied to observed GW events from the first three observing runs of advanced LIGO-Virgo detectors (Abbott *et al.*, 2021f,g). Further, it has been demonstrated in the past that it is possible to measure spin-induced multipole moments for intermediate mass-ratio (Brown *et al.*, 2007; Rodriguez *et al.*, 2012) and extreme mass-ratio inspirals (Babak *et al.*, 2017; Barack and Cutler, 2007). This parameter can also be constrained through electromagnetic observations of active galactic nuclei (see for instance Laine *et al.*, 2020) and supermassive BHs (Akiyama *et al.*, 2019). Moreover, the possibility of measuring spin-induced quadrupole using future detectors, and simultaneous measurement of spin-induced quadrupole and octupole moment parameters have also been studied (Krishnendu *et al.*, 2019a; Saini and Krishnendu, 2024). A template bank for binaries of exotic compact object searches has recently been developed, accounting for the spin-induced quadrupole moment and tidal effects (Chia *et al.*, 2022). Moreover, LaHaye *et al.* (2023) came up with a fully precessing waveform implementation of SIQM test for low-mass binaries, focusing on binaries in which at least one object is in the lower

mass-gap ($< 3M_{\odot}$) (Lyu *et al.*, 2024). While Abbott *et al.* (2021f,g); Krishnendu *et al.* (2017) report the SIQM measurements using a phenomenological waveform model, IMRPhenomPv2 (Hannam *et al.*, 2014; Husa *et al.*, 2016; Khan *et al.*, 2016), containing only the dominant modes ($\ell = 2, |m| = 2$) in the co-precessing frame and an effective spin parameter, in this **thesis** we extend the test for waveforms in the IMRPhenomX family, thus accounting for double spin-precession and higher modes. Specifically, we use three waveforms from this family: IMRPhenomXHM which is an aligned spin model with higher modes, IMRPhenomXP which contains only the dominant modes along with double spin-precession, and IMRPhenomXPHM which contains the higher modes as well as double spin-precession. We apply the extended test on spin-precessing binary black hole signals and present the results in Chapter 3. We find that waveform with double spin-precession gives better constraints for $\delta\kappa$, compared to waveform with single spin-precession. We also revisit earlier constraints on the SIQM-deviation parameter for selected GW events observed through the first three observing runs (O1-O3) of LIGO-Virgo detectors. The effects of higher-order modes on the test are also explored for various mass-ratio and spin combinations by injecting simulated signals in zero-noise. Our analyses indicate that binaries with mass ratios greater than three and significant spin-precession may require waveforms that account for spin-precession and higher modes to perform parameter estimation reliably.

1.6.5 Interplay of orbital eccentricity, spin-precession, and higher modes

As discussed in the sections above, orbital eccentricity, spin-precession, and higher-order modes play a crucial role in understanding some of the fundamental questions related to the inference of gravitational wave data and formation channels of gravitational wave sources. Each effect presents as oscillations in the gravitational wave signal, as shown in Fig. 1.17 where the *plus* polarization strain in the time domain has been plotted. We have used the model IMRPhenomXPHM (García-Quirós *et al.*, 2020; Pratten *et al.*, 2021) to plot the quasi-circular waveforms (all but the 4th row), and InspiralENIGMA (Huerta *et al.*, 2018; Paul *et al.*, 2024) for the eccentric waveform (4th row). The

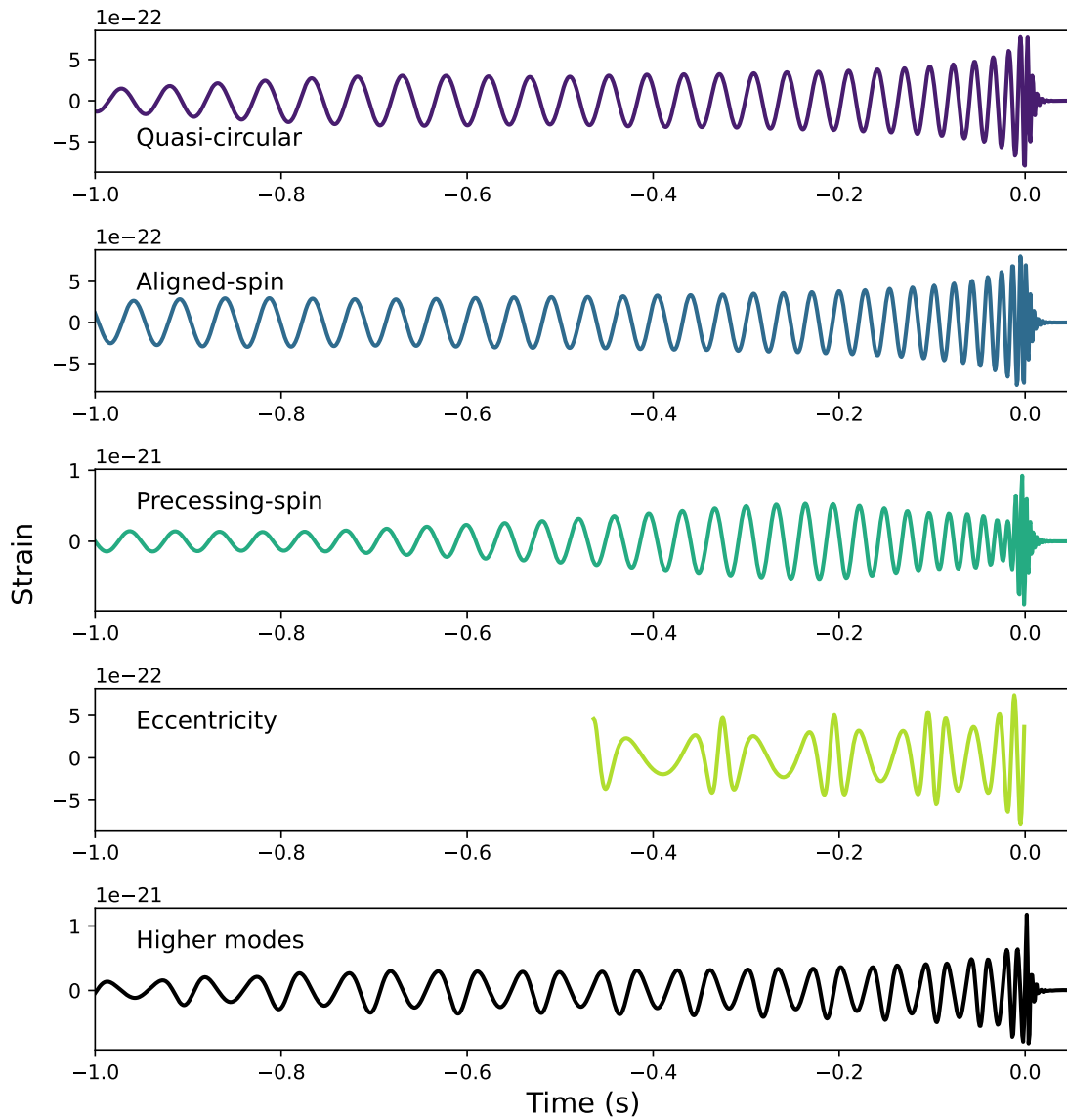


Figure 1.17: Diagrams showing the effect of including (one at a time) higher modes, spins, and orbital eccentricity in a binary black hole gravitational waveform. The waveform models used for generating the data are IMRPhenomXPHM (García-Quirós *et al.*, 2020; Pratten *et al.*, 2021) for quasi-circular (all except 4th row), and InspiralENIGMA (Huerta *et al.*, 2018; Paul *et al.*, 2024) for eccentric waveforms.

plots are generated, with a starting frequency of 20 Hz, for a black hole binary system with $(m_1, m_2) = (60, 15)M_\odot$, inclined at an angle of $\iota = 60^\circ$, placed at a distance of $d_L = 400$ Mpc. In the top row, no additional effect has been added and it portrays a non-spinning, quasi-circular BBH system with $(\ell, |m|) = (2, 2)$ modes only. The next row labelled "Aligned-spin" introduces non-zero values for spin vector components aligned with the orbital angular momentum as $(S_{1z} = 0.45, S_{2z} = 0.2)$ so that the resultant $\chi_{\text{eff}} = 0.4$. Compared to the non-spinning case, this signal is longer in length. For the "precessing-spin" case shown in the 3rd row, all the six spin components have non-zero values $(S_{1x} = 0.65, S_{1y} = 0.26, S_{1z} = 0.45, S_{2x} = 0.6, S_{2y} = 0.3, S_{2z} = 0.2)$. This results in the spin-precession parameter to be $\chi_p = 0.7$, while keeping $\chi_{\text{eff}} = 0.4$. Here, we see modulations in the waveform envelope due to the spin-induced precession of the binary's orbit. The next row shows an eccentric waveform signal with an eccentricity of 0.3 at 20 Hz. And the last row corresponds to a non-spinning, quasi-circular waveform which contains the $(\ell, |m|) = (2, 2), (3, 3), (4, 4), (2, 1), (3, 2)$ modes. It can be seen from the last three panels that higher-order modes, orbital eccentricity, and spin-precession all induce oscillations in the GW signal and it is important to understand the interplay of these effects in order to characterize the sources correctly. The interplay of these effects has been studied in various combinations (Fairhurst *et al.*, 2020a,b; Hegde *et al.*, 2023; Iglesias *et al.*, 2022; Krishnendu and Ohme, 2022; Moore and Yunes, 2020; Puecher *et al.*, 2022; Romero-Shaw *et al.*, 2023; Xu and Hamilton, 2023). In this **thesis**, we focus extensively on how the detection and parameter estimation of binary black hole systems is affected by one or more of these effects. In Chapter 2, we focus on orbital eccentricity, specifically on the detectability and parameter estimation of eccentric systems and how the analysis of eccentric signals with precessing spin waveforms affects the inference of source parameters (Divyajyoti *et al.*, 2024b). We also analyse eccentric binary black hole signals containing higher modes (Chattaraj *et al.*, 2022). Next, in Chapter 3, we observe the effect of spin-precession and higher modes on the spin-induced quadrupole moment test (see Sec. 1.6.4) and comment on the regions of parameter space where these

effects are dominant (Divyajyoti *et al.*, 2024a). Finally, in Chapter 4, we explore the detectability of higher modes in the future ground-based GW detectors (Divyajyoti *et al.*, 2021).

CHAPTER 2

DETECTION AND PARAMETER ESTIMATION OF ECCENTRIC BINARY BLACK HOLE MERGERS

2.1 INTRODUCTION

As discussed earlier, orbital eccentricity is one of the most important effects in understanding the formation channels of a compact binary system. Since there hasn't been a confident detection of a gravitational wave signal from an eccentric binary system, it is natural to ask whether our search pipelines are competent to search for these signals. Moreover, we need to have a comprehensive understanding of the systematics arising due to waveform models when analysing eccentric signals so as to avoid misinterpretation of the results. This forms the theme of this chapter.

We assess the impact of employing a circular template bank for GW searches when the source population may exhibit eccentricity. To achieve this, we simulate diverse source populations, by varying binary black hole masses and eccentricities. In Sec. 2.2, we determine the detection efficiency of the population by comparing inherent signal strength to the values obtained from the circular template bank. We also investigate the regions in the parameter space where the largest loss in signal strength occurs due to the difference between injection and recovery waveform model or due to non-inclusion of eccentricity. Next, in order to explore the effect of eccentricity on various inferred parameters of a BBH system, in Sec. 2.3, we perform parameter estimation (PE) of injected non-spinning and aligned spin eccentric signals generated using numerical relativity (NR) codes, and recover them using multiple waveform models with different combinations of spins and eccentricity. Our aim is to observe and quantify the biases incurred due to absence of eccentricity in the recovery waveform when analyzing eccentric signals and to verify that those biases can be corrected to a certain extent by using the currently available

eccentric waveforms. To this effect, we perform multiple sets of injections which include synthetic GW signals consistent with non-spinning (Secs. 2.3.1 and 2.3.3) and aligned-spin (Sec. 2.3.2) BBHs in eccentric orbits, and recover these injections with a variety of either quasi-circular or eccentric waveform models, including no spin, aligned spins, or misaligned (precessing) spins. We also perform non-spinning higher mode eccentric injections and recover them with quasi-circular, higher mode, IMR waveforms (Sec. 2.3.4). Due to a lack of available waveform models, we are unable to perform injections using models with both spin-precession and eccentricity. We observe that the state-of-the-art inspiral-merger-ringdown (IMR) quasi-circular waveforms of the IMRPhenomX (Pratten *et al.*, 2020, 2021) family do not recover the true chirp mass of an eccentric signal. Further, analyzing these same signals using a computationally efficient inspiral-only eccentric waveform results in significant reduction of biases in the posteriors on intrinsic parameters of the binary, leading to the recovery of true values within the 90% credible bounds.

While an inspiral-only eccentric waveform model should be better for analyzing eccentric signals than a full IMR quasi-circular model, it is likely that biases can be further reduced and posteriors be better constrained if an IMR eccentric waveform model is used for recovery. However, our results demonstrate that even eccentric waveform models with limited physics (no merger or ringdown, no spin-precession, no higher modes) can reduce errors in the inference of BBH parameters, and may, therefore be a useful stepping stone towards analysis with full IMR models including eccentricity, spin-precession, and higher modes. We comment on the implications of these biases and conclude in Sec. 2.4.

2.2 REDUCED GW SEARCH SENSITIVITY TO ECCENTRIC BINARIES

This section explores the fraction of events that might be missed due to the neglect of eccentricity in template banks used for matched-filter based searches such as PyCBC (Usman *et al.*, 2019) or GSTLAL (Messick *et al.*, 2017). GW searches may miss a fraction

of signals because of the following reasons:

1. The templates may not be accurate representations of the real signal, especially if these signals include additional physics (e.g., eccentricity, misaligned spins, higher modes) not included in the template bank.
2. Template banks are discrete in nature.

To quantify the loss of sensitivity of the search, one can define the *match* between the template $h(\theta_i, \Phi)$ and a signal g in terms of the overlap between them as:

$$m(g, h(\theta_i)) = \max(\langle g|h(\theta_i, \Phi) \rangle), \quad (2.1)$$

where $h(\theta_i, \Phi)$ is a template with intrinsic parameters θ_i and extrinsic parameters Φ , and the RHS in Eq. (2.1) is maximised over all the extrinsic parameters. The fitting factor $FF(g)$, for a signal g is defined as (Dhurkunde and Nitz, 2022):

$$FF(g) = \max(m(g, h(\theta_i))), \quad (2.2)$$

where RHS is maximized over all the templates $h(\theta_i)$. In order to get fraction of recovered signals relative to an optimal search ($FF = 1$), we use the metric described in Buonanno *et al.* (2003), which takes into account the intrinsic SNR of the signal to calculate the signal recovery fraction (SRF), defined as (Dhurkunde and Nitz, 2022):

$$SRF \equiv \frac{\sum_{i=0}^{n_s-1} FF_{\text{TB}}^3(s_i) \sigma^3(s_i)}{\sum_{i=0}^{n_s-1} \sigma^3(s_i)}, \quad (2.3)$$

where FF_{TB} is the fitting factor for a volumetric distribution of n_s sources using a template bank, and $\sigma(s_i)$ is the intrinsic loudness of each signal s_i . We calculate the SRF for a given distribution of sources and a template bank.

2.2.1 Reduced detectability of eccentric systems

We use a reference population distributed uniformly in source frame masses $m_{1,2}^{\text{source}} \in [5, 50]$ and redshift up to 3. For eccentricity parameter (e), log-uniform distribution is used while the sources are distributed uniformly in sky. In this section, we consider non-spinning population to quantify the effects of eccentricity. The population is generated

with three different waveform models:

1. **IMRPhenomD** (Husa *et al.*, 2016; Khan *et al.*, 2016): This is used to create a population of non-spinning, quasi-circular signals.¹ Since we use the same waveform for recovery, this serves as the optimal search and we expect the maximal recovery of the injected signals.
2. **TaylorF2Ecc** (Kim *et al.*, 2019; Moore *et al.*, 2016): This is used to create a population of non-spinning, eccentric signals where the eccentricity distribution is taken as $e_{10} \in [10^{-7}, 0.3]$ for eccentricity defined at 10 Hz (e_{10}). Note: TaylorF2Ecc does not include eccentricity corrections in amplitude of the signal.
3. **EccentricFD** (Huerta *et al.*, 2014): We use the same eccentricity distribution as TaylorF2Ecc but the signals are generated with EccentricFD which includes eccentricity corrections in both the phase and amplitude of the GW signal.

For recovery, we use the ‘quasi-circular’ template bank (non-spinning) constructed with IMRPhenomD. We use stochastic placing algorithms (Babak, 2008; Harry *et al.*, 2009) implemented in PyCBC to generate template bank for component masses in the range $m_{1,2} \in [3, 200] M_{\odot}$, using the minimal match criteria of 0.98. We use this template bank to quantify the fraction of lost signals if the intrinsic population has some eccentricity distribution. We calculate the optimal SNR for each injection using the template bank and then estimate the FF for the set of injections. We use the low-frequency cutoff of 10 Hz and detector sensitivities for i) advanced LIGO (PyCBC, 2018b), and ii) A+ (PyCBC, 2018a).

In Fig. 2.1, we show the fitting factors for all three injection sets considered above. As expected, the quasi-circular injection set generated with IMRPhenomD and recovered with the quasi-circular template bank gives us the maximum FF . The upper cut-off frequency, for each system, is chosen to be the frequency corresponding to the innermost stable circular orbit (f_{ISCO}) for a test particle orbiting a Schwarzschild black hole. We use the lower frequency cut-off of 10 Hz to calculate the match via Eq. (2.1). The loss of FF is visible with both eccentric injection sets. In Fig. 2.2, we explore the parameter regime where the reduction in FF is maximum. As expected, larger eccentricity values

¹While IMRPhenomD is an aligned-spin quasi-circular waveform model, in our study we have restricted to a non-spinning population of binary black holes.

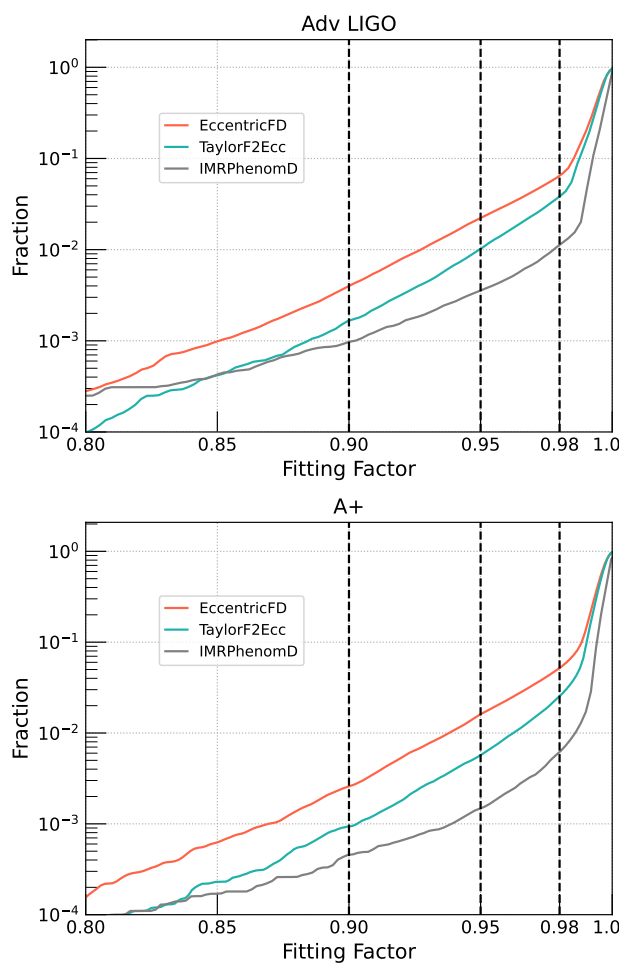


Figure 2.1: Cumulative fraction of events above a given Fitting Factor (FF) for various populations, distributed uniformly in masses and log-uniformly in eccentricity (measured at 10 Hz) with the match calculated against the standard template bank, shown here for detector sensitivities: Adv-LIGO and A+. The grey curves show the fraction recovered for the reference population with no eccentricity, while the green and red curves show the fraction recovered for the eccentric population represented by TaylorF2Ecc and EccentricFD models respectively. Three vertical dashed black lines show the fitting factor values of 0.9, 0.95, and 0.98 increasing in value from the left. These plots show that if we use the quasi-circular template bank to search for a population which contains a log-uniform distribution of eccentricities, we fail to detect a higher fraction of signals in searches. E.g. in the top panel (Adv LIGO sensitivity): eccentric population constructed with TaylorF2Ecc (EccentricFD) waveform has ≈ 1 percent (≈ 2.2 percent) events with fitting factor less than 0.95. FF for baseline model IMRPhenomD is ≈ 0.4 percent. In the bottom panel (A+): eccentric population constructed with TaylorF2Ecc (EccentricFD) waveform has ≈ 0.6 percent (≈ 1.6 percent) events with FF less than 0.95. FF for baseline model IMRPhenomD is ≈ 0.1 percent.

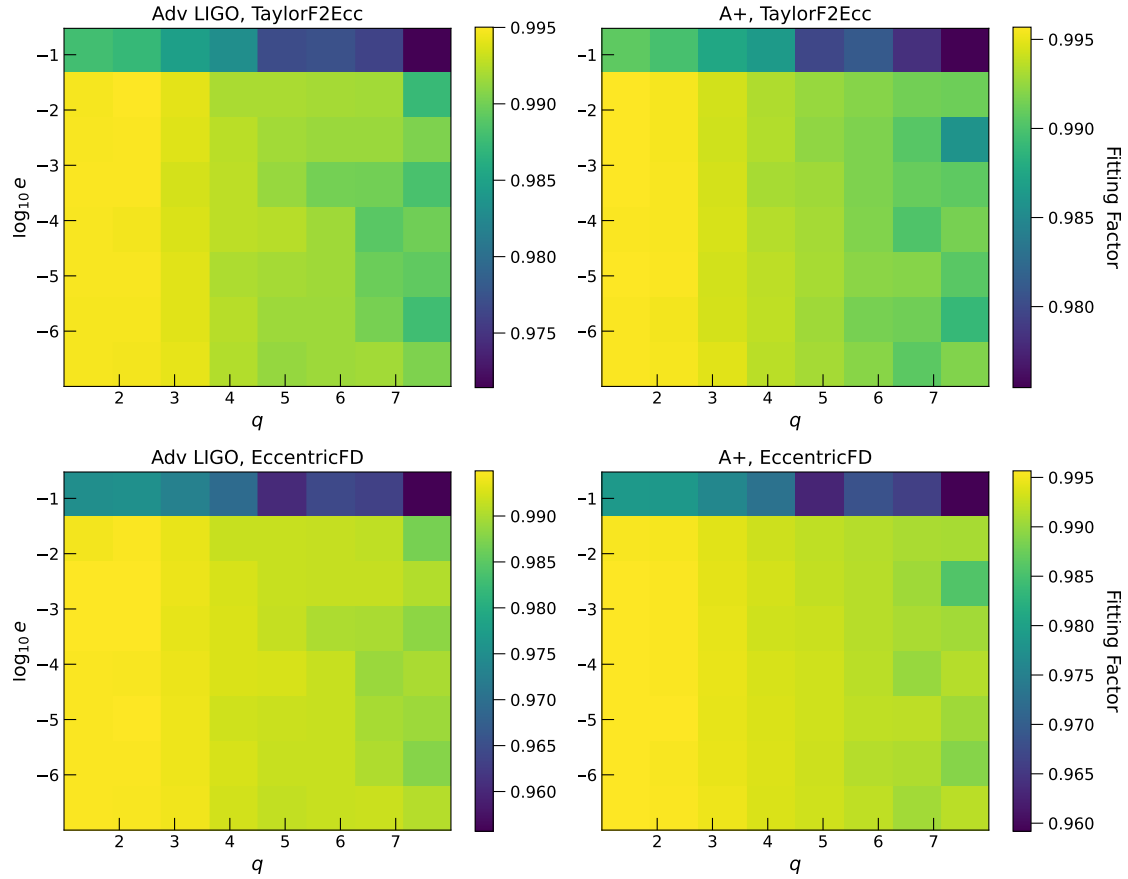


Figure 2.2: The Fitting Factor (FF) varying with mass ratio q and $\log_{10}(e)$ for a population uniform in component masses and log-uniform in eccentricity e_{10} measured at 10 Hz. Top row represents the population generated with TaylorF2Ecc and bottom row represents the population generated with EccentricFD. For all plots, we use the recovery template bank generated with IMRPhenomD. The left column shows results assuming the detector sensitivity of advLIGO and the right column shows results assuming the detector sensitivity of A+. The maximal loss in fitting factor occurs for high mass ratios ($q = m_1/m_2$) and high eccentricity regimes, with high eccentricity values playing dominating role. We use only the inspiral part of the waveform, up to frequency corresponding to innermost stable circular orbit (ISCO), to calculate the FF .

($e_{10} > 0.01$) give us lower FF . We also notice that the combination of high mass ratio and high eccentricity gives us maximum loss in the FF . We propose that more extreme mass ratios lead to a larger reduction in FF for the same value of e_{10} because binaries with more extreme q have longer GW signals in-band, and therefore have more inspiral cycles over which the mismatch due to eccentricity accumulates.

Figures 2.1 and 2.2 show that for a given population of eccentric signals, there will be

Injection Waveform	<i>SRF</i> Full Range	<i>SRF</i> ($e_{10} > 0.01$)	<i>SRF</i> ($q > 3$)	<i>SRF</i> ($e_{10} > 0.01$) & ($q > 3$)
IMRPhenomD	0.992 (0.992)	-	0.986 (0.997)	-
TaylorF2Ecc	0.989 (0.987)	0.973 (0.97)	0.923 (0.978)	0.923 (0.948)
EccentricFD	0.989 (0.987)	0.969 (0.963)	0.923 (0.979)	0.918 (0.944)

Table 2.1: The *SRF*, as described in Eq. (2.3), is calculated for injection sets described in the text to quantify the reduced detectability of eccentric signals when circular template bank is used. For recovery, we use a template bank designed for non-eccentric searches using IMRPhenomD waveform model. For each column, two numbers are shown: one for Advanced LIGO search sensitivity and the numbers in the bracket are quoted for A+ search sensitivity. The *SRF* for the optimal search (injection with IMRPhenomD) indicates the maximum. For eccentric injections, the loss in the *SRF* is maximum in the parameter space ($e_{10} > 0.01$, $q > 3$) which is affected most due to loss in *FF*.

loss of *FF* for signals with eccentricity $e_{10} > 0.01$. This trend becomes more prominent for more extreme values of mass ratio q . The extent of the overall search volume loss depends on the proportion of high-eccentricity signals in the population. In order to include eccentricity in GW searches, we require i) efficient eccentric waveform models and ii) a low computational cost in comparison to the gain in the search volume.

The *SRF* depends on the intrinsic source population under consideration. If the fraction of signals with high eccentricity (> 0.01) is large, we expect to fail to recover a higher fraction of them. In order to estimate *SRF*, we choose a network of three detectors: HLV, with two LIGO detectors H and L at Hanford and Livingston respectively, and the Virgo (V) detector in Italy. For the full population described above, we estimate *SRF* to be 0.992 for optimal search (injection and recovery done with IMRPhenomD) for both the Advanced LIGO and A+ detector sensitivities. We kept the same sensitivity for Virgo (PyCBC, 2012) in both the networks. With eccentric injections using EccentricFD, the *SRF* for the full population is estimated to be 0.989 (0.987) for Advanced LIGO (A+) detector sensitivity. For the other set of eccentric injections generated using TaylorF2Ecc, the estimated *SRF* is 0.989 (0.987) for Advanced LIGO (A+) detector sensitivity. This indicates that the presence of eccentricity in GW signal reduces the

overall SRF if quasi-circular recovery models are used. Moreover, if the population has a significant number of events from the parameter space which is responsible for most loss in FF , the SRF is further reduced, indicating failure of recovering a comparatively large fraction of events in that parameter region. For a targeted region in parameter space of non-negligible eccentricity ($e_{10} > 0.01$) and high mass ratio ($q > 3$), we summarize the results in Table 2.1. In this targeted region, we can get the value of SRF as low as ~ 0.918 compared to the SRF of ~ 0.99 for the optimal pipeline.

To gain insights into a realistic population, we create another injection set. This set incorporates a power-law distribution of source frame masses, consistent with GWTC-3 population analysis (Abbott *et al.*, 2023), and an eccentricity distribution drawn from simulations outlined in Kremer *et al.* (2020); Zevin *et al.* (2021). Figure 1 of Zevin *et al.* (2021) describes the eccentricity distribution at 10 Hz for detectable BBH mergers. We limit the source frame mass distribution to the range $[5, 50]M_{\odot}$, aligning with the template banks we generated. We use the same HLV detector network with two sensitivities for LIGO detectors. For this injection set, the SRF for the baseline model was calculated at ~ 0.986 for both Advanced LIGO and A+ sensitivities. Focusing on targeted regions ($e_{10} > 0.01$, $q > 3$), the SRF is found to be ~ 0.944 (0.946) for EccentricFD (TaylorF2Ecc) injections with Advanced LIGO design sensitivity, and ~ 0.927 (0.928) for EccentricFD (TaylorF2Ecc) injections with A+ design sensitivity.

While we might detect eccentric signals via either quasi-circular template-based searches or unmodelled searches increasing the true fraction of the underlying eccentric population that will enter into our catalogues, bias could be introduced in the subsequently inferred parameters. For this reason, quantifying the bias introduced by analysing eccentric signals with quasi-circular waveform models is necessary. We turn our attention to this in the following section.

2.3 MISCHARACTERIZING ECCENTRIC BINARIES WITH PARAMETER ESTIMATION

In this section, we present results from injection analyses. We assess waveform systematics due to the neglect of eccentricity in PE studies employing quasi-circular waveform models to recover injections into detectors with zero noise (i.e., the detector response to the signal is accounted for, but no additional Gaussian noise is added to the power spectral density representing the detector’s sensitivity). We also perform injections into simulated Gaussian noise and find them to be consistent with zero noise injection analyses. We perform two sets of injections: one with non-spinning simulations based on NR (Chattaraj *et al.*, 2022; Hinder *et al.*, 2018), and one using an EOB-based IMR signal model (TEOBResumS) for aligned-spin injections (Albanesi *et al.*, 2022a,b; Chiaramello and Nagar, 2020; Mora and Will, 2002; Nagar and Rettegno, 2021; Nagar *et al.*, 2018; Placidi *et al.*, 2022, 2023).

Complete inspiral-merger-ringdown waveforms are constructed by matching PN and NR waveforms for individual modes in a region where the PN prescription closely mimics the NR data following the method of Varma and Ajith (2017). These are traditionally referred to as “hybrids” and are used as targets for modelling and data analysis purposes. One such hybrid is shown in Fig. 2.3. The blue dotted line marks the beginning of NR waveform, and the shaded grey region $t \in (1000M, 2000M)$ shows the matching window where hybridization was performed. Overlapping hybrid and NR waveforms on the left of the matching window hint at the quality of hybridization performed here. For non-spinning injections, we use hybrids developed in Chattaraj *et al.* (2022). We analyse non-spinning quasi-circular and eccentric signals with mass ratios $q = (1, 2, 3)$ and a fixed total mass of $M = 35M_{\odot}$ (for dominant mode, zero-noise analyses) and $M = 40M_{\odot}$ (for Gaussian noise injections and HM analyses). For $q = 1$ injection, since the mass ratio prior is restricted to $q \geq 1$, almost the entire posterior lies above the injected value, skewing the posteriors for the other (correlated) parameters; this has been discussed in detail in Sec. 2.3.1. Hence, for dominant mode, aligned-spin eccentric injections, we choose $q = (1.25, 2, 3)$

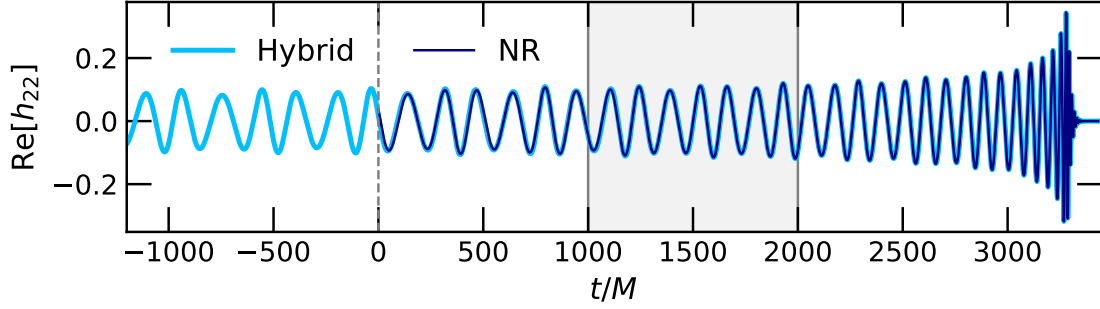


Figure 2.3: [Taken from [Chattaraj et al. \(2022\)](#)] PN-NR hybrid waveform corresponding to NR simulation SXS:BBH:1364, an asymmetric mass binary with mass ratio $q = 2$. The initial eccentricity of the constructed hybrid is $e_0 = 0.108$ at $x_{\text{low}} = 0.045$. The eccentric inspiral waveform used for constructing the target hybrids is presented in [Tanay et al. \(2016\)](#).

with the total mass $M = 35M_{\odot}$ (same as dominant mode, non-spinning injections), and drop the $q = 1$ case. We employ state-of-the-art quasi-circular waveform models (with and without spins) to recover the injections via Bayesian parameter estimation (PE). We also perform PE with an approximate inspiral eccentric waveform TaylorF2Ecc ([Kim et al., 2019](#); [Moore et al., 2016](#)). The approximate eccentric model used here for PE does not include contributions from spin corrections associated with eccentricity and is based on a Taylor approximant ([Buonanno et al., 2009](#); [Damour et al., 2002](#)) different from the one used in TEOBResumS. We assume that our sources are at a luminosity distance of 410 Mpc and inclined at an arbitrary angle of 30° to the line of sight. The sky location angles have been set arbitrarily as ($\alpha \sim 164^{\circ}$, $\delta = 60^{\circ}$, $\psi = 60^{\circ}$), and the geocent time (t_{gps}) is taken to be 1137283217 s. Since the SNR of a GW signal depends on extrinsic parameters in addition to intrinsic parameters like mass and eccentricity, different extrinsic parameters may lead to different SNRs, changing the widths of the posteriors presented here.

To estimate parameters, we perform Bayesian inference (discussed in Sec. 1.5.3) using PyCBC Inference Toolkit ([Biver et al., 2019](#)) and explore the parameter space that includes $(M, q, t_c, d_L, \phi_c, \iota, \alpha, \delta)$. For aligned spin recoveries, we use two additional

Parameter	Prior	Range
\mathcal{M}	Uniform in component masses	5 - 50 M_{\odot}
q	Uniform in component masses	1 - 5
d_L	Uniform radius	100 - 3000 Mpc
ι	Uniform sine	0 - π
t_c	Uniform	$t_{\text{gps}} + (-0.1 - 0.1)$ s
ϕ_c	Uniform	0 - 2π
χ_{iz}^*	Uniform	0 - 0.9
a_1, a_2	Uniform	0 - 0.9
$(S_i^{\Theta} + S_i^{\Phi})^*$	Uniform solid angle	$\Theta \in (0, \pi),$ $\Phi \in (0, 2\pi)$
$(\alpha + \delta)$	Uniform sky	$\delta \in (\pi/2, -\pi/2),$ $\alpha \in (0, 2\pi)$
e	Uniform	0 - 0.4

Table 2.2: Priors for parameters used in various quasi-circular and eccentric recoveries. Here, χ_{iz} is only used for aligned spin recoveries, whereas for precessing spin-recoveries, we have used $a_1, a_2, S_i^{\Theta}, S_i^{\Phi}$. The parameter e is only included in the parameter space for eccentric recoveries. * - where $i = [1, 2]$ refers to the binary components

parameters corresponding to the z -components of the spin vectors *viz.* χ_{1z} and χ_{2z} . For recoveries with spin-precession, we use isotropic spin distribution sampling the six spin components in spherical polar coordinates: $(a_1, a_2, S_1^{\Theta}, S_2^{\Theta}, S_1^{\Phi}, S_2^{\Phi})$. For eccentric recoveries, we include an additional eccentricity (e) parameter in the parameter space. Table 2.2 contains the prior ranges on all the parameters. In our analysis, we marginalise over the polarization angle. We also calculate Bayes factors between recoveries with eccentric (\mathcal{H}_E) and quasi-circular (\mathcal{H}_C) models, given data d , defined as:

$$\mathcal{B}_{E/C} = \frac{p(d|\mathcal{H}_E)}{p(d|\mathcal{H}_C)}. \quad (2.4)$$

where E and C correspond to eccentric and quasi-circular recoveries respectively. The following subsections provide details of the specific injections, as well as various

S. No.	Injection Simulation ID / Waveform	q	e_{20}	χ_{eff}
1	SXS:BBH:1132	1	0	-
2	HYB:SXS:BBH:1355	1	0.104	-
3	HYB:SXS:BBH:1167	2	0.0	-
4	HYB:SXS:BBH:1364	2	0.104	-
5	HYB:SXS:BBH:1221	3	0.0	-
6	HYB:SXS:BBH:1371	3	0.123	-
7	TEOBResumS	1.25	0.0	0.3
8	TEOBResumS	1.25	0.1	0.3
9	TEOBResumS	2	0.0	0.3
10	TEOBResumS	2	0.1	0.3
11	TEOBResumS	3	0.0	0.3
12	TEOBResumS	3	0.1	0.3

Table 2.3: List of non-spinning, eccentric NR hybrid simulations (constructed in [Chattaraj *et al.* \(2022\)](#)) and injections based on aligned-spin eccentric EOB model TEOBResumS. Columns include a unique hybrid ID for each simulation [SXS IDs are retained for identification with SXS simulations ([Abbott *et al.*, 2016c,e, 2017a](#); [Blackman *et al.*, 2015](#); [Boyle *et al.*, 2019](#); [Buchman *et al.*, 2012](#); [Chu *et al.*, 2009, 2016](#); [Hemberger *et al.*, 2013](#); [Hinder *et al.*, 2014](#); [Islam *et al.*, 2021](#); [Kumar *et al.*, 2015](#); [Lovelace *et al.*, 2012, 2011, 2015, 2016](#); [Ma *et al.*, 2021](#); [Mroue and Pfeiffer, 2012](#); [Mroue *et al.*, 2013](#); [Scheel *et al.*, 2015](#); [SXS Collaboration, 2019](#); [Varma *et al.*, 2019a,b,c, 2021](#)) used in constructing the hybrids] and the name of the waveform model used for generating injections, information concerning the mass ratio ($q = m_1/m_2$), eccentricity (e_{20}) at the reference frequency of 20 Hz for a total mass of $M = 35 M_{\odot}$, and effective spin χ_{eff} defined in Eq. (1.32) (only shown for spinning injections).

variations of recovery-waveform spin settings with which these injections have been recovered. While discussing the results in the following subsections, we make use of the term "recovery" to indicate a result in which the 90% credible interval of the posterior includes the injected value, and the systematic bias (difference between the median value and injected value) in the posterior is less than the width of the posterior (at 90% confidence). We judge that the result shows a significant bias if the injected value lies completely outside the 90% credible interval of the posterior. As indicated earlier, these biases are dependent on SNRs which, in this study, fall in the range of typical SNRs

observed in the GW event catalogs. We use the HLV network with design sensitivities of Advanced LIGO (PyCBC, 2018b) and Virgo (PyCBC, 2012) detectors to perform all the parameter estimation analyses shown here.

2.3.1 Dominant mode, non-spinning, eccentric injections

We perform zero-noise injections using non-spinning, quasi-circular as well as quasi-elliptical GW waveforms for BBH mergers of total mass of $M = 35 M_{\odot}$ with mass ratios $q = (1, 2, 3)$. These injections include the dominant modes ($\ell = 2, |m| = 2$) of the eccentric and quasi-circular IMR hybrids constructed in Chattaraj *et al.* (2022), in addition to a quasi-circular SXS simulation (SXS:BBH:1132). Details of the simulations used in this study, including their eccentricity at a reference frequency of 20 Hz, are shown in Table 2.3. To calculate the eccentricity at 20 Hz GW frequency, we have used the reference value (e_0) from Table I of Chattaraj *et al.* (2022) which they have quoted for a dimensionless frequency of $x_0 = 0.045$. Using the following relation we compute the gravitational wave frequency corresponding to $x_0 = 0.045$ and total mass $35 M_{\odot}$:

$$f_{\text{GW}} = \frac{x_0^{3/2}}{\pi M} = 17.62 \text{ Hz} \quad (2.5)$$

where M is the total mass taken in natural units (seconds). Now that we have e_0 at f_{GW} , we evolve it using Eq. (4.17a) of Moore *et al.* (2016) (eccentricity evolution for orbit averaged frequency) to get eccentricity value at 20 Hz (e_{20} shown in Table 2.3). Note that the starting frequency for likelihood calculation is also 20 Hz.

Quasi-circular, IMR recovery

Here, we explore the bias introduced in the source parameters recovered via parameter estimation of GW events when eccentricity is ignored, i.e. we inject an eccentric signal but do not use eccentric waveforms for recovery. For this exercise, we use the quasi-circular IMR phenomenological waveform models IMRPhenomXAS (Pratten *et al.*, 2020) and IMRPhenomXP (Pratten *et al.*, 2021). In figures 2.4 and 2.5, we plot the posterior probability distributions on chirp mass for non-spinning, quasi-circular and eccentric

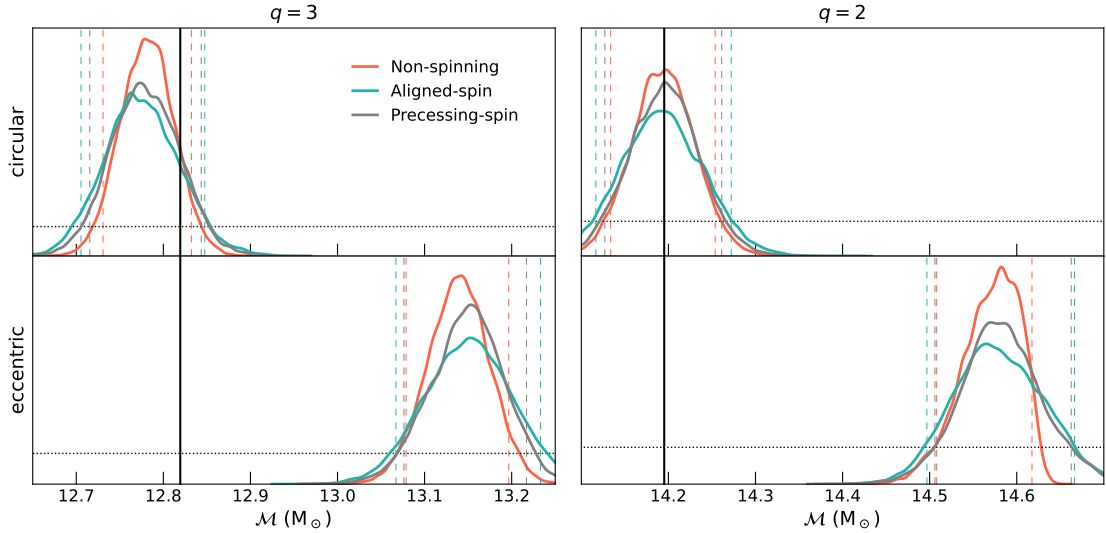


Figure 2.4: Chirp mass posteriors for injections with mass ratios ($q = 2, 3$). The rows indicate the nature of the injections, with the top panel showing results for the quasi-circular injection, and the bottom panel showing results for the eccentric injection ($e_{20} \sim 0.1$). The colours correspond to different spin settings used during recovery. Recovery is performed using quasi-circular waveforms in all cases: IMRPhenomXAS is used for the non-spinning (red) and aligned spin (green) recoveries, and IMRPhenomXP is used for recovery allowing precessing spins (grey). The dashed vertical coloured lines of the same colours denote the 90% credible interval of the corresponding recoveries, the solid black line shows the injected value of \mathcal{M} , and the dotted black curve indicates the prior which is same for all recoveries. The injected value is recovered within the 90% credible interval for the quasi-circular injections, while it is not recovered for the eccentric injections. The slight shift of posteriors for the quasi-circular injection in the $q = 3$ case may be attributed to systematic differences between the waveform models used for injection and recovery. The matched filter SNRs for $q = 2$ and $q = 3$ are 38 and 33 respectively.

injections recovered using IMR quasi-circular waveform models. The injection is recovered using three spin setting configurations: non-spinning (NS), in which we restrict all spins to 0; aligned-spin (AS), in which we restrict spin-tilt angles to 0 and allow spin magnitudes to range between 0 and 0.99; and precessing-spin (PS), in which we allow all spin parameters to vary. By using different spin configurations, we investigate whether spurious measurements of spins occur for non-spinning eccentric injections. In addition to studying biases in spin parameters due to the presence of eccentricity, we also compare the effect of spin settings on the recovery of chirp mass in the presence of eccentricity, since eccentricity and chirp mass are known to be correlated parameters (see

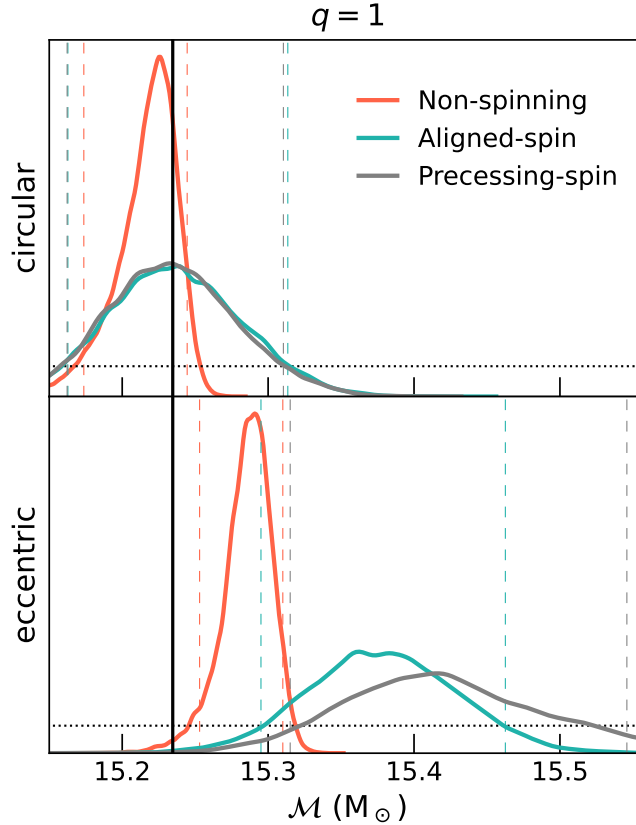


Figure 2.5: Posteriors for $q = 1$ for non-spinning quasi-circular (top) and eccentric (bottom) injections. Recovery with different waveform models is indicated with different colours, corresponding to quasi-circular waveform IMRPhenomXAS for non-spinning (red) and aligned spin (green), and IMRPhenomXP for precessing spins (grey). The injection value is shown with black line. The dotted line shows the prior used, which is same for the recovery of both quasi-circular and eccentric injections. The matched filter SNR for these injections is 41.

for instance [Favata et al., 2022](#)). We use the waveform IMRPhenomXAS for non-spinning and aligned-spin recoveries, and IMRPhenomXP for the precessing-spin recovery. We display the corresponding corner plots in Figs. 2.6, 2.7, and 2.8 for \mathcal{M} , χ_{eff} , and χ_p . Looking at Figs. 2.4 - 2.8 we make the following observations:

- For all the values of mass ratio that we consider, the recovery of eccentric injections with quasi-circular waveform models results in a significant bias of the chirp mass posterior, such that the injected value falls outside the 90% credible interval.
- The spin settings (non-spinning, aligned-spin, or precessing-spin) chosen for recovery do not affect the magnitude of shift in the chirp mass posterior for mass ratios 2 and 3, or in other words; the bias in the recovered chirp mass is the same

regardless of assumptions about the spin magnitudes and tilt angles.

- For $q = 1$, the shift in the chirp mass posteriors for different spin configurations, seen in Fig. 2.5, can partly be explained due to the prior railing of mass ratio leading to almost the entire posterior volume lying outside the injected value. This can lead to the prior railing in component masses and other correlated parameters. This is discussed in detail in the next sub-section.
- The χ_{eff} posterior is largely consistent with zero for both quasi-circular and eccentric injections. The same trend is seen for both the $q = 2$ and $q = 3$ cases. The slight deviation of χ_{eff} from 0 for $q = 1$ case can be explained by looking at the correlation between chirp mass and χ_{eff} (see Fig. 2.8).
- The posterior for χ_p peaks towards 0 for the $q = 2$ and $q = 3$ cases, showing little to no evidence of spin-precession in the signal. For $q = 1$, the χ_p posterior is uninformative. Both the uninformative posterior and posteriors that peak towards 0 support the conclusion that eccentricity is not confused for spin-induced precession in long-duration signals from low-mass BBHs.

For the $q = 3$ case, the slight deviation of posteriors from the injected value for the quasi-circular injection (top left panel of Fig. 2.4) is most likely due to systematic differences between the injection and the recovery waveform. Even at a reasonably modest eccentricity of $e_{20} \sim 0.1$, the chirp mass posterior is shifted enough that the injected value is not recovered within 90% confidence. The shift in the chirp mass posteriors for non-spinning injections is consistent with the ‘*effective chirp mass*’ for eccentric binaries, defined in Bose and Pai (2021) (See also Favata *et al.*, 2022, for a similar definition of ‘*effective chirp mass*’ parameter). Further, for a non-spinning eccentric system with moderate total mass ($M = 35M_{\odot}$), the presence of eccentricity in the signal is not mimicked by a spin-precessing quasi-circular waveform. This is consistent with the findings of Romero-Shaw *et al.* (2023), who find that eccentricity and spin-precession may be distinguished in signals with long inspirals coming from low-mass BBH due to the signal duration exceeding the timescale upon which modulations induced by eccentricity differ significantly from those induced by spin-precession. The fact that the spin posteriors are similar for both eccentric and quasi-circular injections also implies that a lack of spin can be confidently identified in low-mass systems regardless of their eccentricity.

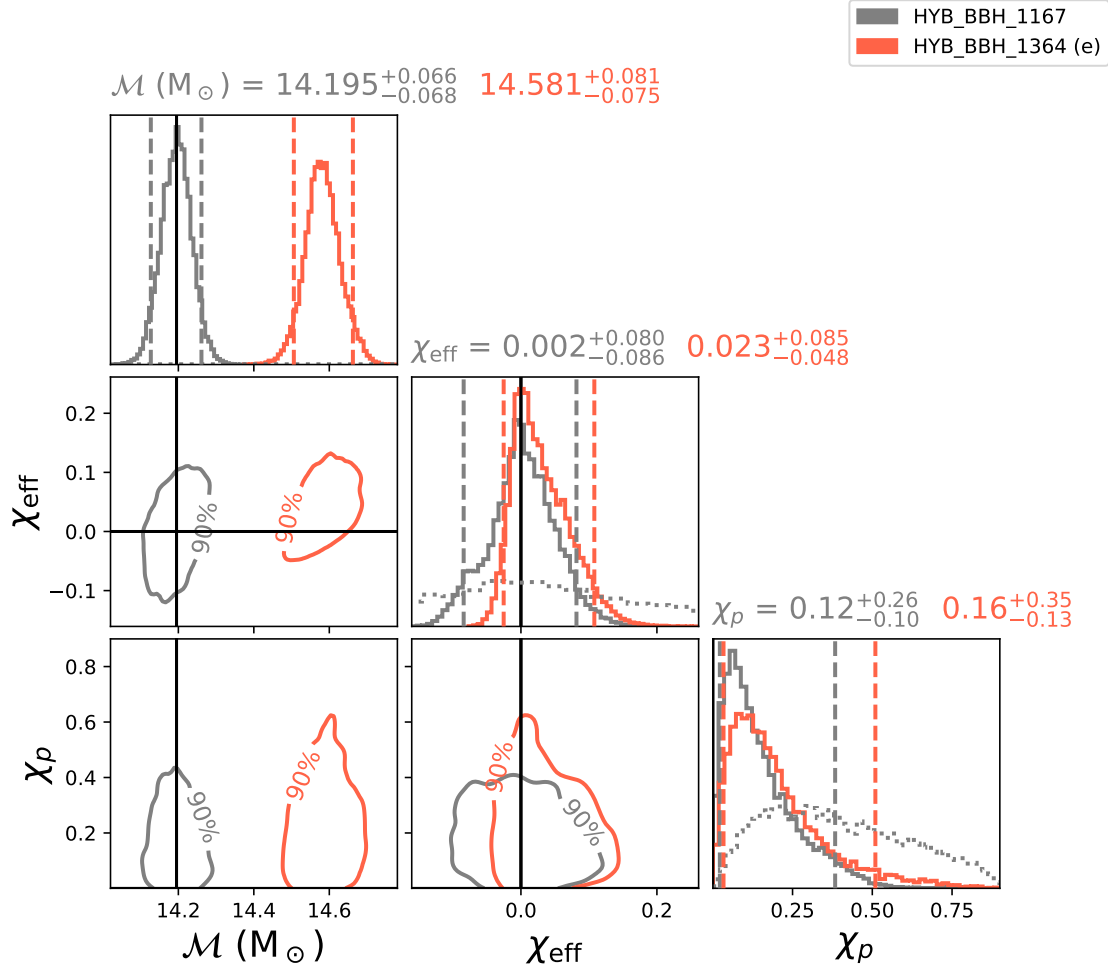


Figure 2.6: The corner plot for $q = 2$ injection showing posteriors on chirp mass (\mathcal{M}), effective spin (χ_{eff}), and spin precession parameter (χ_p), for precessing-spin recovery (performed using IMRPhenomXP) of both quasi-circular (grey) and eccentric (red), non-spinning injections. The injection values are shown with black lines. The histograms shown on the diagonal of the plot are 1D marginalized posteriors for the respective parameters with vertical dashed lines denoting 90% credible intervals. The dotted curves in the 1D plots show the priors used, which are same for the recovery of both quasi-circular and eccentric injections. The prior height for \mathcal{M} is too little compared to the posterior and is not visible in this plot. Therefore, we show the \mathcal{M} prior in Fig. 2.4 instead.

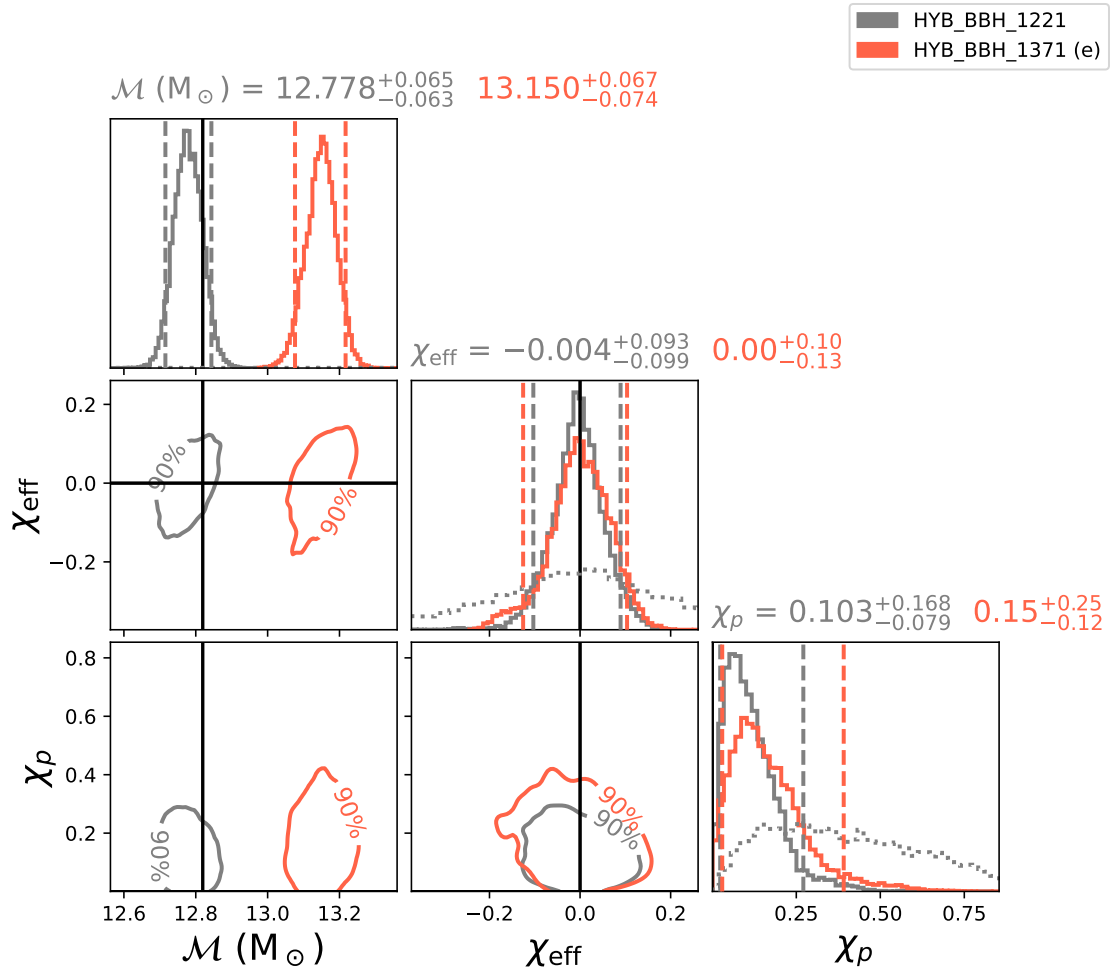


Figure 2.7: Same as Fig. 2.6 but for $q = 3$.

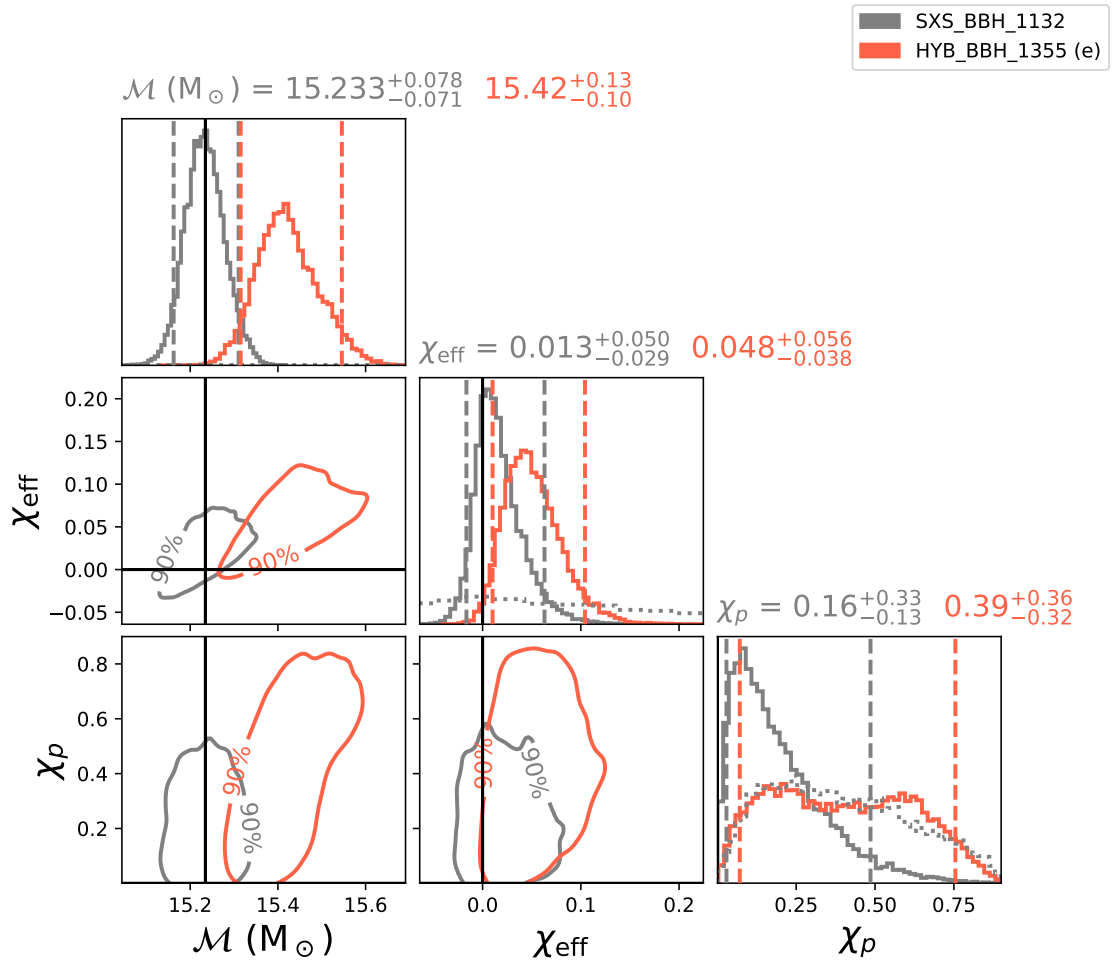


Figure 2.8: Same as Fig. 2.6 but for $q = 1$.

Note on equal-mass case

The $q = 1$ case is different from the other mass ratio cases due to physical limits on the mass ratio prior ($q \geq 1$). The shift in the chirp mass posteriors for different spin configurations, seen in Fig. 2.5, can partly be explained by the prior railing of mass ratio leading to a prior railing in component masses. Since the true value of injection is exactly $q = 1$, parameters correlated with q can become biased due to the entire posterior volume existing above the $q = 1$ boundary. In order to confirm this, we carry out an identical baseline injection run where we inject ($\ell=2, |m|=2$) mode, non-spinning, quasi-circular signal into zero noise using IMRPhenomXAS, and recover it in the same three spin configurations (non-spinning, aligned spin, precessing spin) as used for the hybrids. We observe that the trends are identical to the ones observed using the hybrids. Hence we conclude that for $q = 1$ case, the slight deviation from the usual trend is because of the mass ratio prior skewing the chirp mass posteriors.

Eccentric, inspiral-only recovery

We analyze the same injections as in the previous section with an eccentric inspiral-only waveform model TaylorF2Ecc. We present the results in figures 2.9 and 2.10. In Fig. 2.9, we also show results obtained when the recovery is performed under the constraint $e_{20} = 0$ with the same waveform, in order to account for any biases arising due to systematic differences between waveform model families and/or the lack of merger and ringdown in TaylorF2Ecc. Since TaylorF2Ecc is an inspiral-only model, we have truncated the likelihood integration using the quasi-circular waveform model to the same frequency as the eccentric recovery for a fair comparison and to get comparable SNRs. This frequency has been chosen to be 110 Hz, close to the ISCO frequency for a $35 M_{\odot}$ system.

In the case of $q = (2, 3)$ for eccentric injections (plotted in red in the Fig. 2.9), a quasi-circular recovery excludes the injection value of chirp mass from the 90% credible interval of the posterior when the recovery waveform has arbitrary spin constraints,

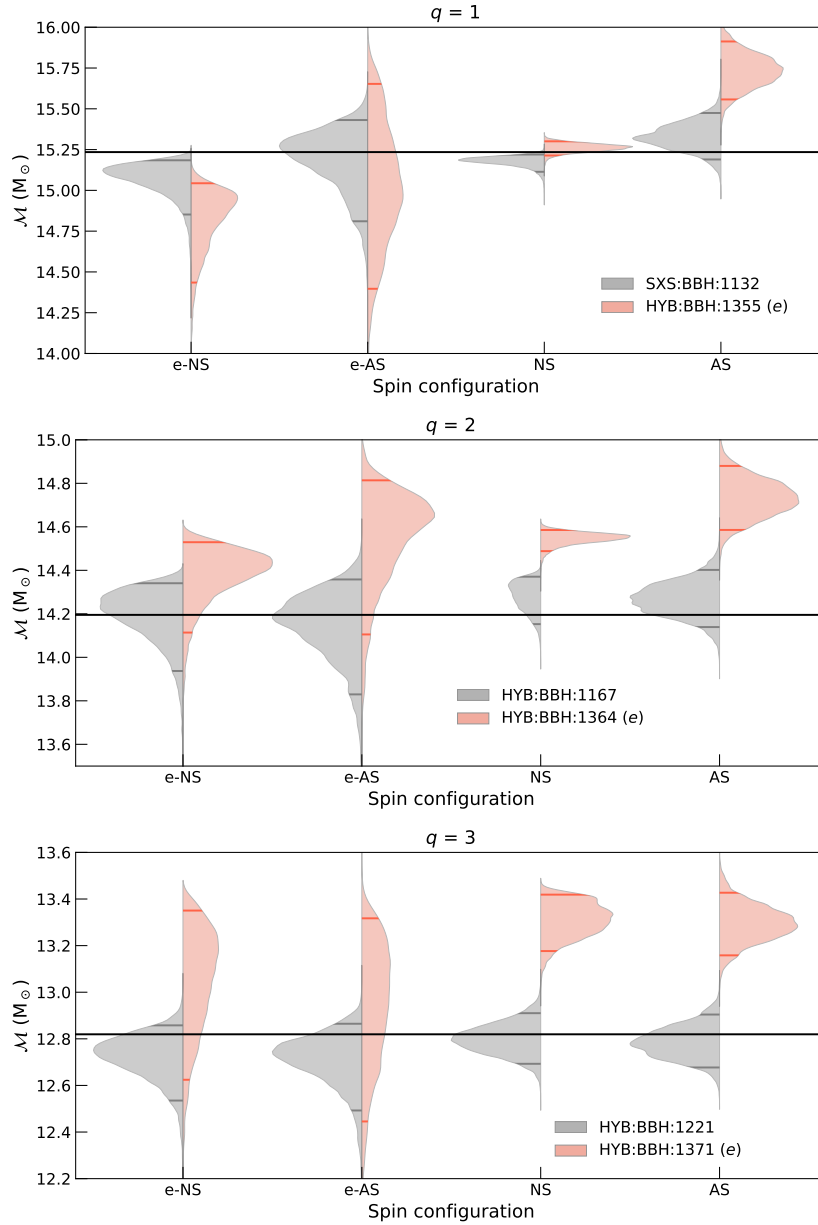


Figure 2.9: We show the recovery with TaylorF2Ecc for eccentric and quasi-circular injections in the form of violin plots. The colours are used to distinguish the injections: red shows eccentric ($e_{20} \sim 0.1$) injections, while grey shows quasi-circular injections. The horizontal axis denotes the spin configuration in the recovery of posteriors. e-NS, e-AS, NS, and AS correspond to eccentric non-spinning, eccentric aligned spin, quasi-circular non-spinning, and quasi-circular aligned spin recoveries, respectively. The vertical axis corresponds to chirp mass \mathcal{M} values. The black horizontal line indicates the injection value and coloured lines inside the shaded posteriors indicate the 90% credible interval. The matched filter SNRs for $q = 2$ and $q = 3$ are 31 and 28 respectively.

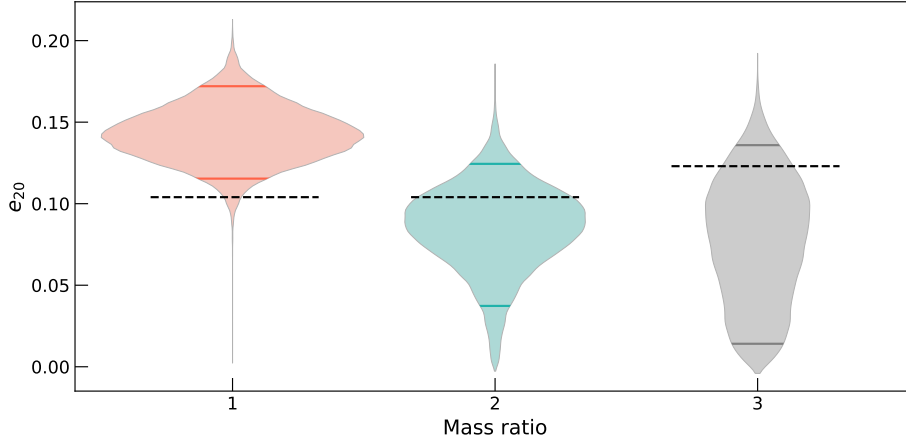


Figure 2.10: Eccentricity posteriors for $q = (1, 2, 3)$ when the injections are non-spinning and eccentric, and the recovery is with TaylorF2Ecc in eccentric, non-spinning configuration. The coloured lines inside the shaded posteriors indicate 90% credible interval whereas the black dashed lines denote the injected eccentricity values.

whereas when eccentricity is included in the recovery waveform model and is sampled over, the injected value is recovered within the 90% credible interval. We show the 1D posteriors for eccentricity in Fig. 2.10, and the 2D contours of e_{20} with \mathcal{M} and q in Figs. 2.11 and 2.12 which highlight the correlations between these parameters. We see that eccentricity shows negative and positive correlations with \mathcal{M} and q , respectively. The log-Bayes factors between eccentric and quasi-circular recoveries performed with TaylorF2Ecc are close to 0 for $q = 2$ and $q = 3$, but for $q = 1$ it is ~ 11 , and thus favours recovery with an eccentric template when the injected waveform is eccentric. However, for $q = 1$ even the quasi-circular recovery (NS) for quasi-circular injection (grey) is not recovered within 90% confidence. Waveform systematics between the injected and recovered waveforms may partially cause this. Additionally, as shown in Fig. 2.10, the injected e_{20} is not recovered within 90% confidence for the eccentric injection. In addition to the waveform systematics, this is likely because the injected q is at the lower boundary of the prior, so the entire q posterior spans higher q than injected, and (as shown in Fig. 2.11) higher q correlates with higher e_{20} . To eliminate possible biases due to this prior effect, we use $q = 1.25$ instead of $q = 1$ in the following section.

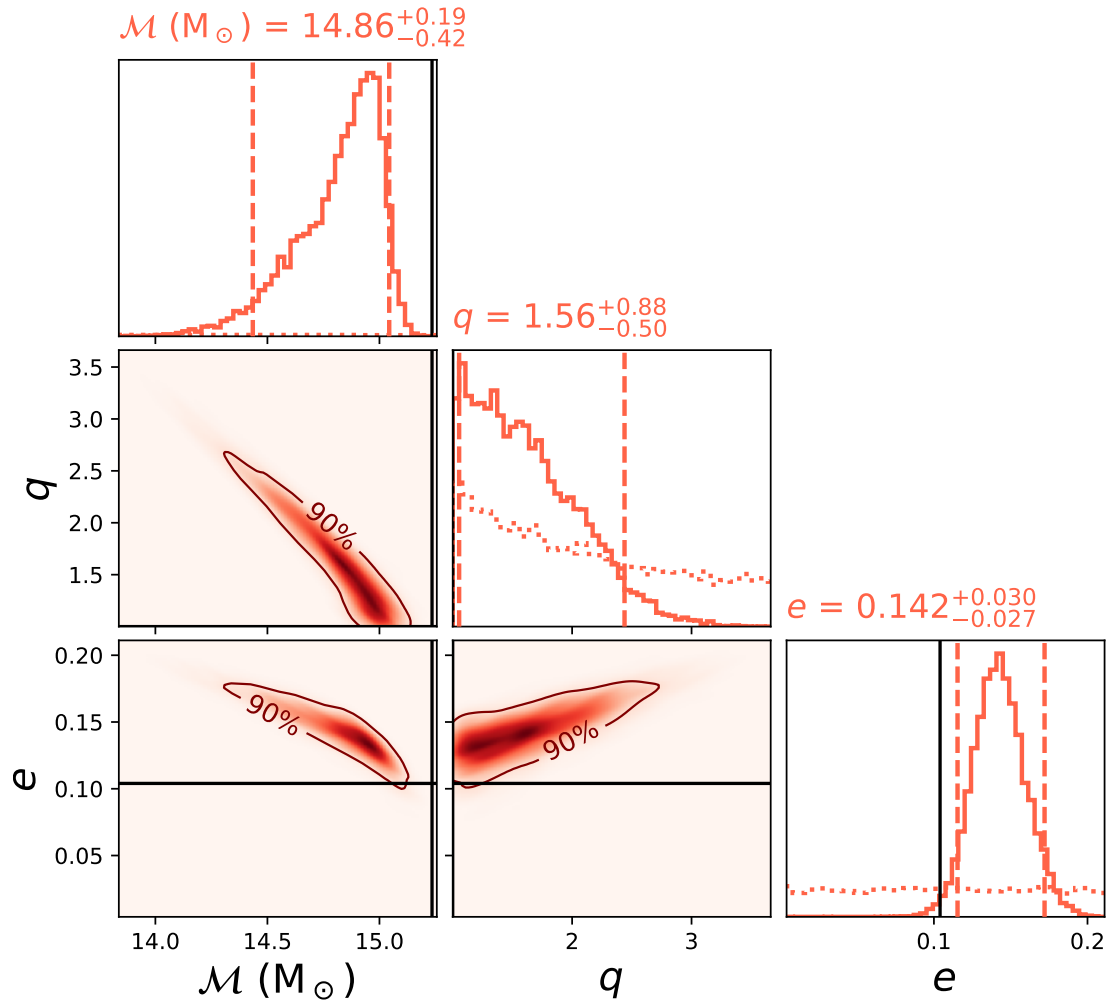


Figure 2.11: The corner plot for $q = 1$ showing chirp mass (\mathcal{M}), mass ratio (q), and eccentricity (e_{20}) posteriors for the non-spinning recovery from Fig. 2.9 performed using TaylorF2Ecc. The histograms on the diagonal of the plot are 1D marginalized posteriors for the respective parameters with vertical dashed lines denoting 90% credible intervals. The dotted curves show the priors used.

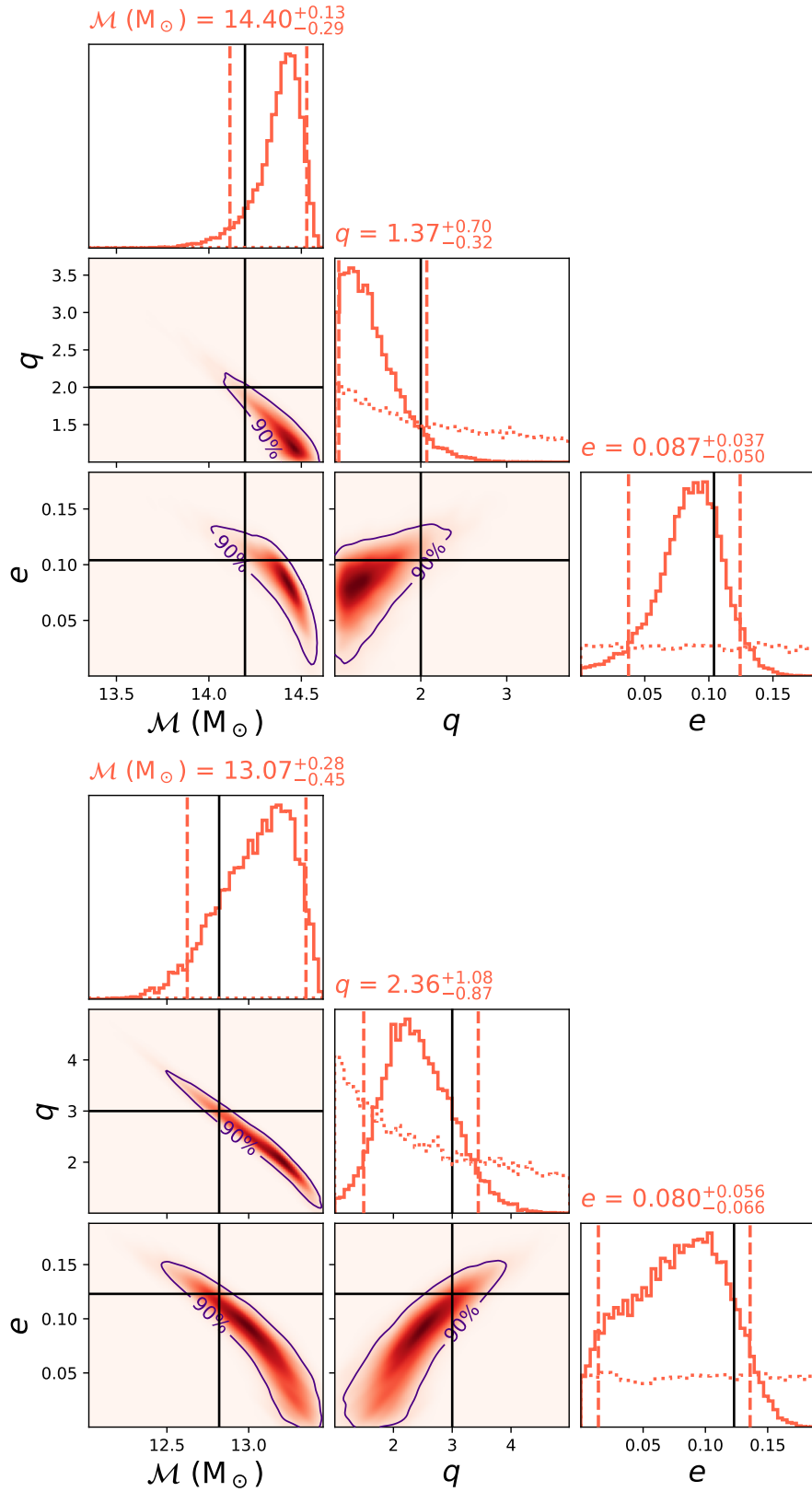


Figure 2.12: Same as Fig. 2.11 but for $q = 2$ (top) and $q = 3$ (bottom).

2.3.2 Dominant mode, aligned-spin, eccentric injections

We inject an aligned-spin eccentric signal using the waveform model `TEOBResumS` (Nagar *et al.*, 2018) and recover in four configurations: quasi-circular aligned spin (AS), eccentric aligned spin (e-AS), eccentric non-spinning (e-NS), and quasi-circular precessing spin (PS). For the first three cases (AS, e-AS, and e-NS) we have used the waveform model `TaylorF2Ecc` for recovery, whereas for the last case (PS), we have used `IMRPhenomXP`. Since `TaylorF2Ecc` is an inspiral-only waveform, we truncate the likelihood calculation for recoveries with both waveforms at 110 Hz in accordance with the choice of total mass as described above. As above, the total mass is $35M_{\odot}$, and here we choose to inject signals with mass ratios $q = (1.25, 2, 3)$. The injected spin magnitudes are $\chi_{1z} = \chi_{2z} = 0.3$, hence $\chi_{\text{eff}} = 0.3$. The eccentric injections have $e_{20} = 0.1$, consistent with injections in earlier sections, with the eccentricity defined at the orbit-averaged frequency of 20 Hz (TEOBResumS, 2021). The chirp mass posteriors are plotted in the form of violin plots in Fig. 2.13. For arbitrary spin settings, the quasi-circular waveform models are not able to correctly recover the chirp mass of the eccentric injection, whereas the eccentric waveform model with aligned spins correctly recovers the injected value. This once again indicates that a quasi-circular precessing waveform model can cause biases in the recovered value of chirp mass if the signal is truly eccentric. Further, looking at figures 2.14 and 2.15, we note that the χ_p posteriors peak at the same value for both eccentric and quasi-circular injections. This again suggests that an aligned spin eccentric signal when recovered with quasi-circular precessing model does not mimic a spin-precessing signal any more than a quasi-circular aligned-spin injection.

We also analyse the same injection with the eccentric waveform model with zero spins (shown as e-NS in the Fig. 2.13). In this case, the posteriors for both the quasi-circular and eccentric injections are biased towards lower masses than injected. Noting that a positively aligned spin system has more cycles compared to its non-spinning counterpart (which is also the case for lower-mass systems), when an aligned-spin signal is recovered using a non-spinning waveform model, it is naturally biased towards lower masses.

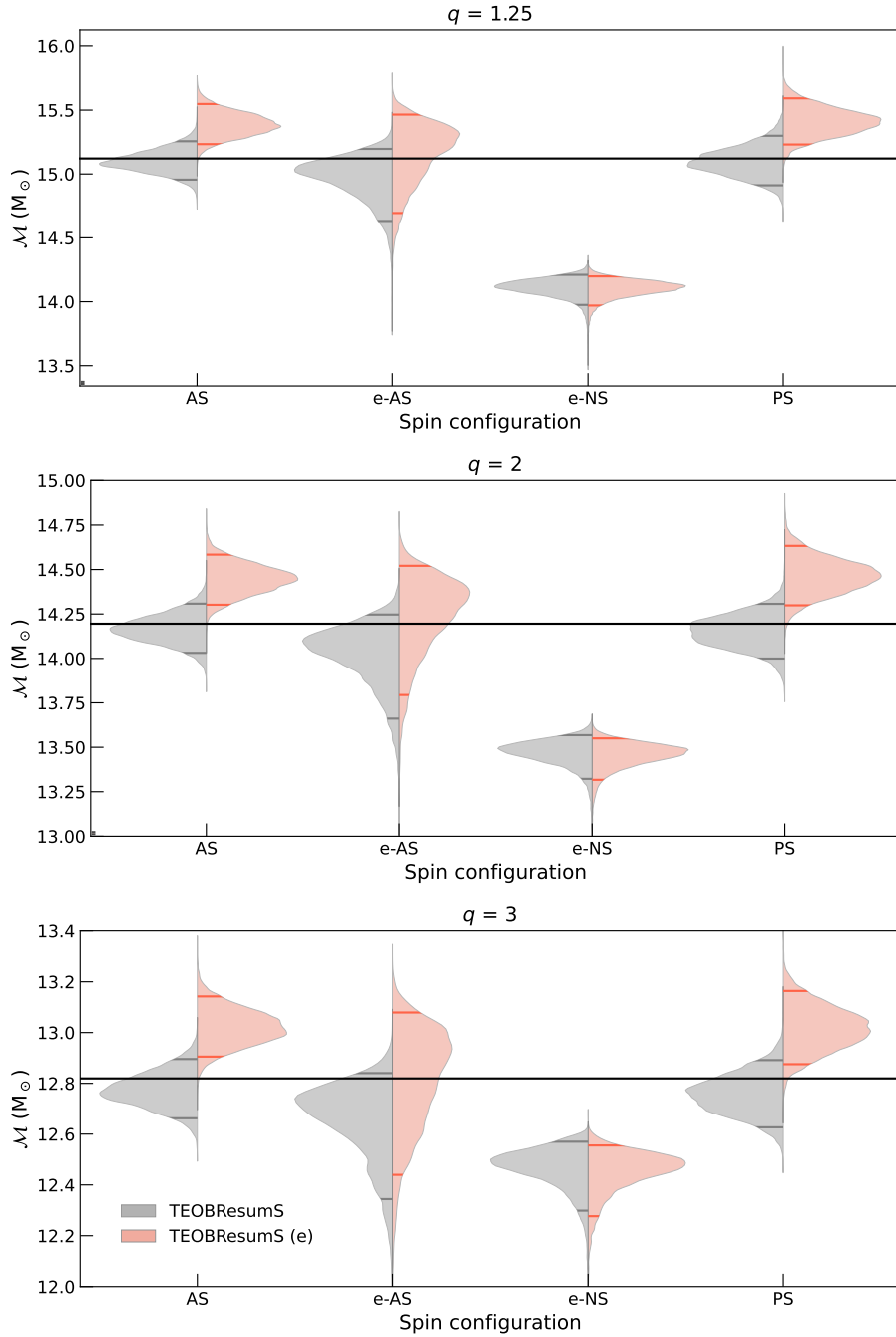


Figure 2.13: Eccentric ($e_{20} = 0.1$) (red) and quasi-circular (grey) aligned-spin injections generated with eccentric waveform model TEOBResumS, recovered with TaylorF2Ecc in quasi-circular aligned-spin (AS), eccentric aligned-spin (e-AS), and eccentric non-spinning (e-NS) configurations, and with quasi-circular waveform model IMRPhenomXP including precessing spin (PS). The aligned-spin eccentric injection is only correctly recovered using the e-AS configuration in the recovery waveform. The matched filter SNRs for $q = 1.25$, $q = 2$ and $q = 3$ are 35, 33 and 30 respectively.

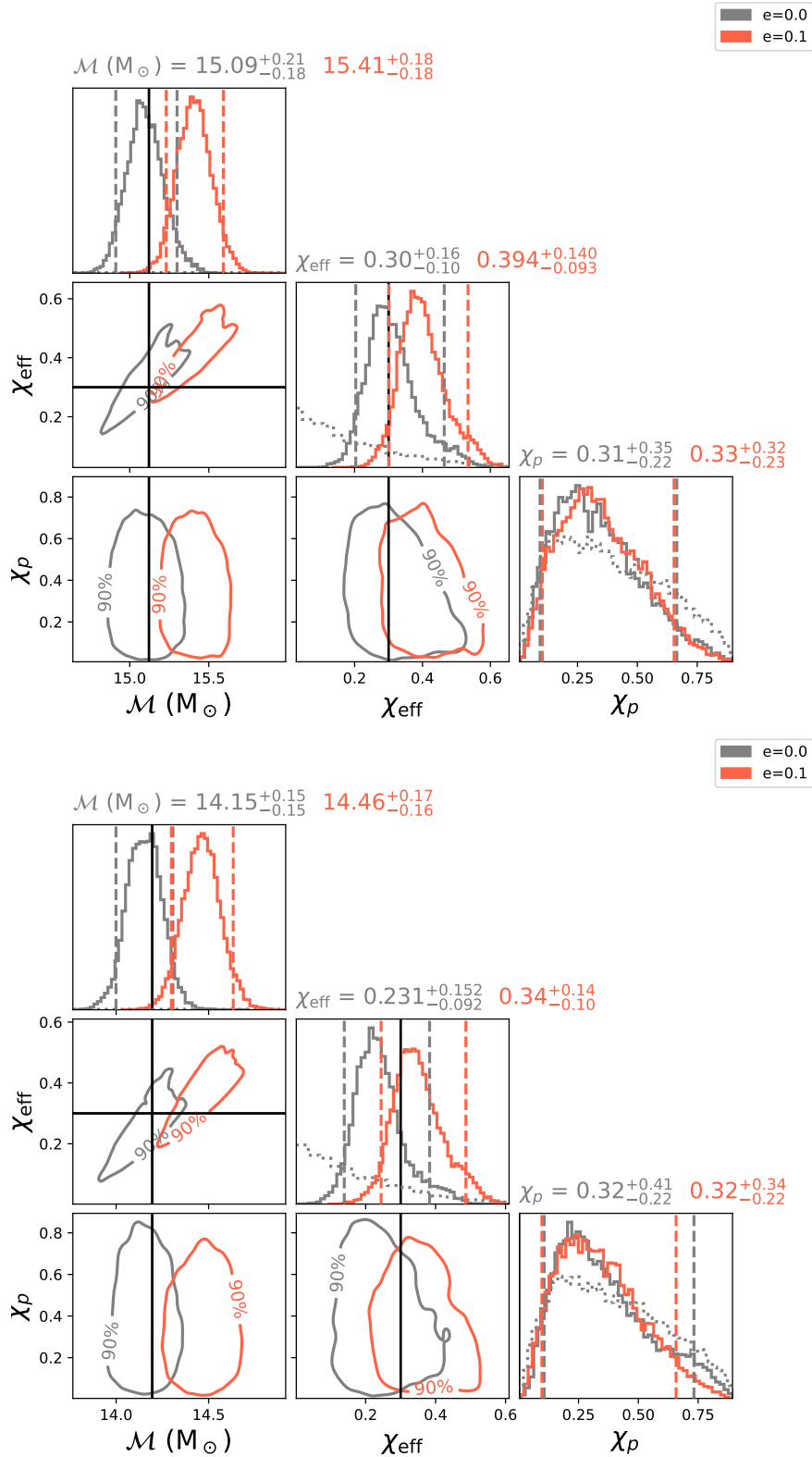


Figure 2.14: Same as Fig. 2.6, but for aligned-spin injections with mass ratios $q = 1.25$ (top) and $q = 2$ (bottom).

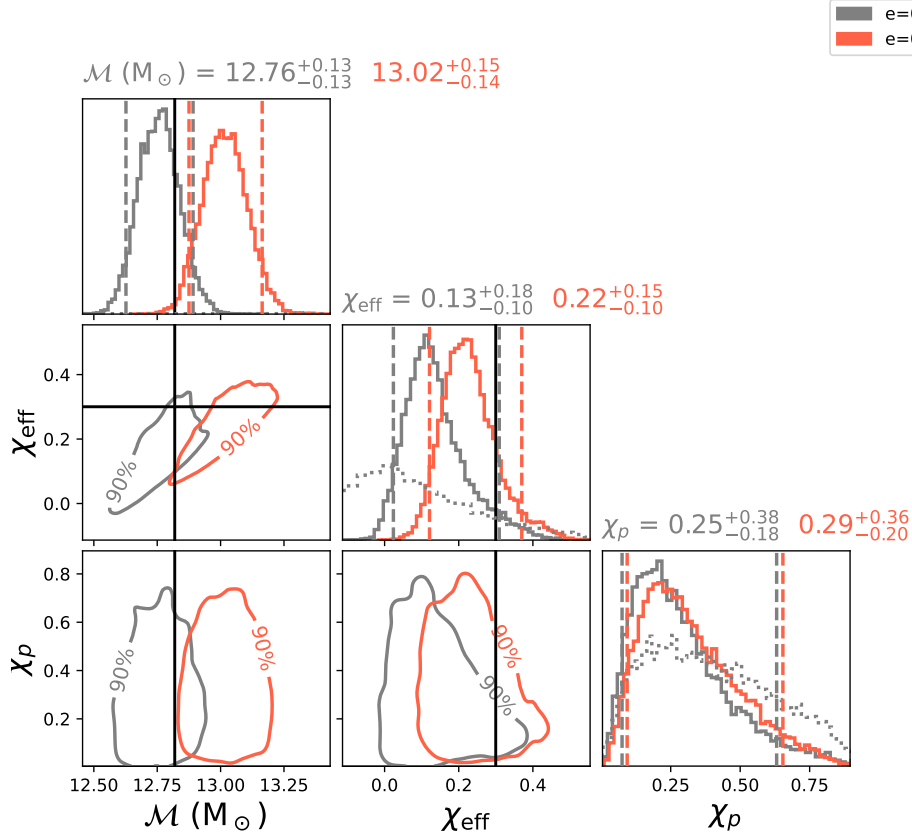


Figure 2.15: Same as Fig. 2.14 but for $q = 3$.

This bias in the chirp mass also causes a bias in the eccentricity posterior, resulting in a higher value of eccentricity due to a negative correlation with chirp mass. This can result in posteriors peaking at non-zero values of eccentricities when an aligned spin quasi-circular signal is analysed with a non-spinning eccentric model. Hence, an eccentric and spinning (aligned) system may be recovered with a positive bias in chirp mass when eccentricity is ignored, and a negative bias when the spins are ignored. Again, we provide the eccentricity posteriors in Fig 2.16 as well as in the form of corner plots along with \mathcal{M} , q , and χ_{eff} parameters in figures 2.17 and 2.18. We see a clear correlation between e_{20} and \mathcal{M} , and a mild correlation between χ_{eff} and e_{20} , consistent with the findings of O’Shea and Kumar (2023). Also, as in Sec. 2.3.1, we find that the Bayes factors ($\mathcal{B}_{E/C}$) for $q = 1.25, 2$, and 3 are not high enough to indicate a clear preference for either the quasi-circular or eccentric waveform model for any injection.

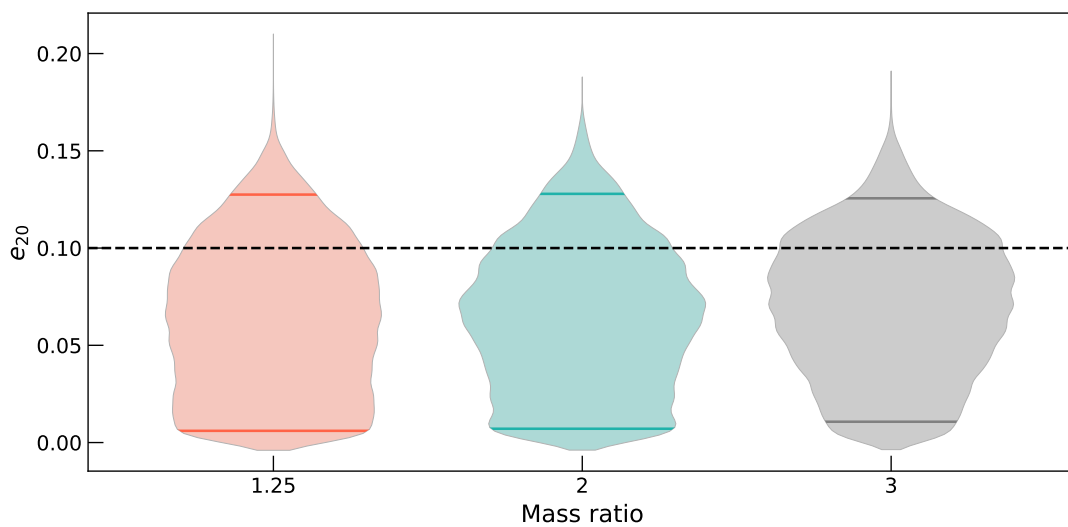


Figure 2.16: Eccentricity posteriors for $q = (1.25, 2, 3)$ when the injections are aligned-spin and eccentric, and the recovery is with TaylorF2Ecc in eccentric, aligned-spin configuration. The coloured lines inside the shaded posteriors indicate 90% credible interval whereas the black dashed lines denote the injected eccentricity value.

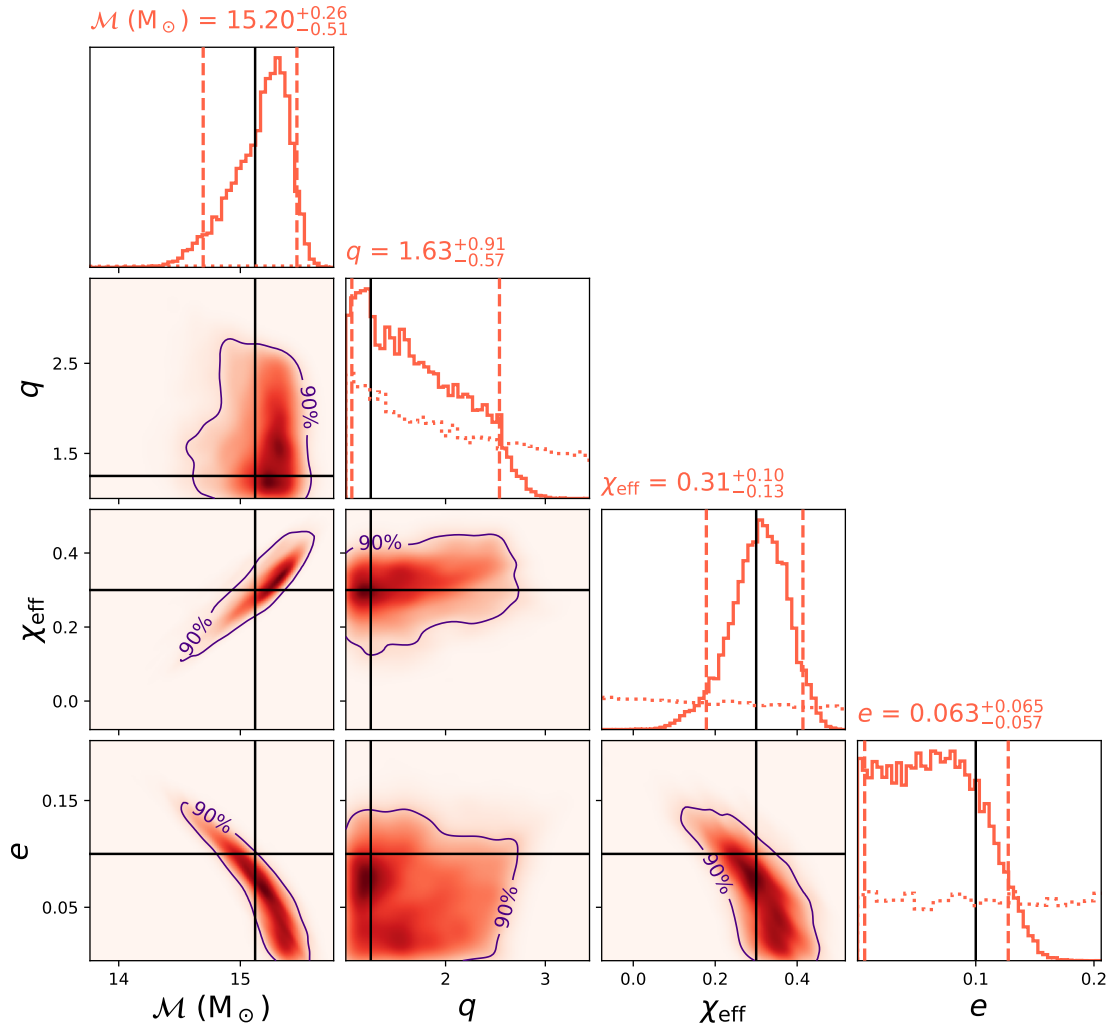


Figure 2.17: The corner plot of chirp mass (\mathcal{M}), mass ratio (q), effective spin parameter (χ_{eff}), and eccentricity (e), for $q = 1.25$ aligned spin recovery from Fig. 2.13 performed using TaylorF2Ecc. The histograms on the diagonal of the plot are 1D marginalized posteriors for the respective parameters with vertical dashed lines denoting 90% credible intervals. The dotted curves show the priors used.

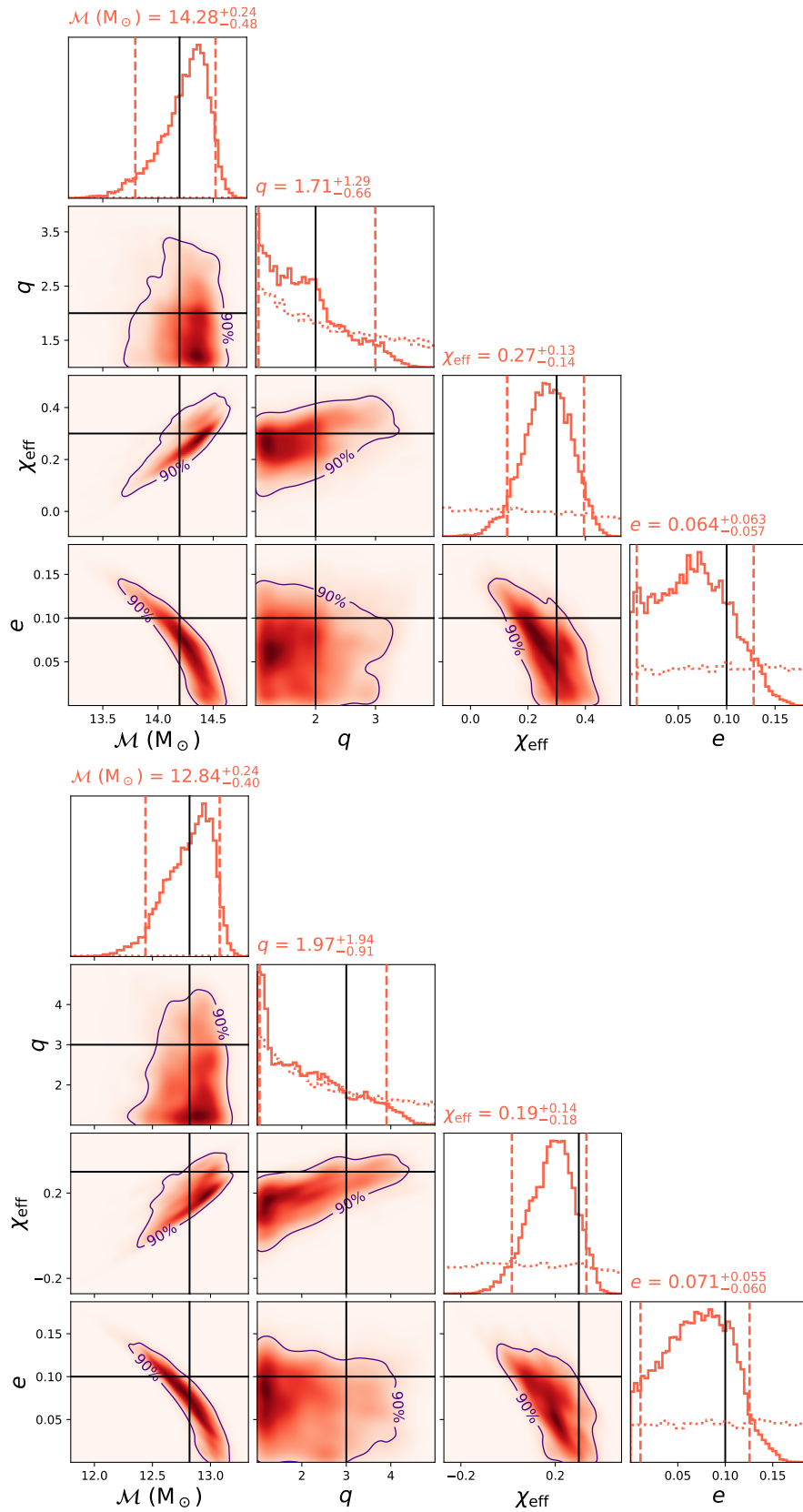


Figure 2.18: Same as Fig. 2.17 but for $q = 2$ (top) and $q = 3$ (bottom).

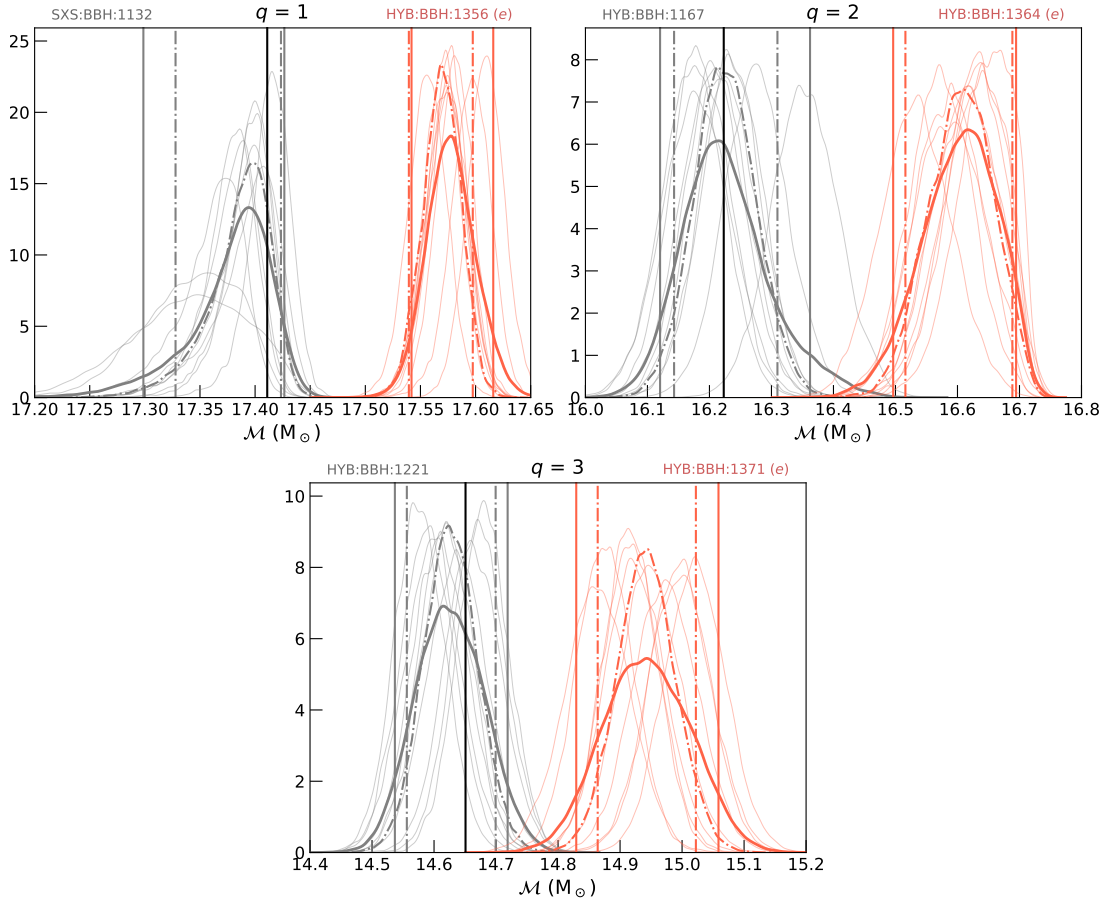


Figure 2.19: The chirp mass posteriors, for injections with mass ratios $q = 1, 2, 3$, compared between eccentric (red) and quasi-circular (grey) non-spinning injections, all recovered using IMRPhenomXAS with zero spins. The faint lines depict injections in different noise realisations, and the dark solid curve is the combined posterior. We have also plotted the zero-noise injection as dashed curve. The coloured vertical lines represent the 90% credible interval of the combined posterior of the same colour as the line, and the black line denotes the injected value.

2.3.3 Simulated noise injections: dominant mode, non-spinning and eccentric

We perform a set of injection recoveries with Gaussian noise simulated using the power spectral densities (PSDs) of the detectors. The total mass of the injected BBH systems is $40M_{\odot}$ and the mass ratios are $q = 1, 2, 3$, with the slightly heavier mass chosen to increase the computational efficiency of the analysis. These are recovered using quasi-circular waveform IMRPhenomXAS with zero spins. The results can be seen in Fig. 2.19. For each case, we have taken 10 noise realizations, which each correspond to the posteriors shown by thin curves in the plot. An equal number of samples were taken from each of

S. No.	Injection Simulation ID / Waveform	q	e_{20}
1	SXS:BBH:1132	1	0
2	HYB:SXS:BBH:1356	1	0.121
3	HYB:SXS:BBH:1167	2	0.0
4	HYB:SXS:BBH:1364	2	0.089
5	HYB:SXS:BBH:1221	3	0.0
6	HYB:SXS:BBH:1371	3	0.105

Table 2.4: List of non-spinning, eccentric NR hybrid simulations (constructed in [Chattaraj *et al.* \(2022\)](#)) used for HM injections. Columns include a unique hybrid ID for each simulation (SXS IDs are retained for identification with SXS simulations used in constructing the hybrids), information concerning the mass ratio ($q = m_1/m_2$), eccentricity (e_{20}) at the reference frequency of 20 Hz for a total mass of $M = 40 M_\odot$.

these runs and combined to form the average posterior shown by the thick coloured curve. We also perform a zero-noise injection for each mass ratio case, which is shown by the dot-dashed curve in the plot. The vertical coloured lines denote 90% credible interval and the black line shows the injected value. As can be seen, the average posterior of all the noisy injections agrees well with the zero-noise curve for each case.

2.3.4 Higher mode, non-spinning, eccentric injections

In this section, we perform injection studies using the higher modes of the eccentric, non-spinning hybrids (one such hybrid is shown in [Fig. 2.20](#)) to assess the biases that are introduced when higher mode, quasi-circular waveforms are used to recover these. [Figure 2.21](#) shows 90% error bounds in the measurement of the binary’s chirp mass for mass ratios $q = (1, 2, 3)$. The total mass of injected signals is assumed to be fixed at $40M_\odot$. The value of eccentricity at 20 Hz (starting frequency of the analysis) is $e_{20} \sim 0.1$ (see [Table 2.4](#) for exact values). The injections here include $(\ell, |m|)=(2, 2), (3, 3), (4, 4), (2, 1),$ and $(3, 2)$ modes. These are then recovered using quasi-circular higher mode waveform `IMRPhenomXHM` ([García-Quirós *et al.*, 2020](#)), which contains all the above-mentioned modes. Additional $(4, 3)$ and $(5, 5)$ modes present in the hybrids have been

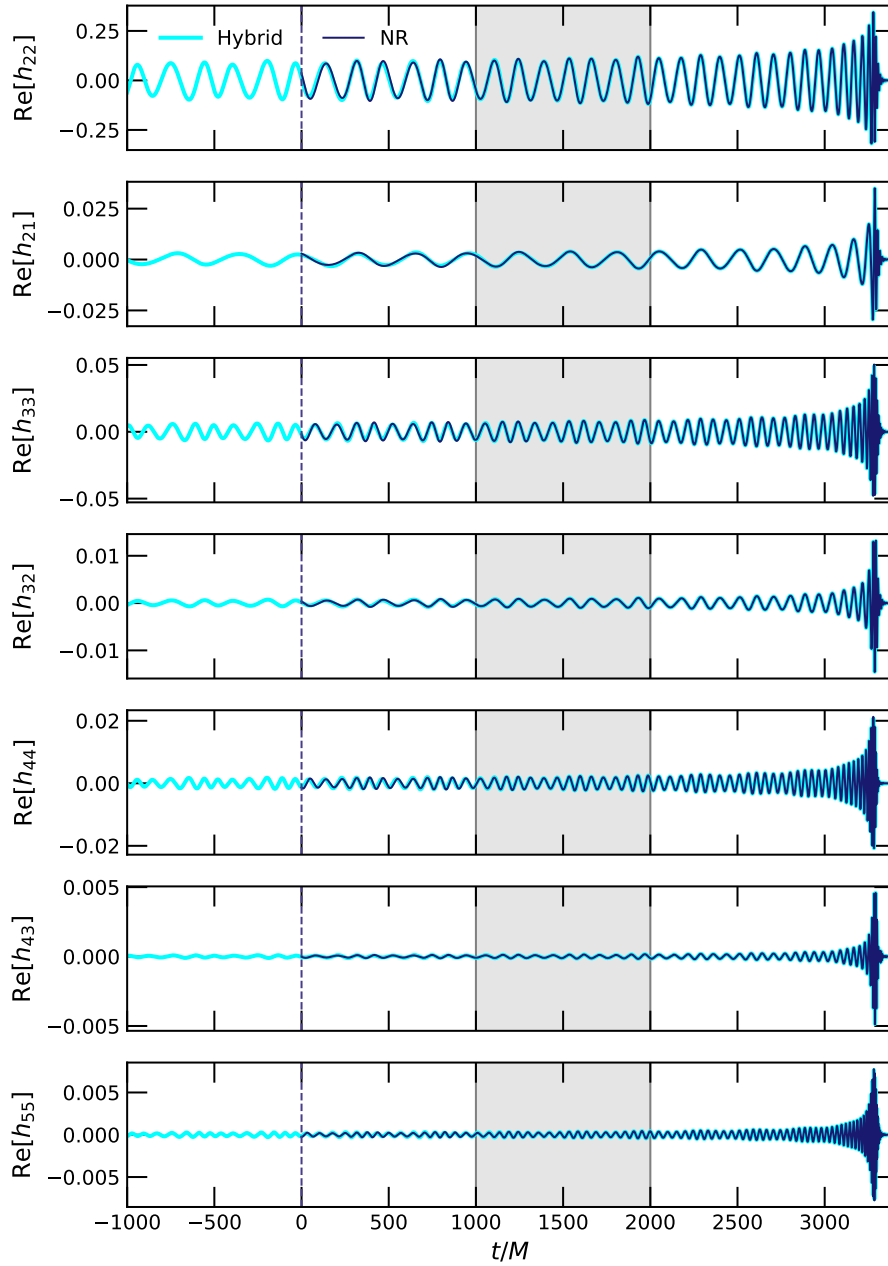


Figure 2.20: [Taken from [Chattaraj et al. \(2022\)](#)] PN-NR hybrid waveform corresponding to NR simulation SXS:BBH:1364, an asymmetric mass binary with mass ratio $q = 2$. The initial eccentricity of the constructed hybrid is $e_0 = 0.108$ at the dimensionless orbital averaged frequency of $x_0 = 0.045$. This frequency parameter, x , is related to the total mass (M) and gravitational wave frequency (f_{GW}) as $x = (\pi M f_{\text{GW}})^{2/3}$. The blue dotted line marks the beginning of the NR waveform and the shaded grey region $t \in (1000M, 2000M)$ shows the matching window where hybridization was performed. Overlapping hybrid and NR waveforms on the left of the matching window hint at the quality of hybridization performed here.

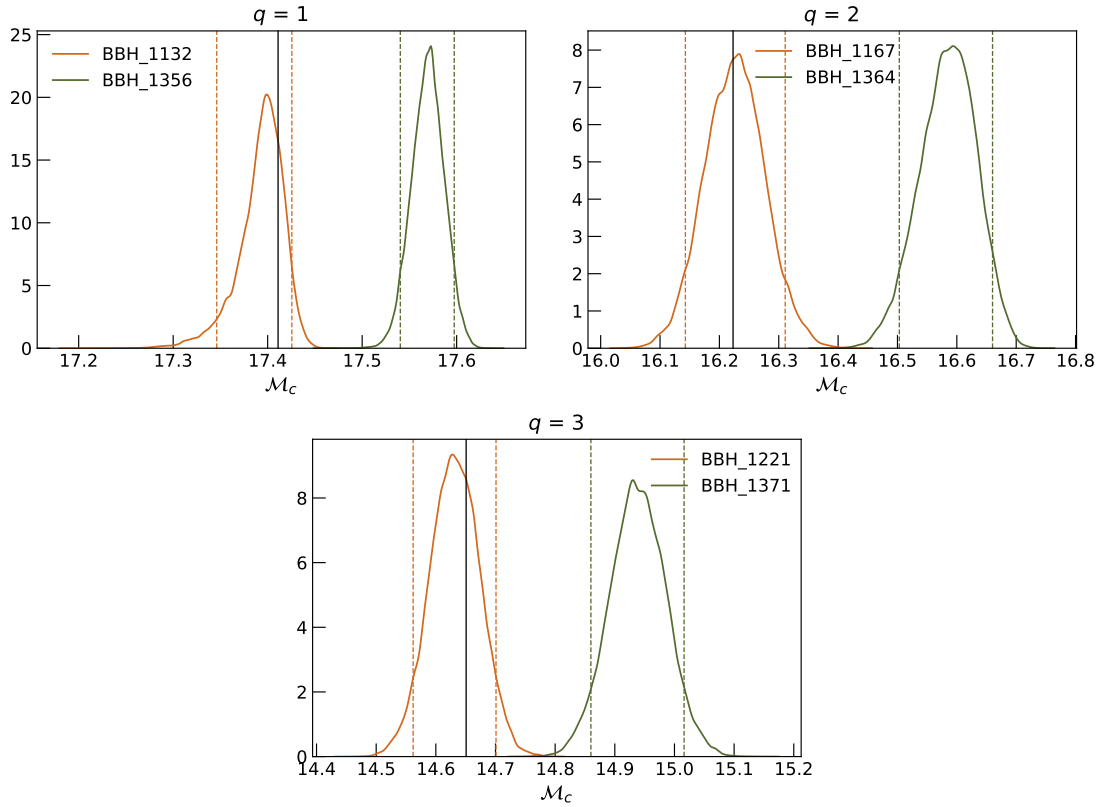


Figure 2.21: Chirp-mass recovery of circular and eccentric injections using quasi-circular, higher mode waveforms. Thick black lines denote the injected value of the chirp-mass parameter and the dashed lines denote 90% credible intervals. The orange (olive) posteriors denote measurement of the chirp mass for the injected circular (eccentric) signal. Both circular and eccentric injections correspond to a BBH of total mass $40M_{\odot}$, and the eccentric simulations have an orbital eccentricity of $e_{20} \sim 0.1$. Non-recovery of the injected value of the chirp mass for the eccentric case can be interpreted as the bias induced due to the neglect of eccentricity and associated higher modes.

dropped to have the same set of modes in injection and the recovery waveforms to avoid misinterpretation of the results. The aim here is to observe if the bias in the parameter estimates is purely due to the combined impact of eccentricity and associated higher-order modes. Vertical black lines in the figure indicate the injected parameter values, while the recovery is shown by posteriors with 90% error bounds (vertical dashed lines). The posteriors in orange denote injections with circular simulations (SXS:BBH:1132, HYB:BBH:1167, HYB:BBH:1221) while those in olive green denote injections with eccentric simulations (HYB:BBH:1356, HYB:BBH:1364, HYB:BBH:1371).

It can be seen in Fig. 2.21 that eccentric injections are not recovered with the quasi-circular waveform. This indicates that the presence of residual eccentricity of the order $e_{20} \sim 0.1$ and eccentricity-induced corrections to the higher modes in systems entering the ground-based detectors will lead to significant biases in recovering source parameters. This observation should motivate including the effect of orbital eccentricity in dominant and other higher modes in waveforms from compact binary mergers. Recovery of other relevant parameters by the means of corner plots for all three mass ratio cases is displayed in Figs. 2.22-2.24. This helps us understand correlations between different parameters.

We see correlations among various mass parameters (\mathcal{M}_c , M , and η) and strong correlations between luminosity distance d_L and inclination angle (ι). Again, η has an upper limit of $\eta \leq 0.25$ (by definition), thus for $q=1$, since $\eta = 0.25$, the posterior hits the prior boundary on the right. Because of the correlations between \mathcal{M}_c and η , this translates into slight shifting of the posterior which results in the injection value not coinciding with the median of the posterior. This is observed both in Figs. 2.21 and 2.22. This feature also appears when we inject a signal using IMRPhenomXHM and recover using the same waveform, thus indicating that this is solely because of the correlations between η and \mathcal{M}_c and not because of differences in the injected and recovery waveform. The slight shift in $q = 3$ posterior of circular injection (HYB:BBH:1221) though can be attributed to the slight differences in the injected and recovered signal.

Another interesting feature of these plots is that, while the mass parameters show a shift in the posterior with eccentric injections, the distance and inclination posteriors are still able to recover the injected values, even for eccentric injections. This hints at the fact that, while the eccentricity parameter is strongly correlated with the mass parameters of the binary, it is not so with the case of extrinsic parameters like luminosity distance and inclination angle (see also O’Shea and Kumar, 2023).

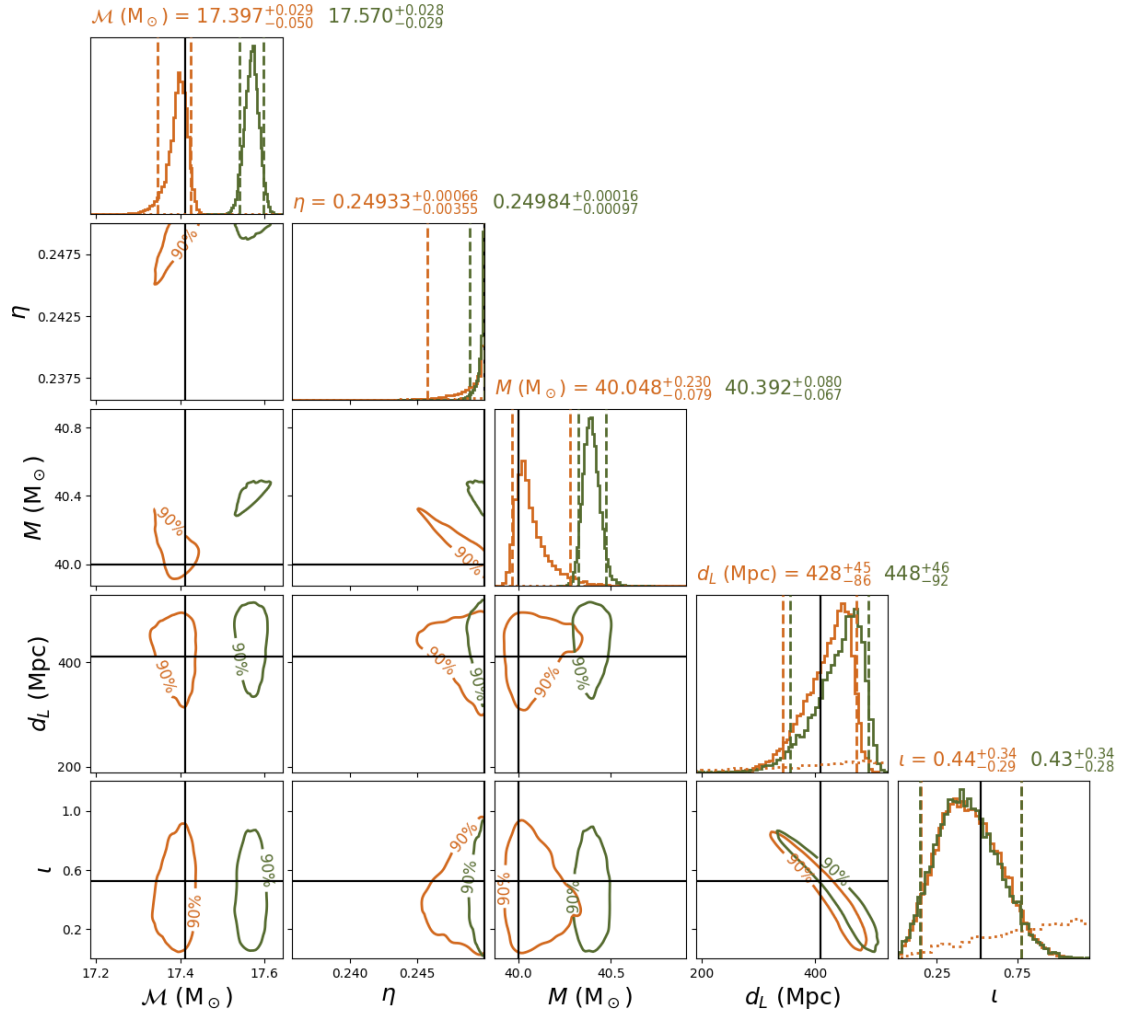


Figure 2.22: Corner plot for $q = 1$, where circular (SXS:BBH:1132) simulation is shown in orange, and eccentric (HYB:BBH:1356) simulation is shown in dark green. Histograms on the diagonal show marginalized 1D posteriors, whereas the contours denote the joint 2D posteriors for various parameters. The vertical dashed lines in 1D histograms mark 90% credible intervals, and dotted lines in orange show the prior. The black lines mark the injected values for various system parameters.

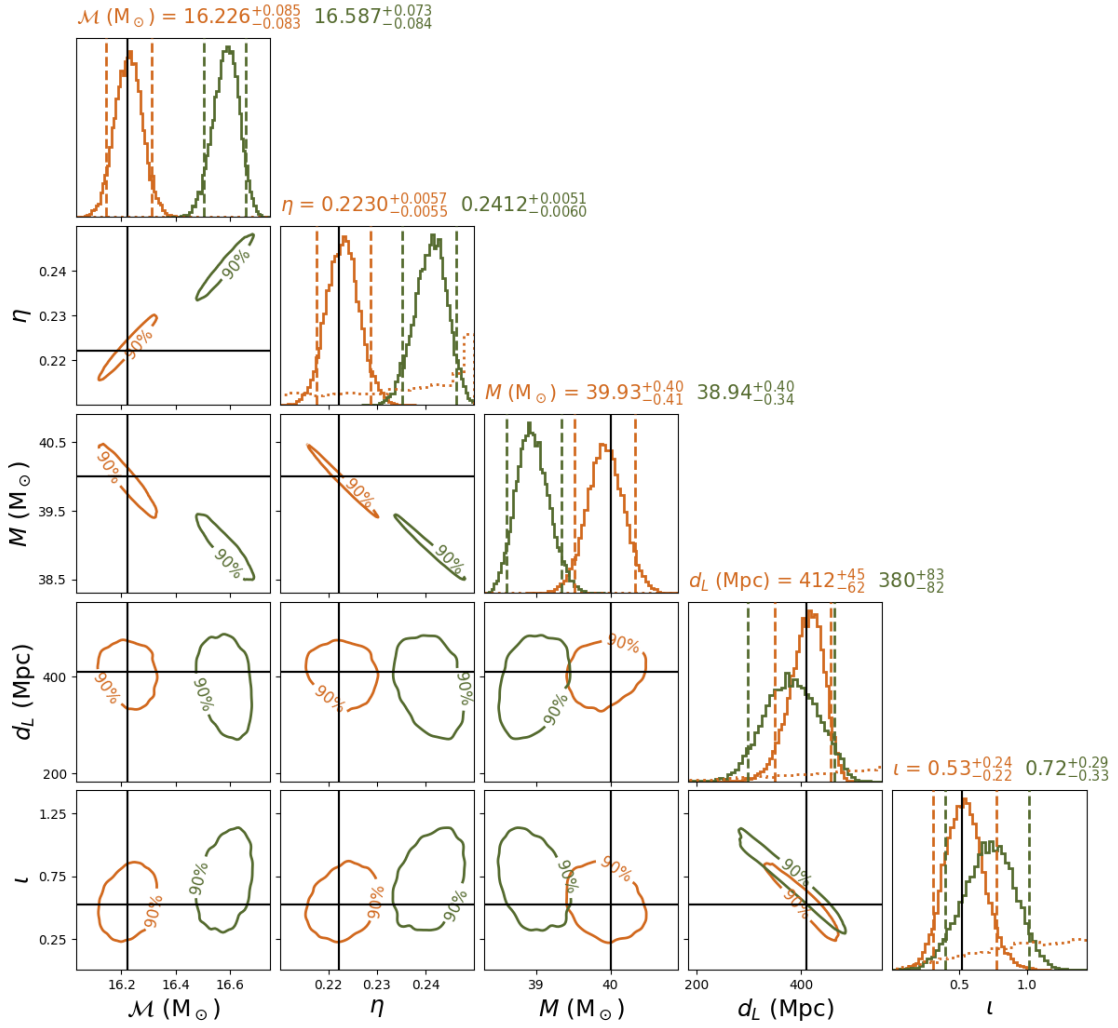


Figure 2.23: Same as Fig 2.22 but for $q = 2$. The hybrids (HYB:BBH:1167) and (HYB:BBH:1364) are used for quasi-circular and eccentric injections respectively.

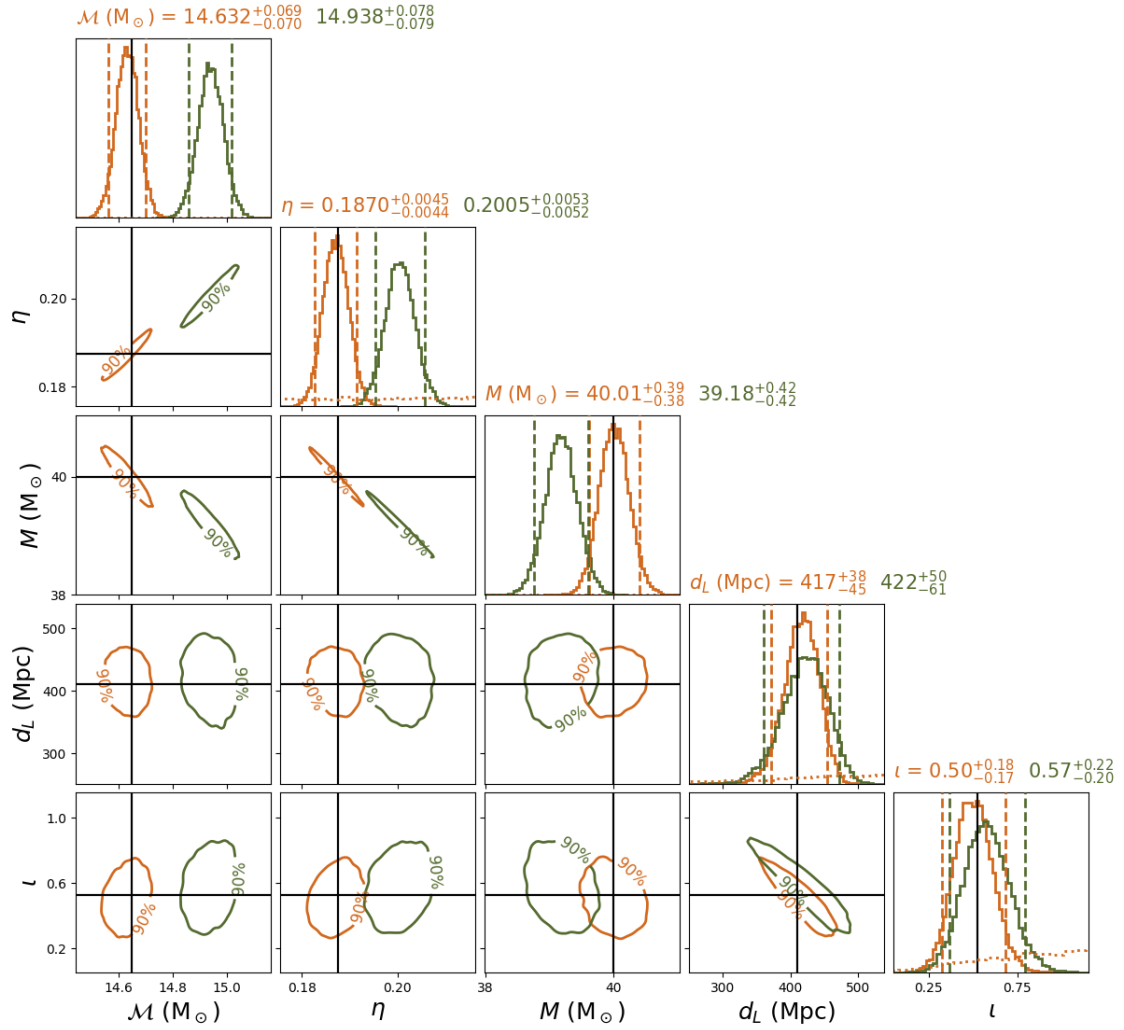


Figure 2.24: Same as Fig 2.22 but for $q = 3$. The hybrids (HYB:BBH:1221) and (HYB:BBH:1371) are used for quasi-circular and eccentric injections respectively.

2.4 SUMMARY AND CONCLUSIONS

Measurable orbital eccentricity is a key indicator of BBH formation channels. However, catalogues of BBH detections, e.g. [Abbott *et al.* \(2021c\)](#), typically neglect this parameter and study all GW candidates using only quasi-circular signal models. Additionally, matched-filter searches for GW signals typically rely on quasi-circular waveform templates. In this work, we explore both the detectability of the eccentric signals when eccentricity is neglected from matched-filtering searches, and the biases that result from performing parameter estimation on eccentric GW signals using quasi-circular waveform models under a variety of spin assumptions.

We find that there is a loss in the fitting factor (< 0.95) for eccentricities higher than 0.01 at 10 Hz in conjunction with high values of mass ratio ($q > 3$). Further, we find that there's a loss in *SRF* up to 6% for the region in parameter space with $e_{10} > 0.01$ and mass ratio $q > 3$. While we restrict this calculation to the inspiral part of the signal, we argue that the loss in *FF* would be similar for full IMR signals, since eccentricity is efficiently radiated away from an inspiralling system and so the binary should be close to circular before the merger and ringdown. The overall loss in the fraction of recovered signals depends on the fraction of events in the population that have a high-eccentricity and high-mass ratio. These population characteristics, in turn, depend on the formation channels contributing to the population. For example, we would detect a higher fraction of binaries that formed in globular clusters (GCs) than those that formed in active galactic nuclei (AGN), since the eccentricity and mass ratio distributions expected from binaries formed in GCs are less extreme than those expected from AGN (e.g., [Tagawa *et al.*, 2021a,b](#); [Yang *et al.*, 2019](#); [Zevin *et al.*, 2019](#)). Therefore, with severity depending on the balance between the formation channels contributing to the observed population, missing eccentric binaries in searches can lead to errors in the inferred merger rate and underlying population characteristics.

Even if an eccentric signal is detected via a matched-template search based on quasi-

circular waveform templates, the recovery of source parameters can be biased when the signal is analysed using a quasi-circular waveform model. We perform parameter estimation on non-spinning and aligned-spin eccentric injections, and recover them using various spin assumptions with quasi-circular and eccentric waveform models. We find that for $e_{20} \sim 0.1$, analyses with the quasi-circular waveform models are unable to recover the injected values of chirp mass within the 90% credible interval. This holds true even for the injections which include both eccentricity and higher modes, which, when analysed with quasi-circular higher mode waveforms, still show the bias in the recovered chirp mass parameter. Further, we note that for the relatively low-mass BBH systems considered in this study, no spurious spin detections are made for non-spinning eccentric injections, and no spurious inferences of precession are made for any eccentric injections. This leads us to conclude that for relatively low mass systems, spin-precession does not mimic eccentricity. The spin parameter posteriors are similar for both quasi-circular and eccentric injections.

Since both eccentricity and spin-precession can indicate that a binary formed in a dynamical environment, our results suggest that a non-spinning low-mass eccentric system if analyzed using quasi-circular waveform models only, may be mistaken for a binary that formed in isolation since the quasi-circular waveform models do not enable measurements of eccentricity and the spin posteriors show no additional signatures of dynamical formation. This may lead to miscategorization of such systems as uninteresting or "vanilla" binaries. Moreover, if we are routinely biased to higher masses even for a small subset of signals that include the influence of binary eccentricity, the population distribution of mass will gradually be shifted higher. Eventually, this could lead to incorrect inferences about, for example, the location of the pair-instability mass gap and the fraction of the population comprised of hierarchical mergers (using hierarchical inference methods such as [Mould *et al.*, 2022](#)). While the shifts in the inferred chirp mass for the low-mass and moderate-eccentricity injections studied here are relatively minor, for higher eccentricities and higher masses the bias would likely be

worse [see, for instance, Eq. (1.1) in [Favata *et al.* \(2022\)](#)]. We also observe that for the eccentricity values chosen here ($e_{20} \sim 0.1$), even an inspiral-only eccentric waveform is able to recover the injected chirp mass within the 90% confidence interval. Therefore, we conclude that for GW signals from relatively low-mass BBH, inspiral-only eccentric waveform models are adequate for identifying and quantifying orbital eccentricity.

CHAPTER 3

TESTING FOR BLACK HOLE MIMICKERS IN GW DATA

3.1 INTRODUCTION

With dozens of gravitational wave events detected by the LIGO-Virgo detectors, and a majority of those being consistent with binary black hole mergers, one naturally asks the fundamental question of whether other binaries, mimicking binary black hole systems, are contaminating the population. We discussed in Sec. 1.6.4 that the nature of the compact objects in a compact binary merger is imprinted on the gravitational wave signal in the form of spin-induced quadrupole moment parameter (κ), and testing the deviation ($\delta\kappa$) on this parameter can give us an idea about the nature of the source. In this chapter, we present the results for spin-induced quadrupole moment (SIQM) test using different waveforms for various GW signals from simulated black hole binaries and real events from the gravitational wave catalogues. We start by outlining the definition of the deviation parameter in Sec. 3.2 along with the details of the waveforms used in the analysis. First, we report on the results (Sec. 3.3) which were obtained by the LVK collaboration from SIQM analysis of events in the 3rd Gravitational wave transient catalog (GWTC-3) and were included in [Abbott *et al.* \(2021g\)](#). These were analysed using a dominant mode, single spin-precessing waveform model (IMRPhenomPv2). Here, we extend the analysis for the waveform models with double spin-precession and higher modes (Secs. 3.4 and 3.5).

The effects of spin-precession and higher-order modes have been extensively studied in the context of testing general relativity (TGR) using binary BHs (see for instance [Breschi *et al.*, 2019](#); [Calderón Bustillo *et al.*, 2017](#); [Islam, 2021](#); [Krishnendu and Ohme, 2021, 2022](#); [Mehta *et al.*, 2023](#); [Puecher *et al.*, 2022](#)). By injecting the most up-to-date

Waveform name	Modes ($\ell, m $)	Features
IMRPhenomPv2	(2,2)	Single spin precession (Hannam <i>et al.</i>, 2014)
IMRPhenomXP	(2,2)	Double spin-precession (Pratten <i>et al.</i>, 2021)
IMRPhenomXHM	(2,2), (2,1), (3,3), (3,2), (4,4)	Higher modes, aligned spin (García-Quirós <i>et al.</i>, 2020)
IMRPhenomXPHM	(2,2), (2,1), (3,3), (3,2), (4,4)	Higher modes, double-spin precession (Pratten <i>et al.</i>, 2021)

Table 3.1: List of waveform models used in this chapter. The columns denote the name of the waveform approximant coded up in `LALSuite`, the spherical harmonic modes (in the co-precessing frame for waveforms with spin-precession), and main features of the waveforms along with relevant publications.

phenomenological waveform models with full spin-precession (IMRPhenomXP) and higher modes (IMRPhenomXHM, IMRPhenomXPHM ([García-Quirós *et al.*, 2020](#); [Pratten *et al.*, 2020, 2021](#))) for binary black hole signals of varying masses and spins, we investigate the effects of spin-precession and higher modes on $\delta\kappa$ measurements. Specifically, our injections include binaries with mass ratios ($q = m_1/m_2$, where m_1 and m_2 are the detector-frame component masses and $m_1 > m_2$) in the range $q \in [1, 5]$, and in-plane & out of plane spin effects for a fixed mass binary ($M = 30M_\odot$). Section 3.4.1 outlines the differences in the bounds of $\delta\kappa$ between IMRPhenomXP (double spin-precessing) and IMRPhenomPv2 (single spin-precessing waveform model) in three scenarios: varying mass ratio, varying effective aligned spin parameter χ_{eff} (Eq. 1.32), and varying effective spin-precession parameter, χ_p (Eq. 1.33). Next, we employ the higher mode waveform models IMRPhenomXHM and IMRPhenomXPHM to study the effect of HMs on $\delta\kappa$ in Sec. 3.4.2. Finally, following the SIQM analyses on GWTC-2 ([Abbott *et al.*, 2021f](#)) and GWTC-3 ([Abbott *et al.*, 2021g](#)) events, which were performed using IMRPhenomPv2, we measure $\delta\kappa$ of the binary systems using IMRPhenomXP and IMRPhenomXPHM instead (Sec. 3.5). We find that together with the effect of spin-precession, the inclusion of higher modes plays a critical role when analysing binaries with mass-asymmetries similar to

that in the event GW190412 (Abbott *et al.*, 2020b) (mass ratio $q \approx 3.7$). In fact, for GW190412, the bounds on $\delta\kappa$ obtained with IMRPhenomXPHM are constrained enough to rule out the boson star binaries, subject to the assumptions in the current work.

3.2 ANALYSIS SETUP

For a binary system composed of two BHs with κ_i , following Krishnendu *et al.* (2019b), we define $\kappa_i = 1 + \delta\kappa_i$, where $i = 1, 2$, and $\delta\kappa_i = 0$ gives the BH limit. With the current detector sensitivities and dominant mode waveform models, the simultaneous measurements of both $\delta\kappa_i$ lead to uninformative results Krishnendu *et al.* (2019b). Thus, we stick to the proposal of Krishnendu *et al.* (2019b), where a symmetric combination of $\delta\kappa_i$ is measured keeping the anti-symmetric combination ($\delta\kappa_a$) to zero. Henceforth, we call this symmetric combination SIQM deviation parameter and use the definition $\delta\kappa_s = (\delta\kappa_1 + \delta\kappa_2)/2$.

GW data analysis has routinely employed phenomenological waveform models with varying properties. For instance, the SIQM analysis in the past was carried out using the precessing dominant mode phenomenological waveform model IMRPhenomPv2 (Khan *et al.*, 2020). With recent developments in phenomenological modelling, it is now possible to describe quasi-circular binaries involving generic spin components. Specifically, the waveform family IMRPhenomXP, developed in Pratten *et al.* (2020), is the current state-of-the-art phenomenological model where double spin-precession effects are introduced. Further, the IMRPhenomXPHM model (which is also double spin-precessing) includes higher order modes $(\ell, |m|) = (3, 3), (4, 4), (2, 1), (3, 2)$ in the co-precessing frame, in addition to the dominant modes $(\ell, |m|) = (2, 2)$ (García-Quirós *et al.*, 2020; Pratten *et al.*, 2021). We modify the inspiral phase coefficients of these waveform models at 2 PN and 3 PN orders by introducing explicit dependence on SIQM parameters, and study the measurement probabilities for simulated GW signals from BBHs and the detected GW events by performing parameter estimation using Bayesian inference (introduced in

Sec. 1.5.3). While there have been Fisher Matrix analyses (such as [Krishnendu et al., 2017, 2019a](#)) estimating bounds on SIQM parameter(s) for aligned-spin systems, Fisher matrix formalism may not yield very good estimates for spin-precessing systems due to higher dimensionality of the parameter space (6 spin vector components compared to only 2 for aligned-spin case), and may require very high SNRs. Hence we use Bayesian inference for the studies performed here. The explicit expressions for modified phase are given in Appendix A. Adding to the generic binary black hole parameter set, $\delta\kappa_s$ is included as a free parameter to be constrained from the data. We can then extract the $\delta\kappa_s$ posterior by marginalizing over all other parameters θ_{BBH} from the multi-dimensional posterior samples as

$$p(\delta\kappa_s|d) = \int p(\theta|d)d\theta_{\text{BBH}}. \quad (3.1)$$

We use LALSimulation ([LIGO Scientific Collaboration, 2018](#)) for generating all waveforms, and *nested* sampling algorithm (described in Sec.1.5.4) implemented through dynesty sampler in bilby and bilby_pipe for parameter estimation in Secs. 3.4 and 3.5. For analysing events from GWTC-3 using IMRPhenomPv2 (Sec. 3.3), *nested* sampling algorithm implemented in LALInference is used.

3.3 RESULTS FROM GWTC-3

Declaration

We declare that the work included in this section is part of the LVK Collaboration paper [Abbott et al. \(2021g\)](#) and has been included in this thesis after obtaining permission from the concerned authorities. The author's contribution to the above-mentioned paper was the Spin-Induced Quadrupole Moment section of the paper, in particular the data analysis of various GWTC-3 events which passed the threshold for SIQM test of GR. Only that part of the paper has been included in this thesis. Various funding agencies that support the work carried out by the LVK Collaboration have been duly acknowledged in the Acknowledgements section of this thesis.

Candidate	\mathcal{M} (M_{\odot})	m_1 (M_{\odot})	m_2 (M_{\odot})	χ_{eff}	D_L (Gpc)	SNR
GW151226	$8.9^{+0.3}_{-0.3}$	$14.2^{+11.1}_{-3.6}$	$7.5^{+2.4}_{-2.8}$	$0.20^{+0.23}_{-0.08}$	$0.46^{+0.16}_{-0.20}$	$12.7^{+0.3}_{-0.4}$
GW170608	$7.9^{+0.2}_{-0.2}$	$10.6^{+4.0}_{-1.4}$	$7.8^{+1.2}_{-1.9}$	$0.05^{+0.13}_{-0.05}$	$0.34^{+0.12}_{-0.13}$	$15.3^{+0.2}_{-0.3}$
GW190412	$13.3^{+0.4}_{-0.3}$	$30.1^{+4.7}_{-5.1}$	$8.3^{+1.6}_{-0.9}$	$0.25^{+0.08}_{-0.11}$	$0.74^{+0.14}_{-0.17}$	$19.0^{+0.2}_{-0.4}$
GW191129	$7.31^{+0.43}_{-0.28}$	$10.7^{+4.1}_{-2.1}$	$6.7^{+1.5}_{-1.7}$	$0.06^{+0.16}_{-0.08}$	$0.79^{+0.26}_{-0.33}$	$13.1^{+0.2}_{-0.3}$
GW191204_17	$8.56^{+0.41}_{-0.28}$	$11.7^{+3.3}_{-1.7}$	$8.4^{+1.3}_{-1.7}$	$0.16^{+0.08}_{-0.05}$	$0.64^{+0.20}_{-0.26}$	$17.4^{+0.2}_{-0.3}$
GW191216	$8.33^{+0.22}_{-0.19}$	$12.1^{+4.6}_{-2.2}$	$7.7^{+1.6}_{-1.9}$	$0.11^{+0.13}_{-0.06}$	$0.34^{+0.12}_{-0.13}$	$18.6^{+0.2}_{-0.2}$
GW200129	$27.2^{+2.1}_{-2.3}$	$34.5^{+9.9}_{-3.1}$	$29.0^{+3.3}_{-9.3}$	$0.11^{+0.11}_{-0.16}$	$0.89^{+0.26}_{-0.37}$	$26.8^{+0.2}_{-0.2}$
GW200225	$14.2^{+1.5}_{-1.4}$	$19.3^{+5.0}_{-3.0}$	$14.0^{+2.8}_{-3.5}$	$-0.12^{+0.17}_{-0.28}$	$1.15^{+0.51}_{-0.53}$	$12.5^{+0.3}_{-0.4}$
GW200316	$8.75^{+0.62}_{-0.55}$	$13.1^{+10.2}_{-2.9}$	$7.8^{+2.0}_{-2.9}$	$0.13^{+0.27}_{-0.10}$	$1.12^{+0.48}_{-0.44}$	$10.3^{+0.4}_{-0.7}$

Table 3.2: Median and 90% symmetric credible intervals for selected source parameters, for GW events analysed in this chapter. The columns show source chirp mass \mathcal{M} , component masses m_i , effective inspiral spin χ_{eff} , luminosity distance D_L , and the network matched-filter SNR. All quoted results are calculated using BBH waveform models. The first two rows show events from first and second observing runs and the values of the source parameters are taken from Table VII of [Abbott et al. \(2024\)](#). Next is GW190412, which is taken from GWTC-2 (Table VI of [Abbott et al., 2021b](#)). The rest of the events are from GWTC-3 (Table IV of [Abbott et al., 2021c](#)).

In this section, we include the results from the SIQM analysis of events from GWTC-3 catalog which were included in the GWTC-3 Test of GR paper ([Abbott et al., 2021g](#)). Events from the second half of the third observing run (O3b) with False Alarm Rate (FAR) $< 10^{-3} \text{ yr}^{-1}$ that were confidently observed in two or more detectors as determined by any search pipeline used in the catalog of O3b events ([Abbott et al., 2021c](#)) were analysed. In addition to the FAR and detector criteria, two additional conditions were considered. First, inspiral-dominated events having an inspiral network $SNR \geq 6$ were selected. Since the test relies on at least one of the binary's components having non-zero spin, events whose effective inspiral spin parameter measurements included zero at the 68% credible level were dropped. The waveform used for this analysis was IMRPhenomPv2.

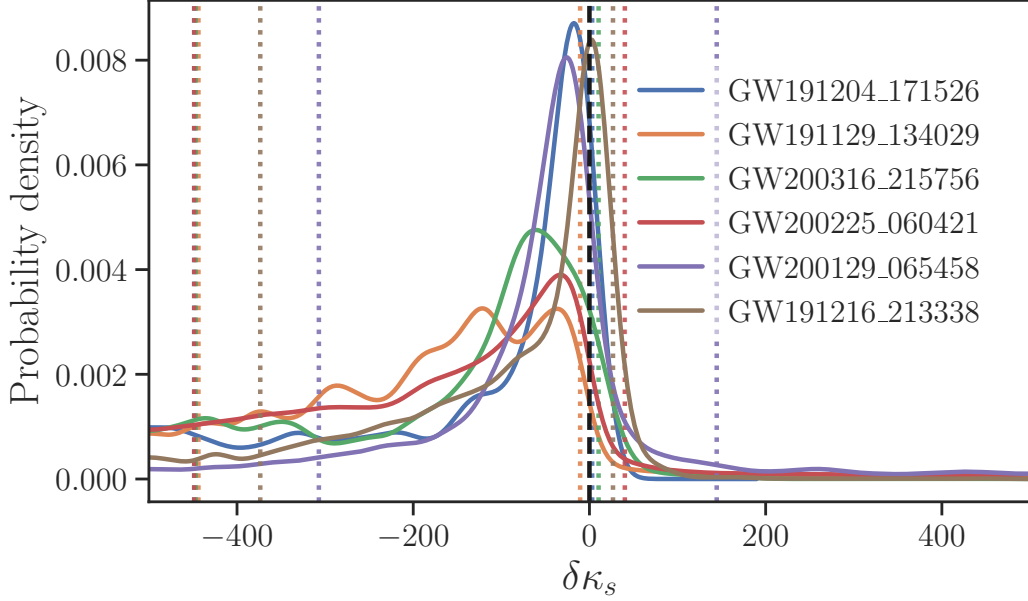


Figure 3.1: [Taken from [Abbott et al. \(2021g\)](#)] The posterior probability distribution on the SIQM deviation parameter, $\delta\kappa_s$, from the O3b events listed Table 3.2. The black dashed vertical line indicates the BBH value ($\delta\kappa_s = 0$). The coloured vertical lines show the 90% symmetric bounds on $\delta\kappa_s$ calculated from the individual events assuming a uniform prior ranging between $[-500, 500]$ on $\delta\kappa_s$.

Figure 3.1 shows the posterior distributions on $\delta\kappa_s$ for the O3b events listed in Table 3.2 assuming a uniform prior on $\delta\kappa_s$ ranging between $[-500, 500]$. Individual events constrain positive values of $\delta\kappa_s$ more strongly than negative ones. This is primarily because of how these parameters correlate with χ_{eff} ([Krishnendu et al., 2019b](#)). As most of the events included here have small but positive χ_{eff} , the combined posterior and the 90% bounds are expected to show this feature. The combined symmetric 90% bound on $\delta\kappa_s$ considering GWTC-3 events was estimated to be $\delta\kappa_s = -16.0^{+13.6}_{-16.7}$ and, conditional on positive values, $\delta\kappa_s < 6.66$ from the joint likelihood analysis. The Bayes factor in support of Kerr nature of the compact binary system was also calculated against $\delta\kappa_s \neq 0$ hypothesis defined as (see Eq. 1.30 for detailed discussion on Bayes factor):

$$\mathcal{B}_{\text{Kerr}/\delta\kappa_s \neq 0} = \frac{\mathcal{Z}(d|\mathcal{H}_{\text{Kerr}})}{\mathcal{Z}(d|\mathcal{H}_{\delta\kappa_s \neq 0})}, \quad (3.2)$$

where $\mathcal{H}_{\text{Kerr}}$ represents parameter estimation using binary black hole waveform model

($\delta\kappa_s = 0$), whereas $\mathcal{H}_{\delta\kappa_s \neq 0}$ represents the analysis with waveform model where SIQM deviation parameter ($\delta\kappa_s$) is included and sampled over. The combined log Bayes factor of $\log_{10} \mathcal{B}_{\text{Kerr}/\delta\kappa_s \neq 0} = 0.9$ was obtained supporting the BBH hypothesis over the hypothesis of all events being non-BBH.

3.4 RESULTS FROM SIMULATED SIGNALS

The analysis of events from GWTC-3 was done using a single spin-precessing, dominant mode waveform, IMRPhenomPv2, and must be revised by employing waveforms which include an improved prescription for spin-precession and higher modes so as to be able to find better constraints on $\delta\kappa_s$. This motivates the investigations presented here that assess the importance of using a waveform model with double spin-precession and higher modes for analysing binary black hole signals with varying properties on the SIQM test. Specifically, we look into different binaries of varying mass-asymmetries and in-plane & out-of-plane spin parameters while fixing all other parameters to look into the effect of mass and spin variations on the $\delta\kappa_s$ measurements. We consider four waveform models, IMRPhenomXPHM (waveform with two-spin effects and higher modes), IMRPhenomXP (waveform with two-spin effects and dominant mode),¹ IMRPhenomXHM (waveform with no spin-precession effects but higher modes), and IMRPhenomPv2 (waveform model with single-spin precession approximation and dominant mode).

For injections, we fix the total mass of the binary to be $30 M_\odot$ and vary mass ratios and spins. The distance is scaled in each case such that we get a fixed network SNR of 40 in a three-detector network consisting of two advanced LIGO and one advanced Virgo detectors, with advanced sensitivities (LIGO Scientific Collaboration, 2022). We have chosen the angles α , δ , ψ , and ϕ_c as 0, and $t_{\text{gps}} = 1126259462$ s for injections. While a different choice of these angles and t_{gps} may lead to a different SNR value, since we are scaling the distance in each case to fix the network SNR, choosing a different value for

¹The solutions employed in IMRPhenomX family are precession-averaged.

Parameter	Prior	Range
q_{inv}	Uniform	0.125 - 1
d_L	Uniform Source Frame	100 - 1000 Mpc
$\cos \theta_{\text{jn}}$	Uniform	-1 - 1
t_c	Uniform	$t_{\text{gps}} \pm 2 \text{ s}$
ϕ_c	Uniform	0 - 2π
a_1, a_2	Uniform	0 - 0.99
θ_1, θ_2^*	Uniform sine	0 - π
ϕ_{12}	Uniform	0 - 2π
ϕ_{JL}	Uniform	0 - 2π
α	Uniform	0 - 2π
δ	Uniform cos	$-\pi/2 - \pi/2$
ψ	Uniform	0 - π
$\delta\kappa_s$	Uniform	-500 - 500

Table 3.3: Priors for parameters used in precessing spin recoveries. We use the subscript "inv" in q_{inv} to indicate that this is the inverse of the *mass ratio* we have used throughout the chapter; bilby uses the variable `mass_ratio` for this. * - Denoted by the spin angle variables `tilt_1` and `tilt_2` in bilby.

these angles should not affect the results. All the injections considered in this section are zero-noise, i.e. we do not introduce any noise in the injected signals and the data on which parameter estimation is performed is generated directly from the waveform models. All of our injections represent BBH mergers ($\delta\kappa_s = 0$). The parameter space taken for precessing-spin analysis is $\{\mathcal{M}, q_{\text{inv}}, a_1, a_2, \theta_1, \theta_2, \phi_{12}, \phi_{\text{JL}}, d_L, \cos \theta_{\text{jn}}, t_c, \phi_c, \alpha, \delta, \psi, \delta\kappa_s\}$. The priors for chirp mass have been modified according to the injection value such that the lower and upper limits are ~ 0.5 and ~ 3 times the injected value, respectively. Note that this is a rather conservative choice compared to the standard priors used while performing parameter estimation with bilby (Romero-Shaw *et al.*, 2020c, see for instance, Table B1 of). Moreover, it can be observed that while our injected values for chirp mass lie in the range $\sim 9\text{-}13M_\odot$ (depending on the choice of injected mass ratio keeping total mass constant), the 90% error bounds on the chirp mass

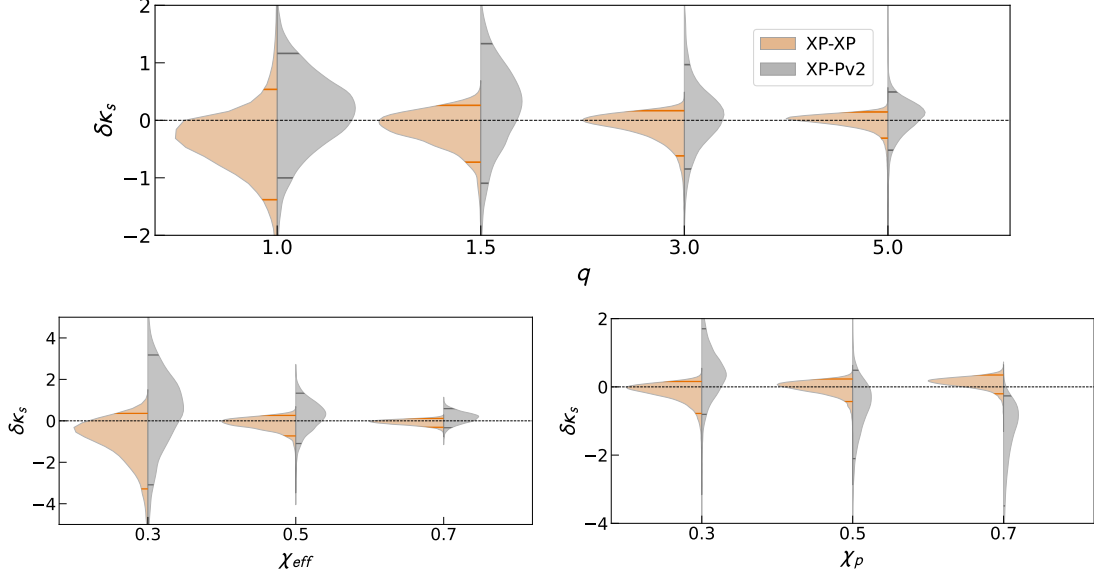


Figure 3.2: The violin plots show posterior distributions for the SIQM-deviation parameter for various injection studies. Top: Four different mass ratio cases are chosen, $q = (1, 1.5, 3, 5)$; the spin magnitudes and related angles are fixed to the values included in Table 3.4. Bottom Left: Three different values for the effective spin parameter are chosen, $\chi_{\text{eff}} = 0.3, 0.5, 0.7$ (see Table 3.5 for complete information); mass ratio is taken to be $q = 1.5$ and $\chi_p = 0.3$. Bottom right: Three different values for spin-precession parameter are chosen, $\chi_p = 0.3, 0.5, 0.7$ (see Table 3.6 for information on other spin parameters); mass ratio is taken to be $q = 3$ and $\chi_{\text{eff}} = 0.5$. The total mass is fixed to $M = 30 M_\odot$, and the network SNR is 40 for all cases. The injections are performed using the fully spin-precessing dominant mode waveform (IMRPhenomXP) and recovered with the same (orange) as well as with single spin-precessing dominant mode waveform IMRPhenomPv2 (grey). The horizontal black-dashed lines denote the injected value, and the coloured lines inside the violins indicate the 90% credible intervals for the respective posterior distributions. The legend follows the pattern ”injected waveform - recovery waveform”.

never exceed $0.2M_\odot$ in width around the median value (see for instance the chirp mass posterior in Figs. 3.3-3.9). Hence, we can safely assert that the prior limits on chirp mass are wide enough not to affect the final posterior distribution. The prior constraints on component masses are also modified accordingly, which means that the sampler rejects the samples drawn outside the range of these constraints during the sampling process. This is done to speed up the parameter estimation process and to avoid samples with very low or very high masses. The priors for the rest of the parameters are given in Table 3.3. For aligned spin recovery, instead of the six spin parameters ($a_1, a_2, \theta_1, \theta_2, \phi_{12}, \phi_{\text{JL}}$), we

use the parameters χ_1 and χ_2 using the `AlignedSpin` prior mentioned in `bilby` which puts a uniform range of $[0, 0.99]$ on the spin magnitudes. For real event analyses with `IMRPhenomXP` and `IMRPhenomXPHM`, we have used the same priors as were used for the respective analyses of the events in GWTC-2 (Abbott *et al.*, 2021f) and GWTC-3 (Abbott *et al.*, 2021g) TGR papers.

3.4.1 Comparison of $\delta\kappa_s$ estimates: `IMRPhenomXP` and `IMRPhenomPv2`

The effect of χ_{eff} on the posteriors of $\delta\kappa_s$ is well established and was explored in Krishnendu *et al.* (2019b), albeit using `IMRPhenomPv2`. Furthermore, while the study in Krishnendu *et al.* (2019b) was performed for aligned-spin systems, here we choose systems with precessing spins and hence also explore the effect of varying χ_p on $\delta\kappa_s$. In this section, we wish to compare the bounds on $\delta\kappa_s$ obtained from `IMRPhenomXP` and `IMRPhenomPv2`. We consider three cases:

- Fixed spins (magnitudes and angles) with varying mass ratio (q).
- Fixed mass ratio & spin-precession parameter (χ_p), varying effective spin parameter (χ_{eff}).
- Different spin-precession values, keeping the mass ratio and aligned-spin components fixed.

For all cases, we inject binary black hole ($\delta\kappa_s = 0$) signals with precessing spins using `IMRPhenomXP` model and recover these with `IMRPhenomXP` and `IMRPhenomPv2`. We present the results in the form of violin plots in Fig. 3.2. These are 1D kernel density estimate (KDE) plots for the posterior samples, and the posterior distribution is plotted vertically such that the parameter being plotted appears on the vertical axis. The posteriors are plotted for two cases simultaneously, denoted in different colours (like orange and grey in Fig. 3.2), such that the height of the posteriors (or width of the violin) is "normalised by area" for each pair, i.e. each violin in a pair has the same area. The horizontal axis simply acts as a separator for various violin pairs, denoting different cases, to be depicted in the same plot.

$q = \frac{m_1}{m_2}$	χ_{1x}	χ_{1y}	χ_{1z}	χ_{2x}	χ_{2y}	χ_{2z}	χ_{eff}	χ_p
1	0.0992	0.1008	0.6	0.3343	0.3397	0.35	0.48	0.48
1.5	0.1013	0.0987	0.6	0.3414	0.3326	0.35	0.5	0.3
3	0.1015	0.0984	0.6	0.3422	0.3318	0.35	0.54	0.14
5	0.0997	0.1003	0.6	0.3359	0.3381	0.35	0.56	0.14

Table 3.4: Values of dimensionless spin components ($\chi_{1x}\dots\chi_{2z}$), effective spin parameter (χ_{eff}), and precessing-spin parameter (χ_p) for different mass ratios when the dimensionless spin magnitude and spin angles have been fixed as follows: $a_1 = 0.6164$, $a_2 = 0.5913$, $\theta_{\text{JN}} = 0.4606$, $\phi_{\text{JL}} = 3.7926$, $\theta_1 = 0.2315$, $\theta_2 = 0.9374$, $\phi_{12} = 0.0$. This has been used for studying the effect of higher modes (Sec. 3.4.2) and the effect of mass ratio variation (Sec. 3.4.1).

Effect of mass ratio variation on $\delta\kappa_s$

To see the effect of mass ratio on $\delta\kappa_s$ measurements, we inject binaries with fixed spin magnitudes and angles, and vary the mass ratio as $q = 1, 1.5, 3, 5$. The spin parameter values are listed in Table 3.4. The injection signals are created using IMRPhenomXP and are analysed with both IMRPhenomPv2 and IMRPhenomXP.

For all the cases, we observe that IMRPhenomXP outperforms IMRPhenomPv2, especially for binaries with higher mass asymmetry. Moreover, we observe from the top panel of Fig. 3.2, that an increase in mass ratio results in better constraints on $\delta\kappa_s$. This is consistent with the findings of [Krishnendu *et al.* \(2019a\)](#) where the dependence of mass ratio on the errors of SIQM parameter ($\Delta\kappa_s$) are discussed in detail [see Fig. 2 and the discussion around Eq. (4.2)-(4.4) there]. Moreover, the values of χ_{eff} also increase gradually as we go from equal mass case to unequal mass while keeping spin magnitudes and angles fixed. Both of these effects result in the improvement of $\delta\kappa_s$ bounds with increasing mass ratio. We show the corresponding corner plots in Figs. 3.3-3.6.

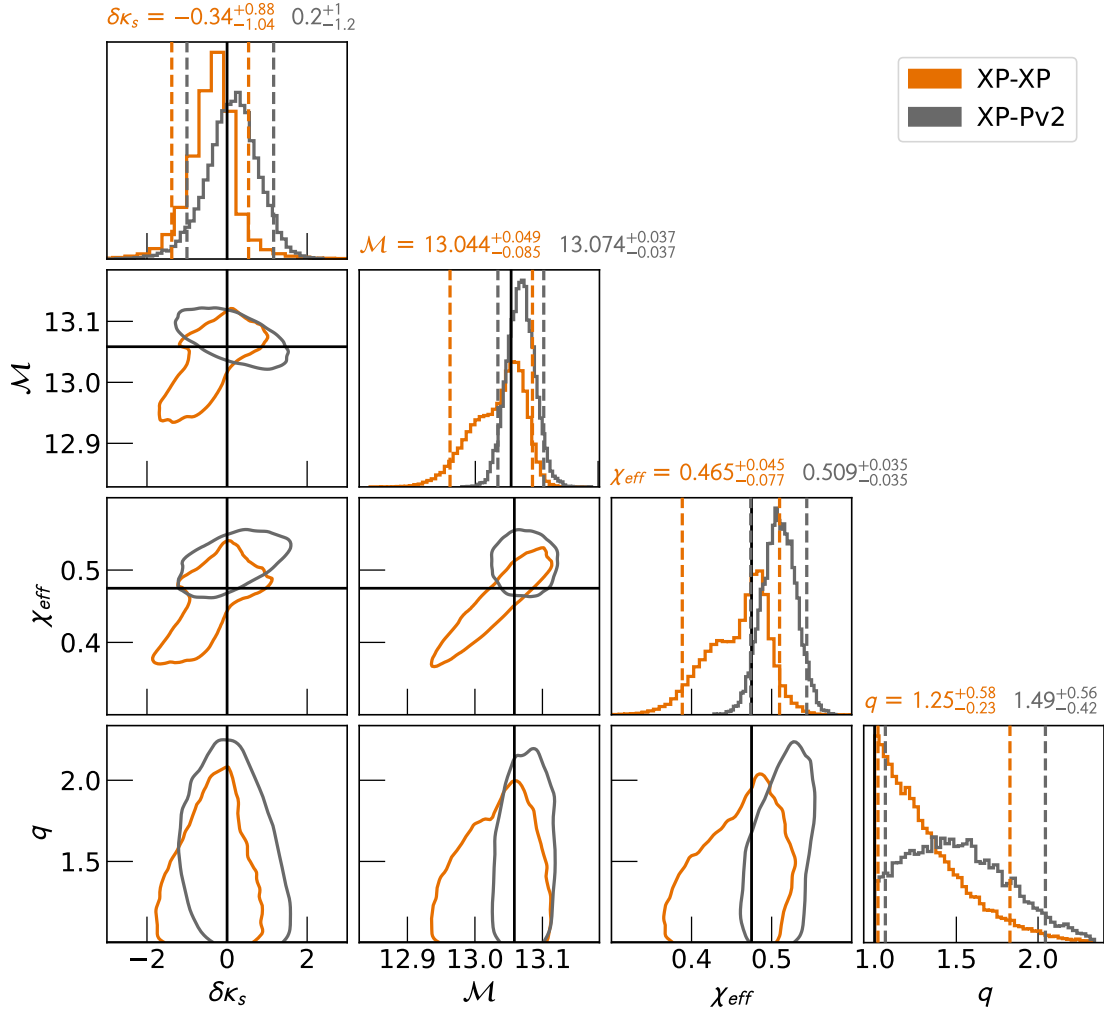


Figure 3.3: Corner plot for fixed spin magnitudes and angles given in Table 3.4 for $q = 1$. The plots show 1D and 2D posteriors for the SIQM deviation parameter ($\delta\kappa_s$), chirp mass (\mathcal{M}), effective spin (χ_{eff}), and mass ratio (q). Injections are performed using the fully spin-precessing dominant mode waveform (IMRPhenomXP) and recovered with the same (orange) as well as with single spin-precessing dominant mode waveform IMRPhenomPv2 (grey). The histograms shown on the diagonal of the plots are 1D marginalized posteriors for the respective parameters with vertical dashed lines denoting 90% credible intervals and black lines indicating the injected value of the parameters. The contours in the 2D plots are also drawn for 90% credible interval. The titles on the 1D marginalized posteriors for respective parameters and recoveries indicate 50% quantiles with error bounds at 5% and 95% quantiles.

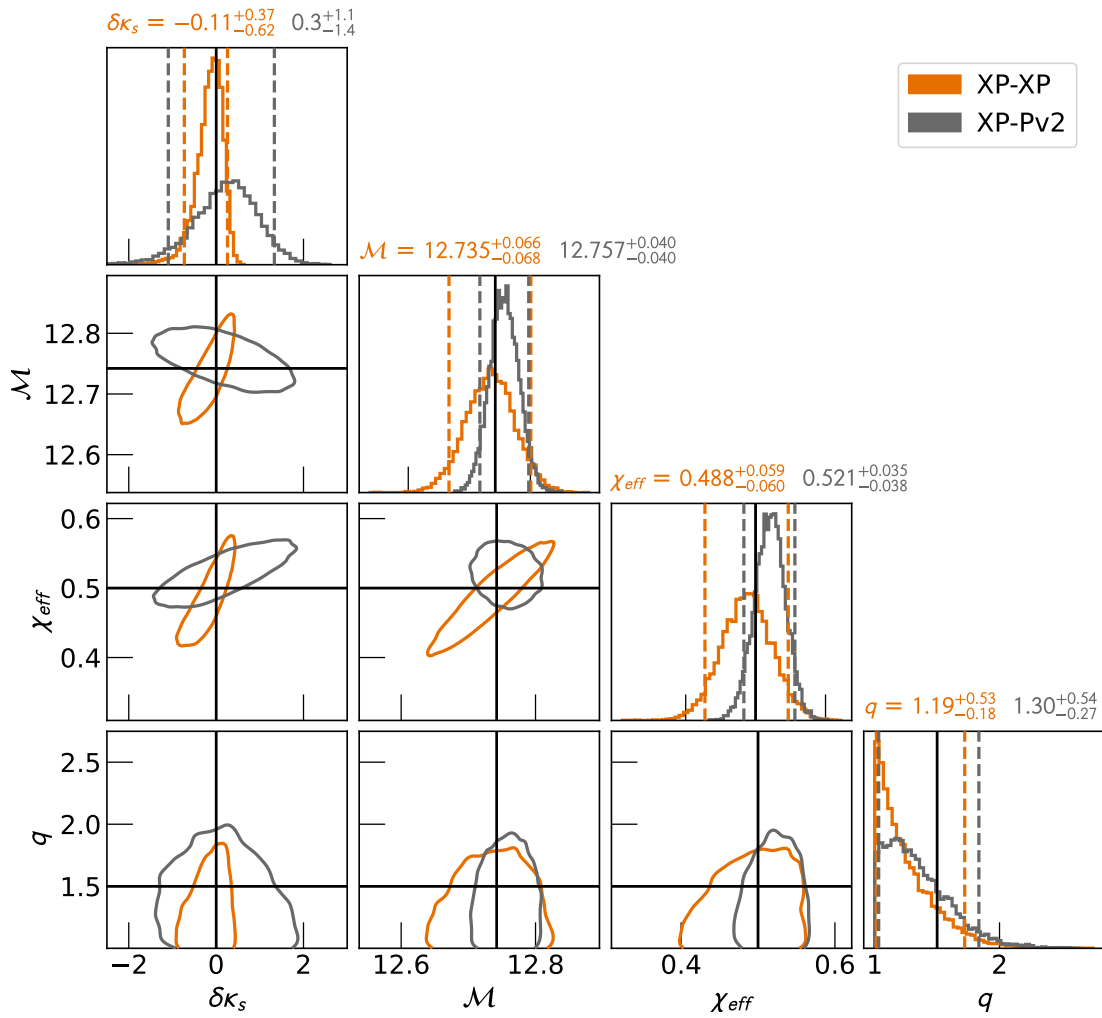


Figure 3.4: Same as Fig. 3.3 but for $q = 1.5$.

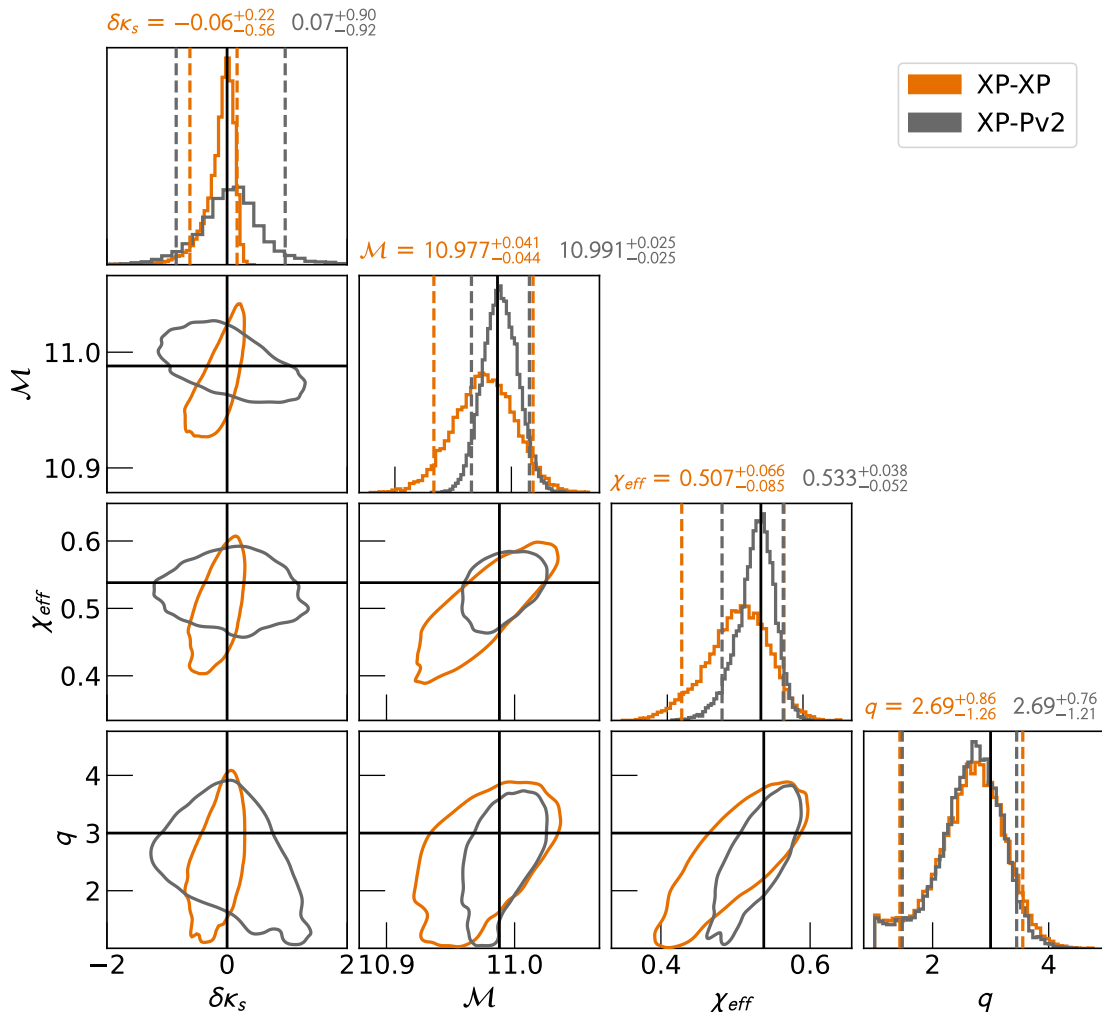


Figure 3.5: Same as Fig. 3.3 but for $q = 3$.

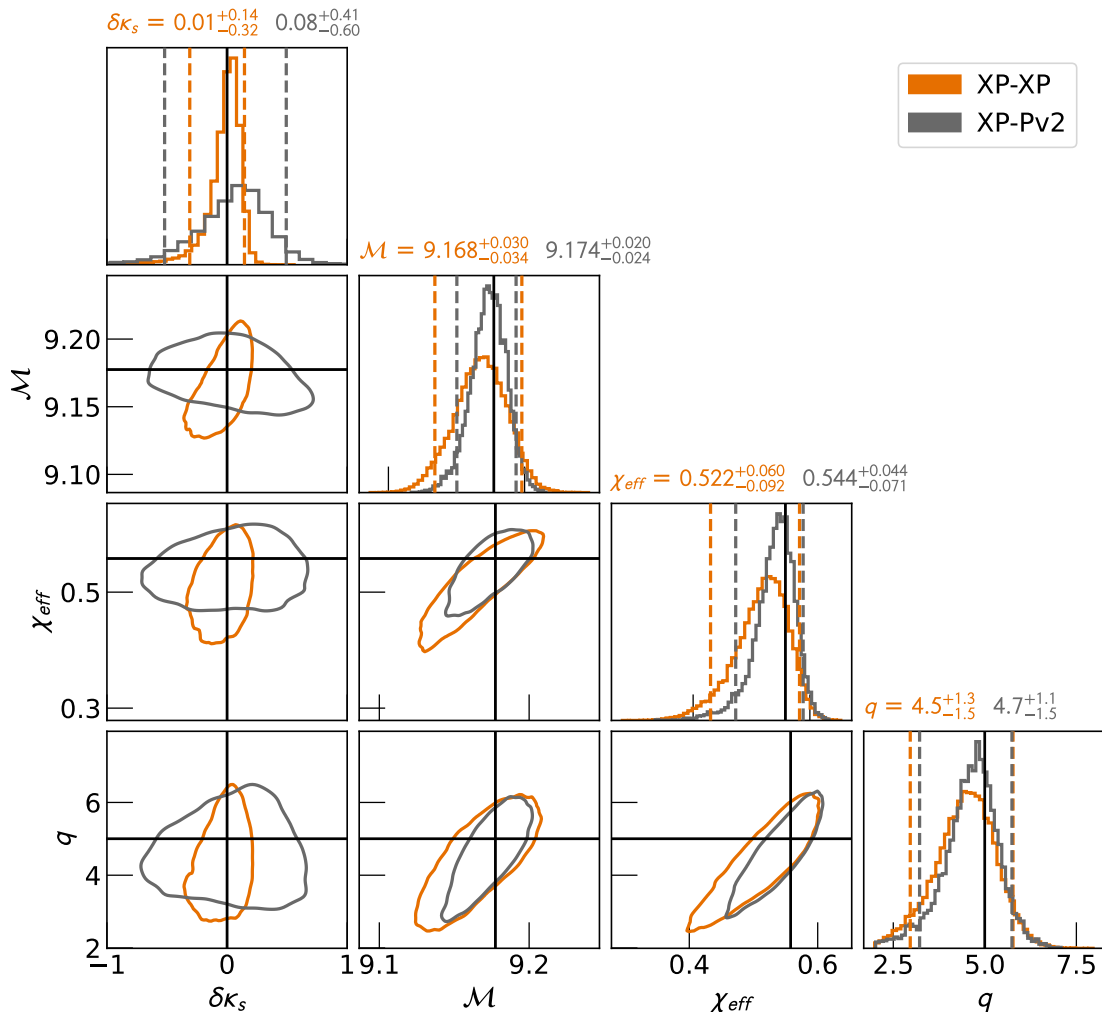


Figure 3.6: Same as Fig. 3.3 but for $q = 5$.

χ_{eff}	χ_{1x}	χ_{2x}	χ_{1y}	χ_{2y}	χ_{1z}	χ_{2z}
0.3	0.1013	0.3414	0.0987	0.3326	0.4	0.15
0.5					0.6	0.35
0.7					0.8	0.55

Table 3.5: Here we fix the mass ratio $q = 1.5$, inclination angle $\iota = 0.5162$ rad, and x- and y- components of dimensionless spin vectors while varying the z- components in order to obtain different values of χ_{eff} . The χ_p value remains constant at 0.3. This has been used to study the effect of χ_{eff} on $\delta\kappa_s$ (Sec. 3.4.1).

Effect of χ_{eff} variation on $\delta\kappa_s$

Here we choose a nearly equal-mass binary, with mass ratio $q = 1.5$ and $\chi_p = 0.3$. Since we are not exploring the effect of HMs in this injection set, a nearly equal-mass system serves the purpose well. We vary the χ_{eff} parameter as $\chi_{\text{eff}} = 0.3, 0.5, 0.7$. This is done by fixing the x- and y- components of the two spin vectors and varying the z- components χ_{1z} and χ_{2z} to obtain three values of χ_{eff} as 0.3, 0.5, and 0.7 (see Table 3.5).

As observed in [Krishnendu *et al.* \(2019b\)](#), the estimates on $\delta\kappa_s$ improve as we choose large positive χ_{eff} values. Also, for all values of χ_{eff} , the bounds obtained using IMRPhenomXP are better than IMRPhenomPv2. These improvements can be explained by looking at correlations between χ_{eff} and $\delta\kappa_s$ shown in Figs. 3.7-3.9.

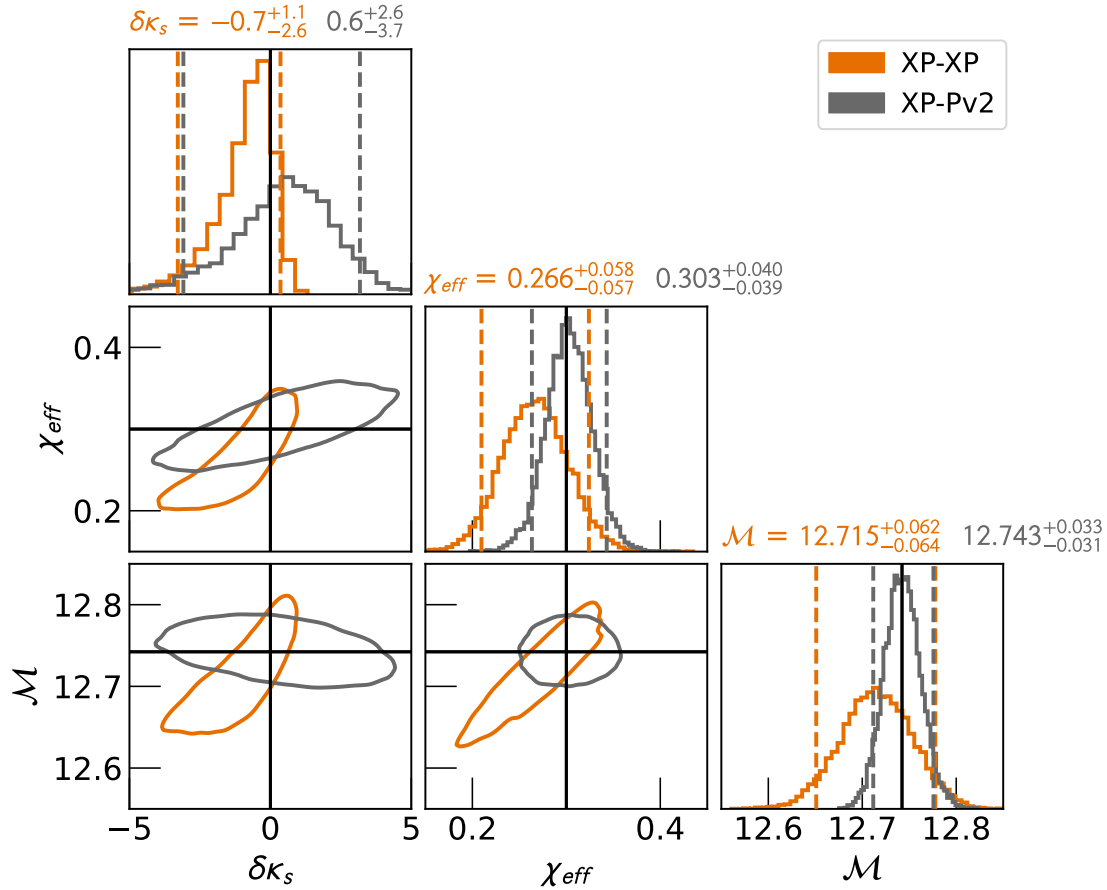


Figure 3.7: Corner plot for $q = 1.5$, $\chi_p = 0.3$, and $\chi_{\text{eff}} = 0.3$ with the other spin values given in Table 3.5. The plots show 1D and 2D posteriors for the SIQM deviation parameter ($\delta\kappa_s$), effective spin (χ_{eff}), and chirp mass (\mathcal{M}). Injections are performed using the fully spin-precessing dominant mode waveform (IMRPhenomXP) and recovered with the same (orange) as well as with single spin-precessing dominant mode waveform IMRPhenomPv2 (grey). The histograms shown on the diagonal of the plots are 1D marginalized posteriors for the respective parameters with vertical dashed lines denoting 90% credible intervals and black lines indicating the injected value of the parameters. The contours in the 2D plots are also drawn for 90% credible interval. The titles on the 1D marginalized posteriors for respective parameters and recoveries indicate 50% quantiles with error bounds at 5% and 95% quantiles.

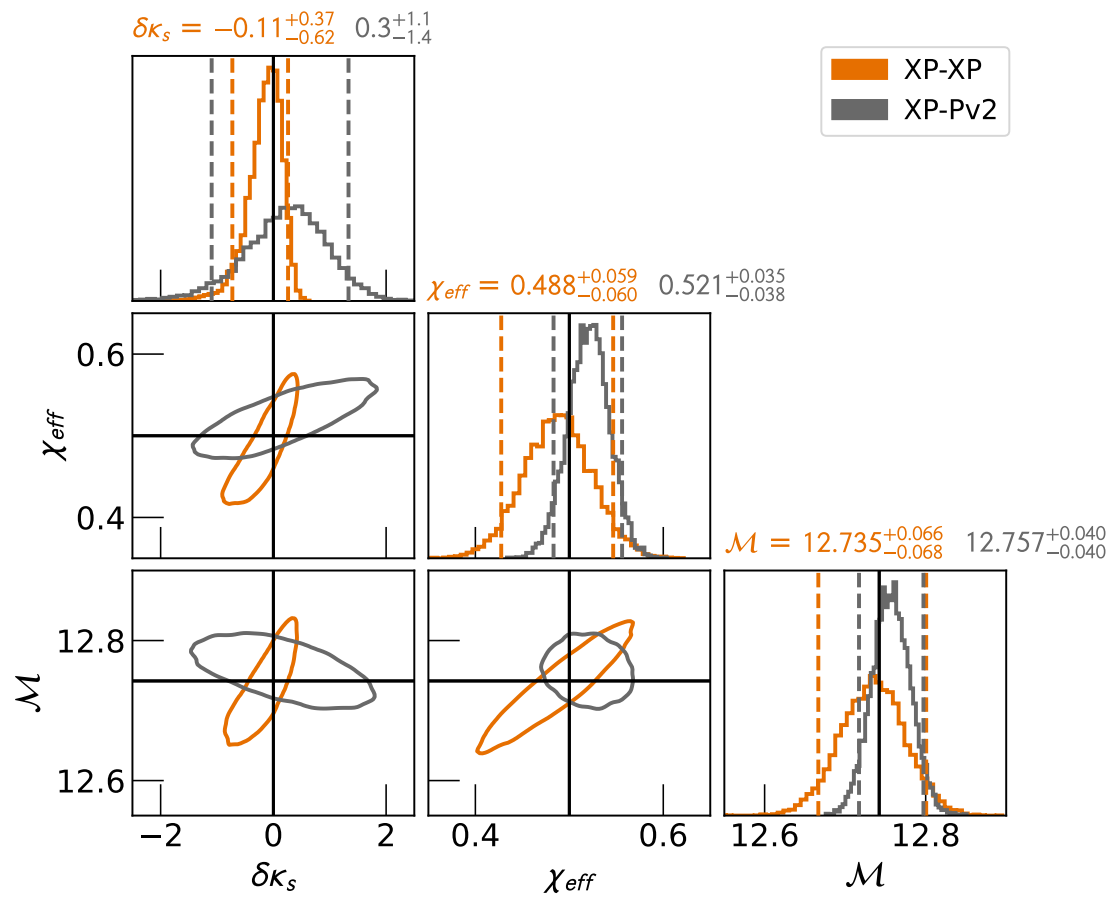


Figure 3.8: Same as Fig. 3.7 but for $\chi_{eff} = 0.5$

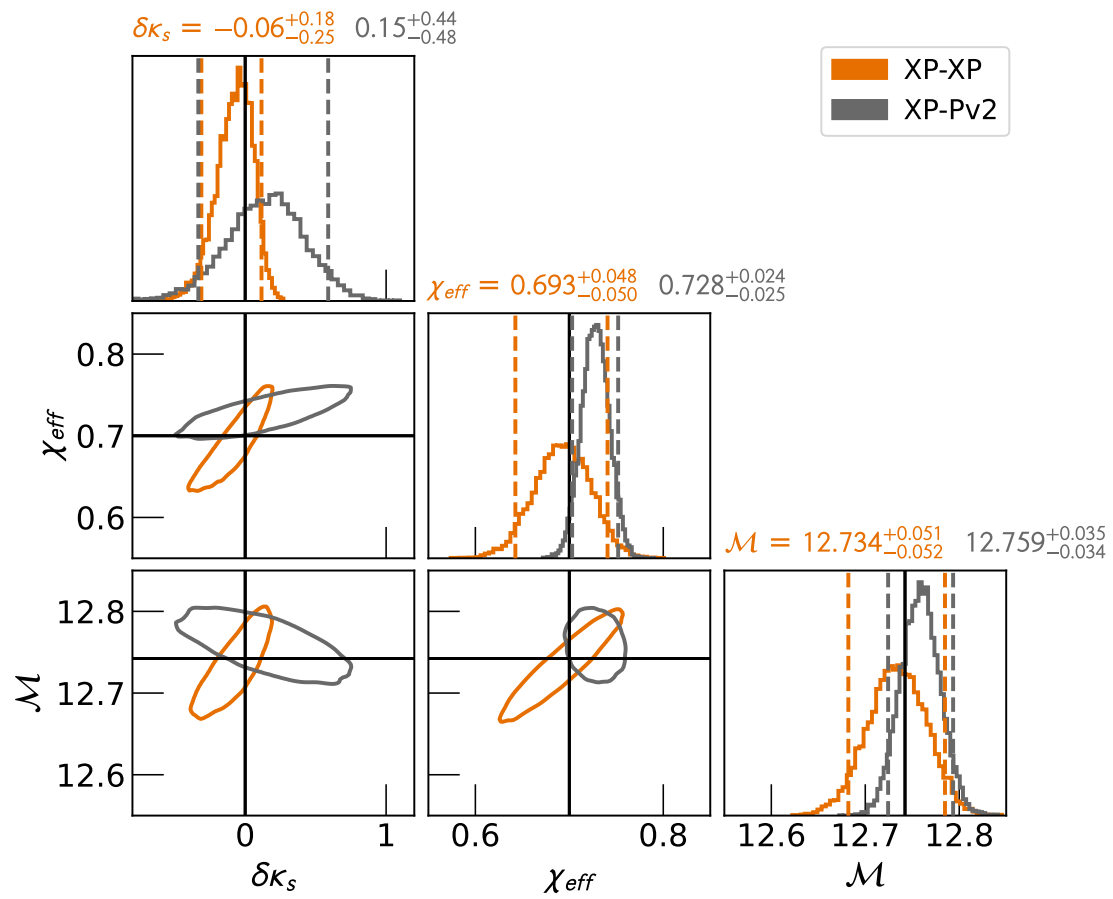


Figure 3.9: Same as Fig. 3.7 but for $\chi_{eff} = 0.7$

χ_p	χ_{1x}	χ_{2x}	χ_{1y}	χ_{2y}	χ_{1z}	χ_{2z}
0.3	0.2792	0.1	0.11	0.1	0.56	0.32
0.5	0.4	0.2	0.3	0.2		
0.7	0.5524	0.3	0.43	0.3		

Table 3.6: Here we fix the mass ratio $q = 3$, inclination angle $\iota = 0.5149$ rad, and z-components of the dimensionless spin vectors while varying the x- and y- components in order to obtain different values of χ_p . The value of χ_{eff} remains constant at 0.5. This has been used to study the effect of spin-precession on $\delta\kappa_s$ (Sec. 3.4.1).

Effect of χ_p variation on $\delta\kappa_s$

Here we choose a mass ratio of $q = 3$ and a moderate value of $\chi_{\text{eff}} = 0.5$. Compared to the previous section, a slightly larger mass ratio is chosen here to avoid the uninformative inference on the analyses due to unconstrained spin-precession effects for near-equal mass binaries. Keeping the z- component of spin vectors same, we vary the x- and y- components to obtain three distinct values of χ_p as 0.3, 0.5, and 0.7 (see Table 3.6).

As the values of χ_p increase, the bounds on $\delta\kappa_s$ with IMRPhenomXP become tighter, enhancing the differences between IMRPhenomXP and IMRPhenomPv2 waveforms. IMRPhenomPv2 bounds shift away from the injected value as we move from low to high χ_p values, excluding 0 from the 90% credible interval for $\chi_p = 0.7$. Additionally, they become increasingly worse (the posteriors become broader) compared to IMRPhenomXP as we go to higher values of χ_p . We suspect that the double spin-precessing model IMRPhenomXP is helping to break certain degeneracies between the SIQM parameter and the spins leading to a more symmetric estimate of $\delta\kappa_s$ for all the χ_p values compared to the IMRPhenomPv2 waveform model.

3.4.2 Effect of higher modes and possible systematic biases

In the previous sections we compared the two waveforms with single and double spin-precession effects but using the dominant modes only. Here, we are interested in extending the analysis to higher modes. In the discussion in Sec. 1.6.3, we noted that

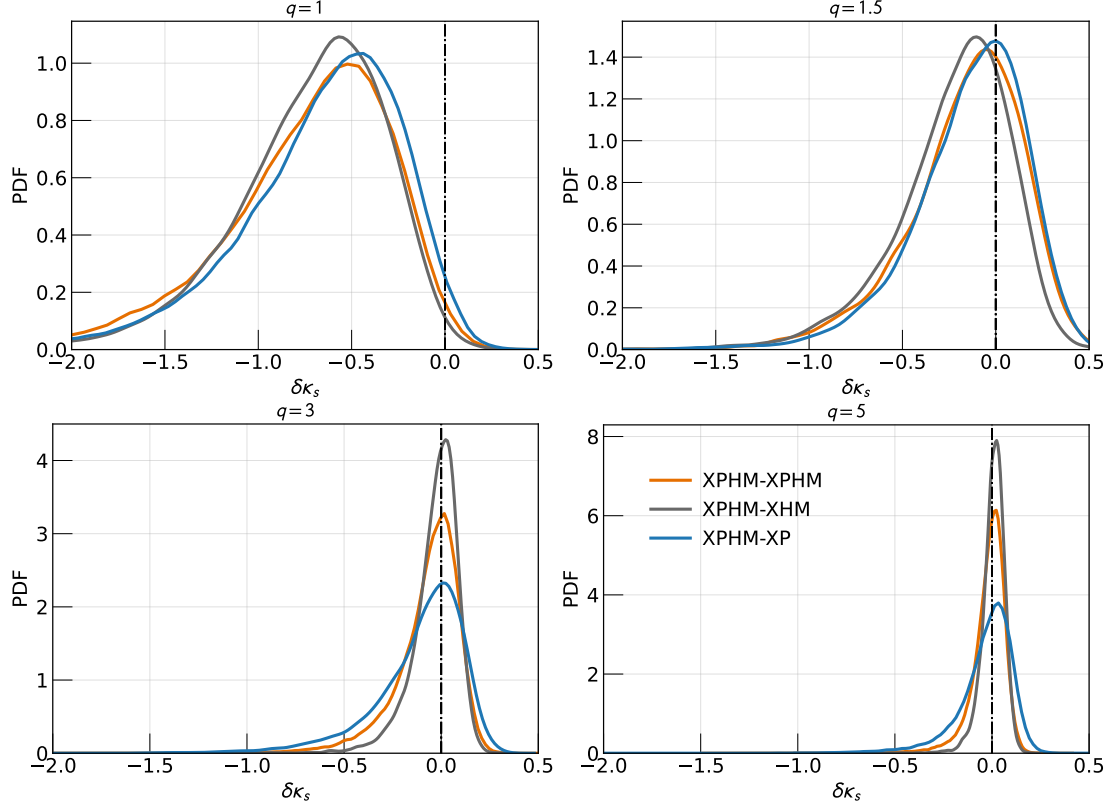


Figure 3.10: Posterior distributions of the SIQM deviation parameter for higher mode, precessing-spin injections with mass ratios $q = 1, 1.5, 3, 5$. The total mass is fixed to $M = 30 M_{\odot}$, and network SNR is 40 for all cases. The spin magnitudes and angles are fixed (see Table 3.4). We use IMRPhenomXPHM for injections and recover using the same (orange), IMRPhenomXHM (grey), and IMRPhenomXP (blue) to study the effect of higher modes on $\delta\kappa_s$ measurements. The vertical black-dashed lines denote the injected value. The legend follows the pattern ”injected waveform - recovery waveform”.

the relative contribution from higher modes increases as the binary systems become more asymmetric in masses. Thus, we simulate GW signals from BBHs with a total mass of $30 M_{\odot}$ and vary the mass ratios as $q = 1, 1.5, 3, 5$. We fix the spin magnitudes ($a_1 = 0.6164$, $a_2 = 0.5913$), spin angles ($\phi_{\text{JL}} = 3.7926$, $\theta_1 = 0.2315$, $\theta_2 = 0.9374$, $\phi_{12} = 0.0$), and inclination angle ($\theta_{\text{JN}} = 0.4606$), taking a different mass ratio in each case, leading to different values for the dimensionless spin components ($\chi_{1x}, \chi_{1y}, \chi_{1z}, \chi_{2x}, \chi_{2y}, \chi_{2z}$) and hence different values of χ_{eff} and χ_p as listed in Table 3.4. We generate simulations assuming IMRPhenomXPHM model and analyse them using the same (orange), IMRPhenomXHM (grey), and IMRPhenomXP (blue) shown in Fig. 3.10.

The aim is to demonstrate the importance of using a waveform model with higher modes in measuring $\delta\kappa_s$ and to examine the possible biases that could arise by neglecting them. As expected, we see the significance of higher modes when we go to higher mass ratio binaries. The posteriors are tightly constrained to the true value ($\delta\kappa_s = 0$) as the binary becomes asymmetric, and the 90% bound on $\delta\kappa_s$ improves from 1.3 to 0.18 (nearly seven times) when moving from near-equal mass binary ($q = 1.5$) to the most asymmetric binary ($q = 5$) when using the higher mode waveform IMRPhenomXHM. For comparison, the improvement is only three times when we use the dominant mode waveform IMRPhenomXP. For both $q = 3$ and $q = 5$ cases, IMRPhenomXHM constraints are better than the other models. This is because the relative contribution from the higher modes increases for higher mass ratios, and hence IMRPhenomXHM performs better than IMRPhenomXP. While IMRPhenomXPHM is also a higher mode waveform, the binary's spin parameters (six in total) increase the dimensionality of the parameter space. This is not the case with IMRPhenomXHM as it is an aligned-spin waveform model and has only two spin parameters. Since the system is only mildly precessing ($\chi_p \sim 0.14$), the additional spin parameters do not contribute much towards improving the bounds on $\delta\kappa_s$, and the four extra parameters in IMRPhenomXPHM add a disadvantage compared to recovery with IMRPhenomXHM. Additionally, we observe that the time of coalescence (t_c) posteriors show a bias when the injected signal includes the effect of spin-precession and the recovery waveforms do not. The bias increases with an increase in the mass ratio of the system. While right ascension and declination do not improve while using IMRPhenomXPHM waveform, the polarization angle posterior is drastically improved with the use of higher modes in the waveform. Thus, a higher mode waveform plays a significant role in improving the sky localization of the binary system.

We believe the non-recovery of the injected $\delta\kappa_s = 0$ value for $q = 1$ case is because of the prior railing effect which arises when the injection is exactly at $q = 1$. Since nearly the entire posterior volume lies outside the injected value of the mass ratio (see Fig. 3.11), this causes a bias in the recovery of the chirp mass parameter. Given that both χ_{eff} and

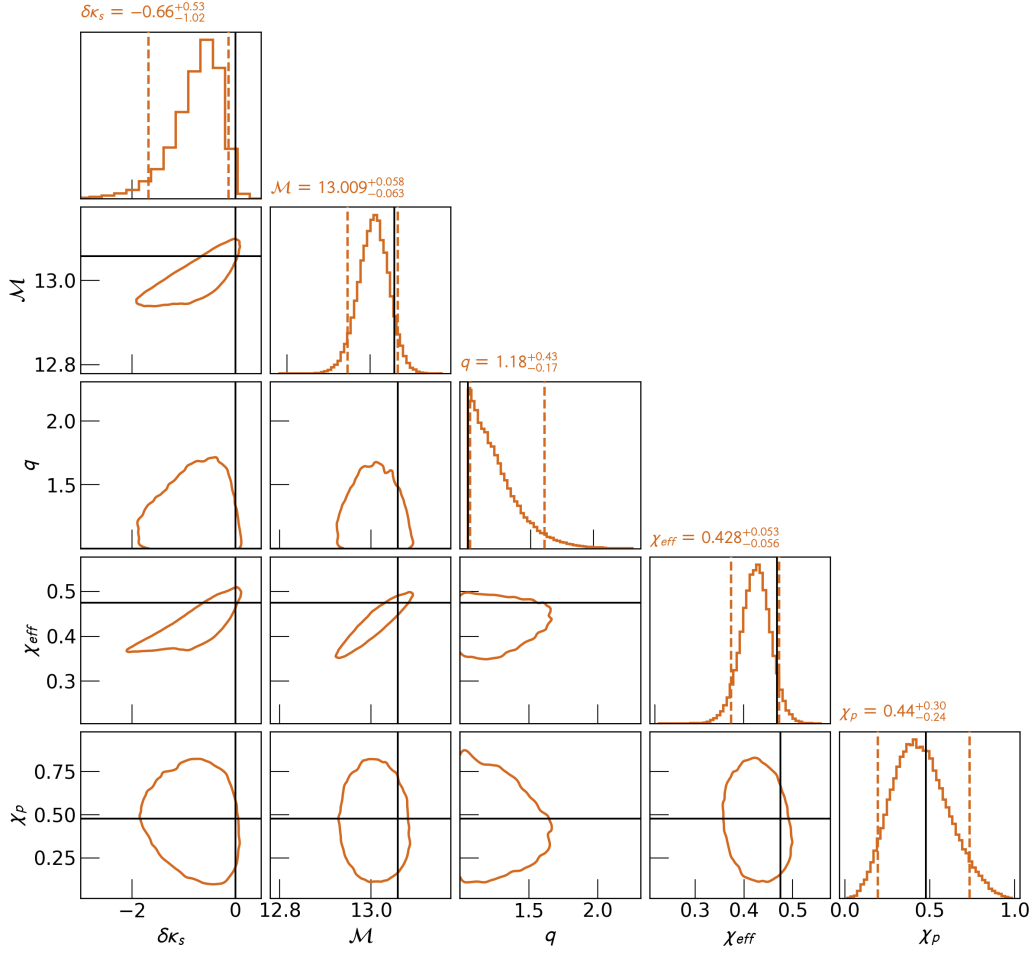


Figure 3.11: Corner plot for the equal-mass case ($q = 1$) showing posterior on the SIQM deviation parameter ($\delta\kappa_s$), chirp mass (\mathcal{M}), mass ratio (q), the effective spin parameter (χ_{eff}), and the spin-precession parameter (χ_p). We have used a fully spin-precessing waveform model including HMs (IMRPhenomXPHM) for both injection and recovery. The histograms shown on the diagonal of the plot are 1D marginalized posteriors for the respective parameters with vertical dashed lines denoting 90% credible intervals. The contours in the 2D plots are also drawn for 90% credible interval. The black lines denote the injected value of the parameters, and the titles on the 1D marginalized posteriors for respective parameters indicate 50% quantiles with error bounds at 5% and 95% quantiles.

$\delta\kappa_s$ are correlated with chirp mass, it causes a bias in both of these parameters, and the injected value of $\delta\kappa_s$ is not recovered. These correlations can be seen in the corner plot (Fig. 3.11) where we see biases in the values of \mathcal{M} and χ_{eff} , resulting in a biased $\delta\kappa_s$ posterior. In fact, by fixing $q = 1$ for recovery waveforms, we have verified that the IMRPhenomXPHM injections are recovered with both IMRPhenomXP and IMRPhenomXPHM templates and thus confirming the claim about prior railing issue for $q = 1$ case.

3.5 REVISITING REAL EVENTS WITH MODELS INCLUDING THE EFFECT OF SPIN-PRECESSION AND HIGHER MODES

In this section, we return to the re-analysis of selected LVK events, with the aim of comparing the performance of different waveform models in constraining $\delta\kappa_s$ from the GW transient catalogues. We show the results for different waveforms used for each event in Fig. 3.12. The IMRPhenomPv2 results (Abbott *et al.*, 2021f,g) are shown with blue dot-dashed lines along with the IMRPhenomXPHM (orange) and IMRPhenomXP (grey) results.

For events with nearly equal mass ($q \approx 1.4 - 1.7$), GW151226 and GW170608, even if we use the more informed models IMRPhenomXPHM and IMRPhenomXP, the bounds do not alter considerably compared to IMRPhenomPv2. On the other hand, the posteriors show a considerable difference from the IMRPhenomPv2 counterpart for GW190412. Note that GW190412 is the first asymmetric BBH event ($q \approx 3.75$) with an indication for moderate spins and higher modes (Abbott *et al.*, 2020b). Hence, we expect the most noticeable effect on the bounds of $\delta\kappa_s$ for this event. The requirement of using waveform models with higher modes is also evident from the IMRPhenomXPHM and IMRPhenomXP comparison for GW190412 (bottom-left panel of Fig. 3.12). This can also be seen in the corner plot shown in Fig. 3.13 where the bounds on mass ratio and χ_{eff} are considerably different for IMRPhenomXPHM compared to the dominant mode waveform models. As discussed in the previous sections, bounds on $\delta\kappa_s$ strongly depend on these parameters, and hence, for an event with non-negligible higher mode content, we observe that IMRPhenomXPHM performs much better. In fact, the bounds for GW190412 obtained using IMRPhenomXPHM exclude boson star binaries as the source, subject to the assumptions made in our study (such as neglect of the tidal corrections, assumption that $\delta\kappa_a = 0$, and that spin-induced effects are accounted for only in the inspiral part of the waveform).

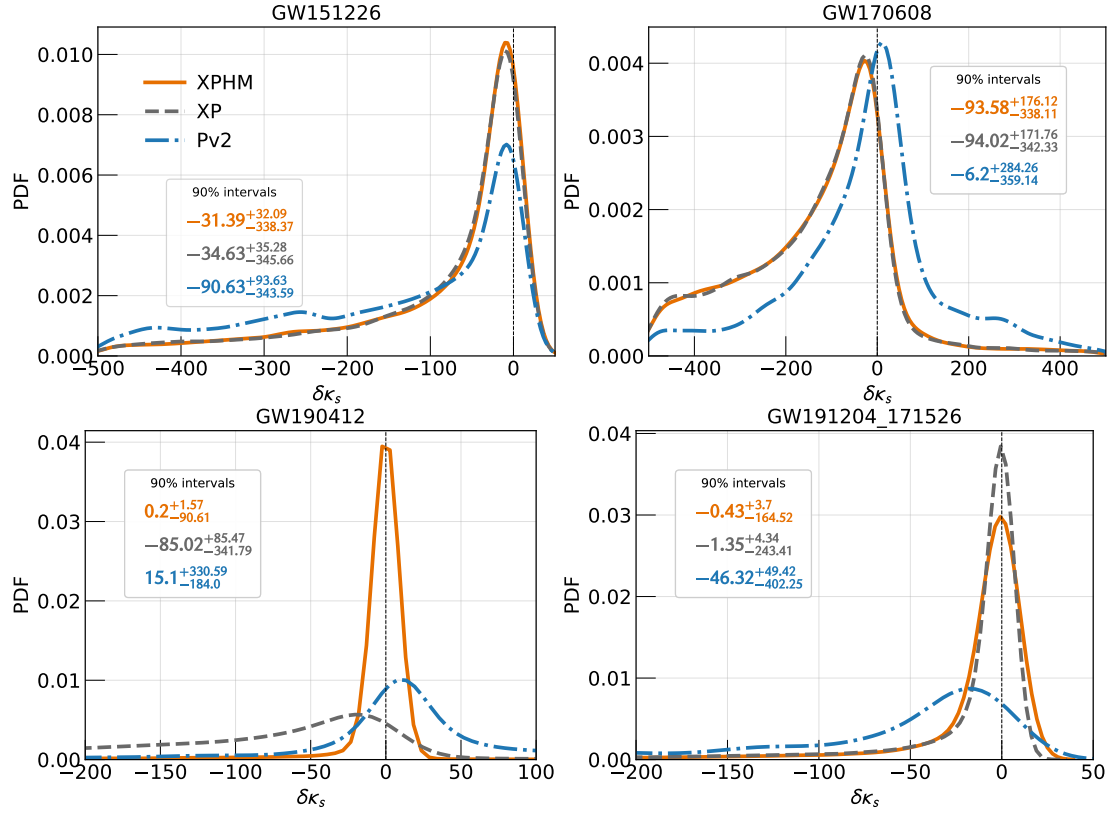


Figure 3.12: Posterior distributions on SIQM-deviation parameter for observed GW events. The curves labeled with IMRPhenomPv2 (blue) correspond to the previous results (Abbott *et al.*, 2021f,g) using IMRPhenomPv2 waveform model. These are being compared with the new models IMRPhenomXP (grey) and IMRPhenomXPHM (orange). The vertical dotted line indicates the BBH limit $\delta\kappa_s = 0$ and the numbers written inside the plots denote the 50% quantiles with error bounds at 5% and 95% quantiles for different waveform model recoveries in respective colours.

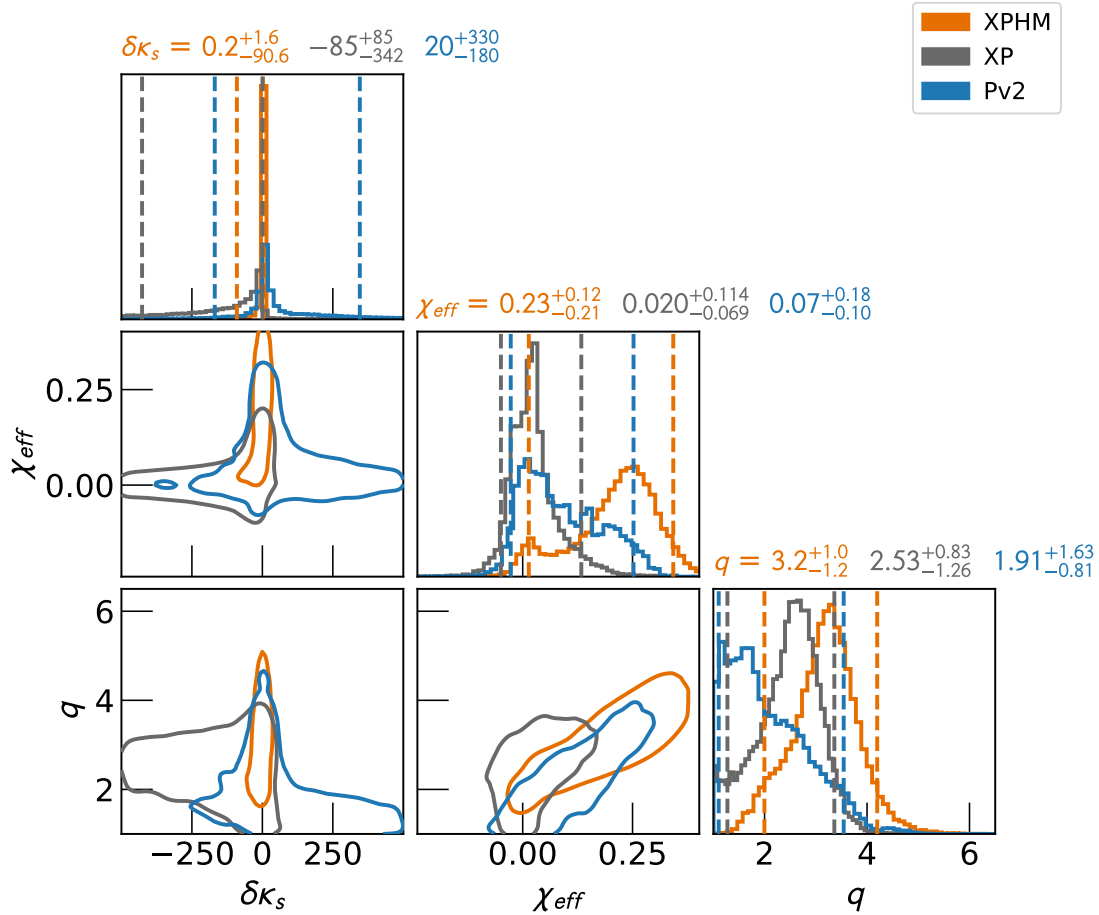


Figure 3.13: Corner plot for GW190412 showing posteriors on the SIQM deviation parameter ($\delta\kappa_s$), effective spin (χ_{eff}), and mass ratio ($q = m_1/m_2$). We show on the same plot results from single spin-precessing dominant mode waveform model IMRPhenomPv2 (blue), fully spin-precessing dominant mode waveform model IMRPhenomXP (grey), and fully spin-precessing HM waveform model IMRPhenomXPHM (orange). The histograms shown on the diagonal of the plot are 1D marginalized posteriors for the respective parameters with vertical dashed lines denoting 90% credible intervals. The contours in the 2D plots are also drawn for 90% credible interval. The titles on the 1D marginalized posteriors for respective parameters and recoveries indicate 50% quantiles with error bounds at 5% and 95% quantiles.

3.6 SUMMARY

Spin-induced multipole moment-based tests were routinely employed to determine the nature of compact binary signal during the first three observing runs of the advanced LIGO and advanced Virgo detectors ([Abbott *et al.*, 2021f,g](#)). In this study, we extend the applicability of the test to binaries with double spin-precession effects not considered in previous versions of the test, and discuss the possible improvements in the measurement of the SIQM deviation parameter using a more informed waveform model containing two spin-precession effects and higher modes. Starting with a simulation study, we demonstrate the applicability of the SIQM test on binaries with large spin-precession and moderate mass asymmetries. We find considerable differences in the bounds of $\delta\kappa_s$ obtained using IMRPhenomPv2 compared to IMRPhenomXP for systems with high spin values. We also report on the improvements and biases observed in the $\delta\kappa_s$ bounds with the choice of different mass ratios and compare them between IMRPhenomXP and IMRPhenomPv2 waveform models. Further, by injecting higher mode spin-precessing signals, we find that higher mode waveforms are essential when analysing GW signals with high mass asymmetries. Finally, we re-analyse selected events from GWTC 1-3 with the most up-to-date waveform models including double spin-precession effects and higher modes. Our findings show that IMRPhenomXPHM may be preferred for analysing GW events such as GW190412 ([Abbott *et al.*, 2020b](#)), where there is evidence for mass asymmetry and non-negligible spin effects.

CHAPTER 4

DETECTABILITY OF NON-QUADRUPOLE MODES IN FUTURE DETECTORS

4.1 INTRODUCTION

We discussed in Section 1.6.3, how the gravitational wave strain can be expanded into multipoles and how these multipoles play a role in extending the GW spectrum to lower frequencies. In this chapter, we explore the detection of these non-quadrupole modes/higher-order modes (HMs) in detail, especially in the context of future GW detectors. While there was a hint of higher mode presence in the data for the event GW170729 (Chatziioannou *et al.*, 2019), clear evidence of a higher order mode was found during the analysis of two events namely, GW190412 (Abbott *et al.*, 2020b) and GW190814 (Abbott *et al.*, 2020d), both quite asymmetric in component masses. Further, for about six events (all observed during the first part of the third observing run of the LIGO-Virgo network), the inclusion of higher modes in waveform models was found to improve the parameter estimation accuracies (Abbott *et al.*, 2020c, 2021b), hinting at their presence. As ground-based detectors continue to improve their sensitivities over the next few years, they will detect more massive and more distant BBHs, should they exist (Borhanian and Sathyaprakash, 2022). The increased mass reach is mostly due to the improved lower cutoff frequency of these detectors, which may be as low as a few Hz. Note that including higher modes also improves the detector's mass reach, as discussed earlier. The increased distance reach is due to the improved sensitivity at different frequency bands. Going by the present estimates (Baibhav *et al.*, 2019), these observations would unravel more asymmetric binary systems, many of which may not be face-on. This should facilitate the detection of several higher modes by the next-generation detectors. As these higher modes would very likely bring in improvements to the parameter estimation in various contexts, a study of their detectability is a very

important first step towards understanding the impact they will have on GW science. This forms the context of this chapter, where we quantify the detectability of higher modes using a network of future ground-based gravitational wave detectors.

4.2 DETECTION CRITERIA AND DETECTOR NETWORKS

For our study, we choose to work with an inspiral-merger-ringdown (IMR) waveform model of Phenom family for BBHs in quasi-circular orbits including the effect of higher order modes and non-precessing spins (coded up in LALSuite with the name IMRPhenomHM) (London *et al.*, 2018). In addition to the dominant 22 mode, this model also contains the higher modes $(\ell, |m|) = (2, 1), (3, 3), (3, 2), (4, 4),$ and $(4, 3)$ and is valid for mass ratios up to 18, and component dimensionless spin magnitudes up to 0.85 (up to 0.98 for the equal mass case. See London *et al.*, 2018, for details).

4.2.1 Detection criteria

A robust method to quantify confident detection of a weak gravitational wave signal in noisy detector data involves computing the signal-to-noise ratio (SNR) discussed in Sec. 1.5. Following the definition of optimal SNR [given by Eq. (1.25)], we can quantify the power in higher-order modes by defining the optimal SNR tied to individual modes. We define

$$\rho_{\ell m}^2 = (h_{\ell m}|h_{\ell m}) = 4 \int_0^\infty \frac{|\tilde{h}_{\ell m}(f)|^2}{S_h(f)} df, \quad (4.1)$$

where $\tilde{h}_{\ell m}(f)$, analogous to the GW strain in the frequency domain, represents strain for any $(\ell, \pm m)$ mode pair and can be expressed as a linear combination of associated polarizations, $\tilde{h}_+^{\ell m}(f)$ and $\tilde{h}_\times^{\ell m}(f)$, as

$$\tilde{h}_{\ell m}(f) = F_+(\theta, \phi, \psi) \tilde{h}_+^{\ell m}(f) + F_\times(\theta, \phi, \psi) \tilde{h}_\times^{\ell m}(f) \quad (4.2)$$

where the antenna pattern functions $F_+(\theta, \phi, \psi)$ and $F_\times(\theta, \phi, \psi)$ are functions of two angles (θ, ϕ) giving binary's location in the sky and the polarization angle (ψ) . The two polarizations associated with each $(\ell, \pm m)$ mode pair $[\tilde{h}_+^{\ell m}(f), \tilde{h}_\times^{\ell m}(f)]$ can suitably

be expressed using a basis of spin-weighted spherical harmonics of weight -2 in the frequency domain as (see Appendix C of [Mehta et al., 2017](#), for details and derivation)

$$\tilde{h}_+^{\ell m}(f) = \left[(-)^{\ell} \frac{d_2^{\ell, -m}(\iota)}{d_2^{\ell m}(\iota)} + 1 \right] Y_{-2}^{\ell m}(\iota, \varphi_0) \tilde{h}_{\ell m}^{\text{R}}(f) \quad (4.3a)$$

$$\tilde{h}_\times^{\ell m}(f) = -i \left[(-)^{\ell} \frac{d_2^{\ell, -m}(\iota)}{d_2^{\ell m}(\iota)} - 1 \right] Y_{-2}^{\ell m}(\iota, \varphi_0) \tilde{h}_{\ell m}^{\text{R}}(f) \quad (4.3b)$$

where $\tilde{h}_{\ell m}^{\text{R}}(f)$ represents the Fourier transform of real part of $h_{\ell m}(t)$ appearing in Eq. (1.34), $d_2^{\ell, m}(\iota)$ are the Wigner d functions, and $Y_{-2}^{\ell, m}(\iota, \varphi_0)$ are spin-weighted spherical harmonics of weight -2 (see for example, [Wiaux et al., 2007](#)).¹ Note that $\tilde{h}_{\ell m}^{\text{R}}(f)$ can be expressed in terms of an amplitude and a phase associated with each mode as

$$\tilde{h}_{\ell m}^{\text{R}}(f) = A_{\ell m}(f) e^{i\varphi_{\ell m}(f)}, \quad (4.4)$$

where $A_{\ell m}(f)$ and $\varphi_{\ell m}(f)$, for instance, can be obtained by performing fits to a set of target waveforms chosen appropriately (see, for instance, [Mehta et al., 2017](#)). Details and the explicit expressions for the amplitude and the phase models used in this work can be found in Eqs. (4)-(9) of [London et al. \(2018\)](#).

This definition of mode SNR [given by Eq. (4.1)] closely follows the one in [Mills and Fairhurst \(2021\)](#) which was used for quantifying the SNR of the 33 mode for GW190814 ([Abbott et al., 2020d](#)) and GW190412 ([Abbott et al., 2020b](#)). For our purposes, we choose to work with a threshold of 3 on SNR for individual higher modes ($\rho_{\ell m}$) defined above, and of 10 for the dominant 22 mode. This would mean that a confident detection of a source in the dominant 22 mode requires the corresponding SNR to be above 10, and that of a higher mode requires the corresponding SNR to be above 3. The choice of the higher mode SNR threshold of 3 is motivated by the measures adopted in [Abbott et al. \(2020b\)](#) that discusses the detection of the 33 mode in data for the event GW190412.

¹In writing Eq. (4.3) we have set the spherical angles appearing in Eq. (1.34) as, $(\Theta, \Phi) \equiv (\iota, \varphi_0)$, where ι is binary's inclination angle and φ_0 is a reference phase.

It is important to note that the observed gravitational waveform is a superposition of different spherical harmonic modes [as in Eq. (1.34)], and hence the total SNR would contain contributions from the *interference* terms between different harmonics (Arun *et al.*, 2007a; Van Den Broeck and Sengupta, 2007a). They are likely to contribute negligibly to the total SNR, compared to the dominant contributions [given by Eq. (4.1)] as shown in Mills and Fairhurst (2021) in the context of aLIGO detectors. Regardless of the magnitude of the interference terms, Eq. (4.1) may be seen as a definition of SNR in different modes.

For all practical purposes, we can choose to work with a low- and high-frequency cutoff ($f_{\text{low}}, f_{\text{cut}}$) and re-express the optimal SNR for each mode as

$$\rho_{\ell m}^2 = 4 \int_{f_{\text{low}}}^{f_{\text{cut}}} \frac{|\tilde{h}_{\ell m}(f)|^2}{S_h(f)} df. \quad (4.5)$$

We choose a universal lower frequency cutoff of 5Hz following Chamberlain and Yunes (2017). The high-frequency cutoff (f_{cut}), though, is decided by the mass of the binary and chosen automatically by the waveform module with a high enough value so as not to lose any signal power (London *et al.*, 2018). The investigations presented in Secs. 4.3 and 4.4 are in the context of a single 3G configuration using Cosmic Explorer (CE), whereas we use different detector networks in our population study described in Sec. 4.5.

It is worth mentioning that the inclusion of higher harmonics in search pipelines may come at the cost of a higher false alarm rate because of the ability of the template to fit the noise (Brown *et al.*, 2013; Calderón Bustillo *et al.*, 2016; Pekowsky *et al.*, 2013). Studies such as Capano *et al.* (2014) deal with this by splitting the template bank such that HM templates are only used for a part of the parameter space. Vetoes based on modified false alarm probability are beyond the scope of this work and we use only SNR as a detection criteria in this study.

Event	M	q	χ_{eff}	SNR in mode				
				22	33	44	21	32
GW190412	42.6	3.2	0.2	649	81	17	14	3.9
GW190519_153544	159.5	1.6	0.4	685	79	48	19	14
GW190521	279.8	1.4	0.1	424	22	19	7.1	7.5
GW190602_175927	173.8	1.4	0.1	330	15	9.4	4.3	4.7
GW190630_185205	69.9	1.5	0.1	708	31	14	7.9	5.8
GW190706_222641	183.5	1.7	0.3	223	18	7.6	3.4	3.3
GW190814	27.2	9.0	0	982	172	33	32	4.4
GW190828_065509	44.4	2.4	0.1	418	34	7.2	6.7	3.0

Table 4.1: Detectability of higher modes in GWTC-2 events using a 3G detector. We have sampled the parameter values from the posteriors of these events (Abbott *et al.*, 2020*b,c,d*, 2021*b*; LIGO Scientific Collaboration and Virgo Collaboration, 2023), and have quoted the median values of SNRs obtained from 10,000 posterior samples. The total mass values quoted above are the detector frame masses. While in GWTC-2, only GW190412 and GW190814 showed detection of the 33 mode, it can be seen here that many more events would have shown detectability of HMs in a 3G detector configuration.

4.3 DETECTING HIGHER MODES OF GWTC-2 EVENTS USING 3G DETECTORS

In this section, we investigate the detectability of higher modes for a few selected GWTC-2 catalog events, assuming the sensitivity of 3G detectors. This helps us assess the improved detection rates that can be expected due to the use of an advanced detector configuration over what we already have from the present detectors. For this, we have chosen a few representative events from the GWTC-2 catalog (LIGO Scientific Collaboration and Virgo Collaboration, 2023) with high detection significance, either because higher modes have already been detected for them by the LIGO-Virgo observations (GW190814, GW190412), or because the inclusion of higher modes in the waveform significantly improved the parameter estimation of the events (Abbott *et al.*, 2021*b*).

In this analysis, we consider the SNRs corresponding to a single CE detector placed at the location L (see Table 4.3). For each event, to compute the distribution of SNRs

for different higher-order modes, we take 10,000 random posterior samples from the corresponding dataset available for that event (complete datasets can be found at [LIGO Scientific Collaboration and Virgo Collaboration, 2023](#)). We then take the median value of SNR from this distribution of 10,000 points and quote this value for each mode in Table 4.1.

As expected, there is a significant improvement in the detection rate of higher modes compared to the aLIGO and Virgo with their current sensitivities. The single 3G detector shows promise of detecting 33, 44, 21, and 32 modes for all of the above-mentioned events. It is noteworthy that GW190814 shows the highest SNR values for the higher modes, as well as the highest relative SNR for 33 mode. This can clearly be explained by the higher mass ratio value ($q \sim 9$) of this event. The 33 mode network SNR reported by LIGO-Virgo for this event was ~ 6.6 , whereas we can see that for a single CE detector, this number becomes ~ 170 . Similarly, the relative contribution of higher modes is considerable (by a factor larger than 20) for GW190412. Such high SNR can be attributed to the event's mass ratio ($q \sim 3.2$) and nonzero effective spin. To summarize, several GWTC-2 events would have led to reliable detection of all four leading modes of gravitational waveforms with the sensitivities of the proposed 3G detectors.

4.4 HIGHER MODES IN DIFFERENT REGIONS OF THE PARAMETER SPACE

We discussed at the beginning of this chapter (Sec. 4.1) that HMs not only become relevant when binary has mass asymmetry ($q > 1$) and is not optimally inclined, ($\iota \neq 0$) but might also be detected frequently by the next-generation detectors such as those in the 3G era. Hence, quantifying the detectability of higher modes in the $(q - \iota)$ plane is very important for the physics associated with compact binary mergers. This section explores the parameter space in the $(q - \iota)$ plane which will be accessible through higher-order modes in the 3G era. The results of this investigation are summarized in Figs. 4.1 and

4.2.

The analysis here considers the SNR corresponding to a single detector: CE placed at the location L (refer Table 4.3). Binaries, which act as representative systems, have a fixed value of dimensionless spin components as $\chi_{1z}=0.9$ and $\chi_{2z}=0.8$ and are assumed to be kept at a distance of 3 Gpc, with sky location and polarization angles as $\theta = 30^\circ$, $\phi = 45^\circ$, and $\psi = 60^\circ$, a choice that, although arbitrary, has no impact on the conclusions, since the change of angles will only result in an overall change of SNR. Here, we have drawn contours of fixed SNR for each mode; hence, the trends and shape of the contours should remain unchanged.

Figure 4.1 shows the fixed SNR contours for various higher-order modes in the $(q - \iota)$ plane. Each contour corresponds to a fixed (single-detector) SNR of 3, and the region inside each contour has an SNR higher than 3. Contours corresponding to different choices of total mass are displayed in the plot. The contours provide the regions in the $(q - \iota)$ plane where detection of different subdominant modes will be plausible. In other words, sources that lie inside the contours will be detectable, whereas those that lie outside will not. We observe that while the detection of 33 mode is possible for masses as low as $20M_\odot$, 44 mode can only be detected in heavier systems as displayed by contours in the middle right panel of Fig. 4.1. This is unsurprising since the 44 mode (compared to the 33 mode) is more sensitive to high frequencies. As heavier systems merge at lower frequencies, they bring the higher mode content to the sweet spot of the detector band, allowing the accumulation of SNR. Note also, that for a given binary, the 44 mode amplitudes are relatively lower than the 33 amplitude and more or less increase linearly with its total mass. This naturally affects the power in a given mode and can explain the non-detection of 44 mode in lighter systems. Similar arguments (based on the frequency sweep of each mode in the detector's band and their relative amplitude) can be outlined to explain the trends seen in Fig. 4.1 with respect to the minimum mass for which a certain mode is detected.

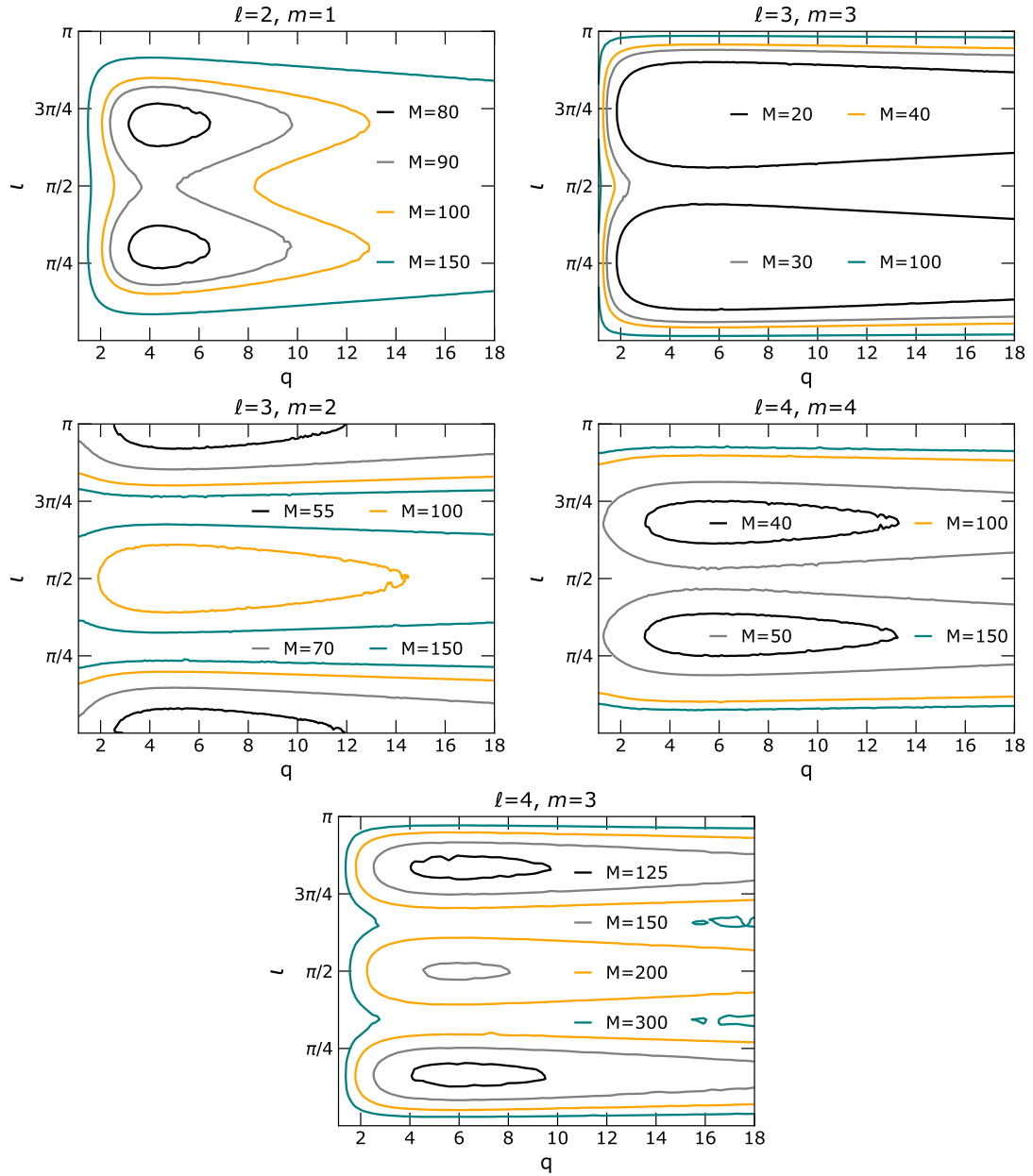


Figure 4.1: Figure shows fixed SNR (=3) contours for various higher modes, corresponding to different total mass systems in the $(q - \iota)$ plane. Each plot corresponds to a particular mode (see panel title). In a particular plot, the contours correspond to different values of total mass. All the systems have been taken at a fixed distance of 3 Gpc, and with spin values $\chi_{1z} = 0.9$ and $\chi_{2z} = 0.8$.

The trends in q and ι are distinct for each mode. For a particular total mass value, as q increases, the contours become narrower until they close at a point. Any binary with a mass ratio value higher than this point will not be detectable. The maximum mass ratio for detectable binary is very different for each mode. For a total mass of $100 M_{\odot}$, the mass ratio reach of 33, 44, and 32 modes is well beyond 18, whereas for 21 mode it is only up to 13, and for 43 mode, the binary is not even detectable. This is also because the SNR keeps reducing, so the detectability of HMs also reduces. But, as we have discussed earlier, the relative contribution of HMs increases as we go to higher values of q .

We can see these distinct (and somewhat complementary) trends in ι as well. Again, for a total mass of $100 M_{\odot}$, and a fixed mass ratio (say $q = 10$), 33 mode covers almost the entire ι range, whereas for 44 mode it is somewhat restricted. It is interesting to note that for 21 and 32 modes, the ι coverage is almost complementary, with 21 covering (a little more than) the range between $(\pi/4, 3\pi/4)$ and 32 covering the rest. It can also be seen that as the total mass increases, the contours include a larger region of the parameter space. The bi- and tri-modality of these contours reflects the symmetries these modes possess with respect to change in ι .

While Fig. 4.1 shows the contours for high spin case, the trends remain the same for low spins too. Going from low spins ($\chi_{1z} = 0.3, \chi_{2z} = 0.2$) to high spins ($\chi_{1z} = 0.9, \chi_{2z} = 0.8$) the SNR increases very slightly in 33 mode (less than 15% increase), moderately in 44 and 32 modes (nearly 30% increase), and visibly in 21 and 43 modes (nearly 50% increase). This, however, does not change the overall shape of the contour (Fig. 4.2). Due to the increase in SNR when going from lower to higher spins, some of the mass contours in the respective mode plots are absent in Fig. 4.2 compared to Fig. 4.1. For instance, we see that $M = 55$ is absent for 32 mode in Fig. 4.2.

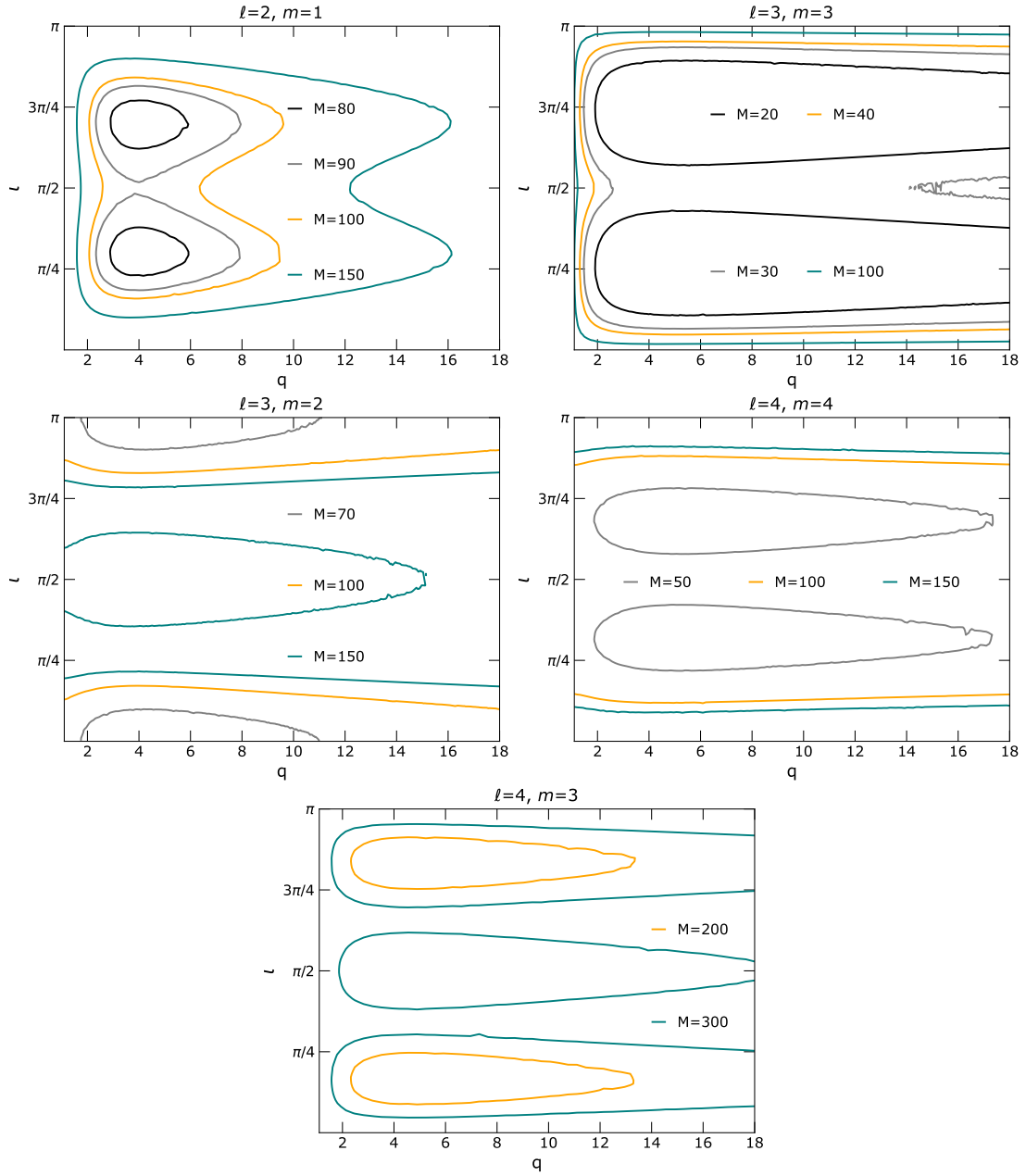


Figure 4.2: Same as Fig. 4.1 but for low spin values $\chi_{1z} = 0.3$ and $\chi_{2z} = 0.2$.

4.5 POPULATION STUDY

Our knowledge of the BBH population in the universe has evolved from the first observation run through the third observation run of the LIGO/Virgo detectors (Abbott *et al.*, 2019a, 2021e, 2023). Here, we employ the population models of Abbott *et al.* (2021e) to synthesize a BBH population and assess the detectability of various subdominant modes by using the method introduced earlier.

4.5.1 Population models

We consider two different mass distribution models, POWER LAW + PEAK (PL+P) and BROKEN POWER LAW (BPL) outlined in Abbott *et al.* (2021e). The primary mass distribution for the PL+P model is given by

$$p(m_1) = [(1 - \lambda_{\text{peak}})\mathcal{B}(m_1) + \lambda_{\text{peak}}G(m_1)]S(m_1), \quad (4.6a)$$

$$\mathcal{B}(m) = Cm^{-\alpha}, \quad m < m_{\text{max}}, \quad \text{and} \quad (4.6b)$$

$$G(m) = \frac{1}{\sqrt{2\pi}\sigma_m} \left[e^{-(m-\mu_m)^2/2\sigma_m^2} \right]. \quad (4.6c)$$

Here C is a normalization constant, and $S(m_1)$ is the smoothing function given by Eq. (B6) of Abbott *et al.* (2021e). The mass ratio for both mass distribution models (PL+P and BPL) is given by a power law that also includes the smoothing term and is given as

$$p(q) = q^\beta S(m_1 q). \quad (4.7)$$

For the BPL model, the primary mass (m_1) is distributed as follows

$$p(m_1) \propto \begin{cases} m_1^{-\alpha_1} S(m_1), & m_1 < m_{\text{break}} \\ m_1^{-\alpha_2} S(m_1), & m_1 > m_{\text{break}} \\ 0, & \text{otherwise,} \end{cases} \quad (4.8)$$

where $m_{\text{break}} = m_{\text{min}} + b(m_{\text{max}} - m_{\text{min}})$. The values of hyper-parameters used in the above-mentioned models are given in Table 4.2. We have distributed the primary mass (m_1) in the limit of $[5, 100]M_\odot$ and the mass ratio ($q = m_1/m_2$) in the range of $[1, 18]$,

POWER LAW + PEAK		BROKEN POWER LAW	
Parameter	Value	Parameter	Value
α	2.63	α_1	1.58
μ_m	33.07	α_2	5.59
σ_m	5.69	b	0.43
δ_m	4.82	δ_m	4.83
β	1.26	β	1.4
m_{\min}	4.59	m_{\min}	3.96
m_{\max}	86.22	m_{\max}	87.14
λ_{peak}	0.10		

Table 4.2: Values of model parameters for mass models used in the population study.

which is the maximum q up to which the waveform used here is calibrated (London *et al.*, 2018).

To distribute these sources to redshifts accessible to a 3G detector network, we have employed the Madau-Dickinson-Belczynski-Ng model for field BBH merger rate of Ng *et al.* (2021). The volumetric merger rate reads

$$\dot{n}_{\text{F}}(z) \propto \frac{(1+z)^{\alpha_{\text{F}}}}{1 + [(1+z)/C_{\text{F}}]^{\beta_{\text{F}}}}, \quad (4.9)$$

with $\alpha_{\text{F}} = 2.57$, $\beta_{\text{F}} = 5.83$, $C_{\text{F}} = 3.36$. Further details can be found in Appendix B of Ng *et al.* (2021). Using this model for the merger rates, the redshift is then distributed as follows:

$$p(z) \propto \frac{4\pi\dot{n}_{\text{F}}(z)}{1+z} \left(\frac{dV_{\text{c}}}{dz} \right), \quad (4.10)$$

where V_{c} represents the comoving volume. We have used the recently developed python package gwbench (Borhanian, 2021) for the distribution of redshift. The range for z has been taken as $[0, 10]$. The redshift distribution of population of sources, along with the resultant (total) mass distribution from the PL+P and BPL mass models, is shown in Fig. 4.3.

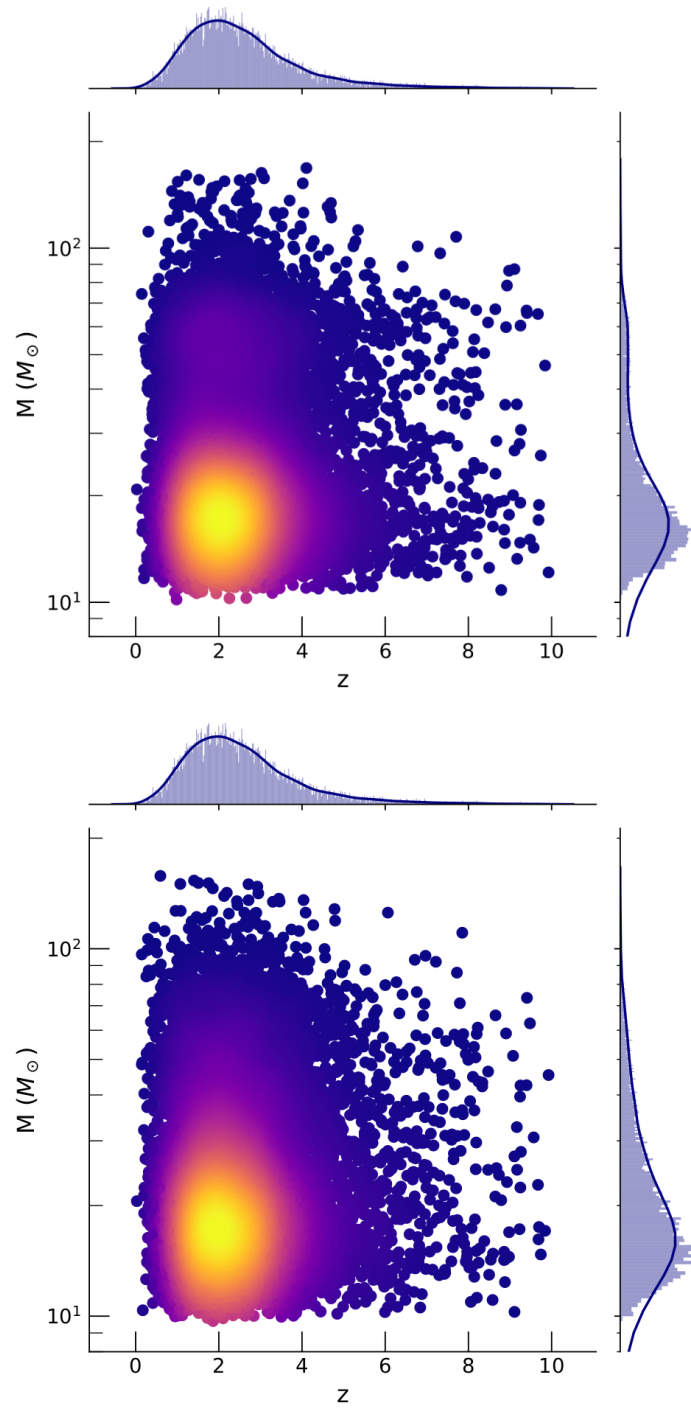


Figure 4.3: 2D distribution of injected values of total mass (M) and redshift(z). Top: Mass model is POWER LAW + PEAK, Bottom: Mass model is BROKEN POWER LAW. Redshift has been distributed according to the MDBN merger rate and taken to be the same for both mass distributions. The colours (in the scatter plot) from yellow to blue denote the number density of samples going from most to least dense regions.

The spins are distributed using the DEFAULT MODEL of [Abbott *et al.* \(2021e\)](#) for dimensionless spin magnitude ($\chi_{1,2}$) given by

$$p(\chi) = \text{Beta}(\alpha_\chi, \beta_\chi). \quad (4.11)$$

The values of α_χ and β_χ are computed using the mean (μ_χ) and variance (σ_χ^2) for the Beta distribution. We found these values to be $\alpha_\chi = 6.3788$ and $\beta_\chi = 2.2412$ and used them in constructing the distribution for dimensionless spin magnitudes ($\chi_{1,2}$). Further the cosine of the tilt angle, defined as $z_\chi = \cos(\theta_{1,2})$, is distributed as $p(z_\chi)$ (see Sec. D1 of [Abbott *et al.*, 2021e](#), for related details). The distribution χ_{1z} and χ_{2z} reads

$$p(\chi_{1z,2z}) = p(\chi_{1z,2z}) p(z_\chi). \quad (4.12)$$

We have taken the same distribution for χ_{1z} and χ_{2z} , in the range $[-1,1]$.² We simulate 10,000 sources following the above-mentioned prescription. We vary all the nine parameters $\{d_L, \iota, M, q, \theta, \phi, \psi, \chi_{1z}, \chi_{2z}\}$, following the population models. The ranges for total mass, mass ratio, spins, and redshift have been mentioned with their respective population models above. The cosines of the angles ι and θ have been varied uniformly between $[-1, 1]$, and ϕ and ψ are uniform between $[0, 2\pi]$. It is worth mentioning that due to the low mass of the secondary, which falls in the NS-BH mass gap, GW190814 is an outlier. Thus, the O3a population models do not include it while calculating the hyper-parameters ([Abbott *et al.*, 2021e](#)).

4.5.2 Detector networks

We consider the detection of higher modes with network(s) consisting of two kinds of 3G detectors: CE and ET. We also compare the detection of higher modes in the 3G network with that in the upgraded 2G networks with LIGO A+ configuration ([LIGO Scientific Collaboration, 2016](#); [Shoemaker and LIGO Scientific Collaboration, 2019](#)) and LIGO Voyager ([LIGO Scientific Collaboration, 2016](#)). Both LIGO A+ and LIGO Voyager

²Note that the waveform we use (IMRPhenomHM) is calibrated up to spin magnitude of 0.85 (0.98 for equal mass systems); however, we have extended this up to 1 to include the complete range of spin magnitudes.

Label	Location	Latitude	Longitude	Orientation	Type(s)
L	Louisiana, USA	0.53	-1.58	-1.26	CE/A+/Voyager
H	Washington, USA	0.81	-2.08	-2.51	CE/A+/Voyager
V	Cascina, Italy	0.76	0.18	2.8	CE/A+/Voyager
A	New South Wales, Australia	-0.59	2.53	0.78	CE
E	Cascina, Italy	0.76	0.18	2.8	ET

Table 4.3: The detector locations which have been used in this study (Borhanian, 2021). All angle values are in radians. Some of these sites have not been finalized yet and have been planned/proposed for future detectors.

are expected to have an overall improved sensitivity compared to current generation detectors.

A three-detector network of 3G detectors is used in the analyses presented here. Our primary 3G network consists of a detector with CE configuration in the US (LIGO-Livingston site), ET in Europe (at the Virgo site), and another CE detector in Australia. We refer to this network as the LAE network of 3G detectors. Additionally, three different 3-detector networks have been used to study the detectability of higher-order modes as detectors evolve through LIGO A+, LIGO Voyager, and CE configurations. The sensitivity curves and locations of these detectors are shown in Fig. 1.9 and Table 4.3, respectively. For each detector, we put the lower frequency bound (f_{low}) as 5 Hz following Chamberlain and Yunes (2017).³ While signals in 3G detector networks are expected to last much longer than the current ground-based detectors, in our study we have not included the effect of rotation of the Earth on the observed signals. This is because majority of the systems taken in our study lie in the mass range of $[10, 30] M_{\odot}$ and the signals will last only a few minutes. Thus we posit that the conclusions drawn in

³Note that in Chamberlain and Yunes (2017), authors have used a low-frequency cutoff of 1 Hz for ET configuration; however, we work with a universal low-frequency cutoff of 5 Hz for all detector configurations (LIGO A+, LIGO Voyager, CE, or ET) in this work.

our study are not affected by ignoring this effect.

4.5.3 SNR distribution of higher modes

Figure 4.4 shows the cumulative histograms for the SNRs of various modes in the LAE network (two CE detectors at L & A, and one ET detector at E) of 3G detectors (see Table 4.3 for details). The numbers in brackets are the median values of SNR for each mode. For a particular value of SNR (on the x -axis), the y -axis corresponds to the fraction of the population having SNR up to that value. The dashed lines correspond to the population distributed according to the BPL mass model, while the solid lines correspond to the PL+P distribution. Since the results from the two models are very close, we only quote numbers corresponding to the PL+P model. We find that 99.8% of the simulated population following the PL+P model has SNR >10 in 22 mode. Note that the detection fractions we quote in the subsequent sections are obtained by putting a minimum cutoff of SNR > 10 for the 22 mode, and SNR > 3 for all the other modes.

We find that the 33 mode is detectable in nearly 33% of the sources, and 44 mode is detected in $\sim 28\%$ of the population. 32 and 21 modes are detectable in nearly 15% and 10% sources, respectively, while the detected fraction is only $\sim 0.1\%$ for the 43 mode. This demonstrates that for a population of sources similar to those detected in GWTC-2, with the increased reach of 3G detectors to higher redshifts, we will detect most higher modes in many sources.

Comparison between various generations of detector networks

In this section, we investigate how the detectability of higher modes changes for a population across various generations of detector networks. We consider three kinds of detector networks for this study: LIGO-A+, LIGO-Voyager, and CE detector networks. To avoid detector location bias, we have chosen the same locations, Livingston and Hanford in the U.S. and Cascina in Italy (LHV), for all three networks. For constructing this population, we have considered the POWER LAW + PEAK mass model. We have

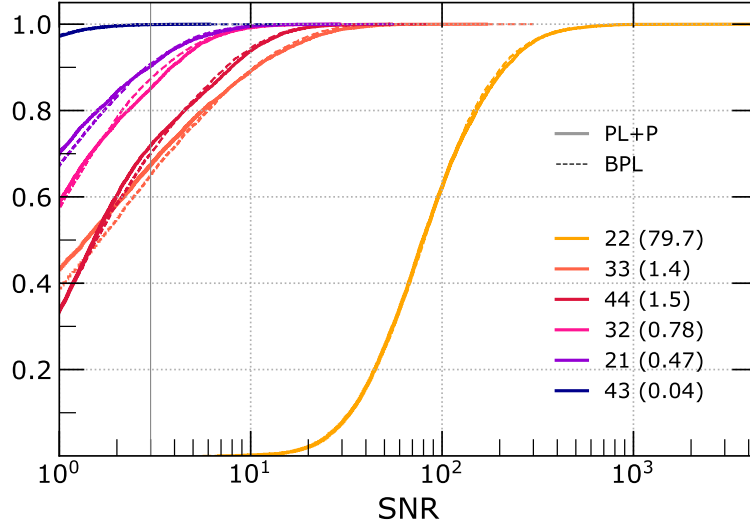


Figure 4.4: Cumulative SNR histograms for six leading modes, with the two mass distribution models (PL+P and BPL) coupled with the MDBN model for redshift evolution. The plot shows trends for each mode for SNRs > 1 . The solid and dashed coloured lines correspond to the population drawn from the PL+P and BPL models, respectively. The values in the brackets are the median values of SNR for each mode. The detector network used here consists of a detector with CE configuration in the U.S. (at the LIGO-Livingston site), a detector with ET design in Europe (at the Virgo site), and another CE detector in Australia, and referred to as 3G LAE network in this chapter.

shown the results for CE and Voyager networks in Fig. 4.5. A quick look at Fig. 4.5 reveals that the LIGO Voyager detector network can barely detect the two additional modes besides the (dominant) 22 mode, whereas 3G detectors have a good detection percentage for 33 and 44 modes. As expected, the improvement with 3G detectors is highly significant compared to the upgraded 2G configurations. Note that here, we quote the detection percentages of higher modes, over and above the detection of 22 mode. Again, as seen in the previous section, nearly 100% sources are detectable in 22 mode in the detector network formed by the CE detectors at locations of current LIGO and Virgo detector sites. Out of these, nearly 35% and 30% of the sources show a detection in 33 and 44 modes, respectively. This detection percentage drastically decreases for Voyager and A+. For Voyager, only 40% of the simulated population is detectable in 22 mode, out of which only $\sim 6\%$ and $\sim 2\%$ show a detection in 33 and 44 modes, respectively. For A+, only about 7% of the systems show a detection in 22 mode, out of which $\sim 1\%$

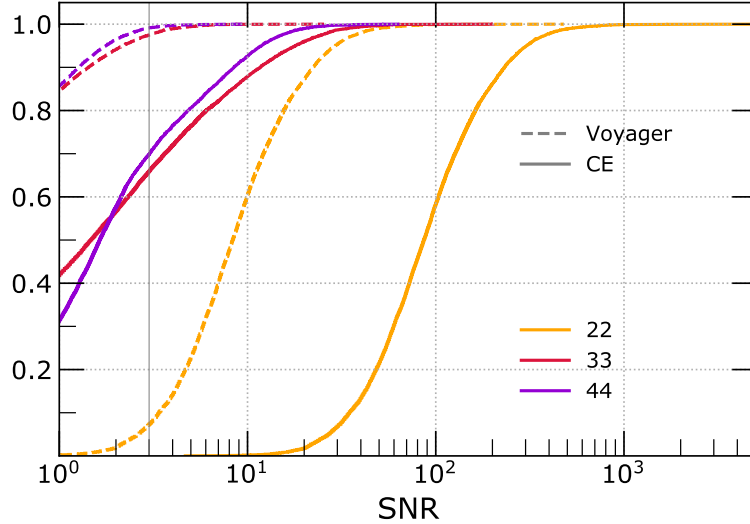


Figure 4.5: Cumulative histograms of SNR for various higher modes as a comparison between various generations of detectors. The solid, coloured lines denote the 3G detector network with CE, while the dashed lines denote the detector network using LIGO Voyager. Both the detectors have been placed at the locations of the LHV network. We have taken $q_{max} = 18$.

show 33 mode, and $\sim 0.5\%$ show a detection in 44 mode. Considering the detection rate numbers from [Baibhav *et al.* \(2019\)](#), these percentages can still result in the detection of a considerable number of HMs in the detected population. This shows the tremendous potential of a network of 3G detectors, and how the number of higher mode detections will significantly rise compared to the currently operating 2G detectors. This, in turn, will also have a profound impact on the overall parameter estimation capabilities of the 3G detectors, and hence influence the astrophysics and fundamental physics in the 3G era in a big way.

4.6 SUMMARY

We have investigated the detectability of higher modes of gravitational radiation in mass ratio and inclination angle space (Sec. 4.4). The effect of increasing total mass (in discrete values) was also noted in Sec. 4.4. We find that various modes activate different regions of the $(q-\iota)$ plane, and show various symmetries in ι , leading to bi- and

tri-modality in the contours. We also explored the detectability of higher modes for a few events from the GWTC-2 catalog, assuming they were detected during the 3G era (Sec. 4.3). For the GWTC-2 events, we observe a massive improvement of SNR (by a factor larger than 20 times) for the events reported to show detection in 33 mode by LIGO/Virgo observations (GW190814, GW190412). In the 3G era, events like these promise to show detection in other higher harmonics as well. Additionally, we also see detectable SNRs in higher modes for other GWTC-2 events, which emphasizes that the number of events that permit the measurement of higher modes will also increase in the 3G era.

We also performed a population study for 10,000 sources, which will be detected by the 3G network, and quote the fraction of the population which will show the presence of higher modes (Sec. 4.5.3). It is found that nearly 33% and 28% of the sources will have detectable SNRs in 33 and 44 modes, respectively, and other modes will also be detectable in a small percentage of the population. Additionally, we compared this fraction with the fraction of higher modes detectable in the upgraded 2G gravitational wave detector networks, such as LIGO A+ and LIGO Voyager, using the PL+P mass model. We conclude that this fraction significantly increases from less than 6% to nearly 35% for the 33 mode, with the 3G network.

All of the above-mentioned investigations were performed using a spinning inspiral-merger-ringdown higher mode waveform of the Phenom family (IMRPhenomHM), and using a different waveform may alter the numbers only slightly.

CHAPTER 5

CONCLUSIONS AND FUTURE DIRECTIONS

In this **thesis** we have explored the effects of orbital eccentricity, spin-precession, and higher modes on data analysis of gravitational signals from binary black hole systems. We have studied the interplay of these effects from various angles performing a variety of injection studies. We started with investigating the loss of signals when searches do not include eccentric waveform models for a population which contained eccentric signals, by calculating the signal recovery fraction. We found that high mass ratio binaries with non-negligible values of eccentricities show the maximum loss of signal recovery fraction. This was followed by a detailed parameter estimation study of simulated eccentric signals, which were analysed with eccentric and quasi-circular waveforms in various spin configurations. We observed that quasi-circular waveforms in any spin-configuration were incapable of correctly characterizing the chirp mass of the source. This also shed some light on the interplay of orbital eccentricity with spin-precession and we concluded that these effects do not mimic each other for signals with long inspirals and moderate eccentricities. We also performed a few injections using eccentric higher mode signals and showed that quasi-circular higher mode waveforms also bias the recovered parameters, same as was observed using only dominant mode waveforms.

Next, the effect of spin-precession on spin-induced quadrupole moment parameter, which presents as a null test for binary black hole nature of the GW signal source, was explored. For various low and high precessing spin systems, comparisons were made between the analyses with two different waveforms, highlighting the difference between them and recommending the use of waveforms with double spin-precession for the test when dealing with signals which have non-negligible spin precession. Here too, the interplay of spin-precession was studied along with higher modes and it was observed that for

real events which have non-negligible spins and mass asymmetry, use of higher mode waveforms with double-spin precession would lead to better results.

Finally, we studied the detectability of higher modes in the next-generation ground-based GW detectors such as Cosmic Explorer and Einstein telescope. We showed that the improvement in sensitivities, especially in the lower range of these detector frequencies, will lead to a considerable signal-to-noise ratio in the higher modes in addition of the dominant mode. We also quantified the regions in mass ratio and inclination angle space to highlight how various modes get excited in different portions of the parameter space and sometimes complement each other. For the 3G detector networks, the population of binary black holes showed detection of several higher-order modes, which was not the case for the upgraded 2G network of detectors.

All of the studies performed above lead to various implications about the formation channels of the black hole binary systems. Orbital eccentricity and spin-precession are important markers to indicate that the binary may not have formed in isolation. Studying these effects in details can help us categorize the populations better and estimate the merger rates. Injection studies which highlight the biases when using different waveform models, both for null tests of general relativity and for parameter estimation of binary black hole systems, help keep the scientific community informed of the limitations that the present waveform models possess, and caution the community against various inferences drawn from the results. The detection and inclusion of higher modes in waveform models helps break degeneracies between various parameters that aid in their more accurate and precise estimation. This in turn has larger applications in cosmology such as the estimation of Hubble constant.

While at present there are no IMR models that include all three physical effects (orbital eccentricity, spin-precession, and higher order modes), several groups are actively working on their development. Once these models become available, studies included

in Chapter 2 of this **thesis** can be extended further. While the analysis presented in Chapter 3 studies waveform systematics on the SIQM tests for various spin and mass ratio configurations by injecting BBH waveforms consistent with GR, a detailed follow-up study with non-GR injections may be carried out in a future work. While in Chapter 4 we have shown the detectability of various modes for spinning systems, a more detailed study can be done by including the effect of spin-precession along with higher modes. Further, the effect of higher modes in the error analysis of various parameters in 3G detector era can be explored.

APPENDIX A

SPIN-INDUCED QUADRUPOLE MOMENT

The definition of a Kerr black hole (BH) is closely associated with the "no-hair" conjecture, which states that all the characteristics of a Kerr black hole are entirely determined by its mass and spin. Measuring the spin-induced quadrupole moments (SIQM) of a compact binary's constituents can test for the black hole nature of the binary's compact objects since these values are unique for Kerr BHs due to the no-hair conjecture. For an isolated Kerr BH, the quadrupole moment scalar is given by $Q \propto \chi^2 m^3$ (Poisson and Will, 1995), where m is the mass and the spin magnitude χ is defined as $\chi = \frac{|\vec{S}|}{m^2}$ with \vec{S} as the spin angular momentum of the BH. For a non-black hole compact object, this can be generalized to $Q = -\kappa m^3 \chi^2$, where $\kappa = 1$ represents the black hole limit. For a binary system, one can define the symmetric and anti-symmetric combinations of κ as:

$$\kappa_s = \frac{\kappa_1 + \kappa_2}{2} \quad (\text{A.1})$$

$$\kappa_a = \frac{\kappa_1 - \kappa_2}{2}. \quad (\text{A.2})$$

Now, in order to pose this as a null test of binary black hole nature, one can introduce a deviation parameter $\delta\kappa$ such that $\kappa_i = 1 + \delta\kappa_i$. In this parameterization, $\delta\kappa_i = 0$ represents the black hole limit. Again, we can define the symmetric and anti-symmetric combinations as:

$$\delta\kappa_s = \frac{\delta\kappa_1 + \delta\kappa_2}{2} \quad (\text{A.3})$$

$$\delta\kappa_a = \frac{\delta\kappa_1 - \delta\kappa_2}{2}. \quad (\text{A.4})$$

Here, choosing $\delta\kappa_a = 0$, a measurement of $\delta\kappa_s = 0$ recovers the *binary* black hole limit.

Here, we explicitly write the phasing coefficients which have been changed to include the SIQM deviation parameter ($\delta\kappa_i$). These have been derived from [Krishnendu et al.](#)

(2017)¹. Schematically, the expression for phase in Stationary Phase Approximation (SPA) (Arun *et al.*, 2009) can be written as:

$$\Psi_{\text{SPA}}(f) = 2\pi f t_c - \phi_c + \left\{ \frac{3}{128\eta v^5} [\psi_{\text{NS}} + \psi_{\text{spin}}] \right\}. \quad (\text{A.5})$$

Here, $v = (\pi M f)^{1/3}$, where the total mass M is taken in natural units, and ϕ_c denotes the phase at the time of coalescence t_c . Now, we can separate the spinning part of phase ψ_{spin} as:

$$\psi_{\text{spin}} \equiv \psi_{\text{SO}} + \psi_{\text{SS}} + \psi_{\text{SSS}} = v^3 [\mathcal{P}_3 + \mathcal{P}_4 v + \mathcal{P}_5 v^2 + \mathcal{P}_6 v^3 + \dots]. \quad (\text{A.6})$$

Expressions for the coefficients \mathcal{P}_n can be found in Arun *et al.* (2009); Vallisneri (2008), where the explicit dependence on κ_s and κ_a is omitted by setting them to their respective values for Kerr BBHs. Here, we list the expressions which contain the symmetric and anti-symmetric forms of SIQM deviation parameters ($\delta\kappa_s$ and $\delta\kappa_a$) that have been included in the waveform used for SIQM studies in this **thesis**.

$$\begin{aligned} \mathcal{P}_4 = & -\frac{5}{8}(\chi_s \cdot \hat{\mathbf{L}}_N)^2 \left[1 + 156\eta + 80\nu(1 + \delta\kappa_a) + 80(1 - 2\eta)(1 + \delta\kappa_s) \right] \\ & + (\chi_a \cdot \hat{\mathbf{L}}_N)^2 \left[-\frac{5}{8} - 50\nu(1 + \delta\kappa_a) - 50(1 + \delta\kappa_s) + 100\eta(2 + \delta\kappa_s) \right] \\ & - \frac{5}{4}(\chi_a \cdot \hat{\mathbf{L}}_N)(\chi_s \cdot \hat{\mathbf{L}}_N) \left[\nu + 80(1 - 2\eta)(1 + \delta\kappa_a) + 80\nu(1 + \delta\kappa_s) \right], \end{aligned} \quad (\text{A.7a})$$

$$\begin{aligned} \mathcal{P}_6 = & \pi \left[\frac{2270}{3} \nu \chi_a \cdot \hat{\mathbf{L}}_N + \left(\frac{2270}{3} - 520\eta \right) \chi_s \cdot \hat{\mathbf{L}}_N \right] + (\chi_s \cdot \hat{\mathbf{L}}_N)^2 \left[-\frac{1344475}{2016} \right. \\ & + \frac{829705}{504} \eta + \frac{3415}{9} \eta^2 + \nu \left(\frac{26015}{28} - \frac{1495}{6} \eta \right) (1 + \delta\kappa_a) + \left(\frac{26015}{28} - \frac{44255}{21} \eta \right. \\ & \left. \left. - 240\eta^2 \right) (1 + \delta\kappa_s) \right] + \chi_a \cdot \hat{\mathbf{L}}_N)^2 \left[-\frac{1344475}{2016} + \frac{267815}{252} \eta - 240\eta^2 \right. \\ & \left. + \nu \left(\frac{26015}{28} - \frac{1495}{6} \eta \right) (1 + \delta\kappa_a) + \left(\frac{26015}{28} - \frac{44255}{21} \eta - 240\eta^2 \right) (1 + \delta\kappa_s) \right] \\ & + (\chi_a \cdot \hat{\mathbf{L}}_N)(\chi_s \cdot \hat{\mathbf{L}}_N) \left[\left(\frac{26015}{14} - \frac{88510}{21} \eta - 480\eta^2 \right) (1 + \delta\kappa_a) + \nu \left[-\frac{1344475}{1008} \right. \right. \\ & \left. \left. + \frac{745}{18} \eta + \left(\frac{26015}{14} - \frac{1495}{3} \eta \right) (1 + \delta\kappa_s) \right] \right], \end{aligned} \quad (\text{A.7b})$$

¹See the supplemental material of Krishnendu *et al.* (2017) for complete waveform expressions.

where ν is the difference mass ratio given by $|m_1 - m_2|/(m_1 + m_2)$. Since \mathcal{P}_3 and \mathcal{P}_5 only contain spin-orbit terms, they do not exhibit a dependence on κ parameters and hence have not been included here.

These changes have been included in the `LALSimulation` module of the `LALSuite` package and can be called by various `Phenom` waveforms such as `IMRPhenomD`, `IMRPhenomPv2`, `IMRPhenomPv3`, `IMRPhenomHM`, `IMRPhenomPv3HM`, and `PhenomX` family of waveforms such as `IMRPhenomXAS`, `IMRPhenomXHM`, `IMRPhenomXP`, `IMRPhenomXPHM`. We have used these waveforms for the injection studies and real event analyses presented in Chapter 3 of this **thesis**.

BIBLIOGRAPHY

1. **A-sharp** (2022). URL: <https://gravitationalwaves.syracuse.edu/advanced-ligo/>. (cited on pg. 20).
2. **Aasi, J. et al.** (2015). Advanced LIGO. *Class. Quant. Grav.*, **32**, 074001. DOI. ARXIV:1411.4547. (cited on pg. 18).
3. **Abac, A. G. et al.** (2023). Search for Eccentric Black Hole Coalescences during the Third Observing Run of LIGO and Virgo. ARXIV:2308.03822. (cited on pgs. 46 and 47).
4. **Abadie, J. et al.** (2012). Search for Gravitational Waves from Low Mass Compact Binary Coalescence in LIGO's Sixth Science Run and Virgo's Science Runs 2 and 3. *Phys. Rev. D*, **85**, 082002. DOI. ARXIV:1111.7314. (cited on pg. 48).
5. **Abbott, B. et al.** (2016a). Observation of Gravitational Waves from a Binary Black Hole Merger. *Phys. Rev. Lett.*, **116**(6), 061102. DOI. ARXIV:1602.03837. (cited on pgs. 7 and 8).
6. **Abbott, B. P. et al.** (2016b). Astrophysical Implications of the Binary Black-Hole Merger GW150914. *Astrophys. J. Lett.*, **818**(2), L22. DOI. ARXIV:1602.03846. (cited on pg. 26).
7. **Abbott, B. P. et al.** (2016c). Directly comparing GW150914 with numerical solutions of Einsteins equations for binary black hole coalescence. *Phys. Rev.*, **D94**(6), 064035. DOI. ARXIV:1606.01262. (cited on pg. 74).
8. **Abbott, B. P. et al.** (2016d). GW150914: First results from the search for binary black hole coalescence with Advanced LIGO. *Phys. Rev. D*, **93**(12), 122003. DOI. ARXIV:1602.03839. (cited on pgs. 26 and 27).
9. **Abbott, B. P. et al.** (2016e). GW151226: Observation of Gravitational Waves from a 22-Solar-Mass Binary Black Hole Coalescence. *Phys. Rev. Lett.*, **116**(24), 241103. DOI. ARXIV:1606.04855. (cited on pgs. 26 and 74).
10. **Abbott, B. P. et al.** (2016f). Properties of the Binary Black Hole Merger GW150914. *Phys. Rev. Lett.*, **116**(24), 241102. DOI. ARXIV:1602.03840. (cited on pg. 26).
11. **Abbott, B. P. et al.** (2016g). Tests of general relativity with GW150914. *Phys. Rev. Lett.*, **116**(22), 221101. DOI. [Erratum: Phys.Rev.Lett. 121, 129902 (2018)]. ARXIV:1602.03841. (cited on pg. 31).
12. **Abbott, B. P. et al.** (2017a). Effects of waveform model systematics on the interpretation of GW150914. *Class. Quant. Grav.*, **34**(10), 104002. DOI. ARXIV:1611.07531. (cited

on pgs. [39](#), [45](#), and [74](#)).

13. **Abbott, B. P. et al.** (2017*b*). Exploring the Sensitivity of Next Generation Gravitational Wave Detectors. *Class. Quant. Grav.*, **34**(4), 044001. DOI. ARXIV:[1607.08697](#). (cited on pg. [20](#)).
14. **Abbott, B. P. et al.** (2017*c*). Gravitational Waves and Gamma-rays from a Binary Neutron Star Merger: GW170817 and GRB 170817A. *Astrophys. J. Lett.*, **848**(2), L13. DOI. ARXIV:[1710.05834](#). (cited on pg. [27](#)).
15. **Abbott, B. P. et al.** (2017*d*). GW170104: Observation of a 50-Solar-Mass Binary Black Hole Coalescence at Redshift 0.2. *Phys. Rev. Lett.*, **118**(22), 221101. DOI. [Erratum: *Phys.Rev.Lett.* 121, 129901 (2018)]. ARXIV:[1706.01812](#). (cited on pg. [29](#)).
16. **Abbott, B. P. et al.** (2017*e*). GW170814: A Three-Detector Observation of Gravitational Waves from a Binary Black Hole Coalescence. *Phys. Rev. Lett.*, **119**(14), 141101. DOI. ARXIV:[1709.09660](#). (cited on pg. [29](#)).
17. **Abbott, B. P. et al.** (2017*f*). GW170817: Observation of Gravitational Waves from a Binary Neutron Star Inspiral. *Phys. Rev. Lett.*, **119**(16), 161101. DOI. ARXIV:[1710.05832](#). (cited on pgs. [27](#), [40](#), and [41](#)).
18. **Abbott, B. P. et al.** (2017*g*). Multi-messenger Observations of a Binary Neutron Star Merger. *Astrophys. J. Lett.*, **848**(2), L12. DOI. ARXIV:[1710.05833](#). (cited on pg. [27](#)).
19. **Abbott, B. P. et al.** (2018*a*). GW170817: Measurements of neutron star radii and equation of state. *Phys. Rev. Lett.*, **121**(16), 161101. DOI. ARXIV:[1805.11581](#). (cited on pg. [28](#)).
20. **Abbott, B. P. et al.** (2018*b*). Prospects for observing and localizing gravitational-wave transients with Advanced LIGO, Advanced Virgo and KAGRA. *Living Rev. Rel.*, **21**(1), 3. DOI. ARXIV:[1304.0670](#). (cited on pg. [20](#)).
21. **Abbott, B. P. et al.** (2019*a*). Binary Black Hole Population Properties Inferred from the First and Second Observing Runs of Advanced LIGO and Advanced Virgo. *Astrophys. J. Lett.*, **882**(2), L24. DOI. ARXIV:[1811.12940](#). (cited on pgs. [51](#) and [143](#)).
22. **Abbott, B. P. et al.** (2019*b*). GWTC-1: A Gravitational-Wave Transient Catalog of Compact Binary Mergers Observed by LIGO and Virgo during the First and Second Observing Runs. *Phys. Rev. X*, **9**(3), 031040. DOI. ARXIV:[1811.12907](#). (cited on pgs. [9](#) and [24](#)).
23. **Abbott, B. P. et al.** (2019*c*). Properties of the binary neutron star merger GW170817. *Phys. Rev. X*, **9**(1), 011001. DOI. ARXIV:[1805.11579](#). (cited on pgs. [27](#) and [36](#)).
24. **Abbott, B. P. et al.** (2019*d*). Search for Eccentric Binary Black Hole Mergers with Advanced LIGO and Advanced Virgo during their First and Second Observing Runs.

- Astrophys. J.*, **883**(2), 149. DOI. ARXIV:1907.09384. (cited on pgs. 46 and 47).
25. **Abbott, B. P. et al.** (2019e). Tests of General Relativity with the Binary Black Hole Signals from the LIGO-Virgo Catalog GWTC-1. *Phys. Rev. D*, **100**(10), 104036. DOI. ARXIV:1903.04467. (cited on pg. 31).
 26. **Abbott, B. P. et al.** (2020a). A guide to LIGO–Virgo detector noise and extraction of transient gravitational-wave signals. *Class. Quant. Grav.*, **37**(5), 055002. DOI. ARXIV:1908.11170. (cited on pgs. 38, 39, and 40).
 27. **Abbott, R. et al.** (2020b). GW190412: Observation of a Binary-Black-Hole Coalescence with Asymmetric Masses. *Phys. Rev. D*, **102**(4), 043015. DOI. ARXIV:2004.08342. (cited on pgs. 28, 52, 107, 128, 131, 133, 135, and 137).
 28. **Abbott, R. et al.** (2020c). GW190521: A Binary Black Hole Merger with a Total Mass of 150 M_{\odot} . *Phys. Rev. Lett.*, **125**(10), 101102. DOI. ARXIV:2009.01075. (cited on pgs. 28, 44, 133, and 137).
 29. **Abbott, R. et al.** (2020d). GW190814: Gravitational Waves from the Coalescence of a 23 Solar Mass Black Hole with a 2.6 Solar Mass Compact Object. *Astrophys. J. Lett.*, **896**(2), L44. DOI. ARXIV:2006.12611. (cited on pgs. 28, 52, 133, 135, and 137).
 30. **Abbott, R. et al.** (2020e). Properties and Astrophysical Implications of the 150 M_{\odot} Binary Black Hole Merger GW190521. *Astrophys. J. Lett.*, **900**(1), L13. DOI. ARXIV:2009.01190. (cited on pgs. 28, 31, and 44).
 31. **Abbott, R. et al.** (2021a). All-sky search for short gravitational-wave bursts in the third Advanced LIGO and Advanced Virgo run. *Phys. Rev. D*, **104**(12), 122004. DOI. ARXIV:2107.03701. (cited on pg. 12).
 32. **Abbott, R. et al.** (2021b). GWTC-2: Compact Binary Coalescences Observed by LIGO and Virgo During the First Half of the Third Observing Run. *Phys. Rev. X*, **11**, 021053. DOI. ARXIV:2010.14527. (cited on pgs. 9, 24, 109, 133, and 137).
 33. **Abbott, R. et al.** (2021c). GWTC-3: Compact Binary Coalescences Observed by LIGO and Virgo During the Second Part of the Third Observing Run. *arXiv preprint*. ARXIV:2111.03606. (cited on pgs. 9, 24, 29, 35, 49, 102, and 109).
 34. **Abbott, R. et al.** (2021d). Observation of Gravitational Waves from Two Neutron Star–Black Hole Coalescences. *Astrophys. J. Lett.*, **915**(1), L5. DOI. ARXIV:2106.15163. (cited on pg. 29).
 35. **Abbott, R. et al.** (2021e). Population Properties of Compact Objects from the Second LIGO-Virgo Gravitational-Wave Transient Catalog. *Astrophys. J. Lett.*, **913**(1), L7. DOI. ARXIV:2010.14533. (cited on pgs. 30, 143, and 146).
 36. **Abbott, R. et al.** (2021f). Tests of general relativity with binary black holes from

- the second LIGO-Virgo gravitational-wave transient catalog. *Phys. Rev. D*, **103**(12), 122002. DOI. ARXIV:2010.14529. (cited on pgs. 57, 58, 106, 114, 128, 129, and 131).
37. **Abbott, R. et al.** (2021g). Tests of General Relativity with GWTC-3. ARXIV:2112.06861. (cited on pgs. vii, viii, ix, 31, 57, 58, 105, 106, 108, 109, 110, 114, 128, 129, and 131).
 38. **Abbott, R. et al.** (2023). Population of Merging Compact Binaries Inferred Using Gravitational Waves through GWTC-3. *Phys. Rev. X*, **13**(1), 011048. DOI. ARXIV:2111.03634. (cited on pgs. 30, 70, and 143).
 39. **Abbott, R. et al.** (2024). GWTC-2.1: Deep extended catalog of compact binary coalescences observed by LIGO and Virgo during the first half of the third observing run. *Phys. Rev. D*, **109**(2), 022001. DOI. ARXIV:2108.01045. (cited on pgs. viii, 9, 24, and 109).
 40. **Abdelsalhin, T., L. Gualtieri, and P. Pani** (2018). Post-Newtonian spin-tidal couplings for compact binaries. *Phys. Rev.*, **D98**(10), 104046. DOI. ARXIV:1805.01487. (cited on pg. 55).
 41. **Abedi, J., H. Dykaar, and N. Afshordi** (2017). Echoes from the Abyss: Tentative evidence for Planck-scale structure at black hole horizons. *Phys. Rev. D*, **96**(8), 082004. DOI. ARXIV:1612.00266. (cited on pg. 32).
 42. **Accadia, T. et al.** (2012). Virgo: a laser interferometer to detect gravitational waves. *Journal of Instrumentation*, **7**(3), 3012. DOI. (cited on pg. 5).
 43. **Acernese, F. et al.** (2015). Advanced virgo: a second-generation interferometric gravitational wave detector. *Classical Quantum Gravity*, **32**(2), 024001. DOI. ARXIV:1408.3978. (cited on pg. 18).
 44. **Acernese, F. et al.** (2019). Increasing the astrophysical reach of the advanced virgo detector via the application of squeezed vacuum states of light. *Phys. Rev. Lett.*, **123**(23), 231108. DOI. (cited on pg. 18).
 45. **Adams, T. et al.** (2016). Low-latency analysis pipeline for compact binary coalescences in the advanced gravitational wave detector era. *Class. Quant. Grav.*, **33**(17), 175012. DOI. ARXIV:1512.02864. (cited on pg. 35).
 46. **Adhikari, R. X. et al.** (2020). A cryogenic silicon interferometer for gravitational-wave detection. *Class. Quant. Grav.*, **37**(16), 165003. DOI. ARXIV:2001.11173. (cited on pg. 20).
 47. **Agazie, G. et al.** (2023). The NANOGrav 15 yr Data Set: Evidence for a Gravitational-wave Background. *Astrophys. J. Lett.*, **951**(1), L8. DOI. ARXIV:2306.16213. (cited on pg. 13).
 48. **Aguilar, O. D.** (2011). The Past, Present and Future of the Resonant-Mass Gravitational

- Wave Detectors. *Res. Astron. Astrophys.*, **11**, 1–42. DOI. ARXIV:1009.1138. (cited on pg. 13).
49. **Ajith, P.** and **S. Bose** (2009). Estimating the parameters of non-spinning binary black holes using ground-based gravitational-wave detectors: Statistical errors. *Phys. Rev. D*, **79**, 084032. DOI. ARXIV:0901.4936. (cited on pg. 42).
 50. **Ajith, P.** *et al.* (2011). Inspiral-merger-ringdown waveforms for black-hole binaries with non-precessing spins. *Phys. Rev. Lett.*, **106**, 241101. DOI. ARXIV:0909.2867. (cited on pg. 49).
 51. **Ajith, P.** *et al.* (2012). The NINJA-2 catalog of hybrid post-Newtonian/numerical-relativity waveforms for non-precessing black-hole binaries. *Class. Quant. Grav.*, **29**, 124001. DOI. [Erratum: *Class. Quant. Grav.* 30, 199401 (2013)]. ARXIV:1201.5319. (cited on pg. 53).
 52. **Akiyama, K.** *et al.* (2019). First M87 Event Horizon Telescope Results. I. The Shadow of the Supermassive Black Hole. *Astrophys. J. Lett.*, **875**, L1. DOI. ARXIV:1906.11238. (cited on pg. 57).
 53. **Akutsu, T.** *et al.* (2021). Overview of KAGRA: Detector design and construction history. *PTEP*, **2021**(5), 05A101. DOI. ARXIV:2005.05574. (cited on pgs. 18 and 19).
 54. **Albanesi, S., A. Nagar, S. Bernuzzi, A. Placidi, and M. Orselli** (2022a). Assessment of effective-one-body radiation reactions for generic planar orbits. *Phys. Rev. D*, **105**(10), 104031. DOI. ARXIV:2202.10063. (cited on pg. 71).
 55. **Albanesi, S., A. Placidi, A. Nagar, M. Orselli, and S. Bernuzzi** (2022b). New avenue for accurate analytical waveforms and fluxes for eccentric compact binaries. *Phys. Rev. D*, **105**(12), L121503. DOI. ARXIV:2203.16286. (cited on pg. 71).
 56. **Allen, B.** (2005). χ^2 time-frequency discriminator for gravitational wave detection. *Phys. Rev. D*, **71**, 062001. DOI. ARXIV:gr-qc/0405045. (cited on pg. 35).
 57. **Allen, B., W. G. Anderson, P. R. Brady, D. A. Brown, and J. D. E. Creighton** (2012). FINDCHIRP: An Algorithm for detection of gravitational waves from inspiraling compact binaries. *Phys. Rev. D*, **85**, 122006. DOI. ARXIV:gr-qc/0509116. (cited on pgs. 33 and 35).
 58. **Allen, W. D.** and **C. Christodoulides** (1975). Gravitational Radiation Experiments at the University of Reading and the Rutherford Laboratory. *J. Phys. A*, **8**, 1726–1733. DOI. (cited on pg. 5).
 59. **Almheiri, A., D. Marolf, J. Polchinski, and J. Sully** (2013). Black Holes: Complementarity or Firewalls? *JHEP*, **02**, 062. DOI. ARXIV:1207.3123. (cited on pg. 32).

60. **Amaro-Seoane, P. et al.** (2017). Laser Interferometer Space Antenna. ARXIV:[1702.00786](#). (cited on pg. 51).
61. **American Institute of Physics** (1995). Interview of Bryce DeWitt and Cecile DeWitt-Morette by Kenneth W. Ford on 1995 February 28. URL: <https://www.aip.org/history-programs/niels-bohr-library/oral-histories/23199>. (cited on pg. 3).
62. **Antonini, F. and H. B. Perets** (2012). Secular evolution of compact binaries near massive black holes: Gravitational wave sources and other exotica. *Astrophys. J.*, **757**, 27. DOI. ARXIV:[1203.2938](#). (cited on pg. 51).
63. **Antonini, F. and F. A. Rasio** (2016). Merging black hole binaries in galactic nuclei: implications for advanced-LIGO detections. *Astrophys. J.*, **831**(2), 187. DOI. ARXIV:[1606.04889](#). (cited on pg. 51).
64. **Antonini, F., C. L. Rodriguez, C. Petrovich, and C. L. Fischer** (2018). Precessional dynamics of black hole triples: binary mergers with near-zero effective spin. *Mon. Not. Roy. Astron. Soc.*, **480**(1), L58–L62. DOI. ARXIV:[1711.07142](#). (cited on pg. 51).
65. **Antonini, F., S. Toonen, and A. S. Hamers** (2017). Binary black hole mergers from field triples: properties, rates and the impact of stellar evolution. *Astrophys. J.*, **841**(2), 77. DOI. ARXIV:[1703.06614](#). (cited on pgs. 44, 45, and 51).
66. **Apostolatos, T. A., C. Cutler, G. J. Sussman, and K. S. Thorne** (1994). Spin-induced orbital precession and its modulation of the gravitational waveforms from merging binaries. *Phys. Rev. D*, **49**, 6274–6297. DOI. (cited on pgs. 48 and 49).
67. **Arun, K., L. Blanchet, B. R. Iyer, and M. S. Qusailah** (2004). The 2.5PN gravitational wave polarisations from inspiralling compact binaries in circular orbits. *Class. Quant. Grav.*, **21**, 3771–3802. DOI. [Erratum: *Class. Quant. Grav.* 22, 3115 (2005)]. ARXIV:[gr-qc/0404085](#). (cited on pg. 53).
68. **Arun, K., B. R. Iyer, B. Sathyaprakash, and S. Sinha** (2007a). Higher harmonics increase LISA’s mass reach for supermassive black holes. *Phys. Rev. D*, **75**, 124002. DOI. ARXIV:[0704.1086](#). (cited on pgs. 54 and 136).
69. **Arun, K., B. R. Iyer, B. Sathyaprakash, S. Sinha, and C. Van Den Broeck** (2007b). Higher signal harmonics, LISA’s angular resolution and dark energy. *Phys. Rev. D*, **76**, 104016. DOI. [Erratum: *Phys. Rev. D* 76, 129903 (2007)]. ARXIV:[0707.3920](#). (cited on pg. 52).
70. **Arun, K., H. Tagoshi, C. K. Mishra, and A. Pai** (2014). Synergy of short gamma ray burst and gravitational wave observations: Constraining the inclination angle of the binary and possible implications for off-axis gamma ray bursts. *Phys. Rev. D*, **90**(2), 024060. DOI. ARXIV:[1403.6917](#). (cited on pgs. 52 and 55).

71. **Arun, K.** and **C. M. Will** (2009). Bounding the mass of the graviton with gravitational waves: Effect of higher harmonics in gravitational waveform templates. *Class. Quant. Grav.*, **26**, 155002. DOI. ARXIV:0904.1190. (cited on pgs. 53 and 55).
72. **Arun, K. G., A. Buonanno, G. Faye,** and **E. Ochsner** (2009). Higher-order spin effects in the amplitude and phase of gravitational waveforms emitted by inspiraling compact binaries: Ready-to-use gravitational waveforms. *Phys. Rev. D*, **79**, 104023. DOI. [Erratum: Phys.Rev.D 84, 049901 (2011)]. ARXIV:0810.5336. (cited on pgs. 53, 54, and 158).
73. **Arun, K. G., B. R. Iyer, M. S. S. Qusailah,** and **B. S. Sathyaprakash** (2006a). Probing the non-linear structure of general relativity with black hole binaries. *Phys. Rev. D*, **74**, 024006. DOI. ARXIV:gr-qc/0604067. (cited on pg. 31).
74. **Arun, K. G., B. R. Iyer, M. S. S. Qusailah,** and **B. S. Sathyaprakash** (2006b). Testing post-Newtonian theory with gravitational wave observations. *Class. Quant. Grav.*, **23**, L37–L43. DOI. ARXIV:gr-qc/0604018. (cited on pg. 31).
75. **Ashton, G. et al.** (2016). Comments on: “Echoes from the abyss: Evidence for Planck-scale structure at black hole horizons”. ARXIV:1612.05625. (cited on pg. 32).
76. **Aso, Y. et al.** (2013). Interferometer design of the KAGRA gravitational wave detector. *Phys. Rev. D*, **88**(4), 043007. DOI. ARXIV:1306.6747. (cited on pg. 18).
77. **Aubin, F. et al.** (2021). The MBTA pipeline for detecting compact binary coalescences in the third LIGO–Virgo observing run. *Class. Quant. Grav.*, **38**(9), 095004. DOI. ARXIV:2012.11512. (cited on pg. 35).
78. **Babak, S.** (2008). Building a stochastic template bank for detecting massive black hole binaries. *Class. Quant. Grav.*, **25**, 195011. DOI. ARXIV:0801.4070. (cited on pg. 66).
79. **Babak, S., M. Hannam, S. Husa,** and **B. F. Schutz** (2008a). Resolving Super Massive Black Holes with LISA. ARXIV:0806.1591. (cited on pg. 52).
80. **Babak, S., A. Petiteau,** and **M. Hewitson** (2021). LISA Sensitivity and SNR Calculations. ARXIV:2108.01167. (cited on pgs. 21 and 49).
81. **Babak, S. et al.** (2008b). The Mock LISA Data Challenges: From Challenge 1B to Challenge 3. *Class. Quant. Grav.*, **25**, 184026. DOI. ARXIV:0806.2110. (cited on pg. 40).
82. **Babak, S. et al.** (2010). The Mock LISA Data Challenges: From Challenge 3 to Challenge 4. *Class. Quant. Grav.*, **27**, 084009. DOI. ARXIV:0912.0548. (cited on pg. 40).
83. **Babak, S. et al.** (2017). Science with the space-based interferometer LISA. V: Extreme mass-ratio inspirals. *Phys. Rev. D*, **95**(10), 103012. DOI. ARXIV:1703.09722. (cited

- on pg. 57).
84. **Baibhav, V. et al.** (2019). Gravitational-wave detection rates for compact binaries formed in isolation: LIGO/Virgo O3 and beyond. *Phys. Rev. D*, **100**(6), 064060. DOI. ARXIV:1906.04197. (cited on pgs. 133 and 150).
 85. **Bailes, M. et al.** (2021). Gravitational-wave physics and astronomy in the 2020s and 2030s. *Nature Rev. Phys.*, **3**(5), 344–366. DOI. (cited on pg. 23).
 86. **Banerjee, S.** (2018). Stellar-mass black holes in young massive and open stellar clusters and their role in gravitational-wave generation – II. *Mon. Not. Roy. Astron. Soc.*, **473**(1), 909–926. DOI. ARXIV:1707.00922. (cited on pg. 44).
 87. **Barack, L. and C. Cutler** (2007). Using LISA EMRI sources to test off-Kerr deviations in the geometry of massive black holes. *Phys. Rev. D*, **75**, 042003. DOI. ARXIV:gr-qc/0612029. (cited on pg. 57).
 88. **Bavera, S. S. et al.** (2020). The origin of spin in binary black holes: Predicting the distributions of the main observables of Advanced LIGO. *Astron. Astrophys.*, **635**, A97. DOI. ARXIV:1906.12257. (cited on pg. 51).
 89. **Bayes, M. and M. Price** (1763). An Essay towards Solving a Problem in the Doctrine of Chances. By the Late Rev. Mr. Bayes, F. R. S. Communicated by Mr. Price, in a Letter to John Canton, A. M. F. R. S. *Philosophical Transactions of the Royal Society of London Series I*, **53**, 370–418. DOI. (cited on pg. 37).
 90. **Beckman, J. E.**, *Gravitational Wave Astronomy*. Springer International Publishing, Cham, 2021, 223–258. DOI. URL: https://doi.org/10.1007/978-3-030-68372-6_8. (cited on pg. 4).
 91. **Belczynski, K., D. E. Holz, T. Bulik, and R. O’Shaughnessy** (2016). The first gravitational-wave source from the isolated evolution of two 40-100 Msun stars. *Nature*, **534**, 512. DOI. ARXIV:1602.04531. (cited on pg. 51).
 92. **Belczynski, K., V. Kalogera, and T. Bulik** (2001). A Comprehensive study of binary compact objects as gravitational wave sources: Evolutionary channels, rates, and physical properties. *Astrophys. J.*, **572**, 407–431. DOI. ARXIV:astro-ph/0111452. (cited on pg. 51).
 93. **Belczynski, K. et al.** (2020). Evolutionary roads leading to low effective spins, high black hole masses, and O1/O2 rates for LIGO/Virgo binary black holes. *Astron. Astrophys.*, **636**, A104. DOI. ARXIV:1706.07053. (cited on pg. 51).
 94. **Bergmann, P. G.**, *The Riddle of Gravitation*. J. Murray, London,, 1968. (cited on pg. 13).
 95. **Berry, C. P. L. et al.** (2015). Parameter estimation for binary neutron-star coalescences

with realistic noise during the Advanced LIGO era. *Astrophys. J.*, **804**(2), 114. DOI. ARXIV:[1411.6934](#). (cited on pg. 39).

96. **Berti, E.** and **V. Cardoso** (2006). Quasinormal ringing of Kerr black holes. I. The Excitation factors. *Phys. Rev. D*, **74**, 104020. DOI. ARXIV:[gr-qc/0605118](#). (cited on pg. 32).
97. **Berti, E. et al.** (2015). Testing General Relativity with Present and Future Astrophysical Observations. *Class. Quant. Grav.*, **32**, 243001. DOI. ARXIV:[1501.07274](#). (cited on pg. 32).
98. **Bhat, S. A., P. Saini, M. Favata, and K. G. Arun** (2023). Systematic bias on the inspiral-merger-ringdown consistency test due to neglect of orbital eccentricity. *Phys. Rev. D*, **107**(2), 024009. DOI. ARXIV:[2207.13761](#). (cited on pg. 45).
99. **Billing, H., P. Kafka, K. Maischberger, F. Meyer, and W. Winkler** (1975). Results of the Munich-Frascati gravitational-wave experiment. *Nuovo Cimento Lettere*, **12**, 111–116. DOI. (cited on pg. 5).
100. **Billing, H.** and **W. Winkler** (1976). The Munich Gravitational Wave Detector. *Nuovo Cim. B*, **33**, 665–680. DOI. (cited on pg. 5).
101. **Biwer, C. M. et al.** (2019). PyCBC Inference: A Python-based parameter estimation toolkit for compact binary coalescence signals. *Publ. Astron. Soc. Pac.*, **131**(996), 024503. DOI. ARXIV:[1807.10312](#). (cited on pgs. 40 and 72).
102. **Blackman, J. et al.** (2015). Fast and Accurate Prediction of Numerical Relativity Waveforms from Binary Black Hole Coalescences Using Surrogate Models. *Phys. Rev. Lett.*, **115**(12), 121102. DOI. ARXIV:[1502.07758](#). (cited on pg. 74).
103. **Blackman, J. et al.** (2017). Numerical relativity waveform surrogate model for generically precessing binary black hole mergers. *Phys. Rev. D*, **96**(2), 024058. DOI. ARXIV:[1705.07089](#). (cited on pg. 53).
104. **Blanchet, L.** (1996). Energy losses by gravitational radiation in inspiraling compact binaries to five halves postNewtonian order. *Phys. Rev. D*, **54**, 1417–1438. DOI. [Erratum: Phys.Rev.D 71, 129904 (2005)]. ARXIV:[gr-qc/9603048](#). (cited on pg. 53).
105. **Blanchet, L.** (2002). Gravitational radiation from postNewtonian sources and inspiraling compact binaries. *Living Rev. Rel.*, **5**, 3. DOI. ARXIV:[gr-qc/0202016](#). (cited on pg. 56).
106. **Blanchet, L., A. Buonanno, and G. Faye** (2006). Higher-order spin effects in the dynamics of compact binaries. II. Radiation field. *Phys. Rev. D*, **74**, 104034. DOI. [Erratum: Phys.Rev.D 75, 049903 (2007), Erratum: Phys.Rev.D 81, 089901 (2010)]. ARXIV:[gr-qc/0605140](#). (cited on pg. 53).

107. **Blanchet, L., T. Damour, G. Esposito-Farèse, and B. R. Iyer** (2004). Gravitational radiation from inspiralling compact binaries completed at the third post-newtonian order. *Phys. Rev. Lett.*, **93**, 091101. DOI. ARXIV:gr-qc/0406012. (cited on pg. 53).
108. **Blanchet, L., T. Damour, and B. R. Iyer** (1995a). Gravitational waves from inspiralling compact binaries: Energy loss and wave form to second postNewtonian order. *Phys. Rev. D*, **51**, 5360. DOI. [Erratum: Phys.Rev.D 54, 1860 (1996)]. ARXIV:gr-qc/9501029. (cited on pg. 53).
109. **Blanchet, L., T. Damour, B. R. Iyer, C. M. Will, and A. G. Wiseman** (1995b). Gravitational radiation damping of compact binary systems to second postNewtonian order. *Phys. Rev. Lett.*, **74**, 3515–3518. DOI. ARXIV:gr-qc/9501027. (cited on pgs. 36 and 53).
110. **Blanchet, L., G. Faye, B. R. Iyer, and B. Joguet** (2002a). Gravitational-wave inspiral of compact binary systems to $7/2$ post-newtonian order. *Phys. Rev. D*, **65**, 061501(R). DOI. Erratum-ibid **71**, 129902(E) (2005). ARXIV:gr-qc/0105099. (cited on pg. 53).
111. **Blanchet, L., G. Faye, B. R. Iyer, and S. Sinha** (2008). The Third post-Newtonian gravitational wave polarisations and associated spherical harmonic modes for inspiralling compact binaries in quasi-circular orbits. *Class. Quant. Grav.*, **25**, 165003. DOI. [Erratum: Class. Quant. Grav. 29, 239501 (2012)]. ARXIV:0802.1249. (cited on pgs. 52 and 53).
112. **Blanchet, L., B. R. Iyer, and B. Joguet** (2002b). Gravitational waves from inspiralling compact binaries: Energy flux to third post-newtonian order. *Phys. Rev. D*, **65**, 064005. DOI. Erratum-ibid **71**, 129903(E) (2005). ARXIV:gr-qc/0105098. (cited on pg. 53).
113. **Blanchet, L., B. R. Iyer, C. M. Will, and A. G. Wiseman** (1996). Gravitational wave forms from inspiralling compact binaries to second postNewtonian order. *Class. Quant. Grav.*, **13**, 575–584. DOI. ARXIV:gr-qc/9602024. (cited on pg. 53).
114. **Blanchet, L. and B. S. Sathyaprakash** (1994). Signal analysis of gravitational wave tails. *Class. Quant. Grav.*, **11**, 2807–2832. DOI. (cited on pg. 31).
115. **Blanchet, L. and B. S. Sathyaprakash** (1995). Detecting the tail effect in gravitational wave experiments. *Phys. Rev. Lett.*, **74**, 1067–1070. DOI. (cited on pg. 31).
116. **Boetzel, Y., C. K. Mishra, G. Faye, A. Gopakumar, and B. R. Iyer** (2019). Gravitational-wave amplitudes for compact binaries in eccentric orbits at the third post-Newtonian order: Tail contributions and postadiabatic corrections. *Phys. Rev. D*, **100**(4), 044018. DOI. ARXIV:1904.11814. (cited on pg. 48).
117. **Bohe, A., S. Marsat, G. Faye, and L. Blanchet** (2013). Next-to-next-to-leading order spin-orbit effects in the near-zone metric and precession equations of compact binaries. *Class. Quant. Grav.*, **30**, 075017. DOI. ARXIV:1212.5520. (cited on pg. 53).

118. **Bondi, H.** (1957). Plane gravitational waves in general relativity. *Nature*, **179**, 1072–1073. DOI. (cited on pg. 3).
119. **Bonino, A. et al.** (2023). Inferring eccentricity evolution from observations of coalescing binary black holes. *Phys. Rev. D*, **107**(6), 064024. DOI. ARXIV:2207.10474. (cited on pg. 47).
120. **Bordé, C. J.** (1985). Méthodes optiques de détection des ondes gravitationnelles - Préface. *Annales de Physique*, **10**(3), R1–R2. DOI. (cited on pg. 6).
121. **Borelli, G. A.**, *Theoricae medicorum planetarum ex causis physicis deductae*. 1666. (cited on pg. 1).
122. **Borhanian, S.** (2021). GWBENCH: a novel Fisher information package for gravitational-wave benchmarking. *Class. Quant. Grav.*, **38**(17), 175014. DOI. ARXIV:2010.15202. (cited on pgs. 144 and 147).
123. **Borhanian, S., A. Dhani, A. Gupta, K. Arun, and B. Sathyaprakash** (2020). Dark Sirens to Resolve the Hubble–Lemaître Tension. *Astrophys. J. Lett.*, **905**, L28. DOI. ARXIV:2007.02883. (cited on pgs. 52 and 54).
124. **Borhanian, S. and B. S. Sathyaprakash** (2022). Listening to the Universe with Next Generation Ground-Based Gravitational-Wave Detectors. ARXIV:2202.11048. (cited on pg. 133).
125. **Bose, N. and A. Pai** (2021). Effective chirp mass in the inspiral frequency evolution of the nonspinning eccentric compact binary. *Phys. Rev. D*, **104**(12), 124021. DOI. ARXIV:2107.14736. (cited on pg. 78).
126. **Boulliau, I.**, *Ismaelis Bullialdi astronomia philolaica*. 1645. (cited on pg. 1).
127. **Boyle, M. et al.** (2019). The SXS Collaboration catalog of binary black hole simulations. *Class. Quant. Grav.*, **36**(19), 195006. DOI. ARXIV:1904.04831. (cited on pgs. 53 and 74).
128. **Braginskii, V. B.** (1966). Gravitational radiation and the prospect of its experimental discovery. *Soviet Physics Uspekhi*, **8**(4), 513. DOI. (cited on pg. 5).
129. **Breschi, M., R. O’Shaughnessy, J. Lange, and O. Birnholtz** (2019). IMR consistency tests with higher modes on gravitational signals from the second observing run of LIGO and Virgo. *Class. Quant. Grav.*, **36**(24), 245019. DOI. ARXIV:1903.05982. (cited on pg. 105).
130. **Brillet, A.** (1985). Interferometric gravitational wave antennae. *Annales de Physique*, **10**(3), 219–226. DOI. (cited on pg. 5).
131. **Brown, D. A., P. Kumar, and A. H. Nitz** (2013). Template banks to search for low-mass

- binary black holes in advanced gravitational-wave detectors. *Phys. Rev. D*, **87**, 082004. DOI. ARXIV:1211.6184. (cited on pg. 136).
132. **Brown, D. A. and P. J. Zimmerman** (2010). The Effect of Eccentricity on Searches for Gravitational-Waves from Coalescing Compact Binaries in Ground-based Detectors. *Phys. Rev. D*, **81**, 024007. DOI. ARXIV:0909.0066. (cited on pg. 45).
 133. **Brown, D. A. et al.** (2007). Prospects for detection of gravitational waves from intermediate-mass-ratio inspirals. *Phys. Rev. Lett.*, **99**, 201102. DOI. ARXIV:gr-qc/0612060. (cited on pg. 57).
 134. **Bruegmann, B. et al.** (2008). Calibration of Moving Puncture Simulations. *Phys. Rev. D*, **77**, 024027. DOI. ARXIV:gr-qc/0610128. (cited on pg. 53).
 135. **Buchman, L. T., H. P. Pfeiffer, M. A. Scheel, and B. Szilagyi** (2012). Simulations of non-equal mass black hole binaries with spectral methods. *Phys. Rev.*, **D86**, 084033. DOI. ARXIV:1206.3015. (cited on pg. 74).
 136. **Buikema, A. et al.** (2020). Sensitivity and performance of the Advanced LIGO detectors in the third observing run. *Phys. Rev. D*, **102**(6), 062003. DOI. ARXIV:2008.01301. (cited on pg. 18).
 137. **Buonanno, A., Y.-b. Chen, and M. Vallisneri** (2003). Detecting gravitational waves from precessing binaries of spinning compact objects: Adiabatic limit. *Phys. Rev. D*, **67**, 104025. DOI. [Erratum: *Phys.Rev.D* 74, 029904 (2006)]. ARXIV:gr-qc/0211087. (cited on pg. 65).
 138. **Buonanno, A. and T. Damour** (1999). Effective one-body approach to general relativistic two-body dynamics. *Phys. Rev. D*, **59**, 084006. DOI. ARXIV:gr-qc/9811091. (cited on pg. 53).
 139. **Buonanno, A. and T. Damour** (2000). Transition from inspiral to plunge in binary black hole coalescences. *Phys. Rev. D*, **62**, 064015. DOI. ARXIV:gr-qc/0001013. (cited on pg. 53).
 140. **Buonanno, A., G. Faye, and T. Hinderer** (2013). Spin effects on gravitational waves from inspiraling compact binaries at second post-Newtonian order. *Phys. Rev.*, **D87**(4), 044009. DOI. ARXIV:1209.6349. (cited on pgs. 53 and 56).
 141. **Buonanno, A., B. Iyer, E. Ochsner, Y. Pan, and B. S. Sathyaprakash** (2009). Comparison of post-Newtonian templates for compact binary inspiral signals in gravitational-wave detectors. *Phys. Rev. D*, **80**, 084043. DOI. ARXIV:0907.0700. (cited on pg. 72).
 142. **Calderón Bustillo, J., S. Husa, A. M. Sintes, and M. Pürrer** (2016). Impact of gravitational radiation higher order modes on single aligned-spin gravitational wave searches for binary black holes. *Phys. Rev. D*, **93**(8), 084019. DOI. ARXIV:1511.02060.

(cited on pgs. 52, 54, and 136).

143. **Calderón Bustillo, J., P. Laguna, and D. Shoemaker** (2017). Detectability of gravitational waves from binary black holes: Impact of precession and higher modes. *Phys. Rev. D*, **95**(10), 104038. DOI. ARXIV:1612.02340. (cited on pgs. 52 and 105).
144. **Callister, T., M. Fishbach, D. Holz, and W. Farr** (2020). Shouts and Murmurs: Combining Individual Gravitational-Wave Sources with the Stochastic Background to Measure the History of Binary Black Hole Mergers. *Astrophys. J. Lett.*, **896**(2), L32. DOI. ARXIV:2003.12152. (cited on pg. 30).
145. **Campanelli, M., C. O. Lousto, Y. Zlochower, and D. Merritt** (2007). Maximum gravitational recoil. *Phys. Rev. Lett.*, **98**, 231102. DOI. ARXIV:gr-qc/0702133. (cited on pg. 51).
146. **Cannon, K. et al.** (2021). GstLAL: A software framework for gravitational wave discovery. *SoftwareX*, **14**, 100680. ISSN 2352-7110. DOI. ARXIV:2010.05082. (cited on pg. 35).
147. **Cao, Z. and W.-B. Han** (2017). Waveform model for an eccentric binary black hole based on the effective-one-body-numerical-relativity formalism. *Phys. Rev. D*, **96**(4), 044028. DOI. ARXIV:1708.00166. (cited on pg. 48).
148. **Capano, C., Y. Pan, and A. Buonanno** (2014). Impact of higher harmonics in searching for gravitational waves from nonspinning binary black holes. *Phys. Rev. D*, **89**(10), 102003. DOI. ARXIV:1311.1286. (cited on pg. 136).
149. **Capano, C. D. and A. H. Nitz** (2020). Binary black hole spectroscopy: a no-hair test of GW190814 and GW190412. *Phys. Rev. D*, **102**(12), 124070. DOI. ARXIV:2008.02248. (cited on pg. 55).
150. **Cardoso, V., E. Franzin, and P. Pani** (2016a). Is the gravitational-wave ringdown a probe of the event horizon? *Phys. Rev. Lett.*, **116**(17), 171101. DOI. [Erratum: Phys.Rev.Lett. 117, 089902 (2016)]. ARXIV:1602.07309. (cited on pg. 32).
151. **Cardoso, V., S. Hopper, C. F. B. Macedo, C. Palenzuela, and P. Pani** (2016b). Gravitational-wave signatures of exotic compact objects and of quantum corrections at the horizon scale. *Phys. Rev.*, **D94**(8), 084031. DOI. (cited on pg. 32).
152. **Cardoso, V. and P. Pani** (2017). Tests for the existence of black holes through gravitational wave echoes. *Nature Astron.*, **1**(9), 586–591. DOI. ARXIV:1709.01525. (cited on pg. 32).
153. **Carter, B.** (1971). Axisymmetric Black Hole Has Only Two Degrees of Freedom. *Phys. Rev. Lett.*, **26**, 331–333. DOI. (cited on pgs. 32 and 33).
154. **Cervantes-Cota, J. L., S. Galindo-Uribarri, and G.-F. Smoot** (2016). A Brief History

of Gravitational Waves. *Universe*, **2**(3), 22. DOI. ARXIV:1609.09400. (cited on pgs. 3, 4, and 6).

155. **Chamberlain, K.** and **N. Yunes** (2017). Theoretical Physics Implications of Gravitational Wave Observation with Future Detectors. *Phys. Rev. D*, **96**(8), 084039. DOI. ARXIV:1704.08268. (cited on pgs. 21, 136, and 147).
156. **Chattaraj, A., T. RoyChowdhury, Divyajyoti, C. K. Mishra, and A. Gupta** (2022). High accuracy post-Newtonian and numerical relativity comparisons involving higher modes for eccentric binary black holes and a dominant mode eccentric inspiral-merger-ringdown model. *Phys. Rev. D*, **106**(12), 124008. DOI. ARXIV:2204.02377. (cited on pgs. vii, viii, xiii, 48, 60, 71, 72, 74, 75, 95, and 96).
157. **Chatterji, S., L. Blackburn, G. Martin, and E. Katsavounidis** (2004). Multiresolution techniques for the detection of gravitational-wave bursts. *Class. Quant. Grav.*, **21**, S1809–S1818. DOI. ARXIV:gr-qc/0412119. (cited on pgs. 8 and 41).
158. **Chatziioannou, K., E. Poisson, and N. Yunes** (2016). Improved next-to-leading order tidal heating and torquing of a Kerr black hole. *Phys. Rev. D*, **94**(8), 084043. DOI. ARXIV:1608.02899. (cited on pg. 55).
159. **Chatziioannou, K. et al.** (2019). On the properties of the massive binary black hole merger GW170729. *Phys. Rev. D*, **100**(10), 104015. DOI. ARXIV:1903.06742. (cited on pgs. 52 and 133).
160. **Cheeseboro, B. D. and P. T. Baker** (2021). Method for detecting highly eccentric binaries with a gravitational wave burst search. *Phys. Rev. D*, **104**(10), 104016. DOI. ARXIV:2108.01050. (cited on pg. 46).
161. **Chen, Z. et al.** (2021). Observation of eccentric binary black hole mergers with second and third generation gravitational wave detector networks. *Phys. Rev. D*, **103**(8), 084018. DOI. ARXIV:2008.03313. (cited on pg. 46).
162. **Chia, H. S. et al.** (2022). Dimensionally Reduced Waveforms for Spin-Induced Quadrupole Searches. ARXIV:2211.00039. (cited on pg. 57).
163. **Chiarangelo, D. and A. Nagar** (2020). Faithful analytical effective-one-body waveform model for spin-aligned, moderately eccentric, coalescing black hole binaries. *Phys. Rev. D*, **101**(10), 101501. DOI. ARXIV:2001.11736. (cited on pgs. xxi, 48, and 71).
164. **Christensen, N.** (2019). Stochastic Gravitational Wave Backgrounds. *Rept. Prog. Phys.*, **82**(1), 016903. DOI. ARXIV:1811.08797. (cited on pg. 30).
165. **Christensen, N. and R. Meyer** (1998). Markov chain Monte Carlo methods for Bayesian gravitational radiation data analysis. *Phys. Rev. D*, **58**, 082001. DOI. (cited on pg. 40).
166. **Christensen, N. and R. Meyer** (2001). Using Markov chain Monte Carlo methods for

- estimating parameters with gravitational radiation data. *Phys. Rev. D*, **64**, 022001. DOI. ARXIV:gr-qc/0102018. (cited on pg. 40).
167. **Chu, Q. et al.** (2022). SPIIR online coherent pipeline to search for gravitational waves from compact binary coalescences. *Phys. Rev. D*, **105**(2), 024023. DOI. ARXIV:2011.06787. (cited on pg. 35).
 168. **Chu, T., H. P. Pfeiffer, and M. A. Scheel** (2009). High accuracy simulations of black hole binaries: Spins anti-aligned with the orbital angular momentum. *Phys. Rev.*, **D80**, 124051. DOI. ARXIV:0909.1313. (cited on pg. 74).
 169. **Chu, T. et al.** (2016). On the accuracy and precision of numerical waveforms: Effect of waveform extraction methodology. *Class. Quant. Grav.*, **33**(16), 165001. DOI. ARXIV:1512.06800. (cited on pg. 74).
 170. **Cokelaer, T. and D. Pathak** (2009). Searching for gravitational-wave signals emitted by eccentric compact binaries using a non-eccentric template bank: Implications for ground-based detectors. *Class. Quant. Grav.*, **26**, 045013. DOI. ARXIV:0903.4791. (cited on pg. 46).
 171. **Collins, H.** (1976). Kafka referees Weiss’s proposal. URL: <http://sites.cardiff.ac.uk/harrycollins/webquote/>. (cited on pg. 5).
 172. **Collins, H.**, *Chapter 30. Moving People: From Small Science to Big Science*. University of Chicago Press, Chicago, 2004. ISBN 9780226113791, 546–557. DOI. URL: <https://doi.org/10.7208/9780226113791-034>. (cited on pg. 6).
 173. **Collins, H. and R. W. P. Drever** (2005). Gravity’s Shadow: The Search for Gravitational Waves. *Physics Today*, **58**(12), 62. DOI. (cited on pg. 5).
 174. **Collins, H. M.** (2003). Ligo becomes big science. *Historical Studies in the Physical and Biological Sciences*, **33**(2), 261–297. ISSN 08909997. URL: <http://www.jstor.org/stable/10.1525/hsp.2003.33.2.261>. (cited on pg. 6).
 175. **Cornish, N. J.** (2010). Fast Fisher Matrices and Lazy Likelihoods. ARXIV:1007.4820. (cited on pg. 40).
 176. **Cornish, N. J. and T. B. Littenberg** (2015). BayesWave: Bayesian Inference for Gravitational Wave Bursts and Instrument Glitches. *Class. Quant. Grav.*, **32**(13), 135012. DOI. ARXIV:1410.3835. (cited on pgs. 40 and 41).
 177. **Cornish, N. J. and K. Shuman** (2020). Black Hole Hunting with LISA. *Phys. Rev. D*, **101**(12), 124008. DOI. ARXIV:2005.03610. (cited on pg. 40).
 178. **Cotesta, R., A. Buonanno, A. Bohé, A. Taracchini, I. Hinder, and S. Ossokine** (2018). Enriching the Symphony of Gravitational Waves from Binary Black Holes by Tuning Higher Harmonics. *Phys. Rev. D*, **98**(8), 084028. DOI. ARXIV:1803.10701. (cited on

pg. 53).

179. **Cotesta, R., S. Marsat, and M. Pürrer** (2020). Frequency domain reduced order model of aligned-spin effective-one-body waveforms with higher-order modes. *Phys. Rev. D*, **101**(12), 124040. DOI. ARXIV:2003.12079. (cited on pg. 53).
180. **Coughlin, M., P. Meyers, S. Kandhasamy, E. Thrane, and N. Christensen** (2015). Prospects for searches for long-duration gravitational-waves without time slides. *Phys. Rev. D*, **92**(4), 043007. DOI. ARXIV:1505.00205. (cited on pg. 47).
181. **Cunningham, C. T., R. H. Price, and V. Moncrief** (1978). Radiation from collapsing relativistic stars. I - Linearized odd-parity radiation. *Astrophys. J.*, **224**, 643. DOI. (cited on pg. 32).
182. **Cuoco, E. et al.** (2001). On line power spectra identification and whitening for the noise in interferometric gravitational wave detectors. *Class. Quant. Grav.*, **18**, 1727–1752. DOI. ARXIV:gr-qc/0011041. (cited on pg. 37).
183. **Cutler, C. and E. E. Flanagan** (1994). Gravitational waves from merging compact binaries: How accurately can one extract the binary’s parameters from the inspiral wave form? *Phys. Rev. D*, **49**, 2658–2697. DOI. ARXIV:gr-qc/9402014. (cited on pg. 34).
184. **Cutler, C. et al.** (1993). The Last three minutes: issues in gravitational wave measurements of coalescing compact binaries. *Phys. Rev. Lett.*, **70**, 2984–2987. DOI. ARXIV:astro-ph/9208005. (cited on pgs. 34 and 49).
185. **Dal Canton, T. et al.** (2014). Implementing a search for aligned-spin neutron star-black hole systems with advanced ground based gravitational wave detectors. *Phys. Rev. D*, **90**(8), 082004. DOI. ARXIV:1405.6731. (cited on pg. 35).
186. **Damour, T.** (2001). Coalescence of two spinning black holes: an effective one-body approach. *Phys. Rev. D*, **64**, 124013. DOI. ARXIV:gr-qc/0103018. (cited on pg. 53).
187. **Damour, T., B. R. Iyer, and B. S. Sathyaprakash** (2002). A Comparison of search templates for gravitational waves from binary inspiral - 3.5PN update. *Phys. Rev. D*, **66**, 027502. DOI. ARXIV:gr-qc/0207021. (cited on pg. 72).
188. **Damour, T., P. Jaranowski, and G. Schaefer** (2000). On the determination of the last stable orbit for circular general relativistic binaries at the third postNewtonian approximation. *Phys. Rev. D*, **62**, 084011. DOI. ARXIV:gr-qc/0005034. (cited on pg. 53).
189. **Damour, T., P. Jaranowski, and G. Schäfer** (2015). Fourth post-Newtonian effective one-body dynamics. *Phys. Rev. D*, **91**(8), 084024. DOI. ARXIV:1502.07245. (cited on pg. 53).

190. **Danielsson, U., L. Lehner, and F. Pretorius** (2021). Dynamics and observational signatures of shell-like black hole mimickers. *Phys. Rev. D*, **104**(12), 124011. DOI. ARXIV:2109.09814. (cited on pg. 32).
191. **Datta, S. and S. Bose** (2019). Probing the nature of central objects in extreme-mass-ratio inspirals with gravitational waves. *Phys. Rev. D*, **99**(8), 084001. DOI. ARXIV:1902.01723. (cited on pg. 55).
192. **Datta, S., K. S. Phukon, and S. Bose** (2021). Recognizing black holes in gravitational-wave observations: Challenges in telling apart impostors in mass-gap binaries. *Phys. Rev. D*, **104**(8), 084006. DOI. ARXIV:2004.05974. (cited on pg. 55).
193. **Davies, G. S., T. Dent, M. Tápai, I. Harry, C. McIsaac, and A. H. Nitz** (2020). Extending the PyCBC search for gravitational waves from compact binary mergers to a global network. *Phys. Rev. D*, **102**(2), 022004. DOI. ARXIV:2002.08291. (cited on pg. 35).
194. **De Greve, J. P. and C. De Loore** (1992). Evolution of massive close binaries. *A&AS*, **96**(3), 653–663. (cited on pg. 51).
195. **De Sabbata, V. and J. Weber**, Topics in theoretical and experimental gravitation physics. volume 27. 1977. DOI. Proceedings: International School of Cosmology and Gravitation, Erice, Sicily, Mar 13-25 1975. (cited on pg. 5).
196. **Denson Hill, C. and P. Nurowski** (2016). How the green light was given for gravitational wave search. ARXIV:1608.08673. (cited on pg. 2).
197. **Dhanpal, S., A. Ghosh, A. K. Mehta, P. Ajith, and B. Sathyaprakash** (2019). A no-hair test for binary black holes. *Phys. Rev. D*, **99**(10), 104056. DOI. ARXIV:1804.03297. (cited on pg. 55).
198. **Dhurkunde, R. and A. H. Nitz** (2022). Sensitivity of spin-aligned searches for neutron star-black hole systems using future detectors. *Phys. Rev. D*, **106**(10), 103035. DOI. ARXIV:2207.14645. (cited on pg. 65).
199. **Di Carlo, U. N. et al.** (2019). Merging black holes in young star clusters. *Mon. Not. Roy. Astron. Soc.*, **487**(2), 2947–2960. DOI. ARXIV:1901.00863. (cited on pg. 44).
200. **Divyajyoti, P. Baxi, C. K. Mishra, and K. G. Arun** (2021). Detectability of gravitational higher order modes in the third-generation era. *Phys. Rev. D*, **104**(8), 084080. DOI. ARXIV:2103.03241. (cited on pgs. vii, ix, x, 21, and 61).
201. **Divyajyoti, N. V. Krishnendu, M. Saleem, M. Colleoni, A. Vijaykumar, K. G. Arun, and C. K. Mishra** (2024a). Effect of double spin-precession and higher harmonics on spin-induced quadrupole moment measurements. *Phys. Rev. D*, **109**(2), 023016. DOI. ARXIV:2311.05506. (cited on pgs. vii, ix, and 61).

202. **Divyajyoti, S. Kumar, S. Tibrewal, I. M. Romero-Shaw, and C. K. Mishra** (2024*b*). Blind spots and biases: The dangers of ignoring eccentricity in gravitational-wave signals from binary black holes. *Phys. Rev. D*, **109**(4), 043037. DOI. ARXIV:2309.16638. (cited on pgs. vii, viii, and 60).
203. **Dominik, M. et al.** (2012). Double Compact Objects I: The Significance of the Common Envelope on Merger Rates. *Astrophys. J.*, **759**, 52. DOI. ARXIV:1202.4901. (cited on pg. 51).
204. **Dominik, M. et al.** (2013). Double Compact Objects II: Cosmological Merger Rates. *Astrophys. J.*, **779**, 72. DOI. ARXIV:1308.1546. (cited on pg. 51).
205. **Douglass, D. H., R. Q. Gram, J. A. Tyson, and R. W. Lee** (1975). Two Detector Coincidence Search for Bursts of Gravitational Radiation. *Phys. Rev. Lett.*, **35**, 480–483. DOI. (cited on pg. 5).
206. **Downing, J. M. B., M. J. Benacquista, M. Giersz, and R. Spurzem** (2010). Compact binaries in star clusters - I. Black hole binaries inside globular clusters. *MNRAS*, **407**(3), 1946–1962. DOI. ARXIV:0910.0546. (cited on pg. 44).
207. **Drever, R. W. P., J. Hough, R. Bland, and G. W. Lessnoff** (1973). Search for short bursts of gravitational radiation. *Nature*, **246**, 340–344. DOI. (cited on pg. 5).
208. **Dreyer, O. et al.** (2004). Black hole spectroscopy: Testing general relativity through gravitational wave observations. *Classical Quantum Gravity*, **21**, 787–804. DOI. ARXIV:gr-qc/0309007. (cited on pg. 32).
209. **Drummond, L.** (2018). URL: <https://astrobites.org/2018/01/29/hunting-for-gravitational-waves-from-spinning-neutron-stars/>. (cited on pg. 10).
210. **Eardley, D. M., D. L. Lee, and A. P. Lightman** (1973*a*). Gravitational-wave observations as a tool for testing relativistic gravity. *Phys. Rev. D*, **8**, 3308–3321. DOI. (cited on pg. 32).
211. **Eardley, D. M., D. L. Lee, A. P. Lightman, R. V. Wagoner, and C. M. Will** (1973*b*). Gravitational-wave observations as a tool for testing relativistic gravity. *Phys. Rev. Lett.*, **30**, 884–886. DOI. (cited on pg. 32).
212. **Ebersold, M., Y. Boetzel, G. Faye, C. K. Mishra, B. R. Iyer, and P. Jetzer** (2019). Gravitational-wave amplitudes for compact binaries in eccentric orbits at the third post-Newtonian order: Memory contributions. *Phys. Rev. D*, **100**(8), 084043. DOI. ARXIV:1906.06263. (cited on pg. 48).
213. **Eddington, A. S.** (1922). The propagation of gravitational waves. *Proc. Roy. Soc. Lond. A*, **102**, 268–282. DOI. (cited on pg. 3).

214. **EGO Consortium** (2003). Ondes gravitationnelles inauguration du détecteur franco-italien virgo. URL: <https://archive.wikiwix.com/cache/index2.php?url=http%3A%2F%2Fwww2.cnrs.fr%2Fpresse%2Fcommuniqu%2F206.htm%3F%26debut%3D400#federation=archive.wikiwix.com&tab=url>. (cited on pg. 7).
215. **Einstein, A.** (1916). The foundation of the general theory of relativity. *Annalen Phys.*, **49**(7), 769–822. DOI. (cited on pg. 1).
216. **Einstein, A.** and **N. Rosen** (1937). On Gravitational Waves. *Journal of The Franklin Institute*, **223**, 43–54. DOI. (cited on pg. 3).
217. **Endal, A. S.** and **S. Sofia** (1977). Detectable Gravitational Radiation from Stellar Collapse. *Phys. Rev. Lett.*, **39**, 1429–1432. DOI. (cited on pg. 5).
218. **ET Science Team** (2011). Einstein gravitational wave telescope conceptual design study. <https://apps.et-gw.eu/tds/?content=3&r=8709>. (cited on pg. 20).
219. **Evans, M. et al.** (2021). A Horizon Study for Cosmic Explorer: Science, Observatories, and Community. ARXIV:2109.09882. (cited on pg. 20).
220. **Fairhurst, S., R. Green, M. Hannam, and C. Hoy** (2020a). When will we observe binary black holes precessing? *Phys. Rev. D*, **102**(4), 041302. DOI. ARXIV:1908.00555. (cited on pg. 60).
221. **Fairhurst, S., R. Green, C. Hoy, M. Hannam, and A. Muir** (2020b). Two-harmonic approximation for gravitational waveforms from precessing binaries. *Phys. Rev. D*, **102**(2), 024055. DOI. ARXIV:1908.05707. (cited on pg. 60).
222. **Farr, B., D. E. Holz, and W. M. Farr** (2018). Using Spin to Understand the Formation of LIGO and Virgo’s Black Holes. *Astrophys. J. Lett.*, **854**(1), L9. DOI. ARXIV:1709.07896. (cited on pg. 51).
223. **Favata, M.** (2014). Systematic parameter errors in inspiraling neutron star binaries. *Phys. Rev. Lett.*, **112**, 101101. DOI. ARXIV:1310.8288. (cited on pg. 45).
224. **Favata, M., C. Kim, K. G. Arun, J. Kim, and H. W. Lee** (2022). Constraining the orbital eccentricity of inspiralling compact binary systems with Advanced LIGO. *Phys. Rev. D*, **105**(2), 023003. DOI. ARXIV:2108.05861. (cited on pgs. 45, 77, 78, and 104).
225. **Ferguson, D. et al.** (2023). Second MAYA Catalog of Binary Black Hole Numerical Relativity Waveforms. ARXIV:2309.00262. (cited on pg. 53).
226. **Feynman, R. P.** (1961). Unpublished letter to Victor F. Weisskopf, January 4–February 11, 1961. URL: <http://www.oac.cdlib.org/findaid/ark:/13030/kt5n39p6k0/dsc/?query=letter>. In Box 3 File 8 of The Papers of Richard P. Feynman, the Archives, California Institute of Technology. (cited on pg. 3).

227. **Finn, L. S.** (1992). Detection, measurement and gravitational radiation. *Phys. Rev. D*, **46**, 5236–5249. DOI. ARXIV:gr-qc/9209010. (cited on pg. 39).
228. **Finn, L. S.** and **D. F. Chernoff** (1993). Observing binary inspiral in gravitational radiation: One interferometer. *Phys. Rev. D*, **47**, 2198–2219. DOI. ARXIV:gr-qc/9301003. (cited on pg. 36).
229. **Fishbach, M., R. Essick,** and **D. E. Holz** (2020). Does Matter Matter? Using the mass distribution to distinguish neutron stars and black holes. *Astrophys. J. Lett.*, **899**, L8. DOI. ARXIV:2006.13178. (cited on pg. 30).
230. **Forward, R. L.** (1978). Wide Band Laser Interferometer Gravitational Radiation Experiment. *Phys. Rev. D*, **17**, 379–390. DOI. (cited on pg. 5).
231. **Foucart, F. et al.** (2021). High-accuracy waveforms for black hole-neutron star systems with spinning black holes. *Phys. Rev. D*, **103**(6), 064007. DOI. ARXIV:2010.14518. (cited on pg. 53).
232. **Fragione, G.** and **B. Kocsis** (2018). Black hole mergers from an evolving population of globular clusters. *Phys. Rev. Lett.*, **121**(16), 161103. DOI. ARXIV:1806.02351. (cited on pg. 51).
233. **Fragione, G.** and **B. Kocsis** (2020). Effective spin distribution of black hole mergers in triples. *Mon. Not. Roy. Astron. Soc.*, **493**(3), 3920–3931. DOI. ARXIV:1910.00407. (cited on pg. 51).
234. **Fragione, G., A. Loeb,** and **F. A. Rasio** (2020). Merging Black Holes in the Low-mass and High-mass Gaps from 2 + 2 Quadruple Systems. *Astrophys. J. Lett.*, **895**(1), L15. DOI. ARXIV:2002.11278. (cited on pg. 51).
235. **Gabbard, H. et al.** (2022). Bayesian parameter estimation using conditional variational autoencoders for gravitational-wave astronomy. *Nature Phys.*, **18**(1), 112–117. DOI. ARXIV:1909.06296. (cited on pg. 40).
236. **Gamba, R. et al.** (2023). GW190521 as a dynamical capture of two nonspinning black holes. *Nature Astron.*, **7**(1), 11–17. DOI. ARXIV:2106.05575. (cited on pgs. 44 and 47).
237. **García-Quirós, C. et al.** (2020). Multimode frequency-domain model for the gravitational wave signal from nonprecessing black-hole binaries. *Phys. Rev. D*, **102**(6), 064002. DOI. ARXIV:2001.10914. (cited on pgs. xxi, 53, 58, 59, 95, 106, and 107).
238. **Gayathri, V. et al.** (2022). Eccentricity estimate for black hole mergers with numerical relativity simulations. *Nature Astron.*, **6**(3), 344–349. DOI. ARXIV:2009.05461. (cited on pgs. 44 and 47).
239. **George, D.** and **E. A. Huerta** (2018). Deep Learning for Real-time Gravitational Wave

- Detection and Parameter Estimation: Results with Advanced LIGO Data. *Phys. Lett. B*, **778**, 64–70. DOI. ARXIV:1711.03121. (cited on pg. 40).
240. **Gerosa, D. et al.** (2018). Spin orientations of merging black holes formed from the evolution of stellar binaries. *Phys. Rev. D*, **98**(8), 084036. DOI. ARXIV:1808.02491. (cited on pg. 51).
 241. **Gertsenshtein, M. E. and V. I. Pustovoit** (1962). On the Detection of Low Frequency Gravitational Waves. *Sov. Phys. JETP*, **16**, 433. (cited on pg. 5).
 242. **Ghonge, S. et al.** (2020). Reconstructing gravitational wave signals from binary black hole mergers with minimal assumptions. *Phys. Rev. D*, **102**(6), 064056. DOI. ARXIV:2003.09456. (cited on pg. 54).
 243. **Ghosh, A. et al.** (2016). Testing general relativity using golden black-hole binaries. *Phys. Rev. D*, **94**(2), 021101. DOI. ARXIV:1602.02453. (cited on pg. 31).
 244. **Ghosh, A. et al.** (2018). Testing general relativity using gravitational wave signals from the inspiral, merger and ringdown of binary black holes. *Class. Quant. Grav.*, **35**(1), 014002. DOI. ARXIV:1704.06784. (cited on pg. 31).
 245. **Giffard, R. P.** (1976). Ultimate Sensitivity Limit of a Resonant Gravitational Wave Antenna Using a Linear Motion Detector. *Phys. Rev. D*, **14**, 2478–2486. DOI. (cited on pg. 5).
 246. **Giudice, G. F., M. McCullough, and A. Urbano** (2016). Hunting for Dark Particles with Gravitational Waves. *JCAP*, **10**, 001. DOI. ARXIV:1605.01209 [hep-ph]. (cited on pg. 32).
 247. **Goldberg, J., A. MacFarlane, E. Newman, F. Rohrlich, and E. Sudarshan** (1967). Spin-s spherical harmonics and δ . *J. Math. Phys.*, **8**, 2155. DOI. (cited on pg. 52).
 248. **Goldberger, W. D. and I. Z. Rothstein** (2006). An Effective field theory of gravity for extended objects. *Phys. Rev. D*, **73**, 104029. DOI. ARXIV:hep-th/0409156. (cited on pg. 53).
 249. **Gonzalez, J. A., M. D. Hannam, U. Sperhake, B. Bruegmann, and S. Husa** (2007a). Supermassive recoil velocities for binary black-hole mergers with antialigned spins. *Phys. Rev. Lett.*, **98**, 231101. DOI. ARXIV:gr-qc/0702052. (cited on pg. 51).
 250. **Gonzalez, J. A., U. Sperhake, B. Bruegmann, M. Hannam, and S. Husa** (2007b). Total recoil: The Maximum kick from nonspinning black-hole binary inspiral. *Phys. Rev. Lett.*, **98**, 091101. DOI. ARXIV:gr-qc/0610154. (cited on pg. 51).
 251. **Graff, P. B., A. Buonanno, and B. S. Sathyaprakash** (2015). Missing Link: Bayesian detection and measurement of intermediate-mass black-hole binaries. *Phys. Rev. D*, **92**(2), 022002. DOI. ARXIV:1504.04766. (cited on pg. 52).

252. **Grote, H.** (2010). The GEO 600 status. *Class. Quant. Grav.*, **27**, 084003. DOI. (cited on pg. 18).
253. **Guo, W. et al.** (2022). Mimicking mergers: mistaking black hole captures as mergers. *Mon. Not. Roy. Astron. Soc.*, **516**(3), 3847–3860. DOI. ARXIV:2203.06969. (cited on pg. 45).
254. **Gürlebeck, N.** (2015). No-hair theorem for Black Holes in Astrophysical Environments. *Phys. Rev. Lett.*, **114**(15), 151102. DOI. ARXIV:1503.03240. (cited on pgs. 32, 33, and 55).
255. **Hamers, A. S.** (2020). Secular dynamics of hierarchical multiple systems composed of nested binaries, with an arbitrary number of bodies and arbitrary hierarchical structure – III. Suborbital effects: hybrid integration techniques and orbit-averaging corrections. *Mon. Not. Roy. Astron. Soc.*, **494**(4), 5492–5506. DOI. ARXIV:2004.08327. (cited on pg. 51).
256. **Hamers, A. S.** and **M. Safarzadeh** (2020). Was GW190412 Born from a Hierarchical 3 + 1 Quadruple Configuration? *Astrophys. J.*, **898**(2), 99. DOI. ARXIV:2005.03045. (cited on pg. 51).
257. **Hanna, C. et al.** (2020). Fast evaluation of multidetector consistency for real-time gravitational wave searches. *Phys. Rev. D*, **101**(2), 022003. DOI. ARXIV:1901.02227. (cited on pg. 35).
258. **Hannam, M., D. A. Brown, S. Fairhurst, C. L. Fryer, and I. W. Harry** (2013). When can gravitational-wave observations distinguish between black holes and neutron stars? *Astrophys. J. Lett.*, **766**, L14. DOI. ARXIV:1301.5616. (cited on pg. 54).
259. **Hannam, M. et al.** (2014). Simple Model of Complete Precessing Black-Hole-Binary Gravitational Waveforms. *Phys. Rev. Lett.*, **113**(15), 151101. DOI. ARXIV:1308.3271. (cited on pgs. xxi, 49, 58, and 106).
260. **Hansen, R. O.** (1974). Multipole moments of stationary space-times. *J. Math. Phys.*, **15**, 46–52. DOI. (cited on pgs. 32 and 33).
261. **Harms, J. et al.** (2021). Lunar Gravitational-wave Antenna. *Astrophys. J.*, **910**(1), 1. DOI. ARXIV:2010.13726. (cited on pg. 22).
262. **Harry, G. M., P. Fritschel, D. A. Shaddock, W. Folkner, and E. S. Phinney** (2006). Laser interferometry for the big bang observer. *Class. Quant. Grav.*, **23**, 4887–4894. DOI. [Erratum: *Class.Quant.Grav.* 23, 7361 (2006)]. (cited on pg. 22).
263. **Harry, I. W., B. Allen, and B. S. Sathyaprakash** (2009). A Stochastic template placement algorithm for gravitational wave data analysis. *Phys. Rev. D*, **80**, 104014. DOI. ARXIV:0908.2090. (cited on pg. 66).

264. **Hartle, J. B.** (1973). Tidal friction in slowly rotating black holes. *Phys. Rev. D*, **8**, 1010–1024. DOI. (cited on pg. 55).
265. **Hastings, W. K.** (1970). Monte Carlo Sampling Methods Using Markov Chains and Their Applications. *Biometrika*, **57**, 97–109. DOI. (cited on pg. 42).
266. **Healy, J., C. O. Lousto, Y. Zlochower, and M. Campanelli** (2017). The RIT binary black hole simulations catalog. *Class. Quant. Grav.*, **34**(22), 224001. DOI. ARXIV:1703.03423. (cited on pg. 53).
267. **Hegde, R., N. Bose, and A. Pai** (2023). Probing eccentric higher order modes through effective chirp mass model. ARXIV:2310.13662. (cited on pg. 60).
268. **Heilbron, J. L.**, *Electricity in the 17th and 18th Centuries*. University of California Press, Berkeley, 1979. ISBN 9780520334601. URL: <https://doi.org/10.1525/9780520334601>. (cited on pg. 1).
269. **Helström, C.**, *Statistical Theory of Signal Detection*, volume 9 of *International Series of Monographs in Electronics and Instrumentation*. Pergamon Press, Oxford, U.K., New York, U.S.A., 1968, 2nd edition. (cited on pg. 33).
270. **Hemberger, D. A. et al.** (2013). Final spin and radiated energy in numerical simulations of binary black holes with equal masses and equal, aligned or anti-aligned spins. *Phys. Rev.*, **D88**, 064014. DOI. ARXIV:1305.5991. (cited on pg. 74).
271. **Henry, Q. and M. Khalil** (2023). Spin effects in gravitational waveforms and fluxes for binaries on eccentric orbits to the third post-Newtonian order. *Phys. Rev. D*, **108**(10), 104016. DOI. ARXIV:2308.13606. (cited on pg. 48).
272. **Henry, Q., S. Marsat, and M. Khalil** (2022). Spin contributions to the gravitational-waveform modes for spin-aligned binaries at the 3.5PN order. *Phys. Rev. D*, **106**(12), 124018. DOI. ARXIV:2209.00374. (cited on pg. 56).
273. **Hild, S. et al.** (2011). Sensitivity Studies for Third-Generation Gravitational Wave Observatories. *Class. Quant. Grav.*, **28**, 094013. DOI. ARXIV:1012.0908. (cited on pg. 20).
274. **Hinder, I., L. E. Kidder, and H. P. Pfeiffer** (2018). Eccentric binary black hole inspiral-merger-ringdown gravitational waveform model from numerical relativity and post-Newtonian theory. *Phys. Rev. D*, **98**(4), 044015. DOI. ARXIV:1709.02007. (cited on pgs. 48 and 71).
275. **Hinder, I. et al.** (2014). Error-analysis and comparison to analytical models of numerical waveforms produced by the NRAR Collaboration. *Class. Quant. Grav.*, **31**, 025012. DOI. ARXIV:1307.5307. (cited on pgs. 53 and 74).

276. **Hirakawa, H.** and **K. Narihara** (1975). Search for Gravitational Radiation at 145-Hz. *Phys. Rev. Lett.*, **35**, 330–334. DOI. [Erratum: Phys.Rev.Lett. 35, 890 (1975)]. (cited on pg. 5).
277. **Hogg, D. W.** and **D. Foreman-Mackey** (2018). Data analysis recipes: Using Markov Chain Monte Carlo. *Astrophys. J. Suppl.*, **236**(1), 11. DOI. ARXIV:1710.06068. (cited on pg. 42).
278. **Hooke, R.** (1674). An attempt to prove the motion of the earth from observations. *Philosophical Transactions of the Royal Society*, **9**(101), 12–20. DOI. Printed for J. Martyn at the bell in St. Pauls Church yard, 1674. (cited on pg. 1).
279. **Hough, J., J. R. Pugh, R. Bland,** and **R. W. P. Drever** (1975). Search for continuous gravitational radiation. *Nature*, **254**(5500), 498–501. DOI. (cited on pg. 5).
280. **Hough, J. et al.** (1986). A British long baseline gravitational wave observatory. *Rutherford Appleton Laboratory Report*, **1**. (cited on pg. 5).
281. **Hough, J. et al.** (1989). Proposal for a joint German-British interferometric gravitational wave detector. URL: <https://eprints.gla.ac.uk/114852/7/114852.pdf>. (cited on pg. 5).
282. **Huerta, E. A., P. Kumar, S. T. McWilliams, R. O’Shaughnessy,** and **N. Yunes** (2014). Accurate and efficient waveforms for compact binaries on eccentric orbits. *Phys. Rev. D*, **90**(8), 084016. DOI. ARXIV:1408.3406. (cited on pgs. xxi and 66).
283. **Huerta, E. A. et al.** (2018). Eccentric, nonspinning, inspiral, Gaussian-process merger approximant for the detection and characterization of eccentric binary black hole mergers. *Phys. Rev. D*, **97**(2), 024031. DOI. ARXIV:1711.06276. (cited on pgs. xxi, 48, 58, and 59).
284. **Husa, S. et al.** (2016). Frequency-domain gravitational waves from nonprecessing black-hole binaries. I. New numerical waveforms and anatomy of the signal. *Phys. Rev. D*, **93**(4), 044006. DOI. ARXIV:1508.07250. (cited on pgs. 58 and 66).
285. **Iglesias, H. L. et al.** (2022). Eccentricity estimation for five binary black hole mergers with higher-order gravitational wave modes. ARXIV:2208.01766. (cited on pgs. 44, 47, 48, and 60).
286. **IPTA** (2016). International Pulsar Timing Array Collaboration. URL: <https://ipta4gw.org/>. (cited on pgs. 13 and 20).
287. **Isi, M., W. M. Farr,** and **K. Chatziioannou** (2022). Comparing Bayes factors and hierarchical inference for testing general relativity with gravitational waves. *Phys. Rev. D*, **106**(2), 024048. DOI. ARXIV:2204.10742. (cited on pg. 39).
288. **Islam, T.** (2021). Applying higher-modes consistency test on GW190814 : lessons on

no-hair theorem, nature of the secondary compact object and waveform modeling. ARXIV:2111.00111. (cited on pg. 105).

289. **Islam, T., A. K. Mehta, A. Ghosh, V. Varma, P. Ajith, and B. Sathyaprakash** (2020). Testing the no-hair nature of binary black holes using the consistency of multipolar gravitational radiation. *Phys. Rev. D*, **101**(2), 024032. DOI. ARXIV:1910.14259. (cited on pg. 55).
290. **Islam, T. et al.** (2021). Eccentric binary black hole surrogate models for the gravitational waveform and remnant properties: Comparable mass, nonspinning case. *Phys. Rev. D*, **103**(6), 064022. DOI. ARXIV:2101.11798. (cited on pgs. 48 and 74).
291. **Jani, K., J. Healy, J. A. Clark, L. London, P. Laguna, and D. Shoemaker** (2016). Georgia Tech Catalog of Gravitational Waveforms. *Class. Quant. Grav.*, **33**(20), 204001. DOI. ARXIV:1605.03204. (cited on pg. 53).
292. **Jiménez Forteza, X., T. Abdelsalhin, P. Pani, and L. Gualtieri** (2018). Impact of high-order tidal terms on binary neutron-star waveforms. *Phys. Rev. D*, **98**(12), 124014. DOI. ARXIV:1807.08016. (cited on pg. 55).
293. **Johnson-Mcdaniel, N. K. et al.** (2020). Constraining black hole mimickers with gravitational wave observations. *Phys. Rev. D*, **102**, 123010. DOI. ARXIV:1804.08026. (cited on pg. 55).
294. **Kafka, P.** (1972). Are Weber’s pulses illegal. *Gravity Research Foundation*. URL: <https://static1.squarespace.com/static/5852e579be659442a01f27b8/t/5873cf113e00be217570425b/1483984659960/kafka.pdf>. (cited on pg. 4).
295. **Kafka, R. and L. Schnupp** (1978). Final Result of the Munich-Frascati Gravitational Radiation Experiment. *A&A*, **70**, 97. (cited on pg. 5).
296. **Kalaghatgi, C., M. Hannam, and V. Raymond** (2020). Parameter estimation with a spinning multimode waveform model. *Phys. Rev. D*, **101**(10), 103004. DOI. ARXIV:1909.10010. (cited on pgs. 52 and 54).
297. **Kalogera, V., K. Belczynski, C. Kim, R. W. O’Shaughnessy, and B. Willems** (2007). Formation of Double Compact Objects. *Phys. Rept.*, **442**, 75–108. DOI. ARXIV:astro-ph/0612144. (cited on pg. 51).
298. **Kapadia, S. J., M. K. Singh, M. A. Shaikh, D. Chatterjee, and P. Ajith** (2020). Of Harbingers and Higher Modes: Improved gravitational-wave early-warning of compact binary mergers. *Astrophys. J. Lett.*, **898**(2), L39. DOI. ARXIV:2005.08830. (cited on pg. 55).
299. **Kastha, S. et al.** (2018). Testing the multipole structure of compact binaries using gravitational wave observations. *Phys. Rev. D*, **98**(12), 124033. DOI. ARXIV:1809.10465. (cited on pg. 55).

300. **Kastha, S. et al.** (2019). Testing the multipole structure and conservative dynamics of compact binaries using gravitational wave observations: The spinning case. *Phys. Rev. D*, **100**(4), 044007. DOI. ARXIV:1905.07277. (cited on pg. 55).
301. **Kawamura, S. et al.** (2021). Current status of space gravitational wave antenna DECIGO and B-DECIGO. *PTEP*, **2021**(5), 05A105. DOI. ARXIV:2006.13545. (cited on pg. 22).
302. **Kennefick, D.** (2005). Einstein Versus the Physical Review . *Physics Today*, **58**(9), 43–48. ISSN 0031-9228. DOI. (cited on pg. 3).
303. **Khalil, M., A. Buonanno, J. Steinhoff, and J. Vines** (2021). Radiation-reaction force and multipolar waveforms for eccentric, spin-aligned binaries in the effective-one-body formalism. *Phys. Rev. D*, **104**(2), 024046. DOI. ARXIV:2104.11705. (cited on pg. 48).
304. **Khan, S., K. Chatziioannou, M. Hannam, and F. Ohme** (2019). Phenomenological model for the gravitational-wave signal from precessing binary black holes with two-spin effects. *Phys. Rev. D*, **100**(2), 024059. DOI. ARXIV:1809.10113. (cited on pg. 53).
305. **Khan, S., F. Ohme, K. Chatziioannou, and M. Hannam** (2020). Including higher order multipoles in gravitational-wave models for precessing binary black holes. *Phys. Rev. D*, **101**(2), 024056. DOI. ARXIV:1911.06050. (cited on pgs. 53 and 107).
306. **Khan, S. et al.** (2016). Frequency-domain gravitational waves from nonprecessing black-hole binaries. II. A phenomenological model for the advanced detector era. *Phys. Rev. D*, **93**(4), 044007. DOI. ARXIV:1508.07253. (cited on pgs. xxi, 58, and 66).
307. **Kidder, L. E.** (1995). Coalescing binary systems of compact objects to postNewtonian $5/2$ order. 5. Spin effects. *Phys. Rev. D*, **52**, 821–847. DOI. ARXIV:gr-qc/9506022. (cited on pg. 53).
308. **Kidder, L. E.** (2008). Using full information when computing modes of post-Newtonian waveforms from inspiralling compact binaries in circular orbit. *Phys. Rev. D*, **77**, 044016. DOI. ARXIV:0710.0614. (cited on pg. 53).
309. **Kim, J., C. Kim, H. W. Lee., M. Favata, and K. G. Arun** (2019). LALSimInspiralsTaylorF2Ecc.c file reference. https://lscsoft.docs.ligo.org/lalsuite/lalsimulation/_l_a_l_sim_inspiral_taylor_f2_ecc_8c.html. (cited on pgs. 66 and 72).
310. **Kimpson, T. O., M. Spera, M. Mapelli, and B. M. Ziosi** (2016). Hierarchical black hole triples in young star clusters: impact of Kozai–Lidov resonance on mergers. *Mon. Not. Roy. Astron. Soc.*, **463**(3), 2443–2452. DOI. ARXIV:1608.05422. (cited on pg. 51).
311. **Klein, A.** (2021). EFPE: Efficient fully precessing eccentric gravitational waveforms for

- binaries with long inspirals. [ARXIV:2106.10291](#). (cited on pgs. 48 and 49).
312. **Klein, A., Y. Boetzel, A. Gopakumar, P. Jetzer, and L. de Vittori** (2018). Fourier domain gravitational waveforms for precessing eccentric binaries. *Phys. Rev. D*, **98**(10), 104043. [DOI](#). [ARXIV:1801.08542](#). (cited on pg. 48).
 313. **Klein, A. and P. Jetzer** (2010). Spin effects in the phasing of gravitational waves from binaries on eccentric orbits. *Phys. Rev. D*, **81**, 124001. [DOI](#). [ARXIV:1005.2046](#). (cited on pg. 48).
 314. **Klimenko, S. and G. Mitselmakher** (2004). A wavelet method for detection of gravitational wave bursts. *Class. Quant. Grav.*, **21**, S1819–S1830. [DOI](#). (cited on pg. 35).
 315. **Klimenko, S., S. Mohanty, M. Rakhmanov, and G. Mitselmakher** (2005). Constraint likelihood analysis for a network of gravitational wave detectors. *Phys. Rev. D*, **72**, 122002. [DOI](#). [ARXIV:gr-qc/0508068](#). (cited on pg. 47).
 316. **Klimenko, S. et al.** (2011). Localization of gravitational wave sources with networks of advanced detectors. *Phys. Rev. D*, **83**, 102001. [DOI](#). [ARXIV:1101.5408](#). (cited on pg. 35).
 317. **Klimenko, S. et al.** (2016). Method for detection and reconstruction of gravitational wave transients with networks of advanced detectors. *Phys. Rev. D*, **93**(4), 042004. [DOI](#). [ARXIV:1511.05999](#). (cited on pg. 35).
 318. **Kokkotas, K. D.** (2007). Gravitational waves. *Acta Phys. Polon. B*, **38**, 3891–3923. (cited on pg. 14).
 319. **Komossa, S. and D. Merritt** (2008). Gravitational Wave Recoil Oscillations of Black Holes: Implications for Unified Models of Active Galactic Nuclei. *Astrophys. J. Lett.*, **689**, L89. [DOI](#). [ARXIV:0811.1037](#). (cited on pg. 51).
 320. **Konigsdorffer, C. and A. Gopakumar** (2006). Phasing of gravitational waves from inspiralling eccentric binaries at the third-and-a-half post-Newtonian order. *Phys. Rev. D*, **73**, 124012. [DOI](#). [ARXIV:gr-qc/0603056](#). (cited on pg. 48).
 321. **Kowalska, I. et al.** (2011). The eccentricity distribution of compact binaries. *A&A*, **527**, A70. [DOI](#). [ARXIV:1010.0511](#). (cited on pg. 45).
 322. **Kozai, Y.** (1962). Secular perturbations of asteroids with high inclination and eccentricity. *Astron. J.*, **67**, 591–598. [DOI](#). (cited on pg. 44).
 323. **Kremer, K. et al.** (2020). Modeling Dense Star Clusters in the Milky Way and Beyond with the CMC Cluster Catalog. *Astrophys. J. Suppl.*, **247**(2), 48. [DOI](#). [ARXIV:1911.00018](#). (cited on pgs. 31 and 70).

324. **Krishnendu, N. V., K. G. Arun, and C. K. Mishra** (2017). Testing the binary black hole nature of a compact binary coalescence. *Phys. Rev. Lett.*, **119**(9), 091101. DOI. ARXIV:1701.06318. (cited on pgs. 57, 58, 108, 157, and 158).
325. **Krishnendu, N. V., C. K. Mishra, and K. G. Arun** (2019a). Spin-induced deformations and tests of binary black hole nature using third-generation detectors. *Phys. Rev. D*, **99**(6), 064008. DOI. ARXIV:1811.00317. (cited on pgs. 57, 108, and 115).
326. **Krishnendu, N. V. and F. Ohme** (2021). Testing General Relativity with Gravitational Waves: An Overview. *Universe*, **7**(12), 497. DOI. ARXIV:2201.05418. (cited on pgs. 54 and 105).
327. **Krishnendu, N. V. and F. Ohme** (2022). Interplay of spin-precession and higher harmonics in the parameter estimation of binary black holes. *Phys. Rev. D*, **105**(6), 064012. DOI. ARXIV:2110.00766. (cited on pgs. 60 and 105).
328. **Krishnendu, N. V. and A. B. Yelikar** (2020). Testing the Kerr nature of supermassive and intermediate-mass black hole binaries using spin-induced multipole moment measurements. *Classical Quantum Gravity*, **37**(20), 205019. DOI. ARXIV:1904.12712. (cited on pg. 57).
329. **Krishnendu, N. V. et al.** (2019b). Constraints on the binary black hole nature of GW151226 and GW170608 from the measurement of spin-induced quadrupole moments. *Phys. Rev. D*, **100**(10), 104019. DOI. ARXIV:1908.02247. (cited on pgs. 57, 107, 110, 114, and 120).
330. **Kumar, P. et al.** (2015). Accuracy and precision of gravitational-wave models of inspiraling neutron star-black hole binaries with spin: Comparison with matter-free numerical relativity in the low-frequency regime. *Phys. Rev.*, **D92**(10), 102001. DOI. ARXIV:1507.00103. (cited on pg. 74).
331. **Kumar, P. et al.** (2019). Constraining the parameters of GW150914 and GW170104 with numerical relativity surrogates. *Phys. Rev. D*, **99**(12), 124005. DOI. ARXIV:1808.08004. (cited on pg. 52).
332. **Kuns, K. A., H. Yu, Y. Chen, and R. X. Adhikari** (2020). Astrophysics and cosmology with a decihertz gravitational-wave detector: TianGO. *Phys. Rev. D*, **102**(4), 043001. DOI. ARXIV:1908.06004. (cited on pg. 22).
333. **Laarakkers, W. G. and E. Poisson** (1999). Quadrupole moments of rotating neutron stars. *Astrophys. J.*, **512**, 282–287. DOI. ARXIV:gr-qc/9709033. (cited on pgs. 55 and 56).
334. **LaHaye, M., H. Yang, B. Bonga, and Z. Lyu** (2023). Efficient fully precessing gravitational waveforms for binaries with neutron stars. *Phys. Rev. D*, **108**(4), 043018. DOI. ARXIV:2212.04657. (cited on pg. 57).

335. **Laine, S. et al.** (2020). Spitzer Observations of the Predicted Eddington Flare from Blazar OJ 287. *Astrophys. J. Lett.*, **894**(1), L1. DOI. ARXIV:2004.13392. (cited on pg. 57).
336. **Lange, J., R. O’Shaughnessy, and M. Rizzo** (2018). Rapid and accurate parameter inference for coalescing, precessing compact binaries. ARXIV:1805.10457. (cited on pgs. 40, 47, and 54).
337. **Le Tiec, A. and M. Casals** (2021). Spinning Black Holes Fall in Love. *Phys. Rev. Lett.*, **126**(13), 131102. DOI. ARXIV:2007.00214. (cited on pg. 55).
338. **Le Tiec, A. and J. Novak**, *Theory of Gravitational Waves*. World Scientific Publishing Co. Pte. Ltd., 2017, 1–41. ARXIV:1607.04202. DOI. (cited on pg. 14).
339. **Lehner, L.** (2001). Numerical relativity: A Review. *Class. Quant. Grav.*, **18**, R25–R86. DOI. ARXIV:gr-qc/0106072. (cited on pg. 56).
340. **Lenon, A. K., D. A. Brown, and A. H. Nitz** (2021). Eccentric binary neutron star search prospects for Cosmic Explorer. *Phys. Rev. D*, **104**(6), 063011. DOI. ARXIV:2103.14088. (cited on pg. 46).
341. **Lenon, A. K., A. H. Nitz, and D. A. Brown** (2020). Measuring the eccentricity of GW170817 and GW190425. *Mon. Not. Roy. Astron. Soc.*, **497**(2), 1966–1971. DOI. ARXIV:2005.14146. (cited on pg. 47).
342. **Lentati, L. et al.** (2014). TempoNest: A Bayesian approach to pulsar timing analysis. *Mon. Not. Roy. Astron. Soc.*, **437**(3), 3004–3023. DOI. ARXIV:1310.2120. (cited on pg. 40).
343. **Leuchs, G. et al.** (1987). Proposal for building a large laser interferometer to measure gravitational waves (extended version). URL: <https://www.mpq.mpg.de/5943300/MPQ129.pdf>. (cited on pg. 5).
344. **Levin, J.**, *Black Hole Blues and Other Songs from Outer Space*. Anchor, 2017. URL: <https://www.penguinrandomhouse.com/books/216287/black-hole-blues-and-other-songs-from-outer-space-by-janna-levin/>. (cited on pgs. 6 and 7).
345. **Levine, J. L. and R. L. Garwin** (1974). New negative result for gravitational wave detection, and comparison with reported detection. *Phys. Rev. Lett.*, **33**, 794–797. DOI. (cited on pg. 5).
346. **Li, T. G. F. et al.** (2012a). Towards a generic test of the strong field dynamics of general relativity using compact binary coalescence. *Phys. Rev. D*, **85**, 082003. DOI. ARXIV:1110.0530. (cited on pg. 31).
347. **Li, T. G. F. et al.** (2012b). Towards a generic test of the strong field dynamics of general

relativity using compact binary coalescence: Further investigations. *J. Phys. Conf. Ser.*, **363**, 012028. DOI. ARXIV:1111.5274. (cited on pg. 31).

348. **Lidov, M.** (1962). The evolution of orbits of artificial satellites of planets under the action of gravitational perturbations of external bodies. *Planetary and Space Science*, **9**(10), 719–759. ISSN 0032-0633. DOI. (cited on pg. 44).
349. **Liebling, S. L.** and **C. Palenzuela** (2023). Dynamical boson stars. *Living Rev. Rel.*, **26**(1), 1. DOI. ARXIV:1202.5809. (cited on pg. 32).
350. **LIGO Caltech** (2015a). URL: <https://www.ligo.caltech.edu/page/gw-sources>. (cited on pg. 9).
351. **LIGO Caltech** (2015b). URL: <https://www.ligo.caltech.edu/page/ligos-ifo>. (cited on pg. 18).
352. **LIGO Caltech** (2015c). URL: <https://www.ligo.caltech.edu/page/ligos-ifo>. (cited on pg. 20).
353. **LIGO Caltech** (2015d). URL: <https://www.ligo.caltech.edu/page/ligo-technology>. (cited on pg. 19).
354. **LIGO Caltech** (2021). URL: <https://www.ligo.caltech.edu/WA/image/ligo20211107a>. (cited on pg. 25).
355. **LIGO-India**, (2023). URL: <https://www.ligo-india.in>. (cited on pg. 20).
356. **LIGO Scientific Collaboration** (2015a). URL: <https://www.ligo.org/science/GW-Sources.php>. (cited on pg. 9).
357. **LIGO Scientific Collaboration** (2015b). URL: <https://www.ligo.org/science/GW-Continuous.php>. (cited on pg. 11).
358. **LIGO Scientific Collaboration** (2016). Instrument science white paper. URL: <https://dcc.ligo.org/LIGO-T1500290/public>. (cited on pg. 146).
359. **LIGO Scientific Collaboration** (2018). LIGO Algorithm Library - LALSuite. free software (GPL). URL: <https://lscsoft.docs.ligo.org/lalsuite/lalsimulation/>. (cited on pgs. 53 and 108).
360. **LIGO Scientific Collaboration** (2022). <https://dcc.ligo.org/LIGO-P1200087-v42/public>. (cited on pg. 111).
361. **LIGO Scientific Collaboration and Virgo Collaboration** (2023). GWTC data release. URL: <https://www.gw-openscience.org/eventapi/html/GWTC/>. (cited on pgs. 137 and 138).

362. **LIGO Voyager** (2023). LIGO Voyager Upgrade: Design Concept. (cited on pg. 20).
363. **Lim, H.** and **C. L. Rodriguez** (2020). Relativistic three-body effects in hierarchical triples. *Phys. Rev. D*, **102**(6), 064033. DOI. ARXIV:2001.03654. (cited on pg. 51).
364. **Linsay, P., P. Saulson,** and **R. Weiss** (1983). A study of a long baseline gravitational wave antenna. URL: https://emvogil-3.mit.edu/~weiss/ligo_history_documents/NSF_bluebook_1983.pdf. (cited on pg. 6).
365. **Littenberg, T. B.** and **N. J. Cornish** (2015). Bayesian inference for spectral estimation of gravitational wave detector noise. *Phys. Rev. D*, **91**(8), 084034. DOI. ARXIV:1410.3852. (cited on pg. 42).
366. **Liu, X., Z. Cao,** and **L. Shao** (2020). Validating the Effective-One-Body Numerical-Relativity Waveform Models for Spin-aligned Binary Black Holes along Eccentric Orbits. *Phys. Rev. D*, **101**(4), 044049. DOI. ARXIV:1910.00784. (cited on pg. 48).
367. **Liu, X., Z. Cao,** and **L. Shao** (2023). Upgraded waveform model of eccentric binary black hole based on effective-one-body-numerical-relativity for spin-aligned binary black holes. *International Journal of Modern Physics D*, **32**(4), 2350015. DOI. ARXIV:2306.15277. (cited on pg. 48).
368. **Liu, X., Z. Cao,** and **Z.-H. Zhu** (2022). A higher-multipole gravitational waveform model for an eccentric binary black holes based on the effective-one-body-numerical-relativity formalism. *Class. Quant. Grav.*, **39**(3), 035009. DOI. ARXIV:2102.08614. (cited on pg. 53).
369. **London, L. et al.** (2018). First higher-multipole model of gravitational waves from spinning and coalescing black-hole binaries. *Phys. Rev. Lett.*, **120**(16), 161102. DOI. ARXIV:1708.00404. (cited on pgs. xxi, 53, 134, 135, 136, and 144).
370. **Lousto, C. O.** and **Y. Zlochower** (2011). Hangup Kicks: Still Larger Recoils by Partial Spin/Orbit Alignment of Black-Hole Binaries. *Phys. Rev. Lett.*, **107**, 231102. DOI. ARXIV:1108.2009. (cited on pg. 51).
371. **Lovelace, G., M. Boyle, M. A. Scheel,** and **B. Szilagyi** (2012). Accurate gravitational waveforms for binary-black-hole mergers with nearly extremal spins. *Class. Quant. Grav.*, **29**, 045003. DOI. ARXIV:1110.2229. (cited on pg. 74).
372. **Lovelace, G., M. Scheel,** and **B. Szilagyi** (2011). Simulating merging binary black holes with nearly extremal spins. *Phys. Rev.*, **D83**, 024010. DOI. ARXIV:1010.2777. (cited on pg. 74).
373. **Lovelace, G. et al.** (2015). Nearly extremal apparent horizons in simulations of merging black holes. *Class. Quant. Grav.*, **32**(6), 065007. DOI. ARXIV:1411.7297. (cited on pg. 74).

374. **Lovelace, G. et al.** (2016). Modeling the source of GW150914 with targeted numerical-relativity simulations. *Class. Quant. Grav.*, **33**(24), 244002. DOI. ARXIV:1607.05377. (cited on pg. 74).
375. **Lower, M. E., E. Thrane, P. D. Lasky, and R. Smith** (2018). Measuring eccentricity in binary black hole inspirals with gravitational waves. *Phys. Rev. D*, **98**(8), 083028. DOI. ARXIV:1806.05350. (cited on pgs. 45, 46, and 47).
376. **Lunin, O. and S. D. Mathur** (2002). AdS / CFT duality and the black hole information paradox. *Nucl. Phys. B*, **623**, 342–394. DOI. ARXIV:hep-th/0109154. (cited on pg. 32).
377. **Luo, J. et al.** (2016). TianQin: a space-borne gravitational wave detector. *Class. Quant. Grav.*, **33**(3), 035010. DOI. ARXIV:1512.02076. (cited on pg. 22).
378. **Lynch, R. S.** (2015). Pulsar Timing Arrays. *J. Phys. Conf. Ser.*, **610**(1), 012017. DOI. (cited on pgs. 13 and 19).
379. **Lyu, Z., M. LaHaye, H. Yang, and B. Bonga** (2024). Probing spin-induced quadrupole moments in precessing compact binaries. *Phys. Rev. D*, **109**(6), 064081. DOI. ARXIV:2308.09032. (cited on pg. 58).
380. **Ma, S., M. Giesler, V. Varma, M. A. Scheel, and Y. Chen** (2021). Universal features of gravitational waves emitted by superkick binary black hole systems. *Phys. Rev. D*, **104**(8), 084003. DOI. ARXIV:2107.04890. (cited on pg. 74).
381. **Maggiore, M.**, *Gravitational Waves. Vol. 1: Theory and Experiments*. Oxford University Press, 2007. ISBN 978-0-19-171766-6, 978-0-19-852074-0. (cited on pgs. 2, 3, and 34).
382. **Mandel, I. and A. Farmer** (2022). Merging stellar-mass binary black holes. *Phys. Rept.*, **955**, 1–24. DOI. ARXIV:1806.05820. (cited on pgs. 44 and 51).
383. **Mapelli, M.**, *Formation Channels of Single and Binary Stellar-Mass Black Holes*. Springer Singapore, Singapore, 2020. ISBN 978-981-15-4702-7, 1–65. DOI. URL: https://doi.org/10.1007/978-981-15-4702-7_16-1. (cited on pgs. 44 and 51).
384. **Mapelli, M. and N. Giacobbo** (2018). The cosmic merger rate of neutron stars and black holes. *Mon. Not. Roy. Astron. Soc.*, **479**(4), 4391–4398. DOI. ARXIV:1806.04866. (cited on pg. 30).
385. **Mapelli, M. et al.** (2021). Mass and Rate of Hierarchical Black Hole Mergers in Young, Globular and Nuclear Star Clusters. *Symmetry*, **13**(9), 1678. DOI. ARXIV:2007.15022. (cited on pg. 30).
386. **Marsat, S., A. Bohe, G. Faye, and L. Blanchet** (2013). Next-to-next-to-leading order

- spin-orbit effects in the equations of motion of compact binary systems. *Classical Quantum Gravity*, **30**, 055007. DOI. ARXIV:1210.4143. (cited on pg. 53).
387. **Marsat, S., A. BohÈ, L. Blanchet, and A. Buonanno** (2014). Next-to-leading tail-induced spin-orbit effects in the gravitational radiation flux of compact binaries. *Class. Quant. Grav.*, **31**(2), 025023. DOI. ARXIV:1307.6793. (cited on pg. 53).
388. **Martel, K. and E. Poisson** (1999). Gravitational waves from eccentric compact binaries: Reduction in signal-to-noise ratio due to nonoptimal signal processing. *Phys. Rev. D*, **60**, 124008. DOI. ARXIV:gr-qc/9907006. (cited on pg. 46).
389. **Martinez, M. A. S. et al.** (2020). Black Hole Mergers from Hierarchical Triples in Dense Star Clusters. *Astrophys. J.*, **903**(1), 67. DOI. ARXIV:2009.08468. (cited on pg. 44).
390. **Max-Planck-Institut für Gravitationsphysik** (2005). Biennial report 2004/2005. URL: <https://www.aei.mpg.de/164680/2004-2005-Biennial-Report.pdf>. (cited on pg. 6).
391. **Mazur, P. O. and E. Mottola** (2004). Gravitational vacuum condensate stars. *Proc. Nat. Acad. Sci.*, **101**, 9545–9550. DOI. ARXIV:gr-qc/0407075. (cited on pg. 32).
392. **Mehta, A. K., C. K. Mishra, V. Varma, and P. Ajith** (2017). Accurate inspiral-merger-ringdown gravitational waveforms for nonspinning black-hole binaries including the effect of subdominant modes. *Phys. Rev. D*, **96**(12), 124010. DOI. ARXIV:1708.03501. (cited on pgs. 53 and 135).
393. **Mehta, A. K. et al.** (2019). Including mode mixing in a higher-multipole model for gravitational waveforms from nonspinning black-hole binaries. *Phys. Rev. D*, **100**(2), 024032. DOI. ARXIV:1902.02731. (cited on pg. 53).
394. **Mehta, A. K. et al.** (2023). Tests of general relativity with gravitational-wave observations using a flexible theory-independent method. *Phys. Rev. D*, **107**(4), 044020. DOI. ARXIV:2203.13937. (cited on pg. 105).
395. **Mendes, R. F. P. and H. Yang** (2017). Tidal deformability of boson stars and dark matter clumps. *Classical Quantum Gravity*, **34**(18), 185001. DOI. ARXIV:1606.03035. (cited on pg. 55).
396. **Merritt, D., M. Milosavljevic, M. Favata, S. A. Hughes, and D. E. Holz** (2004). Consequences of gravitational radiation recoil. *Astrophys. J. Lett.*, **607**, L9–L12. DOI. ARXIV:astro-ph/0402057. (cited on pg. 51).
397. **Messick, C. et al.** (2017). Analysis Framework for the Prompt Discovery of Compact Binary Mergers in Gravitational-wave Data. *Phys. Rev. D*, **95**(4), 042001. DOI. ARXIV:1604.04324. (cited on pgs. 27, 35, and 64).
398. **Metropolis, N. et al.** (1953). Equation of state calculations by fast computing machines.

- J. Chem. Phys.*, **21**, 1087–1092. DOI. (cited on pg. 42).
399. **Mills, C.** and **S. Fairhurst** (2021). Measuring gravitational-wave higher-order multipoles. *Phys. Rev. D*, **103**(2), 024042. DOI. ARXIV:2007.04313. (cited on pgs. 54, 135, and 136).
 400. **Mirshekari, S.**, **N. Yunes**, and **C. M. Will** (2012). Constraining Generic Lorentz Violation and the Speed of the Graviton with Gravitational Waves. *Phys. Rev. D*, **85**, 024041. DOI. ARXIV:1110.2720. (cited on pg. 32).
 401. **Mishra, C. K.**, **K. Arun**, **B. R. Iyer**, and **B. Sathyaprakash** (2010). Parametrized tests of post-Newtonian theory using Advanced LIGO and Einstein Telescope. *Phys. Rev. D*, **82**, 064010. DOI. ARXIV:1005.0304. (cited on pgs. 31 and 55).
 402. **Mishra, C. K.**, **K. G. Arun**, and **B. R. Iyer** (2015). Third post-Newtonian gravitational waveforms for compact binary systems in general orbits: Instantaneous terms. *Phys. Rev. D*, **91**(8), 084040. DOI. ARXIV:1501.07096. (cited on pg. 48).
 403. **Mishra, C. K.**, **A. Kela**, **K. G. Arun**, and **G. Faye** (2016). Ready-to-use post-Newtonian gravitational waveforms for binary black holes with nonprecessing spins: An update. *Phys. Rev. D*, **93**(8), 084054. DOI. ARXIV:1601.05588. (cited on pgs. 53 and 56).
 404. **Moore, B.**, **M. Favata**, **K. G. Arun**, and **C. K. Mishra** (2016). Gravitational-wave phasing for low-eccentricity inspiralling compact binaries to 3PN order. *Phys. Rev. D*, **93**(12), 124061. DOI. ARXIV:1605.00304. (cited on pgs. xxi, 48, 66, 72, and 75).
 405. **Moore, B.** and **N. Yunes** (2019). A 3PN Fourier Domain Waveform for Non-Spinning Binaries with Moderate Eccentricity. *Class. Quant. Grav.*, **36**(18), 185003. DOI. ARXIV:1903.05203. (cited on pg. 48).
 406. **Moore, B.** and **N. Yunes** (2020). Data Analysis Implications of Moderately Eccentric Gravitational Waves. *Class. Quant. Grav.*, **37**(22), 225015. DOI. ARXIV:1910.01680. (cited on pg. 60).
 407. **Mora, T.** and **C. M. Will** (2002). Numerically generated quasiequilibrium orbits of black holes: Circular or eccentric? *Phys. Rev. D*, **66**, 101501. DOI. ARXIV:gr-qc/0208089. (cited on pg. 71).
 408. **Moss, G. E.**, **L. R. Miller**, and **R. L. Forward** (1971). Photon-noise-limited laser transducer for gravitational antenna. *Appl. Opt.*, **10**, 2495–2498. DOI. (cited on pg. 5).
 409. **Mould, M.**, **D. Gerosa**, and **S. R. Taylor** (2022). Deep learning and Bayesian inference of gravitational-wave populations: Hierarchical black-hole mergers. *Phys. Rev. D*, **106**(10), 103013. DOI. ARXIV:2203.03651. (cited on pg. 103).
 410. **Mroue, A. H.** and **H. P. Pfeiffer** (2012). Precessing Binary Black Holes Simulations: Quasicircular Initial Data. ARXIV:1210.2958. (cited on pg. 74).

411. **Mroue, A. H. et al.** (2013). Catalog of 174 Binary Black Hole Simulations for Gravitational Wave Astronomy. *Phys. Rev. Lett.*, **111**(24), 241104. DOI. ARXIV:1304.6077. (cited on pg. 74).
412. **Nagar, A., A. Bonino, and P. Rettegno** (2021a). Effective one-body multipolar waveform model for spin-aligned, quasicircular, eccentric, hyperbolic black hole binaries. *Phys. Rev. D*, **103**(10), 104021. DOI. ARXIV:2101.08624. (cited on pgs. 48 and 53).
413. **Nagar, A. and P. Rettegno** (2021). Next generation: Impact of high-order analytical information on effective one body waveform models for noncircularized, spin-aligned black hole binaries. *Phys. Rev. D*, **104**(10), 104004. DOI. ARXIV:2108.02043. (cited on pg. 71).
414. **Nagar, A., P. Rettegno, R. Gamba, and S. Bernuzzi** (2021b). Effective-one-body waveforms from dynamical captures in black hole binaries. *Phys. Rev. D*, **103**(6), 064013. DOI. ARXIV:2009.12857. (cited on pg. 53).
415. **Nagar, A., G. Riemenschneider, G. Pratten, P. Rettegno, and F. Messina** (2020). Multipolar effective one body waveform model for spin-aligned black hole binaries. *Phys. Rev. D*, **102**(2), 024077. DOI. ARXIV:2001.09082. (cited on pgs. xxi and 53).
416. **Nagar, A. et al.** (2018). Time-domain effective-one-body gravitational waveforms for coalescing compact binaries with nonprecessing spins, tides and self-spin effects. *Phys. Rev. D*, **98**(10), 104052. DOI. ARXIV:1806.01772. (cited on pgs. xiii, 71, and 87).
417. **NAOJ** (2016). URL: <https://gwpo.nao.ac.jp/en/gallery/000061.html>. (cited on pg. 12).
418. **Naoz, S.** (2016). The Eccentric Kozai-Lidov Effect and Its Applications. *ARA&A*, **54**, 441–489. DOI. ARXIV:1601.07175. (cited on pg. 44).
419. **Narayan, P., N. K. Johnson-McDaniel, and A. Gupta** (2023). Effect of ignoring eccentricity in testing general relativity with gravitational waves. *Phys. Rev. D*, **108**(6), 064003. DOI. ARXIV:2306.04068. (cited on pg. 45).
420. **Newton, I.**, *Philosophiae Naturalis Principia Mathematica*.. 1687. (cited on pg. 1).
421. **Ng, K. K. Y., S. Vitale, W. M. Farr, and C. L. Rodriguez** (2021). Probing multiple populations of compact binaries with third-generation gravitational-wave detectors. *Astrophys. J. Lett.*, **913**(1), L5. DOI. ARXIV:2012.09876. (cited on pgs. 31 and 144).
422. **Niels Bohr Library & Archives** (2020). Interview of Rainer Weiss by David Zierler on June 7, 14, 21 & 28, 2020. URL: <https://www.aip.org/history-programs/niels-bohr-library/oral-histories/47250>. American Institute of Physics, College Park, MD USA. (cited on pg. 6).
423. **Nishizawa, A., A. Taruya, K. Hayama, S. Kawamura, and M.-a. Sakagami** (2009).

Probing non-tensorial polarizations of stochastic gravitational-wave backgrounds with ground-based laser interferometers. *Phys. Rev. D*, **79**, 082002. DOI. ARXIV:0903.0528. (cited on pg. 15).

424. **Nitz, A. H., T. Dent, T. Dal Canton, S. Fairhurst, and D. A. Brown** (2017). Detecting binary compact-object mergers with gravitational waves: Understanding and Improving the sensitivity of the PyCBC search. *Astrophys. J.*, **849**(2), 118. DOI. ARXIV:1705.01513. (cited on pg. 35).
425. **Nitz, A. H., A. Lenon, and D. A. Brown** (2019). Search for Eccentric Binary Neutron Star Mergers in the first and second observing runs of Advanced LIGO. *Astrophys. J.*, **890**, 1. DOI. ARXIV:1912.05464. (cited on pg. 47).
426. **Nitz, A. H. and Y.-F. Wang** (2021). Search for Gravitational Waves from the Coalescence of Substellar-Mass Binaries in the First Half of Advanced LIGO and Virgo’s Third Observing Run. *Phys. Rev. Lett.*, **127**(15), 151101. DOI. ARXIV:2106.08979. (cited on pg. 47).
427. **Nobel Prize** (2017). URL: <https://www.nobelprize.org/prizes/physics/2017/press-release/>. (cited on pg. 7).
428. **O’Brien, B. D., C. F. Da Silva Costa, and S. Klimenko** (2019). Measurement of sub-dominant harmonic modes for gravitational wave emission from a population of binary black holes. ARXIV:1901.09072. (cited on pg. 54).
429. **Ohme, F., A. B. Nielsen, D. Keppel, and A. Lundgren** (2013). Statistical and systematic errors for gravitational-wave inspiral signals: A principal component analysis. *Phys. Rev. D*, **88**(4), 042002. DOI. ARXIV:1304.7017. (cited on pg. 54).
430. **Olejak, A., C. L. Fryer, K. Belczynski, and V. Baibhav** (2022). The role of supernova convection for the lower mass gap in the isolated binary formation of gravitational wave sources. *Mon. Not. Roy. Astron. Soc.*, **516**(2), 2252–2271. DOI. ARXIV:2204.09061. (cited on pg. 30).
431. **Olejak, A. et al.** (2020). The Origin of Inequality: Isolated Formation of a $30+10 M_{\odot}$ Binary Black Hole Merger. *Astrophys. J. Lett.*, **901**(2), L39. DOI. ARXIV:2004.11866. (cited on pg. 51).
432. **O’Shaughnessy, R. et al.** (2014). Parameter estimation of gravitational waves from precessing black hole-neutron star inspirals with higher harmonics. *Phys. Rev. D*, **89**(10), 102005. DOI. ARXIV:1403.0544. (cited on pg. 52).
433. **O’Shea, E. and P. Kumar** (2023). Correlations in gravitational-wave reconstructions from eccentric binaries: A case study with GW151226 and GW170608. *Phys. Rev. D*, **108**(10), 104018. DOI. ARXIV:2107.07981. (cited on pgs. 48, 90, and 98).
434. **Ossokine, S. et al.** (2020). Multipolar Effective-One-Body Waveforms for Precessing

- Binary Black Holes: Construction and Validation. *Phys. Rev. D*, **102**(4), 044055. DOI. ARXIV:2004.09442. (cited on pg. 53).
435. **Owen, B. J.** and **B. S. Sathyaprakash** (1999). Matched filtering of gravitational waves from inspiraling compact binaries: Computational cost and template placement. *Phys. Rev. D*, **60**, 022002. DOI. ARXIV:gr-qc/9808076. (cited on pg. 34).
436. **OzGrav** (2020). <https://www.ozgrav.org/news/the-dance-of-destruction-new-insights-into-eccentric-binary-black-holes>. (cited on pg. 46).
437. **Pacilio, C., M. Vaglio, A. Maselli, and P. Pani** (2020). Gravitational-wave detectors as particle-physics laboratories: Constraining scalar interactions with a coherent inspiral model of boson-star binaries. *Phys. Rev. D*, **102**(8), 083002. DOI. ARXIV:2007.05264. (cited on pg. 55).
438. **Pai, A., S. Dhurandhar, and S. Bose** (2001). A Data analysis strategy for detecting gravitational wave signals from inspiraling compact binaries with a network of laser interferometric detectors. *Phys. Rev. D*, **64**, 042004. DOI. ARXIV:gr-qc/0009078. (cited on pg. 35).
439. **Pal, S.** and **K. R. Nayak** (2023). Swarm-intelligent search for gravitational waves from eccentric binary mergers. ARXIV:2307.03736. (cited on pg. 46).
440. **Pankow, C., P. Brady, E. Ochsner, and R. O’Shaughnessy** (2015). Novel scheme for rapid parallel parameter estimation of gravitational waves from compact binary coalescences. *Phys. Rev. D*, **92**(2), 023002. DOI. ARXIV:1502.04370. (cited on pg. 40).
441. **Pankow, C. et al.** (2018). Mitigation of the instrumental noise transient in gravitational-wave data surrounding GW170817. *Phys. Rev. D*, **98**(8), 084016. DOI. ARXIV:1808.03619. (cited on pg. 39).
442. **Pappas, G.** and **T. A. Apostolatos** (2012a). Multipole Moments of numerical spacetimes. ARXIV:1211.6299. (cited on pg. 56).
443. **Pappas, G.** and **T. A. Apostolatos** (2012b). Revising the multipole moments of numerical spacetimes, and its consequences. *Phys. Rev. Lett.*, **108**, 231104. DOI. ARXIV:1201.6067. (cited on pg. 56).
444. **Park, D., C. Kim, H. M. Lee, Y.-B. Bae, and K. Belczynski** (2017). Black Hole Binaries Dynamically Formed in Globular Clusters. *Mon. Not. Roy. Astron. Soc.*, **469**(4), 4665–4674. DOI. ARXIV:1703.01568. (cited on pg. 51).
445. **Paul, K., P. Kumar, and C. K. Mishra** (2024). An eccentric, spinning inspiral waveform model for the detection and characterization of eccentric binary black holes. (in preparation). (cited on pgs. 58 and 59).

446. **Paul, K.** and **C. K. Mishra** (2023). Spin effects in spherical harmonic modes of gravitational waves from eccentric compact binary inspirals. *Phys. Rev. D*, **108**(2), 024023. DOI. ARXIV:2211.04155. (cited on pg. 48).
447. **Payne, E., C. Talbot,** and **E. Thrane** (2019). Higher order gravitational-wave modes with likelihood reweighting. *Phys. Rev. D*, **100**(12), 123017. DOI. ARXIV:1905.05477. (cited on pg. 54).
448. **Pekowsky, L., J. Healy, D. Shoemaker,** and **P. Laguna** (2013). Impact of higher-order modes on the detection of binary black hole coalescences. *Phys. Rev. D*, **87**(8), 084008. DOI. ARXIV:1210.1891. (cited on pg. 136).
449. **Penrose, R.** (1969). Gravitational collapse: The role of general relativity. *Riv. Nuovo Cim.*, **1**, 252–276. DOI. (cited on pg. 32).
450. **Peters, P. C.** (1964). Gravitational radiation and the motion of two point masses. *Phys. Rev.*, **136**, B1224–B1232. DOI. (cited on pgs. 44 and 47).
451. **Peters, P. C.** and **J. Mathews** (1963). Gravitational radiation from point masses in a keplerian orbit. *Phys. Rev.*, **131**, 435–440. DOI. (cited on pg. 43).
452. **Pirani, F. A. E.** (1956). On the Physical significance of the Riemann tensor. *Acta Phys. Polon.*, **15**, 389–405. DOI. (cited on pg. 3).
453. **Placidi, A., S. Albanesi, A. Nagar, M. Orselli, S. Bernuzzi,** and **G. Grignani** (2022). Exploiting Newton-factorized, 2PN-accurate waveform multipoles in effective-one-body models for spin-aligned noncircularized binaries. *Phys. Rev. D*, **105**(10), 104030. DOI. ARXIV:2112.05448. (cited on pg. 71).
454. **Placidi, A., G. Grignani, T. Harmark, M. Orselli, S. Gliorio,** and **A. Nagar** (2023). 2.5PN accurate waveform information for generic-planar-orbit binaries in effective one-body models. *Phys. Rev. D*, **108**(2), 024068. DOI. ARXIV:2305.14440. (cited on pg. 71).
455. **Poincaré, M. H.** (1906). Sur la dynamique de l'électron. *Rendiconti del Circolo Matematico di Palermo (1884-1940)*, **21**(1), 129–175. ISSN 0009-725X. DOI. (cited on pg. 2).
456. **Poisson, E.** (1998). Gravitational waves from inspiraling compact binaries: The quadrupole-moment term. *Phys. Rev. D*, **57**, 5287–5290. DOI. (cited on pg. 55).
457. **Poisson, E.** and **C. M. Will** (1995). Gravitational waves from inspiraling compact binaries: Parameter estimation using second postNewtonian wave forms. *Phys. Rev. D*, **52**, 848–855. DOI. ARXIV:gr-qc/9502040. (cited on pgs. 36, 56, and 157).
458. **Portegies Zwart, S. F.** and **S. McMillan** (2000). Black hole mergers in the universe. *Astrophys. J. Lett.*, **528**, L17. DOI. ARXIV:astro-ph/9910061. (cited on pgs. 44 and 51).

459. **Portegies Zwart, S. F. et al.** (2004). The Formation of massive black holes through collision runaway in dense young star clusters. *Nature*, **428**, 724. DOI. ARXIV:[astro-ph/0402622](#). (cited on pg. 51).
460. **Porto, R. A., A. Ross, and I. Z. Rothstein** (2011). Spin induced multipole moments for the gravitational wave flux from binary inspirals to third Post-Newtonian order. *JCAP*, **03**, 009. DOI. ARXIV:[1007.1312](#). (cited on pg. 53).
461. **Porto, R. A. and I. Z. Rothstein** (2008a). Next to Leading Order Spin(1)Spin(1) Effects in the Motion of Inspiralling Compact Binaries. *Phys. Rev. D*, **78**, 044013. DOI. [Erratum: *Phys. Rev. D* 81, 029905 (2010)]. ARXIV:[0804.0260](#). (cited on pg. 53).
462. **Porto, R. A. and I. Z. Rothstein** (2008b). Spin(1)Spin(2) Effects in the Motion of Inspiralling Compact Binaries at Third Order in the Post-Newtonian Expansion. *Phys. Rev. D*, **78**, 044012. DOI. [Erratum: *Phys. Rev. D* 81, 029904 (2010)]. ARXIV:[0802.0720](#). (cited on pg. 53).
463. **Powell, J.** (2018). Parameter Estimation and Model Selection of Gravitational Wave Signals Contaminated by Transient Detector Noise Glitches. *Class. Quant. Grav.*, **35**(15), 155017. DOI. ARXIV:[1803.11346](#). (cited on pg. 39).
464. **Pratten, G. et al.** (2020). Setting the cornerstone for a family of models for gravitational waves from compact binaries: The dominant harmonic for nonprecessing quasicircular black holes. *Phys. Rev. D*, **102**(6), 064001. DOI. ARXIV:[2001.11412](#). (cited on pgs. xxi, 64, 75, 106, and 107).
465. **Pratten, G. et al.** (2021). Computationally efficient models for the dominant and subdominant harmonic modes of precessing binary black holes. *Phys. Rev. D*, **103**(10), 104056. DOI. ARXIV:[2004.06503](#). (cited on pgs. xxi, 53, 58, 59, 64, 75, 106, and 107).
466. **Pretorius, F.**, *Binary Black Hole Coalescence*. Springer Netherlands, Dordrecht, 2009. ISBN 978-1-4020-9264-0, 305–369. ARXIV:[0710.1338](#). DOI. URL: https://doi.org/10.1007/978-1-4020-9264-0_9. (cited on pg. 56).
467. **Puecher, A. et al.** (2022). Testing general relativity using higher-order modes of gravitational waves from binary black holes. *Phys. Rev. D*, **106**(8), 082003. DOI. ARXIV:[2205.09062](#). (cited on pgs. 60 and 105).
468. **Punturo, M. et al.** (2010a). The Einstein Telescope: A third-generation gravitational wave observatory. *Class. Quant. Grav.*, **27**(19), 194002. DOI. (cited on pg. 20).
469. **Punturo, M. et al.** (2010b). The third generation of gravitational wave observatories and their science reach. *Classical and Quantum Gravity*, **27**(8), 084007. DOI. (cited on pg. 20).
470. **Pürrer, M.** (2016). Frequency domain reduced order model of aligned-spin effective-one-body waveforms with generic mass-ratios and spins. *Phys. Rev. D*, **93**(6), 064041.

- DOI. ARXIV:1512.02248. (cited on pg. 27).
471. **Pürrer, M.** and **C.-J. Haster** (2020). Gravitational waveform accuracy requirements for future ground-based detectors. *Phys. Rev. Res.*, **2**(2), 023151. DOI. ARXIV:1912.10055. (cited on pg. 52).
472. **PyCBC** (2012). AdvVirgo function used for virgo psd. <https://pycbc.org/pycbc/latest/html/pycbc.psd.html>. (cited on pgs. 69 and 75).
473. **PyCBC** (2018a). aLIGOAPlusDesignSensitivityT1800042 function used for a+ psd. <https://pycbc.org/pycbc/latest/html/pycbc.psd.html>. (cited on pg. 66).
474. **PyCBC** (2018b). aLIGOZeroDetHighPower function used for adv ligo psd. <https://pycbc.org/pycbc/latest/html/pycbc.psd.html>. (cited on pgs. 66 and 75).
475. **Ramos-Buades, A., A. Buonanno,** and **J. Gair** (2023). Bayesian inference of binary black holes with inspiral-merger-ringdown waveforms using two eccentric parameters. *Phys. Rev. D*, **108**(12), 124063. DOI. ARXIV:2309.15528. (cited on pg. 36).
476. **Ramos-Buades, A., A. Buonanno, M. Khalil,** and **S. Ossokine** (2022). Effective-one-body multipolar waveforms for eccentric binary black holes with nonprecessing spins. *Phys. Rev. D*, **105**(4), 044035. DOI. ARXIV:2112.06952. (cited on pg. 48).
477. **Ramos-Buades, A., S. Tiwari, M. Haney,** and **S. Husa** (2020a). Impact of eccentricity on the gravitational wave searches for binary black holes: High mass case. *Phys. Rev. D*, **102**(4), 043005. DOI. ARXIV:2005.14016. (cited on pg. 46).
478. **Ramos-Buades, A. et al.** (2020b). First survey of spinning eccentric black hole mergers: Numerical relativity simulations, hybrid waveforms, and parameter estimation. *Phys. Rev. D*, **101**(8), 083015. DOI. ARXIV:1909.11011. (cited on pgs. 45 and 48).
479. **Ravichandran, A., A. Vijaykumar, S. J. Kapadia,** and **P. Kumar** (2023). Rapid Identification and Classification of Eccentric Gravitational Wave Inspirals with Machine Learning. ARXIV:2302.00666. (cited on pg. 46).
480. **Regimbau, T.** (2011). The astrophysical gravitational wave stochastic background. *Res. Astron. Astrophys.*, **11**, 369–390. DOI. ARXIV:1101.2762. (cited on pg. 30).
481. **Reitze, D. et al.** (2019). Cosmic Explorer: The U.S. Contribution to Gravitational-Wave Astronomy beyond LIGO. *Bull. Am. Astron. Soc.*, **51**(7), 035. ARXIV:1907.04833. (cited on pg. 20).
482. **Rickles, D.** and **C. M. DeWitt** (2011). The Role of Gravitation in Physics: Report from the 1957 Chapel Hill Conference. The Role of Gravitation in Physics: Report from the 1957 Chapel Hill Conference, Edited by Dean Rickles and Cécile M. DeWitt. ISBN: 978-3-945561-29-4, 2011. (cited on pg. 3).

483. **Rifat, N. E., S. E. Field, G. Khanna, and V. Varma** (2020). Surrogate model for gravitational wave signals from comparable and large-mass-ratio black hole binaries. *Phys. Rev. D*, **101**(8), 081502. DOI. ARXIV:1910.10473. (cited on pg. 53).
484. **Riles, K.** (2023). Searches for continuous-wave gravitational radiation. *Living Rev. Rel.*, **26**(1), 3. DOI. ARXIV:2206.06447. (cited on pg. 10).
485. **Rodriguez, C. L., P. Amaro-Seoane, S. Chatterjee, and F. A. Rasio** (2018). Post-Newtonian Dynamics in Dense Star Clusters: Highly-Eccentric, Highly-Spinning, and Repeated Binary Black Hole Mergers. *Phys. Rev. Lett.*, **120**(15), 151101. DOI. ARXIV:1712.04937. (cited on pgs. 44 and 45).
486. **Rodriguez, C. L., S. Chatterjee, and F. A. Rasio** (2016a). Binary Black Hole Mergers from Globular Clusters: Masses, Merger Rates, and the Impact of Stellar Evolution. *Phys. Rev. D*, **93**(8), 084029. DOI. ARXIV:1602.02444. (cited on pgs. 44 and 51).
487. **Rodriguez, C. L., I. Mandel, and J. R. Gair** (2012). Verifying the no-hair property of massive compact objects with intermediate-mass-ratio inspirals in advanced gravitational-wave detectors. *Phys. Rev. D*, **85**, 062002. DOI. ARXIV:1112.1404. (cited on pg. 57).
488. **Rodriguez, C. L., M. Zevin, C. Pankow, V. Kalogera, and F. A. Rasio** (2016b). Illuminating Black Hole Binary Formation Channels with Spins in Advanced LIGO. *Astrophys. J. Lett.*, **832**(1), L2. DOI. ARXIV:1609.05916. (cited on pgs. 50 and 51).
489. **Rodriguez, C. L. et al.** (2019). Black holes: The next generation—repeated mergers in dense star clusters and their gravitational-wave properties. *Phys. Rev. D*, **100**(4), 043027. DOI. ARXIV:1906.10260. (cited on pg. 51).
490. **Romano, J. D. and N. J. Cornish** (2017). Detection methods for stochastic gravitational-wave backgrounds: a unified treatment. *Living Rev. Rel.*, **20**(1), 2. DOI. ARXIV:1608.06889. (cited on pgs. 30 and 39).
491. **Romero-Shaw, I. M., N. Farrow, S. Stevenson, E. Thrane, and X.-J. Zhu** (2020a). On the origin of GW190425. *Mon. Not. Roy. Astron. Soc.*, **496**(1), L64–L69. DOI. ARXIV:2001.06492. (cited on pg. 47).
492. **Romero-Shaw, I. M., D. Gerosa, and N. Loutrel** (2023). Eccentricity or spin precession? Distinguishing subdominant effects in gravitational-wave data. *Mon. Not. Roy. Astron. Soc.*, **519**(4), 5352–5357. DOI. ARXIV:2211.07528. (cited on pgs. 47, 48, 60, and 78).
493. **Romero-Shaw, I. M., P. D. Lasky, and E. Thrane** (2019). Searching for Eccentricity: Signatures of Dynamical Formation in the First Gravitational-Wave Transient Catalogue of LIGO and Virgo. *Mon. Not. Roy. Astron. Soc.*, **490**(4), 5210–5216. DOI. ARXIV:1909.05466. (cited on pgs. 47 and 48).
494. **Romero-Shaw, I. M., P. D. Lasky, and E. Thrane** (2021). Signs of Eccentricity in Two

Gravitational-wave Signals May Indicate a Subpopulation of Dynamically Assembled Binary Black Holes. *Astrophys. J. Lett.*, **921**(2), L31. DOI. ARXIV:2108.01284. (cited on pgs. 44 and 47).

495. **Romero-Shaw, I. M., P. D. Lasky, and E. Thrane** (2022). Four Eccentric Mergers Increase the Evidence that LIGO–Virgo–KAGRA’s Binary Black Holes Form Dynamically. *Astrophys. J.*, **940**(2), 171. DOI. ARXIV:2206.14695. (cited on pgs. 44, 47, and 48).
496. **Romero-Shaw, I. M., P. D. Lasky, E. Thrane, and J. C. Bustillo** (2020*b*). GW190521: orbital eccentricity and signatures of dynamical formation in a binary black hole merger signal. *Astrophys. J. Lett.*, **903**(1), L5. DOI. ARXIV:2009.04771. (cited on pgs. 44, 47, and 48).
497. **Romero-Shaw, I. M. et al.** (2020*c*). Bayesian inference for compact binary coalescences with bilby: validation and application to the first LIGO–Virgo gravitational-wave transient catalogue. *Mon. Not. Roy. Astron. Soc.*, **499**(3), 3295–3319. DOI. ARXIV:2006.00714. (cited on pgs. 40 and 112).
498. **Rover, C., R. Meyer, and N. Christensen** (2006). Bayesian inference on compact binary inspiral gravitational radiation signals in interferometric data. *Class. Quant. Grav.*, **23**, 4895–4906. DOI. ARXIV:gr-qc/0602067. (cited on pg. 40).
499. **Rover, C., R. Meyer, and N. Christensen** (2007). Coherent Bayesian inference on compact binary inspirals using a network of interferometric gravitational wave detectors. *Phys. Rev. D*, **75**, 062004. DOI. ARXIV:gr-qc/0609131. (cited on pg. 40).
500. **Roy, S., A. S. Sengupta, and K. G. Arun** (2021). Unveiling the spectrum of inspiralling binary black holes. *Phys. Rev. D*, **103**(6), 064012. DOI. ARXIV:1910.04565. (cited on pg. 54).
501. **Ruthen, R.** (1992). Catching the wave. *Scientific American*, **266**(3), 90. DOI. (cited on pg. 6).
502. **Ryan, F. D.** (1997). Spinning boson stars with large self-interaction. *Phys. Rev. D*, **55**, 6081–6091. DOI. (cited on pgs. 55 and 56).
503. **Sachdev, S. et al.** (2019). The GstLAL Search Analysis Methods for Compact Binary Mergers in Advanced LIGO’s Second and Advanced Virgo’s First Observing Runs. ARXIV:1901.08580. (cited on pg. 35).
504. **Safarzadeh, M.** (2020). The branching ratio of LIGO binary black holes. *Astrophys. J. Lett.*, **892**(1), L8. DOI. ARXIV:2003.02764. (cited on pg. 51).
505. **Safarzadeh, M., W. M. Farr, and E. Ramirez-Ruiz** (2020). A trend in the effective spin distribution of LIGO binary black holes with mass. *Astrophys. J.*, **894**(2), 129. DOI. ARXIV:2001.06490. (cited on pg. 51).

506. **Safarzadeh, M.** and **K. Hotokezaka** (2020). Being Careful with the Field Formation Interpretation of GW190412. *Astrophys. J. Lett.*, **897**(1), L7. DOI. ARXIV:2005.06519. (cited on pg. 51).
507. **Saini, P., M. Favata,** and **K. G. Arun** (2022). Systematic bias on parametrized tests of general relativity due to neglect of orbital eccentricity. *Phys. Rev. D*, **106**(8), 084031. DOI. ARXIV:2203.04634. (cited on pg. 45).
508. **Saini, P.** and **N. V. Krishnendu** (2024). Constraining the nature of dark compact objects with spin-induced octupole moment measurement. *Phys. Rev. D*, **109**(2), 024009. DOI. ARXIV:2308.01309. (cited on pg. 57).
509. **Saleem, M. et al.** (2022a). Population inference of spin-induced quadrupole moments as a probe for nonblack hole compact binaries. *Phys. Rev. D*, **105**(10), 104066. DOI. ARXIV:2111.04135. (cited on pg. 57).
510. **Saleem, M. et al.** (2022b). The science case for LIGO-India. *Class. Quant. Grav.*, **39**(2), 025004. DOI. ARXIV:2105.01716. (cited on pg. 20).
511. **Salemi, F. et al.** (2019). Wider look at the gravitational-wave transients from GWTC-1 using an unmodeled reconstruction method. *Phys. Rev. D*, **100**(4), 042003. DOI. ARXIV:1905.09260. (cited on pg. 47).
512. **Samsing, J., M. MacLeod,** and **E. Ramirez-Ruiz** (2014). The Formation of Eccentric Compact Binary Inspirals and the Role of Gravitational Wave Emission in Binary-Single Stellar Encounters. *Astrophys. J.*, **784**, 71. DOI. ARXIV:1308.2964. (cited on pg. 51).
513. **Samsing, J.** and **E. Ramirez-Ruiz** (2017). On the Assembly Rate of Highly Eccentric Binary Black Hole Mergers. *Astrophys. J. Lett.*, **840**(2), L14. DOI. ARXIV:1703.09703. (cited on pg. 45).
514. **Santamaria, L. et al.** (2010). Matching post-Newtonian and numerical relativity waveforms: systematic errors and a new phenomenological model for non-precessing black hole binaries. *Phys. Rev. D*, **82**, 064016. DOI. ARXIV:1005.3306. (cited on pg. 49).
515. **Sasaki, M.** and **H. Tagoshi** (2003). Analytic black hole perturbation approach to gravitational radiation. *Living Rev. Rel.*, **6**, 6. DOI. ARXIV:gr-qc/0306120. (cited on pg. 56).
516. **Sathyaprakash, B., B. Schutz,** and **C. Van Den Broeck** (2010). Cosmography with the Einstein Telescope. *Class. Quant. Grav.*, **27**, 215006. DOI. ARXIV:0906.4151. (cited on pg. 54).
517. **Sathyaprakash, B. S.** and **B. F. Schutz** (2009). Physics, Astrophysics and Cosmology with Gravitational Waves. *Living Rev. Rel.*, **12**, 2. DOI. ARXIV:0903.0338. (cited on

pgs. 16 and 18).

518. **Scheel, M. A. et al.** (2015). Improved methods for simulating nearly extremal binary black holes. *Class. Quant. Grav.*, **32**(10), 105009. DOI. ARXIV:1412.1803. (cited on pg. 74).
519. **Schmidt, P., M. Hannam, and S. Husa** (2012). Towards models of gravitational waveforms from generic binaries: A simple approximate mapping between precessing and non-precessing inspiral signals. *Phys. Rev. D*, **86**, 104063. DOI. ARXIV:1207.3088. (cited on pg. 49).
520. **Schmidt, P., F. Ohme, and M. Hannam** (2015). Towards models of gravitational waveforms from generic binaries II: Modelling precession effects with a single effective precession parameter. *Phys. Rev. D*, **91**(2), 024043. DOI. ARXIV:1408.1810. (cited on pg. 49).
521. **Schutz, B. F.**, *Data processing, analysis, and storage for interferometric antennas*. Cambridge University Press, 1991, 406–452. DOI. (cited on pg. 33).
522. **Sciama, D. W., G. B. Field, and M. J. Rees** (1969). Upper Limit to Radiation of Mass Energy Derived from Expansion of Galaxy. *Phys. Rev. Lett.*, **23**, 1514–1515. DOI. (cited on pg. 4).
523. **Sennett, N., R. Brito, A. Buonanno, V. Gorbenko, and L. Senatore** (2020). Gravitational-Wave Constraints on an Effective Field-Theory Extension of General Relativity. *Phys. Rev. D*, **102**(4), 044056. DOI. ARXIV:1912.09917. (cited on pg. 53).
524. **Sesana, A.** (2007). Extreme recoils: impact on the detection of gravitational waves from massive black hole binaries. *Mon. Not. Roy. Astron. Soc.*, **382**, 6. DOI. ARXIV:0707.4677. (cited on pg. 51).
525. **Shaik, F. H. et al.** (2020). Impact of subdominant modes on the interpretation of gravitational-wave signals from heavy binary black hole systems. *Phys. Rev. D*, **101**(12), 124054. DOI. ARXIV:1911.02693. (cited on pgs. 52 and 55).
526. **Shao, Y. and X.-D. Li** (2021). Population Synthesis of Black Hole Binaries with Compact Star Companions. *Astrophys. J.*, **920**(2), 81. DOI. ARXIV:2107.03565. (cited on pg. 30).
527. **Shoemaker, D. and LIGO Scientific Collaboration** (2019). Gravitational wave astronomy with LIGO and similar detectors in the next decade. *BAAS*, **51**(3), 452. ARXIV:1904.03187. (cited on pg. 146).
528. **Shoemaker, D. et al.**, Progress with the Garching (West Germany) 30 meter prototype for a gravitational wave detector. *In Presented at 4th Marcel Grossmann Meeting*. 1985. URL: <https://ui.adsabs.harvard.edu/abs/1985magr.meet.....S>. (cited on pgs. 5 and 6).

529. **Shoemaker, D. et al.** (1988). Noise Behavior of the Garching 30-meter Prototype Gravitational Wave Detector. *Phys. Rev. D*, **38**, 423–432. DOI. (cited on pg. 5).
530. **Singer, L. P. and L. R. Price** (2016). Rapid Bayesian position reconstruction for gravitational-wave transients. *Phys. Rev. D*, **93**(2), 024013. DOI. ARXIV:1508.03634. (cited on pg. 40).
531. **Singer, L. P. et al.** (2016). Going the Distance: Mapping Host Galaxies of LIGO and Virgo Sources in Three Dimensions Using Local Cosmography and Targeted Follow-up. *Astrophys. J. Lett.*, **829**(1), L15. DOI. ARXIV:1603.07333. (cited on pg. 40).
532. **Singh, M. K., Divyajyoti, S. J. Kapadia, M. A. Shaikh, and P. Ajith** (2022). Improved early-warning estimates of luminosity distance and orbital inclination of compact binary mergers using higher modes of gravitational radiation. *Mon. Not. Roy. Astron. Soc.*, **513**(3), 3798–3809. DOI. ARXIV:2202.05802. (cited on pgs. viii and 55).
533. **Singh, M. K., S. J. Kapadia, M. A. Shaikh, D. Chatterjee, and P. Ajith** (2021). Improved early warning of compact binary mergers using higher modes of gravitational radiation: A population study. *Mon. Not. Roy. Astron. Soc.*, **502**(2), 1612–1622. DOI. ARXIV:2010.12407. (cited on pg. 55).
534. **Skilling, J.**, Nested Sampling. In **R. Fischer, R. Preuss, and U. V. Toussaint** (eds.), *Bayesian Inference and Maximum Entropy Methods in Science and Engineering: 24th International Workshop on Bayesian Inference and Maximum Entropy Methods in Science and Engineering*, volume 735 of *American Institute of Physics Conference Series*. 2004. DOI. (cited on pg. 42).
535. **Smith, R. J. E., G. Ashton, A. Vajpeyi, and C. Talbot** (2020). Massively parallel Bayesian inference for transient gravitational-wave astronomy. *MNRAS*, **498**(3), 4492–4502. DOI. ARXIV:1909.11873. (cited on pg. 48).
536. **Speagle, J. S.** (2020). DYNesty: a dynamic nested sampling package for estimating Bayesian posteriors and evidences. *MNRAS*, **493**(3), 3132–3158. DOI. ARXIV:1904.02180. (cited on pgs. 42 and 43).
537. **SXS Collaboration** (2019). Numerical relativity simulations. <http://www.black-holes.org/waveforms>. (cited on pg. 74).
538. **Tagawa, H., B. Kocsis, Z. Haiman, I. Bartos, K. Omukai, and J. Samsing** (2021a). Eccentric Black Hole Mergers in Active Galactic Nuclei. *Astrophys. J. Lett.*, **907**(1), L20. DOI. ARXIV:2010.10526. (cited on pgs. 44, 45, and 102).
539. **Tagawa, H., B. Kocsis, Z. Haiman, I. Bartos, K. Omukai, and J. Samsing** (2021b). Mass-gap Mergers in Active Galactic Nuclei. *Astrophys. J.*, **908**(2), 194. DOI. ARXIV:2012.00011. (cited on pg. 102).

540. **Tagoshi, H., C. K. Mishra, A. Pai, and K. Arun** (2014). Parameter estimation of neutron star-black hole binaries using an advanced gravitational-wave detector network: Effects of the full post-Newtonian waveform. *Phys. Rev. D*, **90**(2), 024053. DOI: [ARXIV:1403.6915](#). (cited on pg. 54).
541. **Tai, K. S., S. T. McWilliams, and F. Pretorius** (2014). Detecting gravitational waves from highly eccentric compact binaries. *Phys. Rev. D*, **90**(10), 103001. DOI: [ARXIV:1403.7754](#). (cited on pg. 46).
542. **Tanay, S., M. Haney, and A. Gopakumar** (2016). Frequency and time domain inspiral templates for comparable mass compact binaries in eccentric orbits. *Phys. Rev. D*, **93**(6), 064031. DOI: [ARXIV:1602.03081](#). (cited on pgs. 48 and 72).
543. **Taracchini, A. et al.** (2014). Effective-one-body model for black-hole binaries with generic mass ratios and spins. *Phys. Rev. D*, **89**(6), 061502. DOI: [ARXIV:1311.2544](#). (cited on pg. 27).
544. **Taylor, J. H., L. A. Fowler, and P. M. McCulloch** (1979). Measurements of general relativistic effects in the binary pulsar PSR1913 + 16. *Nature*, **277**(5696), 437–440. DOI: [DOI](#). (cited on pg. 5).
545. **Taylor, S. R., E. A. Huerta, J. R. Gair, and S. T. McWilliams** (2016). Detecting eccentric supermassive black hole binaries with pulsar timing arrays: Resolvable source strategies. *Astrophys. J.*, **817**(1), 70. DOI: [ARXIV:1505.06208](#). (cited on pgs. 45 and 46).
546. **TEOBResumS** (2021). Default setting for generating teobresums eccentric waveforms. https://bitbucket.org/eob_ihes/teobresums/src/a3715ef7b6382f52a801260607814ea836da9b70/Python/Utils/test_eccentric.py?at=eccentric#lines-191. (cited on pg. 87).
547. **Thorne, K. S.**, Gravitational radiation. In **S. Hawking and W. Israel** (eds.), *Three hundred years of gravitation*. Cambridge University Press, 1987. (cited on pgs. 5, 33, and 34).
548. **Tiwari, V. et al.** (2016). Proposed search for the detection of gravitational waves from eccentric binary black holes. *Phys. Rev. D*, **93**(4), 043007. DOI: [ARXIV:1511.09240](#). (cited on pg. 47).
549. **Trias, M. and A. M. Sintes** (2008). LISA observations of supermassive black holes: Parameter estimation using full post-Newtonian inspiral waveforms. *Phys. Rev. D*, **77**, 024030. DOI: [ARXIV:0707.4434](#). (cited on pg. 52).
550. **Tutukov, A. V. and L. R. Yungelson** (1993). The merger rate of neutron star and black hole binaries. *MNRAS*, **260**, 675–678. DOI: [DOI](#). (cited on pg. 51).
551. **Uchikata, N., H. Nakano, T. Narikawa, N. Sago, H. Tagoshi, and T. Tanaka** (2019).

- Searching for black hole echoes from the LIGO-Virgo Catalog GWTC-1. *Phys. Rev. D*, **100**(6), 062006. DOI. ARXIV:1906.00838. (cited on pg. 32).
552. **Uchikata, N.** and **S. Yoshida** (2016). Slowly rotating thin shell gravastars. *Class. Quant. Grav.*, **33**(2), 025005. DOI. ARXIV:1506.06485. (cited on pg. 57).
553. **Uchikata, N.**, **S. Yoshida**, and **P. Pani** (2016). Tidal deformability and i-love-q relations for gravastars with polytropic thin shells. *Phys. Rev. D*, **94**(6), 064015. DOI. ARXIV:1607.03593. (cited on pg. 55).
554. **Unnikrishnan, C. S.** (2024). LIGO-India: A Decadal Assessment on Its Scope, Relevance, Progress, and Future. *International Journal of Modern Physics D*, **0**(0), 2450025. DOI. ARXIV:2301.07522. (cited on pg. 20).
555. **Usman, S. A.**, **J. C. Mills**, and **S. Fairhurst** (2019). Constraining the Inclinations of Binary Mergers from Gravitational-wave Observations. *Astrophys. J.*, **877**(2), 82. DOI. ARXIV:1809.10727. (cited on pgs. 54 and 64).
556. **Usman, S. A. et al.** (2016). The PyCBC search for gravitational waves from compact binary coalescence. *Class. Quant. Grav.*, **33**(21), 215004. DOI. ARXIV:1508.02357. (cited on pgs. 27, 35, and 41).
557. **Vallisneri, M.** (2008). Use and abuse of the Fisher information matrix in the assessment of gravitational-wave parameter-estimation prospects. *Phys. Rev. D*, **77**, 042001. DOI. ARXIV:gr-qc/0703086. (cited on pg. 158).
558. **Van Den Broeck, C.** and **A. S. Sengupta** (2007a). Binary black hole spectroscopy. *Class. Quant. Grav.*, **24**, 1089–1114. DOI. ARXIV:gr-qc/0610126. (cited on pgs. 52, 54, and 136).
559. **Van Den Broeck, C.** and **A. S. Sengupta** (2007b). Phenomenology of amplitude-corrected post-Newtonian gravitational waveforms for compact binary inspiral. I. Signal-to-noise ratios. *Class. Quant. Grav.*, **24**, 155–176. DOI. ARXIV:gr-qc/0607092. (cited on pg. 54).
560. **van der Sluys, M. et al.** (2008a). Parameter estimation of spinning binary inspirals using Markov-chain Monte Carlo. *Class. Quant. Grav.*, **25**, 184011. DOI. ARXIV:0805.1689. (cited on pg. 40).
561. **van der Sluys, M. V. et al.** (2008b). Gravitational-Wave Astronomy with Inspiral Signals of Spinning Compact-Object Binaries. *Astrophys. J. Lett.*, **688**, L61. DOI. ARXIV:0710.1897. (cited on pg. 40).
562. **Varma, V.** and **P. Ajith** (2017). Effects of nonquadrupole modes in the detection and parameter estimation of black hole binaries with nonprecessing spins. *Phys. Rev. D*, **96**(12), 124024. DOI. ARXIV:1612.05608. (cited on pgs. 52, 54, and 71).

563. **Varma, V., P. Ajith, S. Husa, J. C. Bustillo, M. Hannam, and M. Pürrer** (2014). Gravitational-wave observations of binary black holes: Effect of nonquadrupole modes. *Phys. Rev. D*, **90**(12), 124004. DOI. ARXIV:1409.2349. (cited on pgs. 52 and 54).
564. **Varma, V., D. Gerosa, L. C. Stein, F. Hébert, and H. Zhang** (2019a). High-accuracy mass, spin, and recoil predictions of generic black-hole merger remnants. *Phys. Rev. Lett.*, **122**(1), 011101. DOI. ARXIV:1809.09125. (cited on pg. 74).
565. **Varma, V. et al.** (2019b). Surrogate model of hybridized numerical relativity binary black hole waveforms. *Phys. Rev. D*, **99**(6), 064045. DOI. ARXIV:1812.07865. (cited on pgs. 53 and 74).
566. **Varma, V. et al.** (2019c). Surrogate models for precessing binary black hole simulations with unequal masses. *Phys. Rev. Research.*, **1**, 033015. DOI. ARXIV:1905.09300. (cited on pgs. 53 and 74).
567. **Varma, V. et al.** (2021). Up-down instability of binary black holes in numerical relativity. *Phys. Rev. D*, **103**, 064003. DOI. ARXIV:2012.07147. (cited on pg. 74).
568. **Veitch, J. and A. Vecchio** (2008). A Bayesian approach to the follow-up of candidate gravitational wave signals. *Phys. Rev. D*, **78**, 022001. DOI. ARXIV:0801.4313. (cited on pg. 40).
569. **Veitch, J. and A. Vecchio** (2010). Bayesian coherent analysis of in-spiral gravitational wave signals with a detector network. *Phys. Rev. D*, **81**, 062003. DOI. ARXIV:0911.3820. (cited on pg. 40).
570. **Veitch, J. et al.** (2015). Parameter estimation for compact binaries with ground-based gravitational-wave observations using the LALInference software library. *Phys. Rev. D*, **91**(4), 042003. DOI. ARXIV:1409.7215. (cited on pgs. 40 and 43).
571. **Vigeland, S. J. and M. Vallisneri** (2014). Bayesian inference for pulsar timing models. *Mon. Not. Roy. Astron. Soc.*, **440**(2), 1446–1457. DOI. ARXIV:1310.2606. (cited on pg. 40).
572. **Virgo detector technology** (2021). URL: <https://www.virgo-gw.eu/science/detector/>. (cited on pg. 19).
573. **Vishveshwara, C. V.** (1970). Stability of the schwarzschild metric. *Phys. Rev. D*, **1**, 2870–2879. DOI. (cited on pg. 32).
574. **Voss, R. and T. M. Tauris** (2003). Galactic distribution of merging neutron stars and black holes - prospects for short gamma-ray burst progenitors and LIGO/VIRGO. *MNRAS*, **342**(4), 1169–1184. DOI. ARXIV:astro-ph/0303227. (cited on pg. 51).
575. **Wang, Y.-F. and A. H. Nitz** (2021). Prospects for detecting gravitational waves from eccentric subsolar mass compact binaries. *Astrophys. J.*, **912**(1), 53. DOI.

- ARXIV:2101.12269. (cited on pg. 46).
576. **Weber, J.** (1960). Detection and Generation of Gravitational Waves. *Phys. Rev.*, **117**, 306–313. DOI. (cited on pg. 4).
577. **Weber, J.** (1966). Observation of the Thermal Fluctuations of a Gravitational-Wave Detector. *Phys. Rev. Lett.*, **17**, 1228–1230. DOI. (cited on pg. 4).
578. **Weber, J.** (1969). Evidence for discovery of gravitational radiation. *Phys. Rev. Lett.*, **22**, 1320–1324. DOI. (cited on pg. 4).
579. **Weber, J.** (1970). Anisotropy and polarization in the gravitational-radiation experiments. *Phys. Rev. Lett.*, **25**, 180–184. DOI. (cited on pg. 4).
580. **Weber, J.** (1971). The detection of gravitational waves. *Scientific American*, **224**(5), 22–29. ISSN 00368733, 19467087. URL: <http://www.jstor.org/stable/24927792>. (cited on pg. 4).
581. **Weiss, R.** (1976). Interferometric broad band gravitational antenna. URL: https://dspace.mit.edu/bitstream/handle/1721.1/56655/RLE_PR_119_XV.pdf N.S.F. Grant MPS75-04033. (cited on pgs. 5 and 6).
582. **Weiss, R.** (2000). Interview by shirley k. cohen. pasadena, california, may 10, 2000. URL: http://resolver.caltech.edu/CaltechOH:OH_Weiss_R. Oral History Project, California Institute of Technology Archives. (cited on pg. 5).
583. **Westerweck, J. et al.** (2018). Low significance of evidence for black hole echoes in gravitational wave data. *Phys. Rev. D*, **97**(12), 124037. DOI. ARXIV:1712.09966. (cited on pg. 32).
584. **Wiaux, Y., L. Jacques, and P. Vanderghenst** (2007). Fast spin +2 spherical harmonics transforms. *J. Comput. Phys.*, **226**, 2359–2371. DOI. ARXIV:astro-ph/0508514. (cited on pg. 135).
585. **Will, C. M.** (1998). Bounding the mass of the graviton using gravitational wave observations of inspiralling compact binaries. *Phys. Rev. D*, **57**, 2061–2068. DOI. ARXIV:gr-qc/9709011. (cited on pg. 32).
586. **Winkler, W. et al.**, Plans for a large gravitational wave antenna in Germany. *In Presented at 4th Marcel Grossmann Meeting*. 1985. URL: <https://ui.adsabs.harvard.edu/abs/1985magr.meet.....W>. (cited on pg. 5).
587. **Xu, Y. and E. Hamilton** (2023). Measurability of precession and eccentricity for heavy binary-black-hole mergers. *Phys. Rev. D*, **107**(10), 103049. DOI. ARXIV:2211.09561. (cited on pg. 60).
588. **Yang, Y. et al.** (2019). Hierarchical Black Hole Mergers in Active Galactic Nuclei. *Phys.*

Rev. Lett., **123**(18), 181101. DOI. ARXIV:1906.09281. (cited on pg. 102).

589. **Yunes, N., K. G. Arun, E. Berti, and C. M. Will** (2009). Post-Circular Expansion of Eccentric Binary Inspirals: Fourier-Domain Waveforms in the Stationary Phase Approximation. *Phys. Rev. D*, **80**(8), 084001. DOI. [Erratum: *Phys.Rev.D* 89, 109901 (2014)]. ARXIV:0906.0313. (cited on pg. 48).
590. **Yunes, N. and F. Pretorius** (2009). Fundamental Theoretical Bias in Gravitational Wave Astrophysics and the Parameterized Post-Einsteinian Framework. *Phys. Rev. D*, **80**, 122003. DOI. ARXIV:0909.3328. (cited on pgs. 31 and 55).
591. **Yunes, N. and X. Siemens** (2013). Gravitational-Wave Tests of General Relativity with Ground-Based Detectors and Pulsar Timing-Arrays. *Living Rev. Rel.*, **16**, 9. DOI. ARXIV:1304.3473. (cited on pg. 15).
592. **Zackay, B., L. Dai, and T. Venumadhav** (2018). Relative Binning and Fast Likelihood Evaluation for Gravitational Wave Parameter Estimation. ARXIV:1806.08792. (cited on pg. 40).
593. **Zevin, M., I. M. Romero-Shaw, K. Kremer, E. Thrane, and P. D. Lasky** (2021). Implications of Eccentric Observations on Binary Black Hole Formation Channels. *Astrophys. J. Lett.*, **921**(2), L43. DOI. ARXIV:2106.09042. (cited on pgs. 31, 45, and 70).
594. **Zevin, M., J. Samsing, C. Rodriguez, C.-J. Haster, and E. Ramirez-Ruiz** (2019). Eccentric Black Hole Mergers in Dense Star Clusters: The Role of Binary–Binary Encounters. *Astrophys. J.*, **871**(1), 91. DOI. ARXIV:1810.00901. (cited on pg. 102).
595. **Ziosi, B. M., M. Mapelli, M. Branchesi, and G. Tormen** (2014). Dynamics of stellar black holes in young star clusters with different metallicities – II. Black hole–black hole binaries. *Mon. Not. Roy. Astron. Soc.*, **441**(4), 3703–3717. DOI. ARXIV:1404.7147. (cited on pg. 51).